Conceptual Design Optimization of an Augmented Stability Aircraft Incorporating Dynamic Response Performance Constraints

by

Jason Welstead

A dissertation submitted to the Graduate Faculty of
Auburn University
in partial fulfillment of the
requirements for the Degree of
Doctor of Philosophy

Auburn, Alabama
December 13, 2014

Keywords: engineering, conceptual aircraft design, stability,
active control, flight dynamics, multidisciplinary design optimization

Approved by

Gilbert L. Crouse, Jr., Chair, Associate Professor of Aerospace Engineering
Winfred A. Foster, Jr., Professor of Aerospace Engineering
Roy Hartfield, Jr., Professor of Aerospace Engineering
Andrew Sinclair, Associate Professor of Aerospace Engineering

Abstract

This research focused on incorporating stability and control into a multidisciplinary design optimization on a Boeing 737-class advanced concept called the D8.2b. A new method of evaluating the aircraft handling performance using quantitative evaluation of the system to disturbances, including perturbations, continuous turbulence, and discrete gusts, is presented.

A multidisciplinary design optimization was performed using the D8.2b transport aircraft concept. The configuration was optimized for minimum fuel burn using a design range of 3,000 nautical miles. Optimization cases were run using fixed tail volume coefficients, static trim constraints, and static trim and dynamic response constraints. A Cessna 182T model was used to test the various dynamic analysis components, ensuring the analysis was behaving as expected. Results of the optimizations show that including stability and control in the design process drastically alters the optimal design, indicating that stability and control should be included in conceptual design to avoid system level penalties later in the design process.

Acknowledgments

The author would like to thank first and foremost Dr. Gilbert L. Crouse, Jr. for his support and guidance throughout the dissertation process. Also, without the continuous encouragement of Mike Marcolini and Mark Guynn of the Aeronautics Systems Analysis Branch at NASA Langley Research Center, this dissertation would never have been completed. Additional thanks goes to the dissertation committee, Dr. Winfred Foster, Jr., Dr. Roy Hartfield, Jr., and Dr. Andrew Sinclair for their unfailing support over the last five years, answering phone calls and questions whenever possible. The author would like to specifically acknowledge Karl Geiselhart and Erik Olson of the Aeronautics Systems Analysis Branch at NASA Langley Research Center. Karl answered an exuberant number of questions, always with pleasure, gave guidance in computational resources and strategy, immediately made customizations and bug fixes to ModelCenter® ScriptWrappers as needed, and suggested modeling strategies addressing the research needs. A special thanks also goes to Erik Olson, who stayed late one afternoon to work with the author when he was failing to grasp the ModelCenter mentality, letting the software handle the data management. It was through this interaction that the author finally understood how to interconnect different analysis within the ModelCenter environment. The author would also like to thank Andrea Storch for her time, guidance, and advice concerning the optimization techniques used. She was always willing listen and field numerous questions, providing her experience and knowledge of optimization techniques.

Brian Reitz, a best friend and colleague of the author deserves special recognition as without him, the author would have never made it to the end of this process. Starting graduate school together, many trials and challenges, highs and lows have been experienced together since the Fall of 2007 only to finish together in the end. The author would also like

to give a wonderful thanks to all of his family for their continuous support, encouragement, and belief in him, even when he did not believe himself. Finally, the author would like to give a most special thanks to his loving wife, Bethany, whose support was unfailing; always positive, supportive, and encouraging even through the late nights after work and weekends, removing all extraneous distractions to support the completion of this dissertation. Thank you.

Table of Contents

List of Figures

List of Tables

Nomenclature

Acronyms

AEO	All engines operating
AVL	Athena Vortex Lattice
BLI	Boundary layer ingestion
CFD	Computational fluid dynamics
CG	Center of gravity
DCFC	Design-constraining flight conditions
EDET	Empirical Drag Estimation Technique
EOM	Equations of motion
FAA	Federal Aviation Administration
FAR	Federal Aviation Regulation
FDC	Flight dynamics and controls
FLOPS	Flight Optimization System
GW	Gross weight
HT	Horizontal tail
LMI	Linear matrix inequality
LQR	Linear quadratic regulator

LTI	Linear time invariant
MAC	Mean aerodynamic chord
MDO	Multidisciplinary design optimization
MIMO	Multi-input multi-output
MIT	Massachusetts Institute of Technology
NACA	National Advisory Committee for Aeronautics
NASA	National Aeronautics and Space Administration
OEI	One engine inoperative
PI	Performance index
POH	Pilots' Operating Handbook
RMS	Root-mean-square
RSS	Relaxed static stability
S&D	Specification and Description
SISO	Single-input single-output
SM	Static margin
TASOPT	Transport Aircraft System Optimization
TO	Takeoff
TOL	Takeoff and landing
VSP	Open Vehicle Sketch Pad
VT	Vertical tail

Greek Symbols

α	Angle of attack
$\alpha_{HT_{eff}}$	Horizontal tail effective angle of attack
$\alpha_{HT_{L=0}}$	Horizontal tail zero-lift angle of attack
β	Angle of sideslip
δ	Control input vector
δ_a	Aileron deflection angle
δ_e	Elevator deflection angle
δ_r	Rudder deflection angle
Γ	Quarter-chord dihedral angle
Λ	Quarter-chord sweep angle
λ	taper ratio
Ω	Spatial frequency
ω	Temporal frequency
ϕ	Roll Euler angle
Φ_g	One-sided von Kármán turbulence spectra
ψ	Yaw Euler angle
$\sigma_{u,v,w}$	Atmospheric disturbance intensity x, y, z-components
τ	Time constant
θ	Pitch Euler angle

Symbols

A	State matrix
AR	Aspect ratio
B	Input matrix
b	Wing span
B_g	Gust input matrix
$\bar{c}$	Mean aerodynamic chord
C_{D_0}	Parasite drag coefficient
C_D	Drag coefficient
C_H	Horizontal tail volume coefficient
C_L	Lift coefficient
C_l	Rolling moment coefficient
C_m	Pitching moment coefficient
C_n	Yawing moment coefficient
C_S	Side force coefficient
C_T	Thrust coefficient
C_V	Vertical tail volume coefficient
C_{W_0}	Weight coefficient
C_Y	Side force coefficient
d_m	Discrete gust half length

E	Generalized inertial matrix
e	Error
e_m	Maximum allowed constraint violation
e_t	Total constraint violation
f	Fitness function
G	System transfer function
H	Performance output weighting matrix
h	Altitude
$\mathscr{H}$	Hamiltonian
I	Identity matrix
i	Imaginary number ($\sqrt{-1}$)
$I_{x,y,z,xz}$	Mass moments of inertia
J	Linear quadratic regulator performance index
K	Gain matrix
$L_{u,v,w}$	Turbulence length scale
M	Mach number
N_p	Number of preserved designs
o	Objective function
p	Penalty function
p, q, r	Angular rate x, y, z-components

p^*	Percent penalty
P_c	Probability of crossover
P_m	Probability of mutation
Q	State variable weighting matrix
q_∞	Free-stream dynamic pressure
R	Control variable weighting matrix
$R_{x,y,z}$	Radii of gyration
S	Matrix of Lagrange multipliers
S	Wing area
s	Laplace variable
T	Thrust
t	Time
u	Actuator input vector
u, v, w	Velocity x, y, z-components
$\bar{U}$	Steady-state velocity
u_g	Gust input vector
V_m	Discrete gust peak magnitude
W	Control input weighting matrix
W	Weight
x	State vector

$X_{W_{apex}}$	Wing apex location
z	Performance output vector

Chapter 1

Introduction

Current trends in transport aircraft conceptual design search for technologies that provide incremental performance improvements, many focusing on engine efficiency and drag reduction technologies resulting in reduced mission fuel burn. The National Aeronautics and Space Administration (NASA) is pushing for future transport concepts that go beyond incremental reductions in fuel burn, noise, and emissions. Achieving the aggressive reduction goals set forth by NASA will require a complex, multidisciplinary design process, integrating each discipline early in the design phase. Historically, aircraft conceptual design has included aerodynamics, sizing, weight estimation, propulsion, and mission analysis. Stability and control, and structural design, among others, often have been left with a fixed design that is frequently a sub-optimum solution for those disciplines, leading to system level penalties. To achieve the aggressive performance goals set by NASA's Fixed Wing (soon to be Advanced Air Transport Technologies) Project, a full integration of all disciplines is required.

Aircraft drag consists of a combination of lift-independent and lift-dependent, mostly induced when sub-transonic, drag. In commercial aircraft, the trend is to increase wing span to achieve a lift-dependent drag benefit. Increasing aircraft span, and aspect ratio for a fixed wing area, reduces lift-induced drag, but aspect ratio is currently limited both by structural (flutter) and dimensional constraints (airport operations). For subsonic flight, the total aircraft lift-independent (parasite) drag consists mostly of skin-friction and separated flow pressure drag [1]. With fairings and surface blending, much of the pressure drag can be minimized, leaving skin-friction drag as the largest contributor to parasite drag. Effectively, if the wetted area of the aircraft can be minimized, the skin-friction drag will be minimized, resulting in reduced parasite drag. Numerous designs have reduced this wetted area by using tailless configurations, such as the Convair F-106, the Convair B-58, the Messerschmitt 163B, and the Northrop Grumman B-2 [2, 3]. All of these configurations have low aspect ratios, resulting in reduced cruise efficiency and low-speed aerodynamic performance. It would be beneficial if both the induced drag and parasite drag could be reduced simultaneously.

For a conventional configuration, eliminating lift produced by the empennage can reduce aircraft induced drag, even if the tail is producing positive lift. Aerodynamic efficiency is a function of span loading, and the horizontal stabilizer aspect ratio, for stall considerations related to safety, is less than that of the main wing. As induced drag coefficient is a function of aspect ratio, any lift produced by the empennage with span loading less than the main wing is less efficient, resulting in an induced drag penalty.

Adjusting the aircraft static margin is a way to reduce induced drag on the empennage. As the static margin decreases, the aircraft will first become decreasingly statically stable, then neutrally stable, and eventually become unstable as the static margin becomes negative. Decreasing the static stability reduces the load on the horizontal stabilizer, allowing for greater aerodynamic efficiency and reduced structural weight. Many modern aircraft, both commercial and military, are designed with relaxed static stability, the intentional decrease of static margin, which requires some form of stability augmentation in order to reduce the trim-drag penalty [4–6]. As stated by Raymer, "[A] modern and sophisticated aft-tail aircraft is designed to a slight level of instability so that it normally flies with an upload, not a download on its tail. This is the very reason that computerized flight control systems with artificial stability were developed and put into production" [1].

Classical aircraft design uses volume coefficients when sizing an aircraft's empennage, which tends to produce conservative estimates for the stabilizer areas [7]. As a result, the surface area for the horizontal and vertical stabilizers exceed the necessary area for both static and dynamic stability. Additionally, this fails to take into account the benefits of augmented stability provided by the active control systems in modern aircraft. As mentioned previously, a majority of parasite drag results from skin friction over the wetted area of the aircraft.

Augmenting the aircraft's stability will allow the stabilizing surfaces to be reduced in size, thus reducing the total wetted area of the aircraft. In doing so, not only can the induced drag be reduced from the relaxed static stability, but the total parasite drag can be reduced from the decrease in wetted area.

The benefits of designing for relaxed static stability are not unbounded, however. With additional instability, the workload of the active control system increases to a point where it can no longer provide adequate dynamic stability to the aircraft. Although the total drag may continue to decrease, the design becomes infeasible and uncontrollable. Additionally, the active control system needs to stabilize the aircraft dynamics in such a way so as to provide acceptable handling qualities. For manned aircraft, MIL-F-8785C (Ref. [8]) was formulated from years of handling-qualities research as a guideline which has been used extensively in both military and commercial aircraft. These handling-quality guidelines were developed using flight tests and simulators which were influenced by pilot opinion. The current handling qualities specifications, MIL-STD-1797A [9] which evolved from MIL-F-8785C [8], require natural frequencies and damping specific to each system linear mode, a limitation if the typical linear modes do not exist. For unconventional, advanced configurations with stability augmentation systems, this can be the case.

Multidisciplinary analysis is required to capture all the coupled effects between aircraft sizing, aerodynamics, weight estimation, propulsion, and stability and control. Presented here is a methodology for integrating stability and control into the conceptual design process, where emphasis was placed on using conceptual level design parameters and reduced inputs for the controller. Atmospheric disturbances and perturbations were used to stress the flight dynamic system with static and dynamic constraints placed on the system response, used to size the configuration in a design optimization. Using this methodology, the stabilizers were sized using static and dynamic constraints with augmented stability, a physics-based approach, instead of the empirical tail volume coefficient. Multidisciplinary design optimization was used to minimize fuel burn on a D8 advanced transport aircraft concept, shown in Fig. 1.1[1], including stability and control in the design analysis.

Figure 1.1: Conceptual sketch of the D8 advanced transport aircraft concept.

The D8 geometry is a Boeing 737 class unconventional geometry currently being studied by the Massachusetts Institute of Technology (MIT) and NASA, with key features including a double-bubble fuselage and rear embedded engines using boundary layer ingestion (BLI) [10–13]. Two concepts were developed in Ref. [10], both designed for a 3,000 nautical mile mission focusing on fuel burn minimization. The first concept was a current technology concept showing the configuration benefits alone, and the second was an advanced N+3 (now plus three generations beyond current commercial aircraft[2]) technology concept with expected entry into service near 2035. The current technology D8 concept was used in this research.

The process chart of Fig. 1.2 shows a high level overview of the analysis methodology used to incorporate stability and control into the conceptual design process. A combination of the NASA Flight Optimization System (FLOPS) [14] and custom scripts defined the geometry and are discussed in Sections 3.1, 5.2.2, and 5.3.1. The stability and control derivative and aerodynamic analyses used the vortex lattice code Athena Vortex Lattice (AVL) discussed in Section 5.1, and the flight dynamics and system disturbances were programed using MATLAB®, discussed in Chapter 4. The mission analysis was performed

---

[1] `http://www.nasa.gov/topics/aeronautics/features/future_airplanes_index.html`

[2] `http://www.aeronautics.nasa.gov/nra_awardees_10_06_08.htm`

using FLOPS, where the mission fuel burn, including reserve fuel equal to 5% of the total mission fuel, was calculated. Each analysis component of FLOPS is described in detail in Section 5.2. The analyses were integrated into a multidisciplinary analysis software called ModelCenter®, created by Phoenix Integration,[3] and the system was optimized with the objective of reducing total system fuel burn. The multidisciplinary framework and optimization methodology are discussed in Section 5.3.

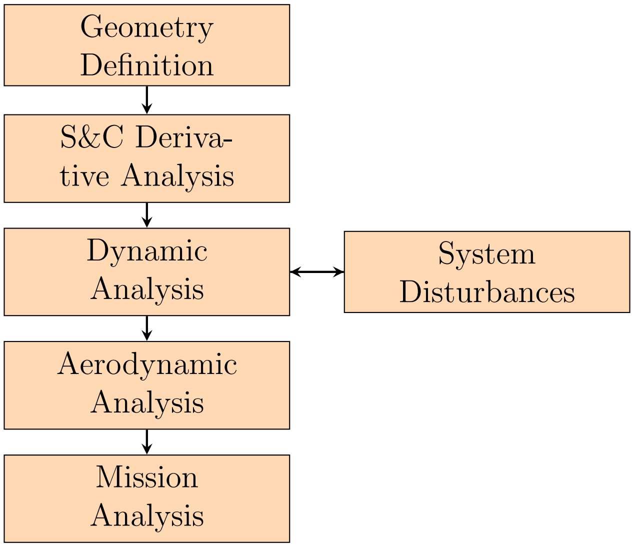

Figure 1.2: High level process chart of the multidisciplinary analysis used in this research.

It was desired to test different pieces of the multidisciplinary design analysis individually. Stability derivative flight test data was available from Ref. [15] for a Cessna 182T aircraft, shown in Fig. 1.3. The stability derivative data was used as a validation case for the aerodynamic analysis, and then the model was used throughout the methodology development to exercise each analysis piece as a sanity check, verifying the flight dynamics and disturbances were producing the desired behavior.

Five optimization cases were run with the current technology D8 geometry. The first case was optimized using traditional fixed tail volume coefficients. Static trim constraints were then added to the optimization and the fixed tail volume coefficients removed from the geometry definition. Case two had a fixed static margin, and case three was allowed to vary

---

[3] `http://phoenix-int.com/`

Figure 1.3: Picture of a Cessna 182T from the Pilot's Operating Handbook [16].

the static margin. Optimization cases four and five added dynamic performance constraints to the optimization, with case four having fixed static margin and case five having varying static margin. Results indicate that the dynamic response constraints drastically altered the optimal designs, actively constraining the design space, highlighting the importance and benefit of incorporating stability and control into the conceptual design process.

Chapter 2

Review of Literature

2.1 Flight Dynamics and Control in Conceptual Design

Classical conceptual design typically focuses on the interaction between the disciplines of aerodynamics, sizing, weights estimation, propulsion, and performance [17]. Any inclusion of stabilizer or control surface design during conceptual design is often limited to estimating sizes from historical data, assuming control effectiveness is proportional to the area and moment arm [7, 18]. Often times, flight dynamics and control (FDC) and handling qualities are examined after the aircraft geometry and structural properties have been defined, which leads, inevitably, to sub-optimal designs or even configurations with deficient flying qualities. FDC is incredibly important when it comes to the overall safety and certification of an aircraft, [7, 19] and deficient handling qualities lead to reduced aircraft performance, large cost increases, and delays as the configuration must be re-evaluated or redesigned.

Collaboration between traditional conceptual design disciplines and flight dynamics and controls is essential when trying to properly size stabilizer surfaces for advanced concepts that lie outside the stabilizer-sizing empirical databases, especially when exploring the design space with reduced static margin, or relaxed static stability (RSS). RSS is the intentional reduction of static margin with the objective of obtaining performance gains. When designing with RSS, it is possible for aircraft performance to be increased through reduction of wetted area drag, trim drag, and tail weight [7, 18, 20]. For a transport aircraft with conventional stability margins, the horizontal tail accounts for 20-30% of the aircraft-lifting surface and approximately 2% of the aircraft empty weight [18]. Any reduction in size of the horizontal stabilizer can provide a significant benefit in reduced drag and aircraft empty weight. However, any relaxation of the stability margin has a detrimental effect on the aircraft's handling qualities that must be addressed [18]. It is this correlation between performance gains and degraded handling qualities that make it essential, and potentially extremely beneficial, to incorporate flight dynamics and control into the conceptual design phase, especially when evaluating large and complex design spaces using an optimizer.

Perez, Liu, and Behdinan in Refs. [7] and [18] incorporate FDC into a multidisciplinary design optimization (MDO) scheme where a manned transport aircraft was allowed to be designed with RSS, taking into account handling qualities as specified in MIL-F-8785C [8]. From this optimization scheme, significant geometry changes occurred compared to using the traditional design approach, where aircraft performance was only a function of the aerodynamic forces. Specifically, the optimizer recognized a benefit from RSS and reduced the static margin, along with moving the wing apex location and, thus, the center of gravity (CG) location by reducing the horizontal stabilizer area (down 28%) and control surface area [7, 18]. By integrating stability and control into the design optimization loop, adequate handling qualities were ensured with feedback control augmenting the stability. Additionally, reduced control deflections were necessary for trim [17].

References [17] and [18] examined the longitudinal dynamics only, a limitation in the ability to fully design the system stabilizers and control surfaces. The lack of fully-coupled aircraft dynamics does not allow the vertical tail design to be incorporated in the MDO. As stated previously, sizing of the vertical tail is traditionally calculated using a vertical tail volume coefficient, developed from historical data. The dutch roll mode, which is primarily damped with the vertical tail, is made sufficiently stable simply by the vertical tail area and moment arm when using the volume coefficient [4]. With stability augmentation, this sizing will be less than optimal and potential performance gains are lost when the lateral/directional modes are not considered as part of the MDO. In 2006, Perez et al. expanded upon their research and incorporated both lateral/directional and longitudinal dynamics into the MDO, but the stability augmentation system only used Single-Input, Single-Output (SISO) feedback controls with simple approximations of the common aircraft modes [7]. This does not account for an aircraft's potentially complex, coupled dynamics, as would be the case with some of the next generation, advanced concepts being explored by the National Aeronautics and Space Administration (NASA).[1] Additionally, the gain direction and value was chosen to guarantee closed-loop stability but gave no indication of an optimal solution. Although able to produce results that showed a performance gain similar to their previous work, incorporating MIMO feedback control gives the potential for more optimal feedback gains on a general configuration for all flight modes, and thus an optimal solution providing greater performance gains.

In a completely different technique, Morris et al. used the method of linear matrix inequalities (LMI) to place constraints on the maximum actuator deflection, actuator rate, and pole placement limitations [21]. This method relies heavily upon the work of Boyd [22] and Kaminer [23] to place constraints on the static feedback gain matrix, K, to obtain desired handling qualities. Morris expanded his work in Ref. [24] by translating the MIL-STD-1797A guidelines into state variance constraints to be used in the development of a state feedback control law using optimal control. A very unique solution to the problem of incorporating FDC into the conceptual design process, the methodology was still linked to a standard set of linear dynamic modes and their associated natural frequency and damping.

References [25–28] describe the SimSAC project using the CEASIOM software which took a different approach than the methods described by Perez et al. and Morris et al. The SimSAC project used higher order tools, such as computational fluid dynamics (CFD), to iterate a conceptual design. The project had good success showing some benefits of relaxed static stability, but the higher order tools reduce the ability to explore a large design space with numerous varying geometric parameters. The optimization time using CEASIOM was on the order of weeks instead of the much faster methods described by Perez and Morris, and the methods presented in this research.

---

[1] `http://www.nasa.gov/topics/aeronautics/features/future_airplanes_index.html`

2.2 Handling Qualities and Stability Guidelines

For years, research has been conducted to obtain a better understanding of the handling qualities of any particular aircraft, taking into account the human element, so a standard set of requirements could be formed. The earliest handling qualities requirement was published in 1965 by Westbrook and simply stated, “During this trial flight of one hour it (the airplane) must be steered in all directions without difficulty and at all times be under perfect control and equilibrium” [29]. Although simple in nature, this less than clear statement has over time evolved into a much more extensive quantitative and sophisticated set of criteria that constantly change with every new class of vehicle [29]. The evolution was far from simple, however. Extensive tests in both simulators and in flight were used to quantify the human response which would allow for control system design to provide specified handling qualities [30, 31].

It has been quite difficult to establish a standard set of guidelines for control systems that encompasses all types of aircraft and the various nuances of each individual pilot. The pilot’s opinion of how the aircraft handles is inevitably skewed by more than just how the aircraft handles, but more how it “feels.” “He or she will be influenced by the ergonomic design of the cockpit controls, the visibility from the cockpit, the weather conditions, the mission requirements, and physical and emotional factors” [4]. A systematic method of quantifying test results was required to catalog all the data. The most widely accepted standard description for pilot rating handling qualities that establishes a quantitative scale was developed by G. E. Cooper and R. P. Harper, Jr. in 1969, and is called the Cooper-Harper scale [4, 5, 29–32]. Shown in Table 2.1, the Cooper-Harper scale provides a way to correlate pilot opinion ratings with the aircraft dynamic model and determine some analytical specifications for good handling qualities [4].

Cooper and Harper grouped the pilot rating scale into three separate levels that would describe the dynamic and control characteristics of an aircraft, described in Table 2.2. These guidelines can be applied to a specific flight mode where the three flying levels are correlated

Table 2.1: Cooper-Harper scale [4].

Aircraft Characteristics	Demands on Pilot in Selected Task or Required Operation	Pilot Rating	Flying Qualities Level
Excellent; highly desirable	Pilot compensation not a factor for desired performance	1	1
Good; negligible deficiencies	as above	2	
Fair; some mildly unpleasant deficiencies	Minimal pilot compensation required for desired performance	3	
Minor but annoying deficiencies	Desired performance requires moderate pilot compensation	4	2
Moderately objectionable deficiencies	Adequate performance requires considerable pilot compensation	5	
Very objectionable but tolerable deficiencies	Adequate performance requires extensive pilot compensation	6	
Major deficiencies	Adequate performance not attainable with maximum tolerable pilot compensation; controllability not in question	7	3
Major deficiencies	Considerable pilot compensation required for control	8	
Major deficiencies	Intense pilot compensation required to retain control	9	
Major deficiencies	Control will be lost during some portion of required operation	10	

Table 2.2: Flying quality levels [31].

Level	Description
1	Flying qualities clearly adequate for the mission flight phase
2	Flying qualities adequate to accomplish the mission flight phase but with some increase in pilot workload and/or degradation in mission effectiveness or both
3	Flying qualities such that the airplane can be controlled safely but pilot workload is excessive and/or mission effectiveness is inadequate or both

to the natural frequency and damping ratio as shown in Fig. 2.1. Using these ratings, specification MIL-F-8785 was written to provide dynamic stability requirements, both natural frequencies and damping coefficients, used both by military and civilian aircraft today. All of the qualities described have been related to how the aircraft handles according to the pilot's opinion of the workload and the degradation of mission effectiveness.

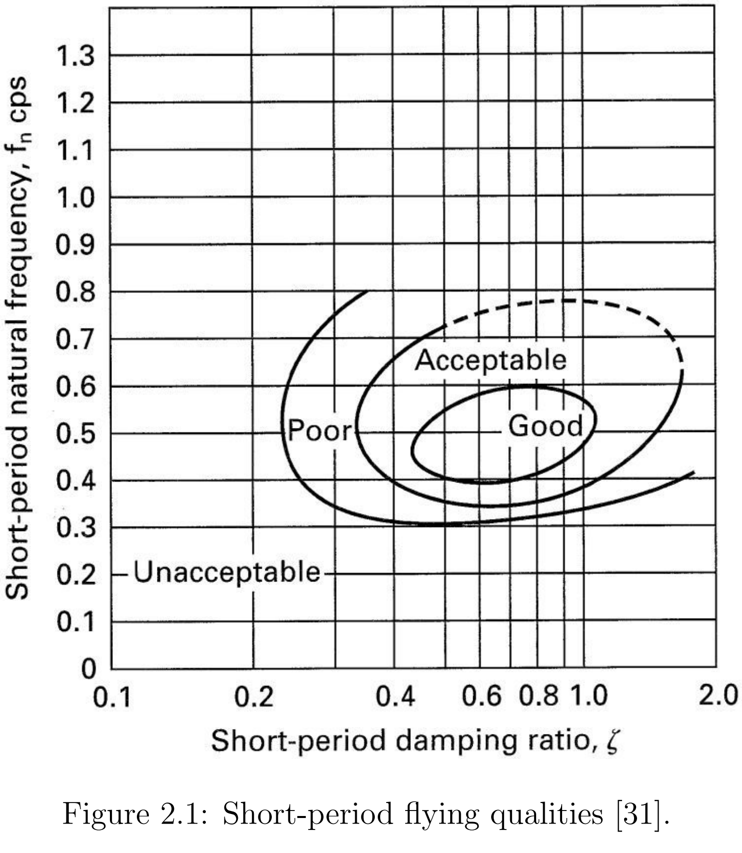

Figure 2.1: Short-period flying qualities [31].

Chapter 3

Configuration Description and Mission Summary

Two geometries were used in this research and are described in this chapter. The D8.2b, a current technology, span-restricted, twin-engine variant of the advanced transport aircraft described in Ref. [10], was used in a multidisciplinary design optimization described in Section 5.3. Throughout the methodology development and integration, a Cessna 182T model was used to test each component ensuring each was performing as expected. The Cessna 182T geometry is described in Section 3.2.

Considerable effort was used to ensure the accuracy of the geometries used in this research with the original geometries. The geometries are described in the following sections along with the original geometry sources of the information, including drawings when applicable.

3.1 D8.2b Geometry and Mission Definition

The D8 series advanced concept tube-and-wing transport aircraft described in Ref. [10] were designed in response to NASA's N+3 initiative to drastically reduce fuel burn, noise, and emissions on a 737-800 class airplane with entry-into-service in the 2035 time frame. Incorporating a "double bubble" fuselage, the D8 series is a twin aisle design in a 2x4x2 passenger seating arrangement that takes advantage of a lifting nose reducing the pitching moment to trim. The engines, mounted in wing pylons on the 737-800, have been embedded in the aft section of the double bubble fuselage. A Pi-tail (π-tail) arrangement surrounds the embedded engines, providing noise shielding while taking advantage of reduced structural weight penalties typically associated with a T-tail empennage. The double mounting point of the all-moving horizontal stabilizer to the top of the twin verticals allows for reduced structure in both the horizontal and verticals.

The D8 configuration was sized for a design range of 3,000 nautical miles with a fuel reserve equal to 5% of the total trip fuel. To reduce fuel burn, the cruise Mach number was reduced from the Boeing 737-800 reference Mach number of 0.78 to Mach 0.72. While keeping Mach number constant, the altitude was allowed to vary to minimize fuel burn throughout the cruise segment. The climb segment was optimized to minimize fuel burn when climbing to altitude, and descent at maximum lift to drag ratio was used. Figure 3.1 shows a summary of the mission profile used in Ref. [10] and in the multidisciplinary design optimization of this research. The mission segments and the different schedules options for each are described in Section 5.2.6.

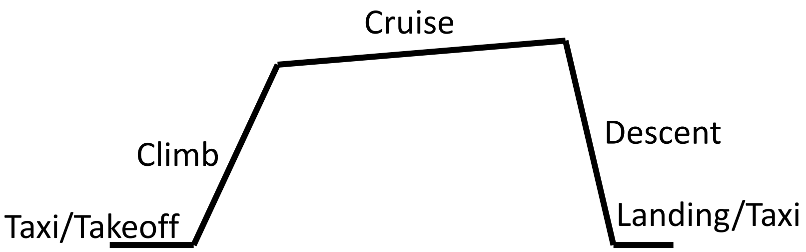

Figure 3.1: Mission profile used in sizing the D8 concept and the multidisciplinary design optimization.

Transitioned from a Boeing 737-800 design, Ref. [10] describes the incremental aircraft changes resulting in the D8.1, a current-technology, double bubble, tube-and-wing concept. Modifications included replacing the traditional tube fuselage with the double bubble style fuselage, pictured in Fig. 3.2, aft embedded engines, reduced wing sweep from reduced cruise Mach number, implementation a doubly supported horizontal stabilizer with the Pi-tail, and increased aspect ratio and wing span. The potential benefits of the double bubble fuselage, embedded engines, and Pi-tail, were fully described in Ref. [10]. The cruise Mach number was decreased from 0.80 (737-800) to 0.72, allowing for reduced wing sweep, increased maximum lift coefficient at takeoff conditions, and reduced structural wing weight. Optimized

(a) Fuselage cross-section forward of wing box.

(b) Fuselage cross-section at wing box.

Figure 3.2: D8 fuselage cross section forward of the wing box (a) and at the wing box (b) [10].

for minimal fuel burn in Massachusetts Institute of Technology's (MIT's) conceptual design software, TASOPT, the D8.1 three-view is shown in Fig. 3.3 with some geometry parameters provided. A more encompassing list of geometric parameters is provided in Table 3.1. Numerical values with a tilde were not specified in Ref. [10] and had to be inferred, or estimated, from drawings provided in the report.

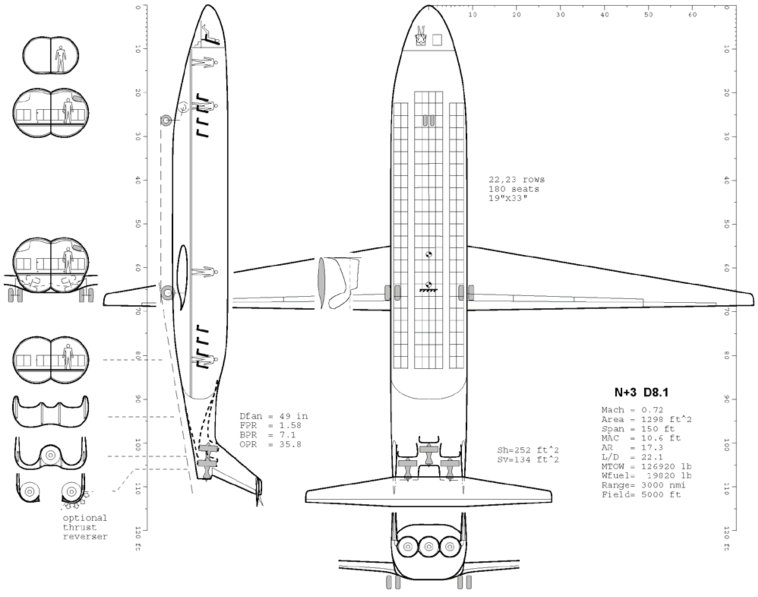

Figure 3.3: Three view of D8.1 geometry including sectional views [10].

With a wing span of 150 feet, the D8.1 configuration benefits were masked by the increase in span efficiency from the large span. To better capture the benefits of the double bubble configuration, the span was limited to 118 feet, placing it in the same operational class as the 737-800. This allowed for the capture of the double bubble configuration benefits without

Table 3.1: D8.1 geometry parameters from Ref. [10] or as measured from a scaled drawing in AutoCAD.

Parameter	Symbol	Value	Units	Comment
Mach number	M	0.72	-	Start of cruise Mach number
Wing Area	S	1298	ft^2	Reference area
Wing Span	b	150	ft	Projected wing span
MAC	$\bar{c}$	10.6	ft	Mean aerodynamic chord
Aspect Ratio	AR	17.3	-	-
Lift-to-Drag	L/D	22.1	-	Start of climb L/D
Sweep	$\Lambda_{c/4}$	~7.2	deg	Quarter-chord sweep angle
Dihedral	Γ	~3.3	deg	-
Taper ratio	λ	~0.15	-	Root chord at fuselage/wing joint

the induced drag benefits of a large wing span, which can be added to any conventional configuration. The twin engine, span restricted, current technology configuration was called the D8.2b. Modifications from the original D8.1 to the D8.2b are described in Table 3.2, as optimized in TASOPT for minimum fuel burn. Approximate values were taken from Fig. 3.4. Not indicated in Table 3.2 was the change from three rear embedded engines to two engines, shown if Fig. 3.4. An Open Vehicle Sketch Pad (OpenVSP) model was created, shown in Fig. 3.5, where the engines have been ignored for model simplicity.

Table 3.2: Parametric geometry changes from D8.1 to D8.2b configuration

Parameter	D8.1	D8.2b
Wing Area	1298 ft^2	1110 ft^2
Wing Span	150 ft	118 ft
MAC	10.6 ft	11.03 ft
AR	17.3	12.5
L/D	22.1	19.45
Sweep	~7.2 deg	~13 deg
Dihedral	~3.3 deg	~5.0 deg
Taper	~0.15	~0.18

TASOPT predicts a maximum gross takeoff weight of 121,295 pounds with a fuel weight of 21,420 pounds. This was the amount of fuel predicted by TASOPT to complete a 3,000 nm mission with 5% of total fuel reserve. Measurements from Fig. 3.4 placed the fore and

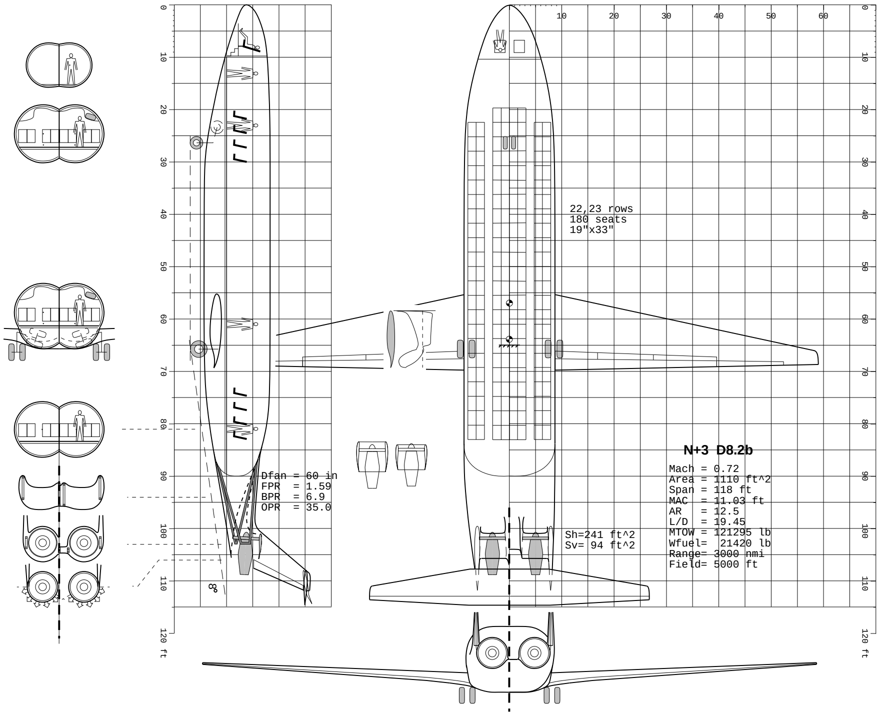

Figure 3.4: Three view of the D8.2b geometry, including sectional views.

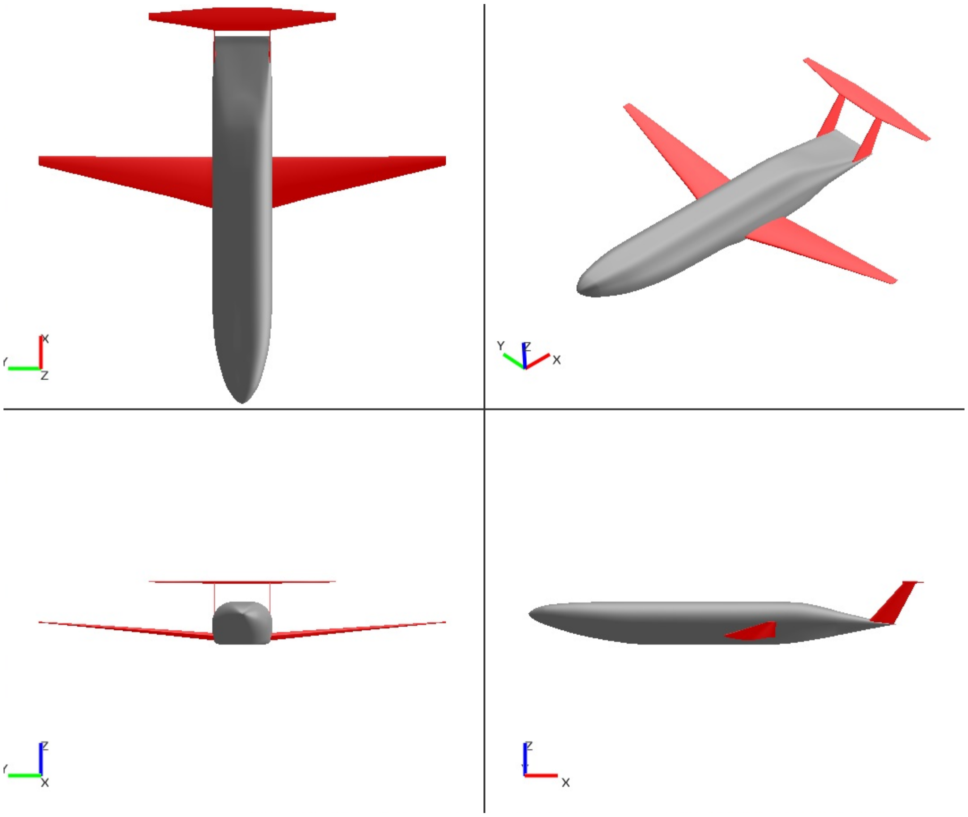

Figure 3.5: OpenVSP model of the D8.2b

aft limits of the center of gravity to be -12% and 54% mean aerodynamic chord, with the MAC specified in Table 3.2. The leading edge of the mean aerodynamic chord was 58.2 feet aft of the aircraft nose. A 10% minimum static margin specified the rear CG limit and the forward CG limit was determined from a landing/decent condition [10]. It should be noted that the elevator deflection angle for the forward CG limit at the landing condition exceeded the allowable deflection used in this research and required an adjustment in the forward CG location, reduced to 30% MAC, discussed in Section 4.4.2.

The Flight Optimization System (FLOPS) [14], described in Section 5.2, calculated weight estimates that were used in this research instead of inputting the fixed gross weight given in Fig 3.4. FLOPS does not require, nor estimate, mass moments of inertia in its analysis, but mass moments of inertia were required for the flight dynamic analysis. A detailed, high-order analysis for predicting the mass moments of inertia was beyond the scope of this research and a simple, conceptual design level, prediction technique was used. Radii of gyration, described by Raymer in Ref. [33], were used to estimate the mass moments of inertia for the D8.2b geometry. Equation 3.1 gives the inertia calculations in the body axis

$$\begin{aligned} I_x &= \frac{b^2 W}{4g} R_x^2 \\ I_y &= \frac{L_f^2 W}{4g} R_y^2 \\ I_z &= \frac{\left(\frac{b}{2} + \frac{L_f}{2}\right)^2 W}{4g} R_z^2 \end{aligned} \tag{3.1}$$

Depending on the aircraft configuration, the radii of gyration vary requiring the selection of a base configuration type to calculate the mass moments of inertia. Reference [33] provided a list of aircraft type and the corresponding radii of gyration. A transport aircraft with fuselage mounted engines was chosen, and the selected radii are given in Table 3.3.

Table 3.3: Radii of gyration used in the mass moments of inertia calculations [33].

Radii of Gyration	R_x	R_y	R_z
Value	0.24	0.36	0.44

3.2 Cessna 182T Skylane Geometry

Reference areas and mass properties for the Cessna 182T came from Refs. [15,34], while the dimensions and component placements came from the Pilot's Operating Handbook [16] and Specification and Description handbook [35]. Table 3.4 summarizes the reference areas and mass properties of the Cessna 182T. Any dimensions not specifically listed in the drawings of the POH or S&D were measured in AutoCAD 2014 using scaled drawings. Figures 3.7 and 3.6 were taken from the S&D and POH respectively and scaled, ensuring proper drawing size and aspect ratio. Using these drawings, the input files for the aerodynamic analysis were created, discussed in Section 5.1. The center of gravity was located at 26.4% from the leading edge of the mean aerodynamic chord ($\bar{c}$), which was located 25.98 inches from the reference datum [16]. The datum—the front face, lower portion of the firewall—was 64.7 inches measured from the front of the propeller spinner.

Table 3.4: Cessna 182T reference parameters and mass properties [15].

Parameter	Symbol	Value	Unit
Reference Area	S	174	ft^2
Mean Aerodynamic Chord	$\bar{c}$	4.9	ft
Wing Span	b	36	ft
Weight	W	2,650	lb
x-axis Inertia	I_x	948	slug-ft^2
y-axis Inertia	I_y	1,346	slug-ft^2
z-axis Inertia	I_z	1,967	slug-ft^2
xz-axis Inertia	I_{xz}	0	slug-ft^2

The wing had a span was 36 feet with a wing reference area of 174 square feet, located at the top of the fuselage approximately 30 inches above the spinner centerline and 89 inches aft of the spinner tip, or 25.98 inches aft of the reference datum. From root to tip, the quarter-chord sweep angle is zero degrees. Broken into two segments, the inboard section is of constant chord 64 inches in length, consisting of the NACA 2412 airfoil, with a dihedral angle of 2 degrees. The inboard section ends where the strut joins the wing, 46% semispan, and the outboard section has a taper ratio of 0.67 and a dihedral angle of 2.5 degrees. The ailerons were a constant 8.75 inches in chord starting at the outboard section and extending to 97% semispan. A front and top view of the main wing can be seen in Fig. 3.6.

A conventional tail configuration, the horizontal stabilizer was located 22.2 feet aft and 1.4 feet above the spinner as extended to the aircraft centerline. Consisting of only one trapezoidal segment, the total span was 11.75 feet with a root chord of 4.34 feet, again as extended to the aircraft centerline. The taper ratio was 0.62 with no dihedral and a quarter-chord sweep angle of 2.25 degrees. A hinge line perpendicular to the x-z plane of the aircraft was used for the elevator resulting in a variable chord elevator. At the root, the elevator was 42.3% local chord and at the tip it was 33.7% local chord.

Figure 3.7 shows the best view of the vertical stabilizer including the vertical strake that extends forward at the base. The vertical stabilizer spans 59.9 inches as measured from the top of the fuselage where the vertical the upper surface of the fuselage. At this location, the reference root chord (trapezoidal vertical without the strake) was 53.9 inches and the tip chord was 27.2 inches. The trapezoidal vertical stabilizer leading edge sweep angle was 41 degrees and the strake leading edge sweep was 79 degrees. The leading edge of the strake joins the upper surface of the fuselage 17 feet behind the front of the spinner. The rudder spans the entire vertical stabilizer trailing edge and was nearly constant percent local chord; at the tip the rudder was 40% local chord and at the base was 41.7% of the vertical reference chord of 53.9 inches.

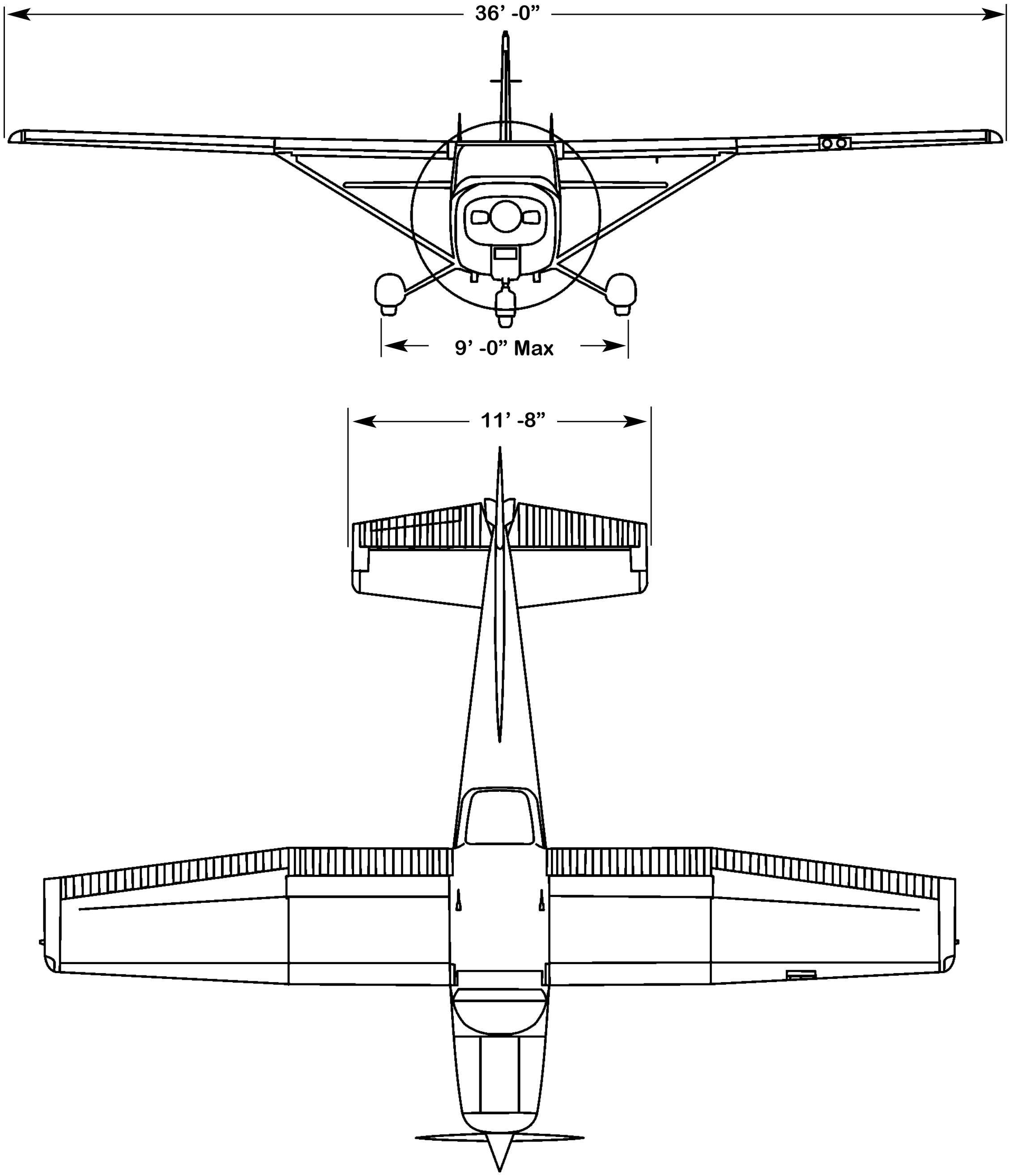

Figure 3.6: Top and front view of Cessna 182T (not to scale) [35].

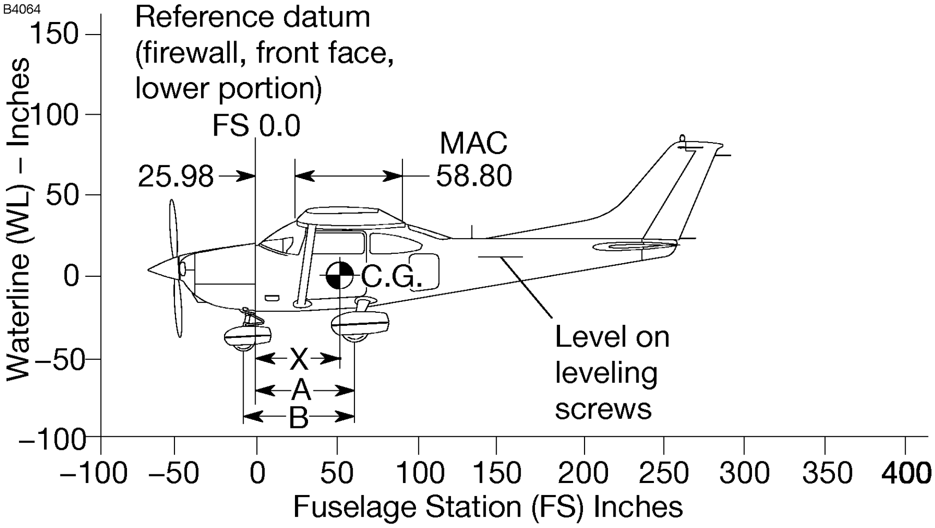

Figure 3.7: Side view of Cessna 182T indicating location of mean aerodynamic chord (MAC) and datum point (not to scale) [16].

Chapter 4

System Flight Dynamics and Disturbances

Described is the stability and control analysis used in the multidisciplinary design optimization. Figure 4.1 shows the general process for the dynamic analysis with system disturbances. The tan boxes are discussed explicitly with the derivations of the system dynamics and the linear quadratic regulator controller presented in Sections 4.1 and 4.2, respectively. The continuous turbulence and discrete gust atmospheric disturbances are described in Section 4.3, and the system perturbations, static trim limits, and dynamic response constraints are discussed in Section 4.5. Additionally, the flight conditions used for the static trim and dynamic analysis are described Section 4.4. Gray boxes with dashed arrows indicate that the analysis does not explicitly occur during the dynamic analysis, and the MATLAB® linear simulation function was used for all dynamic simulations.

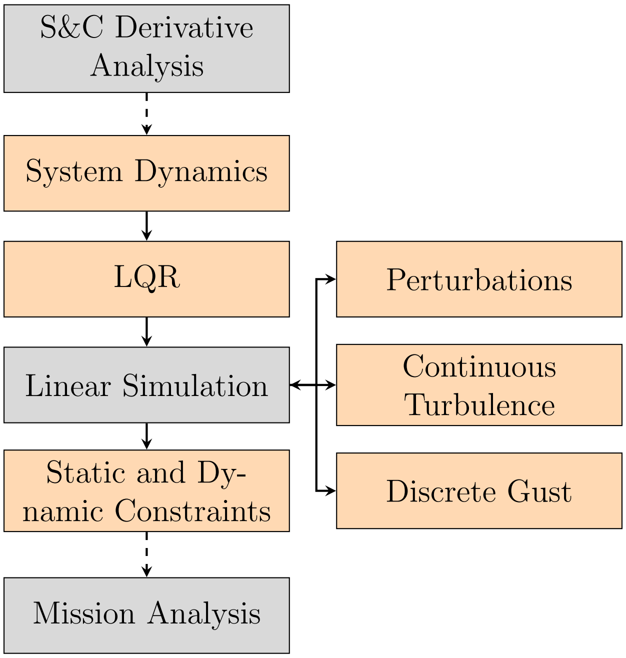

Figure 4.1: System flight dynamics and disturbances process chart.

4.1 Equations of Motion

The dynamics of the aircraft were modeled by starting with the fully coupled equations of motion. These equations were derived and linearized about a steady-state condition resulting in a state-space representation of the perturbation equations. State feedback was chosen for the controller structure due to the guaranteed closed-loop stability properties of the controller, which worked well in a diverse design space explored by an optimizer. Although it is rare to have all the states available, the focus of this research was not to design a robust controller but rather to incorporate active control into the conceptual design space that would give a stable solution. As such, it was undesirable to have the optimizer throw out feasible designs due to instability resulting from a poorly designed controller, and so a controller design with guaranteed closed-loop stability was used.

The perturbation equations were derived assuming a symmetric geometry with zero steady sideslip. The steady-state thrust terms were solved for explicitly and substituted into the state-space form of the perturbation equations. The implicit, state-space form of the fully coupled perturbation equations is given by

$$E\dot{x} = \hat{A}x + \left[\begin{array}{c:c} \hat{B} & \hat{B}_g \end{array}\right] \left\{\begin{array}{c} \delta \\ \hdashline u_g \end{array}\right\} \tag{4.1}$$

where $\hat{B}_g$ is the gust input matrix, and the hat ($\hat{}$) indicates the state and control matrices have yet to be premultiplied by the generalized inertial matrix, E. The state and control vectors are

$$\begin{aligned} x &= \begin{bmatrix} u & v & w & p & q & r & \phi & \theta & \psi \end{bmatrix}^{\mathrm{T}} \\ \delta &= \begin{bmatrix} \delta_e & \delta_a & \delta_r \end{bmatrix}^{\mathrm{T}} \\ u_g &= \begin{bmatrix} u_{gust} & v_{gust} & w_{gust} \end{bmatrix}^{\mathrm{T}} \end{aligned} \tag{4.2}$$

with the full definition of the matrices in Eq. 4.1 given in Appendix A. Inverting the generalized inertial matrix, E, one obtains the standard, explicit, state-space model

$$\dot{x} = E^{-1}\hat{A} + E^{-1}\left[\begin{array}{c:c} \hat{B} & \hat{B}_g \end{array}\right]\left\{\begin{array}{c} \delta \\ \hdashline u_g \end{array}\right\} = Ax + \left[\begin{array}{c:c} B & B_g \end{array}\right]\left\{\begin{array}{c} \delta \\ \hdashline u_g \end{array}\right\} \tag{4.3}$$

A linear actuator model was added to the system dynamics for each control surface and was modeled by a simple-lag filter transfer function given by [4]

$$\frac{\delta(s)}{u(s)} = \frac{1}{\tau s + 1} \tag{4.4}$$

where τ is the time constant of the filter. The time constant was chosen to be the same for all three actuators and was selected as $\tau = 1/(20.2)$ s [4]. The perturbation equations described by Eqs. 4.1-4.3 were augmented to include the actuator dynamics while neglecting all unsteady terms, thrust terms (except $C_{T_{xu}}$), steady-state roll ($\bar{R}$), and negligibly small terms. A vortex lattice aerodynamic analysis tool called Athena Vortex Lattice (AVL),[1] described in Section 5.1, was used for the aerodynamic model, which does not include thrust in the analysis, therefore those terms had to be neglected. The velocity dependent thrust term, $C_{T_{xu}}$, was included in the perturbation equations as it would be the largest in magnitude for the configurations studied in this research. It was approximated using Ref. [32] to be

$$\begin{aligned} \text{Propeller Aircraft: } C_{T_{xu}} &= -3\left(\bar{C}_D + \bar{C}_{W_0}\sin\bar{\theta}\right) \\ \text{Jet Aircraft: } C_{T_{xu}} &= -2\left(\bar{C}_D + \bar{C}_{W_0}\sin\bar{\theta}\right) \end{aligned} \tag{4.5}$$

The augmented perturbation equations are presented in compact form in Eq. 4.6 with the matrix definitions given in Appendix A. Again, the hat used in the Appendix A equations indicates that a matrix has not been premultiplied by the inverted generalized inertial

---

[1] `http://web.mit.edu/drela/Public/web/avl/`

matrix,E_{aug}.

$$\dot{\left\{\begin{array}{c} x \\ \hdashline \delta \end{array}\right\}} = A_{aug} \left\{\begin{array}{c} x \\ \hdashline \delta \end{array}\right\} + \left[\begin{array}{c;{2pt/2pt}c} B_u & B_{g_{aug}} \end{array}\right] \left\{\begin{array}{c} u \\ \hdashline u_g \end{array}\right\} \tag{4.6}$$

The actuator input vector, u, is defined as

$$u = \begin{bmatrix} u_e & u_a & u_r \end{bmatrix}^{\mathrm{T}} \tag{4.7}$$

4.2 State Feedback by Linear Quadratic Regulator

A complete dynamic system of an aircraft incorporating active control is complex, requiring numerous loop closures to provide adequate closed-loop system response. Classical control relies on the iterative selection of gains to achieve the closed-loop system stability, but there is no guarantee the gains chosen will be optimum. Modern control theory takes advantage of current computing power where numerous linear equations can be solved simultaneously to obtain a set of gains that minimizes a chosen performance index (PI). It is in the selection of the performance index that the true engineering of the controller occurs [4].

A linear quadratic regulator (LQR) can be used to simultaneously close all the loops in a linear, time-invariant (LTI), multi-input multi-output (MIMO) system. With the closure of all the loops, the gains are solved for simultaneously, negating the need for successive loop closure as required in classical control theory. Extremely versatile, the LQR is capable of using performance indices with state and control weighting, time weighting, and derivative weighting of the states in both state feedback and output feedback control structures. Without any restrictions on the gains, other than closed-loop stability is required, the LQR may choose to zero a gain, thus leaving a loop unclosed. Additionally, compensators may be used in the form of filters, integral and derivative controllers. This flexibility makes it an excellent tool for finding optimal gains for a controller in an LTI system.

As a regulator, any non-zero states are driven to zero in such a way that a chosen performance index is minimized. By driving all the states to zero, the system is returned to the steady-state condition with the least amount of cost, thus being an optimal solution. This is ideal for a stability augmentation system where any deviation from the steady state is undesired.

4.2.1 The Standard Linear Quadratic Regulator Performance Index

A set of nonlinear equations of motion can be linearized about a condition, a steady-state condition for example, and represented in state-space form as given by

$$\dot{x} = Ax + Bu \tag{4.8}$$

where both x and u are functions of time. Equation 4.8 is a simplified version of Eq. 4.6. The state vector is a vector of perturbations from the steady state condition that the regulator drives to zero. With a state-feedback control law

$$u = -Kx \tag{4.9}$$

the closed-loop system takes on the form

$$\dot{x} = (A - BK)\, x \equiv A_c x \tag{4.10}$$

A performance output can be defined as

$$z = Hx \tag{4.11}$$

where z is a vector of states or a combination of states. An example would be a normal load factor as a function of several longitudinal states such as pitch rate, pitch angle, and angle of attack. Additionally, for a regulator z can be set to the error of a specific state such as a non-zero pitch rate that should be driven to zero.

The LQR finds the optimal gains through the minimization of a performance index that integrates the values of both the state and control vectors over time. Each state and control is weighted in the performance index through the use of weighting matrices, varying the impact of each state and control on the performance. The standard performance index for the LQR is

$$J = \frac{1}{2}\int_0^\infty \left(x^{\mathrm{T}}Qx + u^{\mathrm{T}}Ru\right) dt \tag{4.12}$$

with $Q \geq 0, R > 0$. The performance output, z, can be incorporated into the performance index by setting $Q = H^{\mathrm{T}}H$. Substituting Eq. 4.9 into Eq. 4.12, the performance index becomes

$$\begin{aligned} J &= \frac{1}{2}\int_0^\infty \left(x^{\mathrm{T}}Qx + x^{\mathrm{T}}K^{\mathrm{T}}RKx\right) dt \\ &= \frac{1}{2}\int_0^\infty \left[x^{\mathrm{T}}\left(Q + K^{\mathrm{T}}RK\right)x\right] dt \end{aligned} \tag{4.13}$$

As described by Stevens and Lewis [4], this dynamic optimization problem can be converted into a static optimization problem that is easier to solve. Suppose that a constant, symmetric, positive-semidefinite matrix P can be found such that

$$\frac{d}{dt}\left(x^{\mathrm{T}}Px\right) = -x^{\mathrm{T}}\left(Q + K^{\mathrm{T}}RK\right)x \tag{4.14}$$

Substitute the left side of Eq. 4.14 into Eq. 4.13 to get

$$\begin{aligned} J &= -\frac{1}{2}\int_0^\infty \frac{d}{dt}\left(x^{\mathrm{T}}Px\right) \\ &= \frac{1}{2}\int_\infty^0 \frac{d}{dt}\left(x^{\mathrm{T}}Px\right) \end{aligned} \tag{4.15}$$

Evaluating Eq. 4.15 at the limits of integration gives

$$J = \frac{1}{2}x^{\mathrm{T}}(0)Px(0) - \frac{1}{2}\lim_{t\to\infty} x^{\mathrm{T}}(t)Px(t) \tag{4.16}$$

Assuming the closed-loop system is asymptotically stable, $x^{\mathrm{T}}(t)Px(t)$ will vanish with time leaving

$$J = \frac{1}{2}x^{\mathrm{T}}(0)Px(0) = \frac{1}{2}tr(PX) \tag{4.17}$$

where

$$X = x(0)x^{\mathrm{T}}(0) \tag{4.18}$$

If a positive, semidefinite solution P exists that satisfies Eq. 4.14, a constraint equation can be formed by substituting Eq. 4.10 into Eq. 4.14 giving

$$\begin{aligned} -x^{\mathrm{T}}\left(Q + K^{\mathrm{T}}RK\right)x &= \frac{d}{dt}\left(x^{\mathrm{T}}Px\right) \\ &= \dot{x}^{\mathrm{T}}Px + x^{\mathrm{T}}P\dot{x} \\ &= x^{\mathrm{T}}\left(A_c^{\mathrm{T}}P + PA_c\right)x \end{aligned} \tag{4.19}$$

This constraint equation must be true for all values of $x(t)$ which leaves

$$g \equiv A_c^{\mathrm{T}}P + PA_c + K^{\mathrm{T}}RK + Q = 0 \tag{4.20}$$

The time-dependent optimization problem becomes a time-independent optimization problem subject to the constraint of Eq. 4.20.

One can solve a modified problem using the Lagrange multiplier approach which adjoins the constraint equation (Eq. 4.20) to the performance index using the Hamiltonian

$$\mathscr{H} = tr(PX) + tr(gS) \tag{4.21}$$

where S is a symmetric matrix that needs to be determined, simplifying the constrained optimization problem to minimizing Eq. 4.21 without constraints. This is accomplished by setting the partial derivatives of the Hamiltonian with respect to each independent variable to zero as follows:

$$0 = \frac{\partial \mathscr{H}}{\partial S} = g = A_c^{\mathrm{T}} P + P A_c + K^{\mathrm{T}} R K + Q \tag{4.22}$$

$$0 = \frac{\partial \mathscr{H}}{\partial P} = A_c S + S A_c^{\mathrm{T}} + X \tag{4.23}$$

$$0 = \frac{1}{2} \frac{\partial \mathscr{H}}{\partial K} = RKS - B^{\mathrm{T}} P S \tag{4.24}$$

Detailed derivations of Eqs. 4.22–4.24 are described in Appendix B. Solving Eq. 4.24 for K, the Kalman gain can be found as

$$K = R^{-1} B^{\mathrm{T}} P S S^{-1} = R^{-1} B^{\mathrm{T}} P \tag{4.25}$$

Substituting Eq. 4.25 into Eq. 4.22, and considering that $A_c = A - BK$ for state feedback,

$$0 = A^{\mathrm{T}} P + P A + Q - P B R^{-1} B^{\mathrm{T}} P \tag{4.26}$$

the algebraic Riccati equation is found. Because the Kalman gain is independent of S it does not depend on the initial state, X. Solving the Riccati equation for the symmetric positive semidefinite matrix P, the optimal gain can be found directly using Eq. 4.25.

4.2.2 Derivation of the Modified Performance Index

A limitation of the linear quadratic method is the n x n entities that must be chosen in the weighting matrix Q where the values may not directly correspond to a performance objective due to an observability requirement, initially presented by Kalman [36] and discussed by Stevens and Lewis [4]. This results in a trial-and-error method of selecting Q where the entries are varied until an acceptable transient response is obtained. This method of design is highly undesirable.

Eliminating any restriction of observability in the selection of Q allows for the elements to be chosen strictly on desired performance objectives. With specified performance objectives, the structure of the PI and the number of entities to be chosen for the weighting matrices can be reduced with the closed-loop response dependent on the design of the performance index.

A strength of the linear quadratic method is the selection flexibility of the performance index structure where the standard PI, given in Eq. 4.12, can be modified by adding time and derivative weighting of the states. A benefit of the time-weighted performance index is that it can satisfy the observability requirement, freeing the selection of the weighting matrices. The standard PI only lightly penalizes small errors due to a slow pole(s) with small residue, resulting in the time to reach a steady state condition being rather large. The time-weighted performance index heavily penalizes errors that occur late in the response and, as a result, suppresses the effect of a slow pole and lightly damped settling behavior [4].

The derivative of the state can sometimes be a more accurate representation of the workload on a control system and should be weighted in the performance index rather than the state itself. For example, the rate of change of a control surface is a more accurate representation of required actuator power than the deflection angle itself.

The standard PI for the linear quadratic regulator was modified to include time weighting on the states and derivative of the states is given by

$$J = \frac{1}{2}\int_0^\infty \left(t^k x^{\mathrm{T}} P x + u^{\mathrm{T}} R u + \dot{z}^{\mathrm{T}} W \dot{z}\right) dt \tag{4.27}$$

where R has the same definition as in the standard performance index, Q has been set equal to zero, P is a state weighting matrix for the time weighted terms, and W is a new weighting matrix on the states' time rate of change. Equation 4.27 can be rewritten as

$$J = \frac{1}{2}\int_0^\infty \left(t^k e^{\mathrm{T}} e + u^{\mathrm{T}} R u + \dot{z}^{\mathrm{T}} W \dot{z}\right) dt \tag{4.28}$$

where e is the error, defined as

$$e = z = Hx \tag{4.29}$$

and $P = H^{\mathrm{T}}H$. The solution to Eq. 4.28 can be shown to be

$$J = \frac{1}{2} tr\left(P_k X\right) \tag{4.30}$$

subject to the nested Lyapunov equations given by

$$\begin{aligned}
0 &= g_0 \equiv A_c^{\mathrm{T}} P_0 + P_0 A_c + P \\
0 &= g_1 \equiv A_c^{\mathrm{T}} P_1 + P_1 A_c + P_0 \\
&\vdots \\
0 &= g_{k-1} \equiv A_c^{\mathrm{T}} P_{k-1} + P_{k-1} A_c + P_{k-2} \\
0 &= g_k \equiv A_c^{\mathrm{T}} P_k + P_k A_c + k! P_{k-1} + K^{\mathrm{T}} R K + A_c^{\mathrm{T}} H^{\mathrm{T}} W H A_c
\end{aligned} \tag{4.31}$$

with X defined as

$$X = x(0) x^{\mathrm{T}}(0) = H^{-1} z(0) z^{\mathrm{T}}(0) \left(H^{-1}\right)^{\mathrm{T}} \tag{4.32}$$

Derivations of Eqs. 4.30–4.32 are given in Appendix C. Any non-negative integer can be chosen for the time-weighting exponent, k, where $k = 0$ will give the standard performance index equations without nested Lyapunov equations. Experience with Ref. [4] indicates that $k = 2$ is a good selection and was used in this research.

The solution to this minimization problem is dependent upon the initial conditions, $x(0)$, unlike the state feedback LQR with the standard performance index. A simple solution for eliminating the dependence on the initial state is to average the performance of a set of linearly independent initial conditions. This is equivalent to a random variable uniformly distributed on the surface of a unit sphere of dimension equal to the length of the state vector [37]. In essence, instead of minimizing the performance index in Eq. 4.30, the expected value of J, $E\{J\}$, is minimized such that

$$E\{J\} = \frac{1}{2} E\{x^{\mathrm{T}}(0) P_k x(0)\} = \frac{1}{2} tr(P_k X) \tag{4.33}$$

where the symmetric n x n matrix

$$X \equiv E\{x(0)x^{\mathrm{T}}(0)\} \tag{4.34}$$

is the initial autocorrelation of the state. For the regulator problem, it is practical to set $X = I$ since it is desired to drive arbitrary nonzero states to zero [4].

4.2.3 Selection of the Weighting Matrices

An emphasis was placed on reducing the number of entities that must be chosen in the weighting matrices. As a regulator with state feedback, any nonzero state was considered an error. The performance output, z, was selected as

$$z = e = Hx = \begin{bmatrix} u & \beta & \alpha & p & q & r & \phi & \theta & \psi & \delta_e & \delta_a & \delta_r \end{bmatrix}^{\mathrm{T}} \tag{4.35}$$

with the performance output matrix H defined as

$$H = \frac{180}{\pi} diag \left\{ \tfrac{\pi}{180} \ \ \tfrac{1}{U} \ \ \tfrac{1}{U} \ \ 1 \ \ 1 \ \ 1 \ \ 1 \ \ 1 \ \ 1 \ \ 1 \ \ 1 \ \ 1 \right\} \tag{4.36}$$

The performance output was chosen to give one degree of error equal weighting as one foot per second in the performance index. This was chosen to maintain the generality of the controller while reducing the number of entities to be chosen in the performance index.

The derivative-weighting matrix W was chosen as

$$W = diag \left\{ 0 \ \ 0 \ \ 0 \ \ 0 \ \ 0 \ \ 0 \ \ 0 \ \ 0 \ \ 0 \ \ 1 \ \ 1 \ \ 1 \right\} \tag{4.37}$$

to place a penalty on high control surface deflection rates.

The controls-weighting matrix R was selected as

$$R = 0.1 \begin{bmatrix} 1 & 0 & 0 \\ 0 & 1 & 0 \\ 0 & 0 & 1 \end{bmatrix} \tag{4.38}$$

where smaller values of R give greater authority to the control inputs. However, values less than those given in Eq. 4.38 produce transient responses negligibly different than results using Eq. 4.38.

4.3 Atmospheric Disturbances

To stress the control system, atmospheric disturbances were modeled and used to test the response of the system to deviations from the steady-state condition. Including these disturbances adds validity to the model and eliminates unrealistic configurations. Two atmospheric disturbance models were used as suggested in military standard MIL-STD-1797A [9]: a continuous turbulence model in the frequency domain and a discrete gust model in the time domain.

4.3.1 Continuous Turbulence

The von Kármán continuous turbulence model was used as specified in MIL-STD-1797A. The one-sided spectra are of the form [29, 30, 38]

$$\begin{aligned} \Phi_{u_g}(\Omega) &= \sigma_u^2 \frac{2L_u}{\pi} \frac{1}{\left[1 + (1.339 L_u \Omega)^2\right]^{5/6}} \\ \Phi_{v_g}(\Omega) &= \sigma_v^2 \frac{2L_v}{\pi} \frac{1 + \frac{8}{3}(2.678 L_v \Omega)^2}{\left[1 + (2.678 L_v \Omega)^2\right]^{11/6}} \\ \Phi_{w_g}(\Omega) &= \sigma_w^2 \frac{2L_w}{\pi} \frac{1 + \frac{8}{3}(2.678 L_w \Omega)^2}{\left[1 + (2.678 L_w \Omega)^2\right]^{11/6}} \end{aligned} \tag{4.39}$$

where L_n is the length scale and σ_n is the root-mean-square intensity of the continuous turbulence, $n = u, v, w$. The spatial frequency, Ω, used in the von Kármán form of the spectra is related to the temporal frequency, ω, by $\Omega = \omega/\bar{U}$. The spectra are converted to functions of ω using the simple relationship

$$\Phi_{n_g}(\omega) = \frac{1}{\bar{U}}\Phi_{n_g}(\Omega), \qquad n = u, v, w \tag{4.40}$$

The mean-squared response of each state can be found be integrating the magnitude-squared system transfer function, $|G(i\omega)|^2$, times the power spectral density of the continuous turbulence response at all frequencies, shown in Eq. 4.41.

$$\sigma_{x_n}^2 = \int_0^\infty |G(i\omega)|^2 \Phi_{n_g}(\omega) d\omega, \qquad n = u, v, w \tag{4.41}$$

Medium to High Altitude Clear Air Turbulence

Isotropic turbulence is assumed for clear air turbulence at altitudes of 2,000 feet and above. The turbulence length scales and mean-square intensities are defined as [29,30,38]

$$\begin{aligned} \sigma_u^2 &= \sigma_v^2 = \sigma_w^2 \\ L_u &= 2L_v = 2L_w \end{aligned} \tag{4.42}$$

The length scale for medium to high altitude turbulence is $L_u = 2,500$ ft for the von Kármán form and $L_u = 1,750$ feet for the Dryden form, which is used in the discrete gust model described in Section 4.3.2.

The RMS intensities to be used in Eq. 4.39 were specified in Table 4 of Section 3.2.1.5.1 of SAE-AS94900 [39]. The table gives the vertical RMS intensities for numerous altitudes with varying probability of exceedance, and the longitudinal and lateral intensities can be found by Eq. 4.42. Light, moderate, and severe levels, with probabilities of exceedance of 10^{-2}, 10^{-3}, and 10^{-5}, are given in Table 4.1 and follow the turbulence severity levels shown in Fig. 4.2. Altitudes used between data points were linearly interpolated to allow for any desired altitude between 2,000 and 85,000 feet.

Table 4.1: RMS gust intensities, fps. [39].

Altitude (ft)	Light	Moderate	Severe
500	6.6	8.6	15.6
1,750	6.9	9.6	17.6
3,750	7.4	10.6	23.0
7,500	6.7	10.1	23.6
15,000	4.6	8.0	22.1
25,000	2.7	6.6	20.0
35,000	0.4	5.0	16.0
45,000	0	4.2	15.1
55,000	0	2.7	12.1
65,000	0	0	7.9
75,000	0	0	6.2
85,000	0	0	5.1

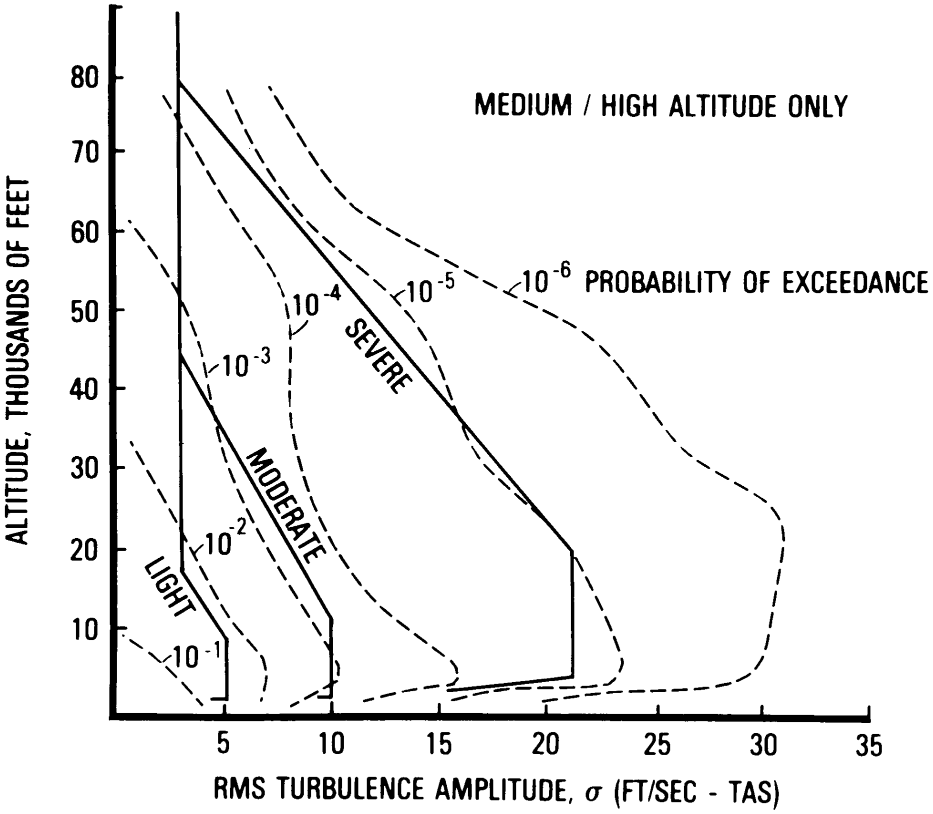

Figure 4.2: Turbulence severity and exeedance probability [9].

Low Altitude Clear Air Turbulence

Isotropic turbulence can no longer be assumed at altitudes below 2,000 feet, invalidating Eq. 4.42. In this altitude region, the von Kármán and Dryden models use the same length and RMS intensity, depending on altitude and probability of exceedance. This altitude region is broken into two regions: less than or equal to 1,000 feet, and between 1,000 feet and 2,000 feet. Nonlinear relationships between the turbulence length and intensity scales are used in the lower region altitudes. For the intensity scales, the longitudinal and lateral intensities are related to the vertical intensity scale by

$$\sigma_u = \sigma_v = \frac{\sigma_w}{(0.177 + 0.000823h)^{0.4}} \tag{4.43}$$

where h is altitude and σ_w is specified by

$$\sigma_w = 0.1u_{20} \tag{4.44}$$

The term u_{20} is the mean wind speed measured 20 feet above the ground, a function the intensity probability of exeedance. Figure 4.3 gives the means wind speed 20 feet above ground level for varying probabilities of exceedance. The intensities used for light, moderate, and severe were 23, 30, and 45 knots respectively; these correlate to probabilities of exeedance of 10^{-2}, 10^{-3}, and 10^{-5}.

The turbulence length scales are given by

$$\begin{aligned} 2L_w &= h \\ L_u = 2L_v &= \frac{h}{(0.177 + 0.000823h)^{1.2}} \end{aligned} \tag{4.45}$$

and, as with the intensities, h is altitude.

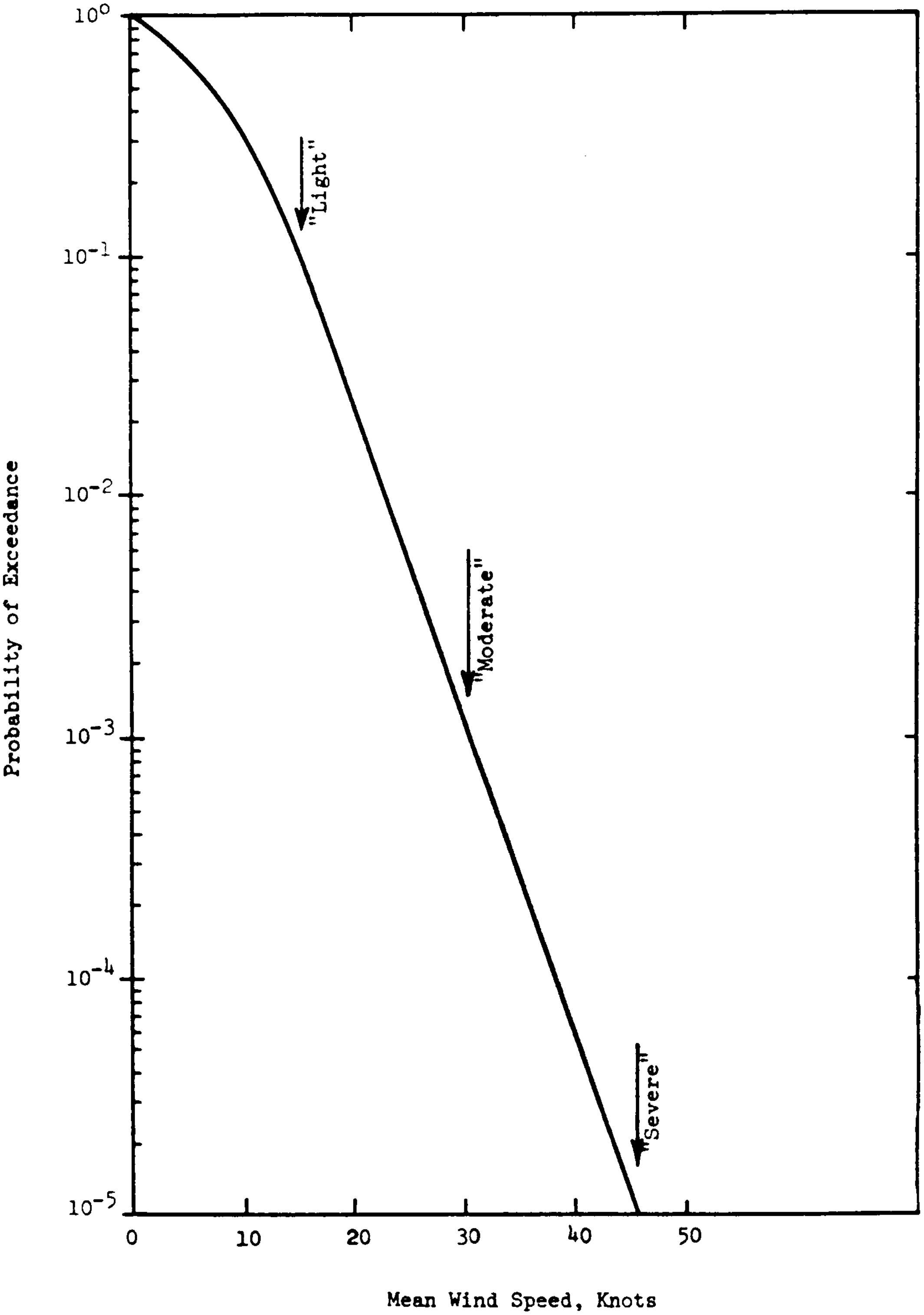

Figure 4.3: Mean velocity as measured 20 feet above the ground [9].

Power-series Approximation of Linear-gradient Turbulence

In addition to uniform immersion of the center of gravity in turbulence, captured by u_g, v_g, and w_g, linear gradients of the turbulence velocities can be modeled [8, 9, 29, 30, 40–42]. Linear gradients of the turbulence field are, in effect, equivalent to aircraft angular velocities and can be modeled as such. Multiple notations are used for the linear gradients (Ref. [43]) but the forms given in MIL-F-8785C were chosen to be presented here as the associated spectrums were also given. The equivalent angular velocities from variations in the gust field across the length and span of the aircraft are defined as [8]

$$\begin{aligned} p_g &= -\frac{\partial w_g}{\partial y} \\ -\dot{\alpha} = q_g &= \frac{\partial w_g}{\partial x} \\ r_g &= -\frac{\partial v_g}{\partial x} \end{aligned} \tag{4.46}$$

The spectrums associated with Eq. 4.46 are

$$\begin{aligned} \Phi_{p_g}(\Omega) &= \frac{\sigma_w^2}{2L_w} \frac{0.8\left(\frac{2\pi L_w}{4b}\right)^{1/3}}{1+\left(\frac{4b}{\pi}\Omega\right)^2} \\ \Phi_{q_g}(\Omega) &= \frac{\Omega^2}{1+\left(\frac{4b}{\pi}\right)^2}\Phi_{w_g} \\ \Phi_{r_g}(\Omega) &= \frac{\Omega^2}{1+\left(\frac{3b}{\pi}\right)^2}\Phi_{v_g} \end{aligned} \tag{4.47}$$

where $\Phi_{w_g}$and Φ_{v_g} were defined in Eq. 4.39. To remain consistent with the turbulence length scale definitions given in Eqs. 4.42 and 4.45, Φ_{p_g} was modified from MIL-F-8785C by adding a factor of two to the L_w term.

Inclusion of this analysis was considered for this research, but it was decided not to implement it into the current methodology. Reviewing Refs. [8, 9, 29, 30, 39, 44], the rotations are added as another input with three new spectrums, given in Eq. 4.47, and therefore produce a separate set of mean-squared responses, responses that do not have an associated requirement in SAE-AS94900. SAE-AS94900 only gives requirements for the RMS gust response to u, v, and w gusts at the center of gravity. Another limitation of the linear-gradient approximation is the limited range of validity of the approximation; only at low frequencies does the approximation apply, wavelengths on the order of eight times the total vehicle length and greater. In the case of the discrete gust, discussed in Section 4.3.2, the gust is tuned to the natural frequencies of the closed-loop system which change with every iteration. This means the approximation could be valid in some cases while not in others, making the analysis inconsistent across all configurations. Finally, structural modes analysis was not included in this research and therefore the current proposed analysis provides a sufficient dynamic constraint for incorporating flight dynamics and control into the conceptual design process.

4.3.2 Discrete Gust

The discrete gust model has the "1-cosine" profile defined by Eq. 4.48 and illustrated in Fig. 4.4

$$\begin{aligned} v &= 0, && x < 0 \\ v &= \frac{V_m}{2}\left(1 - \cos\frac{\pi x}{d_m}\right), && 0 \leq x \leq d_m \\ v &= 0, && x > d_m \end{aligned} \tag{4.48}$$

where V_m is the magnitude of the gust and d_m is one-half the total gust length. The gust length was calculated to provide maximum system excitation by tuning the gust to the least damped, one longitudinal and one lateral, system natural frequencies [39]. The magnitude of the gust, V_m, was calculated using Fig. 4.5 [9]; $P(0.01)$ corresponds to light turbulence intensities and $P(0.001)$ corresponds to moderate turbulence intensities. The Dryden length scales were used with Fig. 4.5 as directed by MIL-STD-1797A for the discrete gust model, and

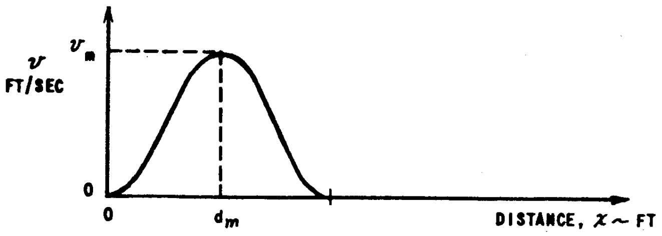

Figure 4.4: "1-cos" discrete gust profile [30].

SAE-A94900 specifies the discrete gust peak amplitude of 60 fps for severe turbulence. The moderate turbulence intensity curve in Fig. 4.5 was added in addition to the light turbulence intensity curve given in MIL-STD-1797A [9]. The data used to create the second curve was presented by Roskam in Ref. [30] and is summarized in Fig. 4.6. The analysis is capable of using either the calculated gust magnitude taken from Fig. 4.5, or the severe turbulence case of 60 fps.

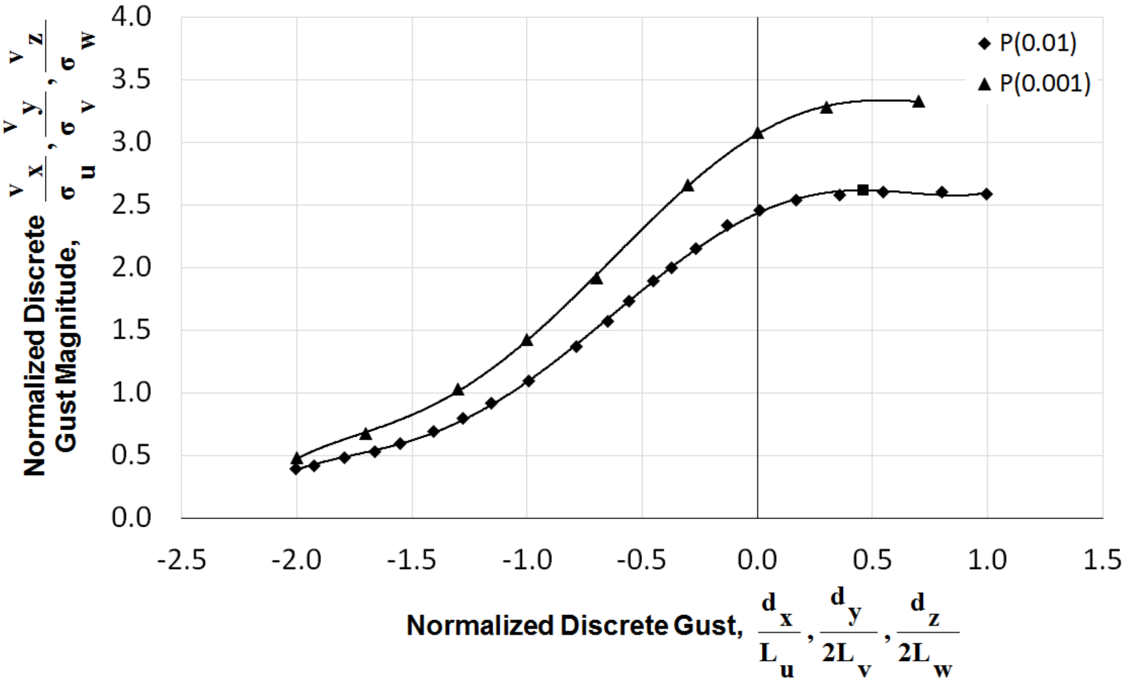

Figure 4.5: Normalized discrete gust for determining gust magnitude [8, 9].

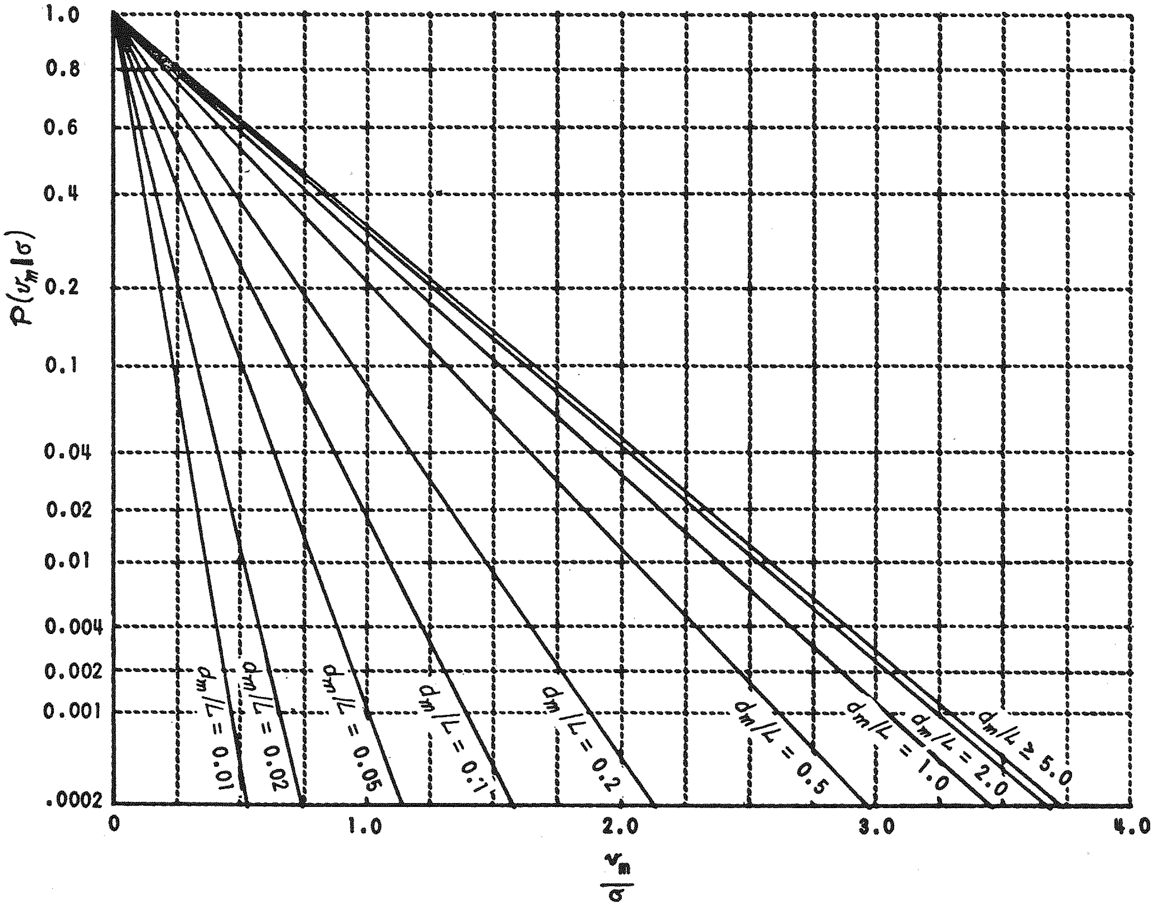

Figure 4.6: Probability of equaling or exceeding a given gust magnitude [30].

4.4 Flight Conditions for Dynamic Response Analysis

A single flight condition cannot be used to fully analyze the capability of a flight control system. Numerous flight conditions must be used to ensure the flight control system is able to provide acceptable dynamic response throughout the flight envelope for a given configuration. Both nominal and degraded flight control system capabilities directly affect the sizing of the stabilizer and control surfaces. In this research, only nominal flight control system performance was explored as bounds for the conceptual design space were desired without the necessity of robust control system design. Once a configuration is chosen for preliminary or detailed analysis, a robust controller, including failure modes, must be designed to ensure adequate handling qualities. This detailed controller design was beyond the scope of this research.

4.4.1 Cessna 182T Flight Condition for Tool Development and Exercise

The Cessna 182 is a very common four place, single-engine aircraft. A model of this airplane was used to verify that the various analysis components of the flight dynamics analysis tool were working as expected before proceeding with the full system analysis. As such, only a single flight condition was used. Experimental data were available for the Cessna 182T at the cruise condition from Refs. [15, 34]. At 5,000 feet above sea level, the cruise velocity was 220.1 fps and the Mach number was 0.201. This gives a dynamic pressure of 49.6 lbs/ft^2 and an air density of 0.002048 slug/ft^3. This, in combination with the Cessna geometry data from Section 3.2 was used as inputs for the stability augmentation system.

4.4.2 Flight Conditions for Evaluating D8.2b Closed-loop Performance

Adequate sizing of the control effectors is essential to the controllability and safety of any aircraft configuration despite their detrimental effect on system performance. Identifying the design constraining flight conditions for sizing the control effectors in conceptual design is key to linking the conceptual phase and flight test phase of a design. It is undesirable to evaluate the design stability and control characteristics at every point in the flight envelope, whereas exploring a few specific, worst-case conditions that constrain the control effectors is desired. Chudoba and Cook strived to identify in Ref. [45] a set of design-constraining flight conditions (DCFC) for sizing control effectors in the conceptual design phase.

Using the work of Chudoba and Cook in Ref. [45] as a guide, five flight conditions, with nominal flight control system performance, were chosen to evaluate the adequate sizing of the control effectors and closed-loop dynamic response to system disturbances. Three steady-state flight conditions were used to evaluate the control effectors' ability to properly trim the aircraft under longitudinal and lateral/directional loads. At takeoff, a nose up trim condition at rotation speed was used to evaluate the control power of the elevator with the center of gravity in the most forward position. At the most forward CG position, the greatest amount of pitch trim control power is required, constraining the size of the elevator. The methodology used in this research establishes a rear-most allowable center of gravity position but may not capture the pitch-trim demands of a takeoff condition. To model this, a center of gravity range of 30% mean aerodynamic chord was used to establish the forward-most position, based on the CG envelope of the Boeing 737-800 shown in Fig. 4.7.

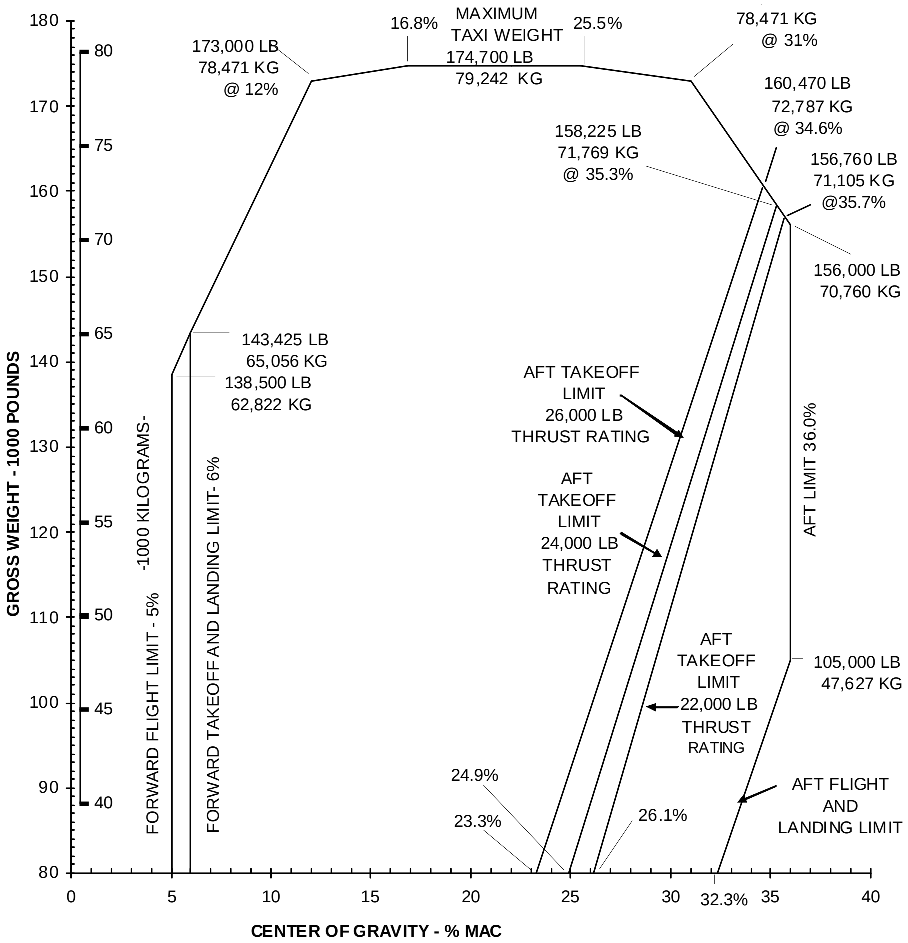

Figure 4.7: Center of gravity envelope for Boeing 737-800 aircraft [46].

For the second static case, a one engine inoperative (OEI) condition was chosen as a test of the lateral/direction control power of the control system. Lateral/directional control effectors must be capable of trimming the adverse moments, specifically a yawing moment, created during an engine failure occurring after the takeoff decision speed. In a conventional configuration empennage, i.e. the rudder is the main effector for producing yawing moments, the OEI takeoff condition can be an active constraint on the sizing of directional control effectors.

The last static case was a low-speed maneuver condition with the center of gravity in the aft position. In the clean configuration, a loading condition of 3.75g's was used to calculate a constant pitch rate required of the control system. This was designed to test the control system under a heavily loaded flight condition at the clean configuration maximum lift coefficient.

Two dynamic flight conditions, both at the aft-most center of gravity position, were selected to evaluate the dynamic response performance of the system to disturbances. A 1g stall flight condition tests the flight control system in a low dynamic pressure state where the disturbance will place a heavy workload on the stability augmentation system, causing the dynamic constraints to become active in the design space. The second dynamic flight condition evaluated was the cruise condition where the dynamic response was evaluated in the mission segment with greatest influence on performance. The altitudes for the stall and maneuver conditions were chosen to be 2,000 feet due to the adverse atmospheric conditions at the lower altitude. For cruise, a target cruise altitude of the D8.2b configuration, calculated by the Flight Optimization System, described in Section 5.2, was used. The number of dynamic flight conditions was limited to reduce the overall analysis time. Table 4.2 summarizes the chosen flight conditions.

Table 4.2: Flight conditions for D8 system evaluation.

Analysis Type	Description	Configuration	CG Position	Atmospheric Disturbances
Trim	Nose up with rotation at main gear ground contact point (SL)	Takeoff	Forward	No
Trim	Single engine out at 35 ft	Takeoff	Aft	No
Trim	Maneuver speed at 2,000 ft	Clean	Aft	No
Dynamic	1g stall at 2,000 ft	Clean	Aft	Yes
Dynamic	Cruise at 40,000 ft	Clean	Aft	Yes

4.5 Static Trim and Dynamic Response Constraints

Reducing horizontal and vertical stabilizer areas results in degraded flying qualities of any configuration, and the damping of dynamic modes is directly affected by the stabilizer areas. Control power is decreased with decreasing empennage size due to reduced control effector area, thus requiring flying quality enhancements to be provided through an active control stability augmentation system. The control system workload increases with decreasing empennage area to a point where the control system cannot provide adequate flying qualities due to limitations in the control system, such as maximum deflection angles and reduced control effectiveness from viscous effects. To capture these control system constraints, maximum control surface deflection angles were chosen and dynamic response requirements were specified. Failure to meet these constraints indicates the system was unable to adequately stabilize the configuration to maintain adequate handling qualities.

4.5.1 Aileron and Rudder Deflection Limits

For the lateral/directional control surfaces, ailerons and rudders, a twenty degree maximum control surface deflection angle was chosen as an upper bound for the control system. Twenty degrees was chosen to prevent the control system from becoming saturated, removing any control authority for commanded controls from the pilot, or autonomous control system, while avoiding the nonlinear effects of very large control surface deflections. The total control surface deflection angle was calculated as the sum of the steady-state deflection angle and any perturbation deflection angle. This maximum deflection angle was checked during the discrete gust simulations, discussed previously, and the steady-state perturbations discussed later in this section, to ensure any constraint violation was accounted for, and penalized.

4.5.2 Cessna 182T Elevator Limit

A simplified elevator constraint was applied to the Cessna 182T flight condition described in Section 4.4.1. Similar to the aileron and rudder constraints, the elevator was limited to a maximum deflection angle of 20 degrees. Again, this was chosen to provide additional control authority to the pilot or autonomous system while avoiding the nonlinear aerodynamics of flow separation on the control surface.

4.5.3 D8.2b Elevator Constraint Derivation

A more comprehensive elevator constraint was appropriate for the D8.2b flight conditions described in Section 4.4.2. The all-moving horizontal stabilizer has aerodynamic properties of a wing rather than the properties of a control surface deflecting aft of a lifting surface. A deflection angle of 20 degrees, used for the Cessna 182T elevator constraint, would be in or beyond the stall region of the D8.2b horizontal stabilizer. Large downwash angles would also be present at high lift conditions, reducing the effective angle of attack experienced by the horizontal stabilizer. As a result, a geometric deflection angle was not appropriate for the application of an D8.2b elevator constraint.

The horizontal stabilizer airfoil was extracted from the OpenVSP D8.2b horizontal tail geometry described in Section 3.1, and shown in Fig. 4.8. The 12% thick airfoil has negative

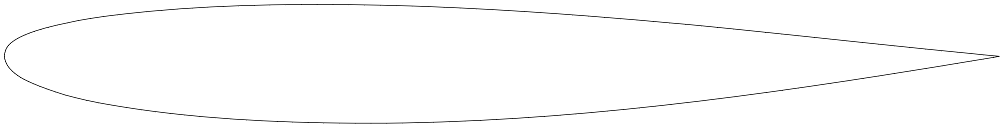

Figure 4.8: D8.2b horizontal tail airfoil used in both root and tip cross sections.

camber of -0.8% providing a download at zero geometric angle of attack. As this custom airfoil was used for the horizontal stabilizer, the aerodynamic properties could not be referenced from any sources. Therefore, the airfoil aerodynamic properties had to be predicted using an analytic method. XFOIL,[2] a subsonic airfoil development system, was used in the prediction of the airfoil lift properties, including maximum lift [47–49]. This airfoil design tool is capable of viscous analysis with free boundary layer transitions, and maximum lift predictions. An angle of attack sweep was performed in XFOIL to determine the airfoil maximum and minimum lift coefficients at Mach 0.26 and a Reynolds number of 10.3 million. Mach 0.26 corresponds to the velocity of the baseline D8.2b configuration at the end of the takeoff roll, and beginning of rotation, at sea level, standard atmospheric conditions. The horizontal tail mean aerodynamic chord (5.5 feet) was used as the reference length in the Reynolds number calculation. Figure 4.9 shows the lift coefficient versus angle of attack as analyzed in XFOIL. From Fig. 4.9, the maximum and minimum lift coefficients were determined to be +1.37 and -1.50 respectively.

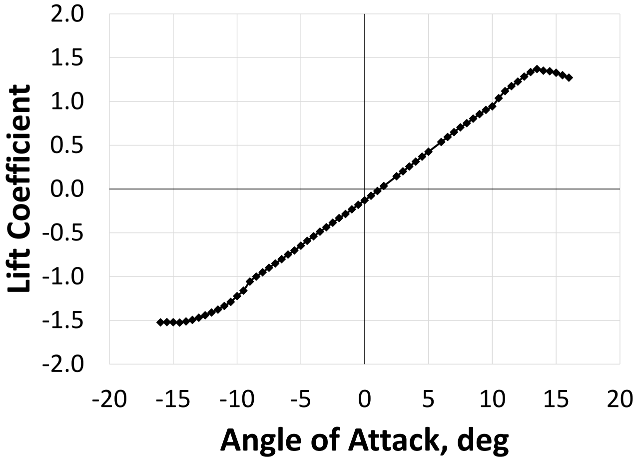

Figure 4.9: Lift coefficient versus angle of attack for the horizontal tail airfoil at Mach 0.26 and Reynolds number of 10.3 million.

The horizontal tail was used for longitudinal pitch control and should not be operated at the airfoil stall condition, otherwise a loss of control authority would occur resulting in

---

[2] `http://web.mit.edu/drela/Public/web/xfoil/`

potential loss of control. Therefore, 75% of the section lift coefficient limits were used in determining the maximum effective angle of attack constraints for the horizontal stabilizer, forcing the stabilizer to remain in the linear range of the lift curve slope. This corresponded to section lift coefficient limits of +1.03 and -1.13.

The baseline horizontal stabilizer, described in Sections 3.1 and 5.1.2, was modeled in isolation using Athena Vortex Lattice (AVL), a vortex lattice solver described in Section 5.1. The vortex lattice code was used to capture the finite span effects from the tip vortices, and to determine the angles of attack where the section lift coefficient equaled either the +1.03 or -1.13 limit. Since the horizontal stabilizer was an all-moving control surface, the angle of attack was varied in AVL, both positive and negative, until the section lift coefficient limit was reached. Figure 4.10 shows the horizontal stabilizer modeled in AVL with the section lift coefficient equal to +1.03. This occurred at 12.2 degrees angle of attack.

AVL provides two outputs for the loads on a single lifting surface. The first is to normalize by the input reference area, typically the wing reference area. The second involves calculating the area of each lifting surface and normalizing the load produced by each lifting surface by their respective areas. Normalizing the horizontal stabilizer load by its calculated area allowed a connection to be made between the full configuration model and the horizontal tail modeled in isolation, even if the horizontal tail area changed. As a result of the configuration changes to the horizontal tail area during the design optimization, it was necessary to use the surface lift coefficient to maintain a connection results similar to those of Fig. 4.10. Using the horizontal stabilizer surface lift coefficient made it possible to determine if the section lift coefficient was exceeding the allowable limits in the presence of downwash/upwash. At the section lift coefficient limits of +1.03 and -1.13, the horizontal stabilizer surface lift coefficients of 0.9553 and -1.054 corresponded to angles of attack of 12.2 and -11.4 degrees. At zero angle of attack, the lift curve slope was calculated in AVL to be 4.943 per radian.

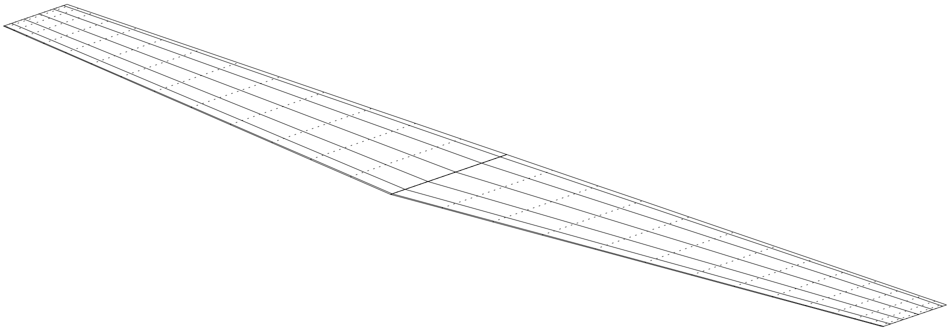

(a) Horizontal stabilizer in AVL.

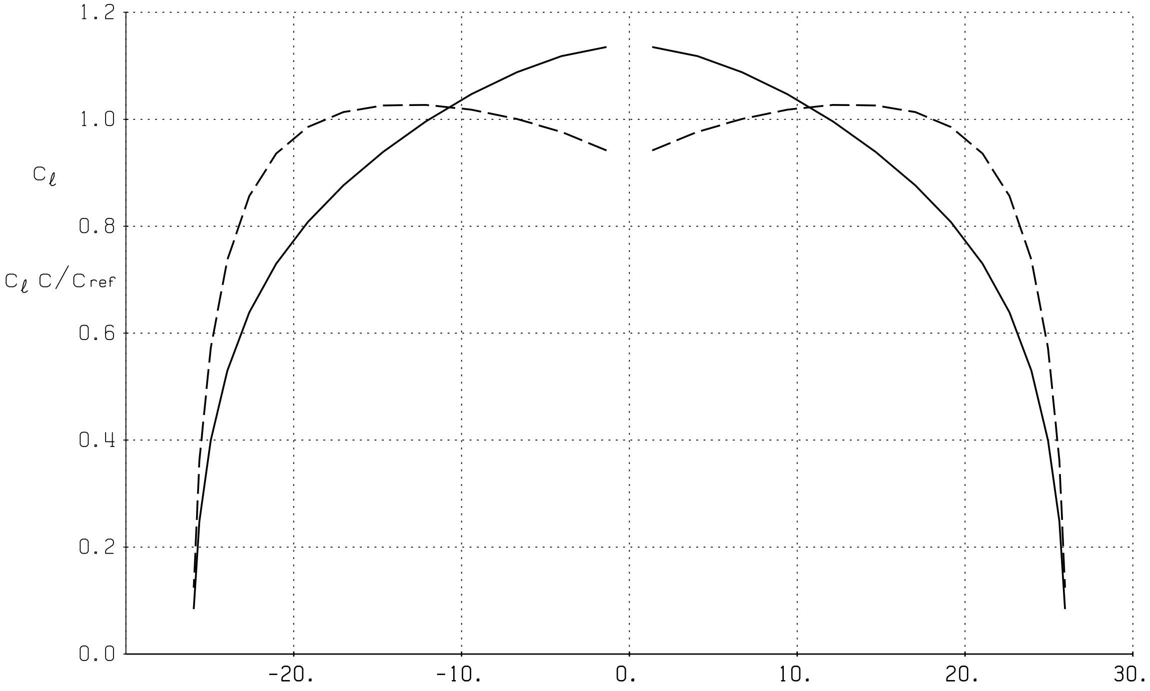

(b) Spanwise lift (dash) and load distribution (solid).

Figure 4.10: Simplified D8.2b horizontal stabilizer as modeled in AVL with the associated spanwise lift and load distributions. Analysis was run at 12.2 degrees which corresponds to maximum section lift coefficient. The dashed line is the section lift coefficient and the solid line is the load distribution.

As the horizontal tail area varies in the optimization, the aspect ratio and sweep remain constant meaning that the lift curve slope was also constant for a specified Mach number. With the surface lift coefficient correlation and lift curve slope, it was possible to calculate the effective angle of attack and determine if the section lift coefficient limit had been exceeded. The effective angle of attack was calculated by

$$\alpha_{HT_{eff}} = \frac{C_{L_{surf}}}{C_{L_{\alpha_{HT}}}} + \alpha_{HT_{L=0}} \tag{4.49}$$

where $\alpha_{HT_{L=0}}$ was the zero lift angle of attack of the horizontal stabilizer, calculated to be -1.0 degrees. Using the lift curve slope, surface lift coefficient, and zero lift angle of attack, the effective angle of attack could be inversely determined and verified in AVL by setting the surface lift coefficient.

By solving for the effective angle of attack using Eq. 4.49 from the surface lift coefficient, a constant constraint could be established for the horizontal stabilizer that would be sensitive to the downwash effects at high loading conditions. The horizontal stabilizer effective angle of attack constraint was set to $-11.4 \leq \alpha_{HT_{eff}} \leq 12.2$ degrees. This constraint was used in all flight conditions described in Section 4.4.2 for the D8.2b configuration. In the dynamic flight conditions, the elevator deflection angle was added to the steady-state effective angle of attack to ensure the maximum deflection did not violate the constraint.

All the flight conditions, with the exception of cruise, were at similar Mach and Reynolds numbers, which means the lift curve slope and airfoil maximum lift coefficients were virtually constant. In the cruise case, the Mach number was significantly higher at Mach 0.72, but the Reynolds number was essentially constant due to the high altitude operation. The increase in Mach number reduces the airfoil maximum lift coefficient and increases the lift curve slope, which will affect the constraints. However, a constant constraint was required for the optimization and therefore the same horizontal tail constraint used in all flight conditions, resulting in optimistic horizontal stabilizer constraints in the cruise condition. It was predicted, and supported by results shown in Chapter 7, that the cruise condition was not constraining on the elevator and was therefore accepted as a constraint.

4.5.4 Dynamic Response Constraints

Military specification SAE-AS94900 [39] specified performance requirements on the transient response of the attitude Euler angles, ϕ, θ, and ψ, that allowed for quantitative evaluation of the flying qualities without having to identify specific dynamic modes; this was advantageous because the traditional dynamics modes may not exist due to the complex dynamics provided by unconventional configurations, and configurations with an active control system. Assessing the transient response allowed for the flying qualities to be evaluated for any geometric configuration with any active control system.

Specified in SAE-AS94900, with active control, the root-mean-square deviations in pitch attitude angle, θ, must be less than or equal to five degrees in a continuous, one-dimensional turbulence field. In response to a five degree pitch perturbation, the control system must be capable of returning the pitch attitude to within plus or minus 0.5 degrees of the steady-state condition within five seconds for aircraft in classes I–III, defined in MIL-STD-1797A [9]. Similar to the pitch attitude, the roll attitude angle, ϕ, root-mean-square deviation in continuous turbulence must be less than ten degrees, and reach a static accuracy of plus or minus one degree within five seconds from a five degree roll perturbation. In continuous turbulence, the heading angle, ψ, must have a root-mean-square heading deviation of less than or equal to five degrees [39].

While climbing at a maximum rate of 2000 feet per minute, the control system must be capable of leveling off and achieving a static airspeed accuracy of plus or minus 10 knots or 2% of the reference airspeed, whichever is greater. This accuracy must be achieved within 30 seconds of engaging the airspeed hold. Any residual oscillations within the static accuracy margin must have a period of oscillation greater than 20 seconds. This requirement was modeled as a small perturbation in the pitch angle, θ. This dynamic constraint was modeled as a perturbation in pitch where the climb rate was used to calculate the flight path angle, γ. The steady-state angle of attack was then added to the flight path angle, shown in Fig. 4.11, to give the total perturbation that the control system must return to within the steady-state tolerance in 30 seconds. The dynamic constraints are summarized in Table 4.3.

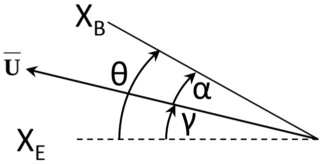

Figure 4.11: Calculation of the pitch Euler angle used in the airspeed hold perturbation.

Table 4.3: Summary of the static trim and dynamic response performance constraints for the D8.2b configuration.

Description	System Disturbance	Constraint
max aileron/rudder deflection	all	$-20 \leq \delta \leq 20$ deg
max elevator deflection	all	$-11.4 \leq \alpha_{HT_{eff}} \leq 12.2$ deg
5 deg pitch	perturbation	± 0.5 deg in < 5 s
5 deg roll	perturbation	± 1.0 deg in < 5 s
airspeed hold	perturbation	± 10 kts or 2% < 30 s
pitch deviation	cont. turbulence	$\sigma_\theta < 5$ deg
roll deviation	cont. turbulence	$\sigma_\phi < 10$ deg
heading deviation	cont. turbulence	$\sigma_\psi < 5$ deg

Chapter 5

Analysis

5.1 Aerodynamic Analysis with Athena Vortex Lattice

The aerodynamic modeling method used in this research was a vortex lattice called Athena Vortex Lattice (AVL). Developed and written at MIT, originally by Harold Youngren in 1988 and continuously updated by Youngren and Mark Drela since, the methodology was based on the original works of Lamar [50–53], Lan [54], and Miranda [55] at NASA Langley Research Center [56]. A low-order aerodynamics tool, the vortex lattice method was chosen due to its low computational cost while providing estimates of the aerodynamic forces and moments, capturing the coupled effects between surfaces and limited span. MIT's AVL was chosen due to the code's ability to run autonomously by reading in a script, its ability to simultaneously solve for both the longitudinal and lateral/direction stability derivatives, and the open source availability of the code.[1] Additionally, the input and output files are formatted in a way that was easy couple with the other processes in this research.

Typically when using a vortex lattice tool, only the lifting surfaces are modeled. This has been successful in capturing the lift and drag forces on a simple geometry. However, in a longitudinal and lateral/directional stability analysis, this representation of the geometry was not sufficiently accurate in predicting the aircraft neutral point, a key prediction in the implementation of the methodology used in this research. Fuselage effects and propulsion effects, destabilizing depending on propulsion type and location, are not captured by modeling the lifting surfaces alone and will erroneously predict the neutral point location. Due to the low-order nature of the vortex lattice method, special modeling practices must be employed to simulate the effects off the propulsion system and the fuselage on aircraft stability.

---

[1] `http://web.mit.edu/drela/Public/web/avl/`

The fuselage can be simulated as a zero camber lifting surface the shape of the outer mold line as viewed from the top and side of the aircraft. Previous work by the author in Ref. [57] showed that, for wing-body configurations having either a high- or mid-wing, a flat-panel surface approximating the shape of the fuselage, as cut by the horizontal plane shown by Fig. 5.1, produced results that matched experimental data well. The original geometry from Ref. [58] was a rectangular wing with a symmetric airfoil and a body of revolution about the x-axis. The vertical placement of the wing was dependent upon the configuration. As can be seen in Fig. 5.1, the body of revolution was modeled as a 2-D surface with the shape matching the outer-mold-line as the x-y plane cuts through. The high-wing modeling methodology was employed for the Cessna 182T and the mid-wing for the initial D8 modeling.

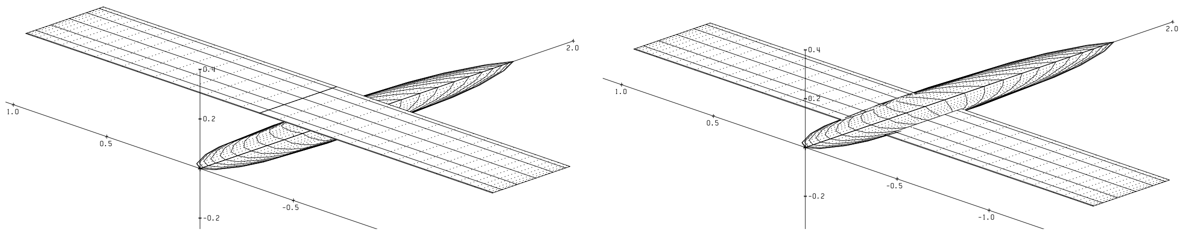

(a) High-wing configuration.

(b) Mid-wing configuration.

Figure 5.1: Wing-body configurations modeled in AVL.

Figures 5.2 and 5.3 show the comparison of the calculated lift and moment curves versus angle of attack to the high-wing configuration experimental data. As indicated in the figures, AVL predicted the lift curve slope reasonably well, only a small under-prediction of the experimental result, while the moment-curve slope was accurately predicted with a small offset in the absolute value. In a stability analysis, the slope of the curve is of greater importance.

The mid-wing configuration was modeled differently than the high-wing configuration. If the wing was brought all the way to the centerline it would interfere with the fuselage lifting surface, giving poor results. To address this issue, the wings were truncated at the

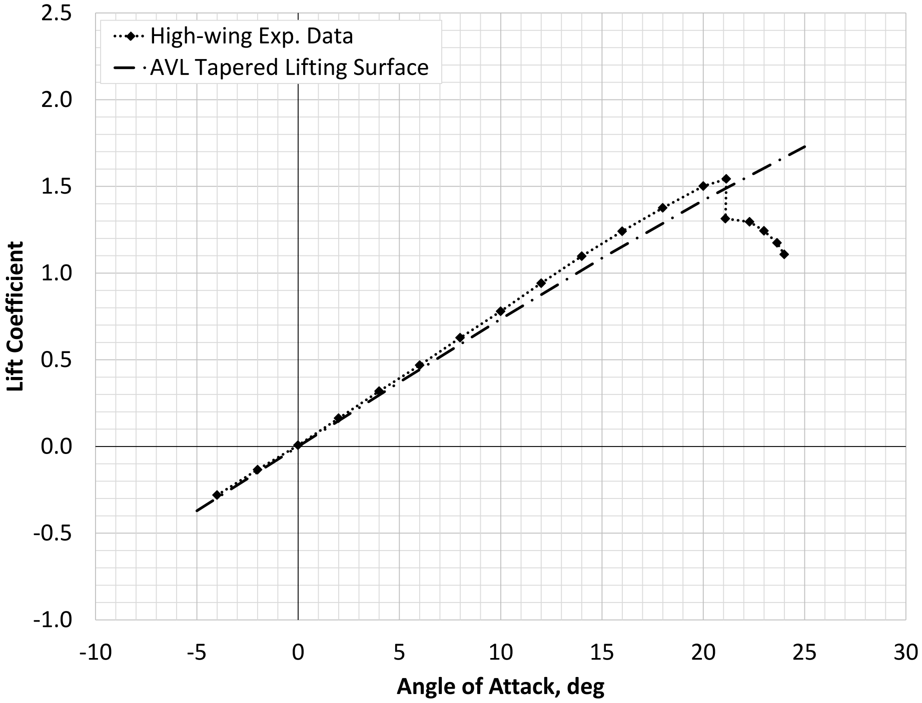

Figure 5.2: Comparison of high-wing configuration lift coefficient with experimental data.

side of the fuselage and the COMPONENT (legacy INDEX) command was used within AVL to indicate that the fuselage and wing were joined, properly distributing the vorticity across the geometry. This is illustrated in Fig 5.1(b).

When reexamining the previous work of Ref. [57], a modeling error was discovered for the tapered lifting surface that produced erroneous results. A slight overlap existed between the wing and the tapered lifting surface that was corrected with the new results presented here. In Fig. 5.4, the original lift curve slops is seen to be much larger than the experimental results. With the correction of the geometry error, the lift coefficient AVL results now agree very well with the experimental results. Surprisingly, the erroneous geometry coincidentally happened to produce an accurate estimate of the pitching moment coefficient. With the corrected geometry, there was a slight under prediction of pitching moment coefficient slope.

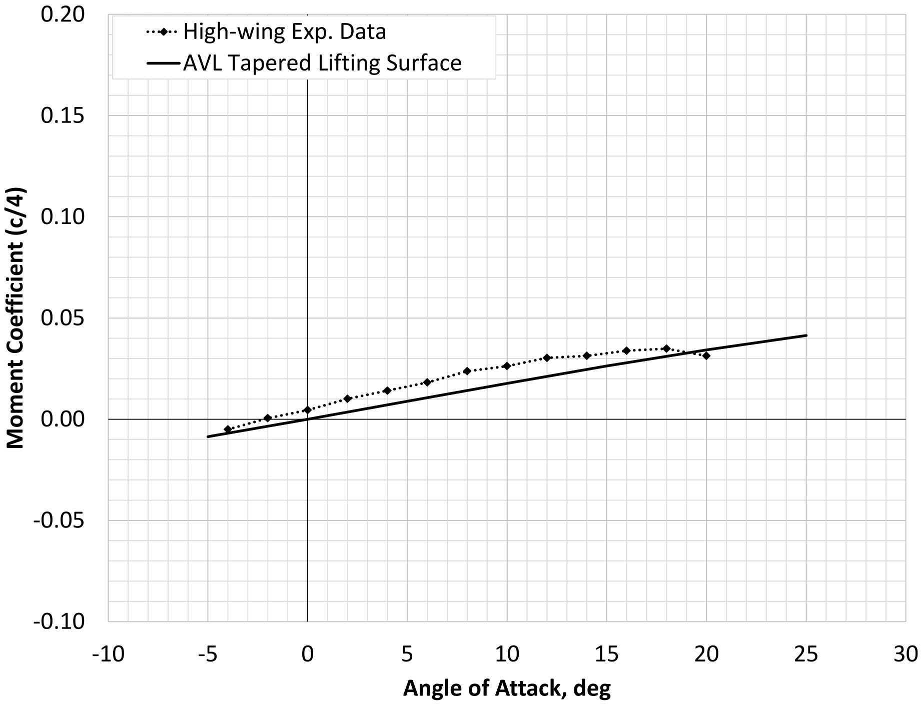

Figure 5.3: Comparison of high-wing configuration pitching moment coefficient with experimental data.

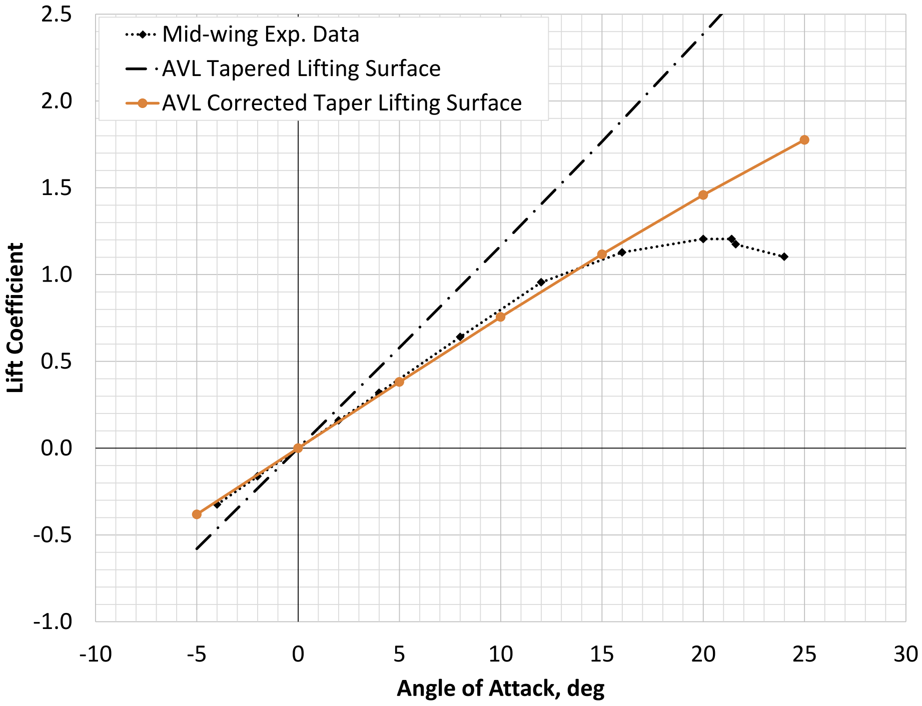

Figure 5.4: Comparison of mid-wing configuration lift coefficient with experimental data.

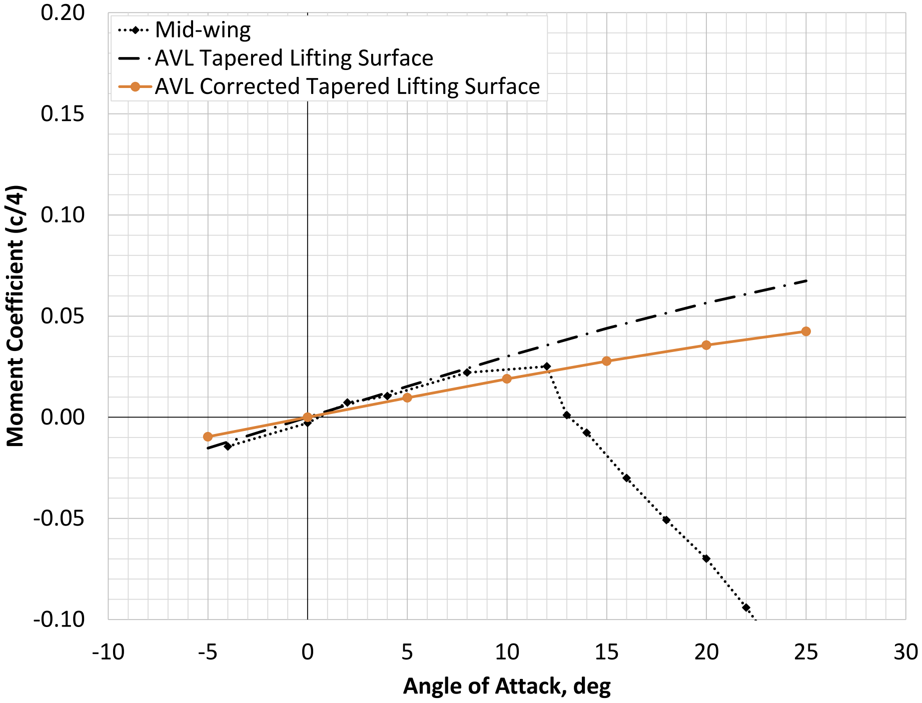

Figure 5.5: Comparison of mid-wing configuration pitching moment coefficient with experimental data.

5.1.1 Cessna 182T Aerodynamic Modeling

With the modeling strategies just discussed, a full Cessna 182T AVL geometry was created. The complex Cessna 182T geometry described in Section 3.2 was simplified down to the lifting surfaces and a cruciform style fuselage. Following the fuselage outer mold line, the vertical cross section was at the aircraft plane of symmetry, and the horizontal cross section was located in a plane offset three inches below the x-y plane, going through the tip of the propeller spinner. The wing struts were not modeled. A rectangular lifting surface was placed in front of the geometry at the spinner to model the destabilizing effects of the spinning propeller. The horizontal and vertical cuts of the fuselage were modeled with the NOWAKE feature of AVL turned on. For those surfaces, no trailing edge wake was shed, eliminating any interference of coplanar components downstream, such as the propeller and the horizontal fuselage. The NOWAKE feature captured the moments produced by the surfaces but no lift was produced. This is a reasonable approximation given that a fuselage is a very poor lifting device but it produces a destabilizing effect, both modeled by a fuselage without trailing edge vortices. A detailed description of the propulsion effects modeling is described in Section 6.3.1.

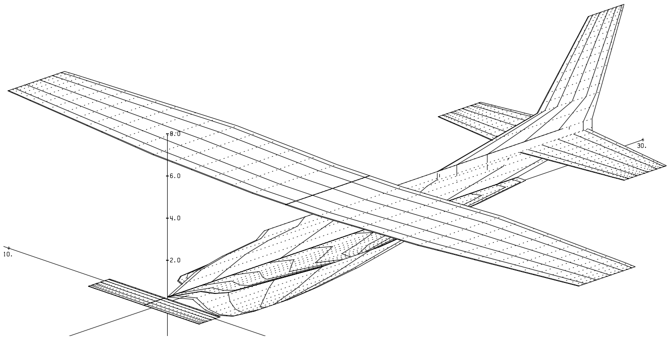

Figure 5.6: Cessna 182T geometry as modeled in AVL.

The Cessna 182T horizontal and vertical stabilizer areas were modified with a fixed center of gravity in a simple, two-variable trade study where the flight dynamics and system disturbances were tested. The results from this testing are given in Section 6.4.

In this initial testing, the only geometrical parameters varied were the horizontal and

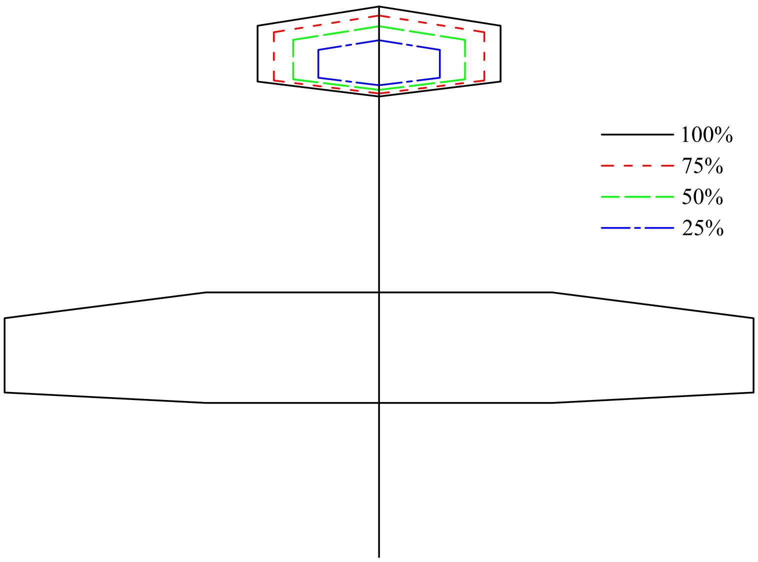

Figure 5.7: Cessna 182T geometry with modified horizontal tail as percentage of baseline volume coefficient.

vertical tail volume coefficients. The vertical tail strake, shown in Fig. 5.6, was neglected to maintain the trapezoidal geometry parameters. To reduce the number of variables, the horizontal and vertical tail moment arms, aspect ratios, quarter-chord sweeps, dihedral angles, taper ratios, and airfoils were unchanged from the baseline model. Regardless of the change in volume coefficient, the root quarter-chord coordinate locations were fixed for both the horizontal and vertical stabilizers. Changing the volume coefficient with these restrictions effectively resulted only in a change of reference area and span.

The horizontal tail volume coefficient is defined as

$$C_H = \frac{S_H l_H}{S \bar{c}} \tag{5.1}$$

Traditionally, l_H is defined as the length between the wing aerodynamic center and the stabilizer aerodynamic center. For simplicity due to the current fixed CG position in this analysis, the length l_H used in Eq. 5.1 was measured from the CG position to the root quarter-chord point on the stabilizer. Of note, the volume coefficient for the vertical stabilizer is the same equation as Eq. 5.1 with the subscript H replaced by subscript V and mean aerodynamic chord, c, replaced by the span, b.

The tail volume coefficients were varied from the Cessna 182 model values of $C_H = 0.7$ and $C_V = 0.28$ to 25% of the baseline over ten equally spaced steps. This resulted in 100 geometries evaluated, each with differing stabilizer areas and spans. As the tool was still in development, computation time was sacrificed to provide extra data, ensuring it was performing as expected.

Figure 5.7 shows a drawing from the top view of the AVL geometry with varying horizontal tail volume coefficients. The coefficients shown are 0.70, 0.52, 0.35, and 0.17 which correspond to 100%, 75%, 50%, and 25% of the baseline. The centerline of the fuselage is indicated by the solid line drawn through the symmetric plane.

Any experienced aircraft designer would notice the small horizontal tail area for the 25% baseline volume coefficient and doubt its ability to achieve adequate handling qualities, much less trim at takeoff conditions. As discussed later in Section 7, all cases passed the dynamic performance checks for adequate handling qualities. However, focusing only on the cruise flight condition was inadequate for accurately sizing the stabilizers, and more constraining flight conditions must be included in the analysis.

To capture any drag benefit from reducing the stabilizer area, and including active control in the design process, the reduction in parasitic drag must be calculated from the reduced wetted area. A zero-lift drag coefficient in the cruise condition was given by Napolitano as $C_{D_0} = 0.027$. This is the total parasitic drag for the Cessna 182 Skylane which was modeled using AVL. Reducing the horizontal and vertical stabilizer areas will reduce the total parasitic skin-friction drag. To model this, the contribution of the baseline empennage to the total parasitic drag was estimated using Raymer's component buildup method where each component is denoted by the subscript c [1]. The subsonic parasitic drag coefficient can be approximated by

$$(C_{D_0})_{subsonic} = \frac{\sum C_{f_c} FF_c Q_c S_{wet_c}}{S} \tag{5.2}$$

where C_f is the skin-friction drag coefficient, FF is a form factor that estimates the pressure drag due to viscous separation, Q is an interference factor, and S_{wet} is the estimated wetted area of the component. The miscellaneous, leakage, and protuberance drag terms were ignored. The empennage contribution to C_{D_0} was subtracted from the baseline configuration C_{D_0} of 0.027 leaving only the wing-body parasitic drag. This allows the stabilizer areas to be varied and the effect on the parasitic drag to be captured. Hence, reduced stabilizer areas result in reduced parasitic drag.

5.1.2 D8.2b Aerodynamic Modeling

As a starting point, the D8.2b was modeled after the D8.1 geometry described Ref. [10]. The D8.2b differed from the D8.1 only in the number of engines—two engines instead of three—and was span limited to 118 feet, falling into the same airport operations class as the Boeing 737-800 [59]. An AVL model of the D8.1 concept, developed at Massachusetts Institute of Technology (MIT), was available from an online repository hosted at MIT.[2] An image of the D8.1 AVL model with visible surface loads resulting from a low-speed analysis can be found in Ref. [10].

The D8.1 model was scaled to full size (the model from MIT's repository was 60% scale) so the full-scale reference areas and lengths could be used when non-dimensionalizing the forces and moments. The wing reference area for the D8.2b was 1110 square feet, and the longitudinal and lateral/directional reference lengths were 11.03 feet and 118 feet respectively, as presented in Table 3.2. It should be noted that these reference areas were references of the baseline only, not actual inputs into the analysis. In the case of the multidisciplinary design optimization, the reference areas and lengths were recomputed with each design iteration, with the exception of the lateral/directional length remaining unchanged as the span was fixed. For the baseline AVL model used in the aerodynamic validation, the reference values were set according to the declared values in Fig. 3.4 for consistency. Slight discrepancies

---

[2] `http://web.mit.edu/drela/Public/web/avl/runs/?N=A`

between the declared values of Fig. 3.4 and the measured 3-view drawing values, used to create the OpenVSP model of Fig. 3.5, were present.

Modeling strategies similar to the Cessna 182T AVL model were used to create the first D8.2b AVL model; horizontal and vertical cross sections of the fuselage were modeled as lifting surfaces, with the horizontal fuselage airfoils provided by the MIT AVL repository. The outer mold line of the fuselage, as cut by the x-y and x-z planes, was maintained by piecewise linear approximation using the trapezoidal sections in AVL, attempting to match the fuselage curvature. The D8.2b AVL model was checked to match the OpenVSP model as closely as possible, including all airfoils and spanwise twist. At the rear of the fuselage in the D8 concept, the engines were embedded to take advantage of boundary layer ingestion, described in Ref. [10]. Due to the complex geometry associated with the embedded engines, they were not included in the OpenVSP model, and were similarly ignored in the AVL model. Since the OpenVSP model was the outer-mold-line geometry analyzed in Cart3D, this was used as absolute truth in the creation of the AVL model, avoiding any unnecessary errors due to geometry discrepancies.

The horizontal tail, visible in Fig. 3.5, consisted of two trapezoidal sections, one of constant chord between the twin vertical tails, and one of constant taper ratio external to the twin vertical tails. It was desired to have simple parametric geometry for the horizontal tail using a single trapezoidal section. The horizontal stabilizer constant chord section was removed and replaced with a representative, constant taper ratio, horizontal stabilizer, and the single section horizontal stabilizer was used in both the OpenVSP and AVL models used in the aerodynamic validation.

With the horizontal stabilizer placed near the tip of the twin verticals, care had to be taken to ensure the horizontal stabilizer remained connected to the verticals, especially during the multidisciplinary design optimization. This was accomplished by placing the horizontal stabilizer using the vertical tail tip leading edge, so as the vertical tail sweep angle changed during the optimization the horizontal stabilizer would move as well. Consistent with transonic transports and the previous D8 study [10], the horizontal stabilizer was modeled as an all-moving surface for longitudinal trim in the analysis of Section 5.3.1.

For validation of the D8 AVL model, described in Section 6.3.2, the vertical stabilizers were placed longitudinally and laterally using known dimensions from the OpenVSP model and 3-view drawing (Fig. 3.4). This laterally placed the vertical tails slightly inboard of the fuselage edge, and the vertical tail root chord trailing edge slightly forward of the fuselage aft edge. This placement was used only in the validation model for the aerodynamic comparison. In the AVL model used in the MDO, the trailing edge of the vertical tail root chord was placed at the rear edge of the fuselage to give a constant reference point, as the fuselage geometry remained fixed in the MDO. As the vertical root chord was increased, the vertical stabilizer leading edge moved forward.

Flaps, ailerons, rudders, and an all-moving horizontal stabilizer were included as control surfaces in the D8 AVL model. To model the all-moving horizontal stabilizer, the hinge line must be placed at the leading edge, or 0% local chord, of the control surface. For a trailing edge device, such as a rudder, the hinge location was placed at the starting point of the control surface, in this case at 60% of the local chord giving a 40% local chord rudder. Ailerons were located on each wing with the inboard location at 67% semispan ending at 89% semispan, and had a control surface chord length of 20% local chord. For low-speed aerodynamics, flaps were modeled inboard of each aileron, starting at the edge of the fuselage and spanning the wing trailing edge to the start of the ailerons. This corresponds to an inboard starting location of 15% semispan and an outboard ending location of 67% semispan. The flap chord was 25% local chord.

AVL models the control surface deflections using a theoretical effectiveness of one, meaning that any deflection results in unrealistic control effectiveness. Torenbeek shows in Ref. [60] that lift effectiveness for plain flaps varies nonlinearly with flap size, deflection angle, and gap type (open or closed). Figure 5.8 shows a carpet plot produced by Torenbeek from data originating in the USAF Stability and Control Datcom [61] and Ref. [62]. Olson in Ref. [63] discussed how the gain parameter in AVL can be used to capture the reduction in control surface effectiveness as a function of deflection angle.

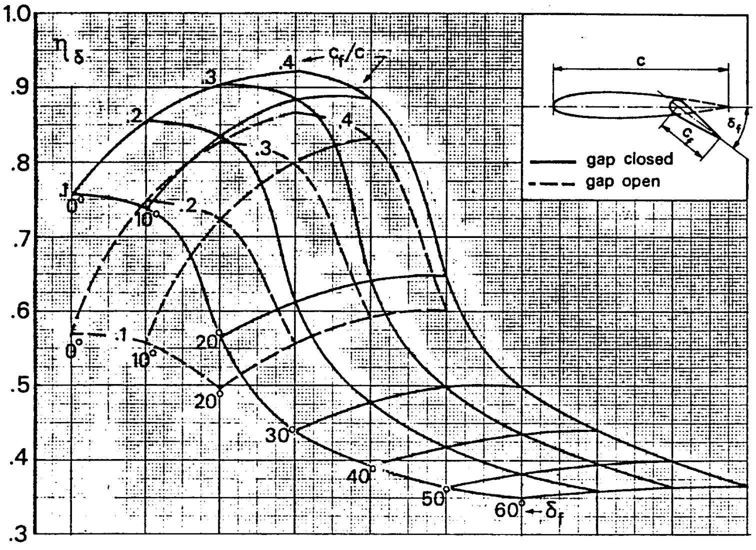

Figure 5.8: Lift effectiveness for plain flaps, both open and closed gap [60].

To accurately correlate the control surface gain with the deflection angle, especially in a trim analysis, a convergence loop would be required. The control surface gain parameter is part of the AVL input file resulting in the aerodynamic analysis solution being insensitive to changes in control surface effectiveness as the surface deflections change. If the control surface deflection matched the gain, then the convergence could be stopped, but if the deflection did not match the gain, the gain was adjusted and the solution rerun until convergence was obtained.

This iterative convergence was undesirable and so an alternative solution was sought. A fixed input gain was chosen that gave accurate control surface deflection effectiveness in the region where the deflection constraints would become active. For the rudders, with a flap chord of 40% of the local chord, a gain of 0.65 was chosen using the closed gap curve of Fig. 5.8. It was decided that this would be a conservative value at deflections less than 20 degrees, but accurate at deflections near 20 degrees, and was better than being overly optimistic. The aileron gain was chosen to be 0.8. As the aileron deflections were envisioned to be less than the rudder deflections, a moderate gain value was selected resulting in pessimistic control effectiveness at angles less than ten degrees, and optimistic control effectiveness for deflections above 12 degrees. Finally, the flap gain was selected to be 0.75 as only one flap angle deflection, fifteen degrees, was used in this research.

The baseline AVL model for the D8.2b geometry is shown is Fig. 5.9 with the moment reference point set to 62.5 feet, as measured from the nose of the aircraft. This reference point was used for the baseline geometry and aerodynamic validation study only. In the multidisciplinary design analysis, the center of gravity, used only as a moment reference point in AVL, was placed a set distance, referenced to static margin, forward of the neutral point. This allowed the center of gravity, again the reference point as used in AVL, to shift with the design variables, a process described in greater detail in Section 5.3.1. In the takeoff flight condition, the reference point was moved 1.874 feet aft of the center of gravity and nine feet below the fuselage centerline, coinciding with the rear tires' point of contact with the ground.

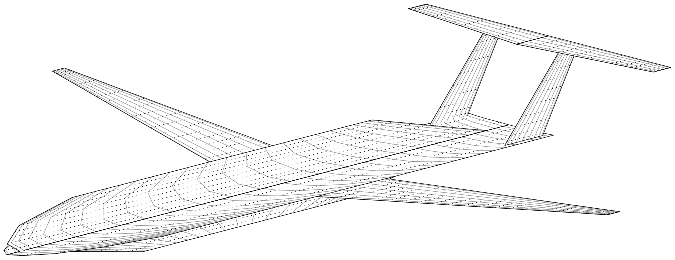

Figure 5.9: Baseline D8.2b AVL model.

Results discussed in Section 6.3.2 indicated that the baseline D8.2b AVL model was not accurately representing the aerodynamic properties as predicted in the Euler code, Cart3D [64, 65]. The vertical cut of the fuselage remained unchanged. To better match the lift, drag, and pitching moment coefficients, the horizontal cut of the fuselage was removed and the wing extended to the vehicle centerline by maintaining a constant taper ratio and quarter-chord sweep angle. Additionally, a two degree wing incidence angle defined in the OpenVSP model was removed in the AVL model to better match the Cart3D results. The AVL D8.2b model used for the design optimization is shown in Fig. 5.10.

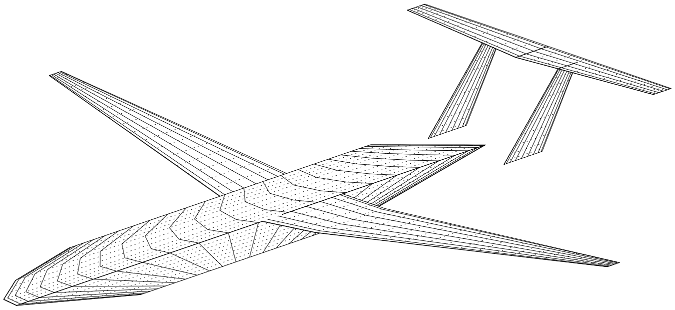

Figure 5.10: Final D8.2b AVL model used in the full system design optimization.

5.2 Sizing and Performance Estimates using NASA's Flight Optimization System (FLOPS)

The Flight Optimization System (FLOPS) is a complete aircraft conceptual design mission analysis and performance code that was in continuous development at NASA Langley Research Center starting the 1980s up until 2011 [14]. The tool is designed to take conceptual level design parameters of conventional designs, such as wing area, aspect ratio, taper ratio, and estimate the system aerodynamics, propulsion capabilities, weights, and mission performance. A strength of the tool, as part of its continuous development, is its extreme flexibility to adjust or tune any analysis, such as adjusting wing component weight, apply k-factors that simulate technology factors, and optimize the mission performance with different objectives and performance constraints. The high-level process flow for FLOPS is shown in Fig. 5.11 with the tool in analysis mode, as opposed to optimization mode, for a fixed design range and an externally provided engine deck. FLOPS is capable of running in optimization, fixed gross weight, and internally generated engine deck modes, but none of those features were used in this analysis.

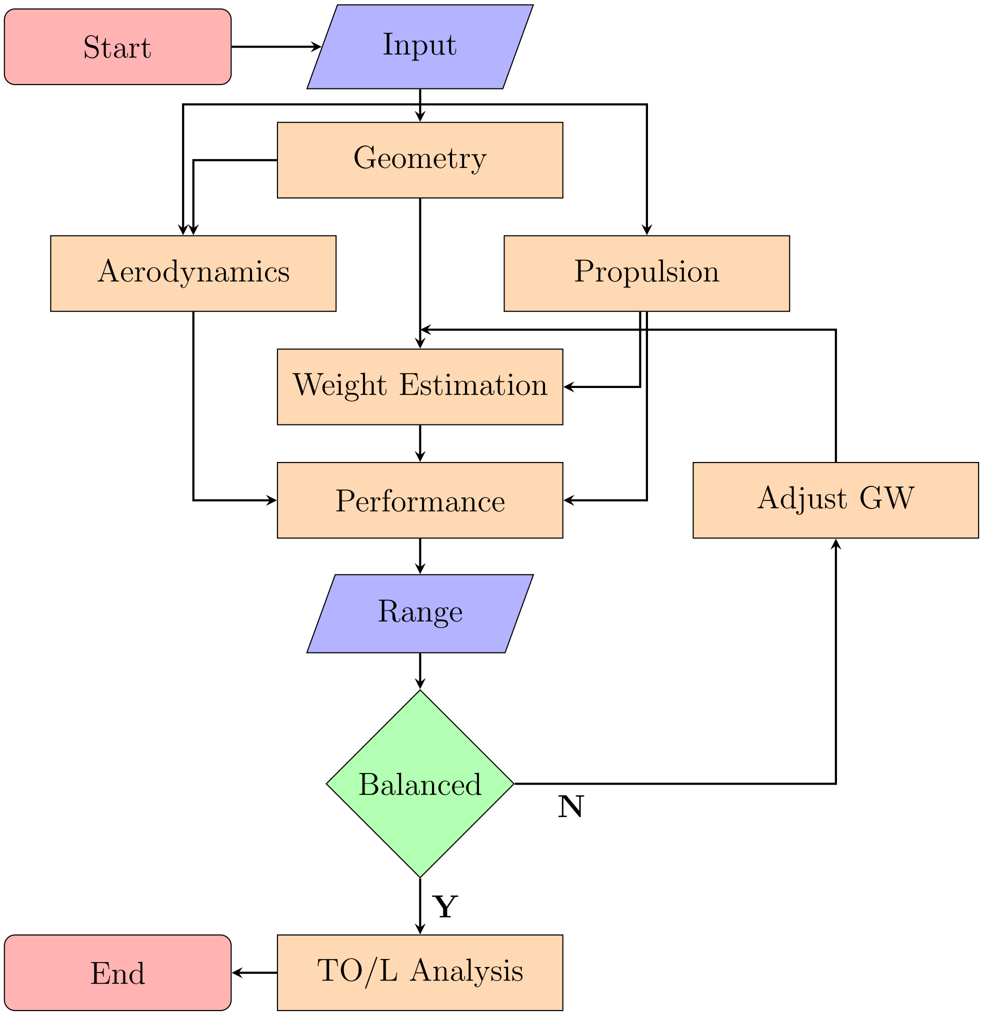

Figure 5.11: FLOPS process flow when run in analysis mode for a fixed design range and provided engine deck.

5.2.1 Overview of FLOPS Input File

Many of the inputs have preprogrammed default values allowing the user to successfully run FLOPS without explicitly including all the inputs. As more information becomes known about the design, such as external aerodynamics, additional inputs can be added increasing the size of the input file and complexity of the model. Sectioned into namelists—FLOPS was written using FORTRAN 77 syntax—the input file contains all the information required for running FLOPS; creating the geometry and running the analysis. The first namelist is the options namelist that controls the type of analysis being run, and flags for enabling specific outputs and their filenames. Options used in this research included running the full analysis—contrary to just performing a weight buildup—the optimization feature turned off, and a detailed takeoff and landing (TOL) analysis used.

As ordered in the input file, the WTIN namelist is next and is where much of the configuration geometry information is input. Items specified in the WTIN namelist include the ultimate load factor, maximum landing weight in percent of the gross weight (it can be directly input as well), wing dihedral, vertical and horizontal tail geometry, fuselage information, etc. The remaining geometry information is declared in the CONFIN namelist where, if the optimizer feature is turned on, a range of aspect ratios, thrusts, wing areas and sweeps could be input. Additional information specified in the input file includes a flag for the internal aerodynamic calculation or external aerodynamic override, if external aerodynamic data is available. Described in Section 5.3.1, both the internal aerodynamic analysis and external data aerodynamic override was used; the first FLOPS analysis used the internal aerodynamic analysis to compute an initial guess of the aircraft properties used to generate the AVL input file, and the second analysis used the external aerodynamics from the cruise condition AVL aerodynamic analysis to calculate the mission performance, predicting total mission fuel burn.

The payload specifications are declared in the WTIN namelist. A single-class passenger layout was used, affecting the furnishing weights calculated in FLOPS, with 180 passengers. Three flight attendants and two flight crew were added. Each passenger was assumed to weight 180 pounds, and have baggage weighing 45 pounds [10]. Fuselage length was specified in the input, eliminating the dependency of fuselage length on passenger count.

The MISSIN namelist is used to specify the mission structure for use in the system performance analysis. In the namelist, items such as taxi in/out and total takeoff time are input and used in FLOPS for total fuel burn calculations. Bounds on the allowable Mach numbers, altitude, and lift coefficient are specified, usually by the default values, and the minimum fuel burn climb profile selected. Additionally, FAA limitations on indicated airspeed are applied for altitudes less than 10,000 feet above sea level. Similar to the climb segment, bounds are set on the cruise segment as to maximum allowable altitude and the type of cruise schedule employed. A maximum allowable altitude of 41,000 feet and a fixed Mach number cruise, with varying altitude to optimize specific range, was used. This was the cruise profile that would allow for the most efficient cruise climb, reducing the total system fuel burn. For the descent, bounds were again placed on the allowable Mach numbers, and the descent profile was selected to maximize lift over drag (${}^{L}/_{D}$). Finally, a reserve mission was added where 5% total fuel reserve was added to the total fuel weight, which was consistent with the N+3 concept D8 studies of Ref. [10].

5.2.2 Geometry Process

Most parametric geometry variables are specified in the input file, but some features, either not specified in the input or dependent upon multiple inputs, are calculated in the geometry process. Examples would be aspect ratio, if span and wing area are specified, engine nacelle size, multiple vertical tails (only one vertical tail geometry is input with the number of vertical tails as a separate input), wetted area estimates, and landing gear length. These calculated geometry features are passed to the aerodynamic analysis and weight estimation, indicated in Fig. 5.11.

5.2.3 Aerodynamic Process

Receiving data from both the input file and the geometry generation process, the aerodynamics used in the performance process are calculated in the aerodynamic process. The empirically based aerodynamic analysis, a modified version of the Empirical Drag Estimation Technique (EDET) [66], calculates the lift and drag characteristics of the input aircraft configuration from low speed, Mach 0.2, to the maximum input Mach number, which in this research was Mach 0.82. Modifications to the EDET include smoothing of the drag polars, increased accuracy Reynolds number calculations, and the inclusion of the Sommer and Short T' method for skin friction calculations [67]. Lift and drag polars are generated for a series of Mach numbers, automatically distributed by the aerodynamic analysis process, that are functions of the geometry and any tuning parameters that are added in the input file. Examples of aerodynamic tuning capabilities include scaling lift-independent drag, lift-dependent drag, all subsonic drag, and all supersonic drag. Additional technology factors are included, such as an airfoil technology factor and the ability to include laminar flow technologies. Specified with the laminar flow technologies are the percent of local length that would experience laminar flow, resulting in viscous drag reductions. For wings this would be chord, whereas for a fuselage it would be fuselage length. Laminar flow was not assumed in this research as the D8.2b was a more current technology aircraft compared to an advanced technology version of the double-bubble configuration, the D8.5 [10].

After the lift and drag polars are generated, the information is fed to the performance process where any interpolations or extrapolations of the aerodynamic data are performed. The internal aerodynamic analysis was used in the initial FLOPS run, indicated in Fig. 5.14, to assist in the cruise flight condition generation and the viscous drag calculation. An option of the aerodynamic process in FLOPS is to override the internal aerodynamic calculations, and this capability was used in the second FLOPS run where AVL was used to generate the polars. This captured the effects of trim drag and the affect of shifting the center of gravity and static margin distance, but the vortex lattice code was only a potential flow analysis which could not capture viscous drag. In order to build up the full drag polar, the viscous drag calculations from the FLOPS aerodynamics analysis were used, calculated in the first FLOPS run, and added to the lift-dependent drag analysis of AVL.

5.2.4 Propulsion Process

FLOPS is capable of internally generating an engine deck using variables and control parameters included in the input file. Engine cycle definition decks are used for creating thrust and fuel flow decks as functions of Mach-altitude conditions for turbojets, turboprops, mixed flow turbofans, separate flow turbofans, and turbine bypass engines [67]. The FLOPS engine cycle analysis, described in the manual [14], was developed and implemented by Karl Geiselhart in Ref. [68]. It was based upon the Quick Navy Engine Program (QNEP) [69], which in turn was based upon the Navy Engine Performance Computer Program (NEPCOMP) [70].

If externally generated engine data is available, FLOPS can read in the engine data and evaluate the mission performance. A CFM56-7BE engine deck (the engine used on the Boeing 737-800 aircraft[3]) that was generated at NASA Glenn Research Center was available and used in this research. When the engine deck table, generated using the Numerical Propulsion System Simulation (NPSS) originally developed by NASA,[4] is read in by FLOPS, a propulsion and scaling module manipulates the data to fill in any missing data points, and the data is then interpolated and extrapolated, either linearly or nonlinearly, as required in the performance module. With the aft-mounted embedded engines of the D8 configuration, true freestream flow would not be ingested by the engines as typical in a pod mounted engine, similar to the 737-800. Modifications to the engine deck were required as the inlet flow to the engines included the fuselage boundary layer, called boundary layer ingestion (BLI). The BLI was included in the engine deck as a ram drag credit based upon the results from the Transport Aircraft System Optimization program (TASOPT), developed at MIT, and documented in Ref. [10].

During the system optimization, the engine static thrust was varied which required the scaling routine to adjust the base engine deck, giving the performance of a new engine with static thrust equal to the input thrust. In the final design, if the scaling was too large it would be best to rerun the engine cycle analysis for the adjusted thrust to obtain an engine model with increased accuracy. As this was only a system optimization study, no rerun engine decks were created for any of the optimal designs.

---

[3] `http://www.boeing.com`

[4] `http://www.swri.org/npss/`

5.2.5 Weight Estimation Process

Unlike many conceptual design tools, FLOPS does not use the traditional weight fraction method described by Raymer [1], Roskam [2], and Nicolai [3] for estimating gross, empty, and fuel weights. Geometric parameters, gross weight, aircraft type, mission range, payload, and maximum Mach number are all used in a set of statistical/empirical weight equations developed from a database of existing aircraft. The equations are dependent upon aircraft type, such as fighter, transport, supersonic transport, and general aviation. The transport aircraft empirical weight equations are based upon 17 aircraft: the C-5B, C-141B, B707-121 B707-321, B720-022, B727-100, B737-200, B747-100, L-1011, DC-9-30, DC-10-40, B727-200, T-39D, L-1329, XB-70, B767-200, and B969-336C [71]. Table 5.1 shows a series of images that represent a majority of the aircraft used in the formulation of the transport weight equations.[5] The weight equations were generated through a curve fit of the component weight data using Bayesian logic to determine the curve shape types, expanding the analysis beyond a simple regression [71]. Checks were included on the weight equations to ensure consistency—weight increases as horizontal tail size increases—and physical limits were applied—horizontal tail weight goes to zero as area goes to zero. Technology factors, like the aerodynamics process, are included to account for improved materials and manufacturing techniques compared to the database used to generate the weight equations.

Data from the input file specifies the aircraft type, in this case a transport aircraft, the initial gross weight guess, parametric geometry inputs, design range, payload weight and configuration (such as number of passengers and seat class type), and the maximum Mach number. Specifying the aircraft type determines which set of weight equations are used and the initial gross weight estimate is used to generate the system weights. For example, the wing weight is a function of aspect ratio, sweep, thickness, dihedral, maximum Mach number, and gross weight, to name a few. Using these parameters, the wing weight is

---

[5] All images in Table 5.1 were taken from `http://www.wikipedia.org` and do not necessarily correspond to a specific sub-model of aircraft. For visual reference only.

Table 5.1: Reference images of aircraft used in the generation of the FLOPS transport weight equations.

C-5 C-141 B707 B720

B727 B737 B747 L-1011

DC-9 DC-10 T-39 L-1329

XB-70 B767

estimated, including the primary and secondary structure. Engines mounted on the wings require additional wing weight but also provide inertia relief, both taken into account in the weight equations. The number of passengers, their class configuration, and weight is used in the fuselage weight equation, consisting of structure and passenger amenities. A small sensitivity to range is included in the weight equations as long range missions have increased passenger amenities compared to short range missions, even for an identical aircraft type.

Weight groups, as output in FLOPS, were a combination of system aircraft components where the groups were combined using typical design level categories. Table 5.2 summarizes the output weight statement from FLOPS [68].

Table 5.2: Aircraft weight statement summary as output from FLOPS [68].

Group	Components
Structure	Wing, HT, VT, Fuselage, Landing Gear, Nacelle
Propulsion	Engines, Thrust Reversers, Misc. Systems, Fuel System
System & Equipment	Surface Controls, APU, Instruments, Hydraulics, Electrical, Avionics, Furnishings, AC, Anti-icing
Operational	Crew & Baggage, Unusable Fuel, Engine Oil, Passenger Service, Cargo Containers
Payload	Passengers, Baggage, Payload

5.2.6 Mission Analysis Process

Composed of multiple mission segments specified by the user, the configuration mission performance is evaluated through a weight-based integration where the total mission fuel burn, range, and detailed flight profiles are calculated. The mission profiles are generated by a sequential input of segments, up to a maximum of 40 segments, with the segment input options indicated in Table 5.3. The analysis must always begin with a start segment, finish with an end segment, and contain at least one cruise segment.

Table 5.3: Available mission segments in FLOPS along with their primary inputs [68].

Segment	Primary Input
Start	Starting Mach number and altitude
Climb	Climb schedule number
Cruise	Cruise schedule number and total distance to end
Refuel	Fuel added and time required
Release	Weight released
Accel	Engine power setting and ending Mach number
Turn	Turn arc and engine power setting or turn acceleration
Hold	Cruise schedule number and time
Descent	Descent schedule
End	Ending Mach number and altitude

Figure 5.12 shows two example mission profiles that would typically be analyzed in FLOPS, and two key features worth noting. They are the marked “free segment” and the “instantaneous descent”. Each mission profile must include a cruise segment that does not have a specified segment range. FLOPS does not “fly” the mission from beginning to end.

Instead, the analysis starts with aircraft ramp weight, subtracts taxi out and takeoff fuel allowances, and then begins stepping through the mission segments until the free cruise segment is reached. The analysis then skips to the end of the profile and starts with the zero fuel weight, adds the reserve fuel, and then steps through the descent, cruise, hold, and other segments in reverse until the free cruise segment is reached from the opposite direction. The difference in fuel between both sides of the free segment then determines the "free" cruise segment distance.

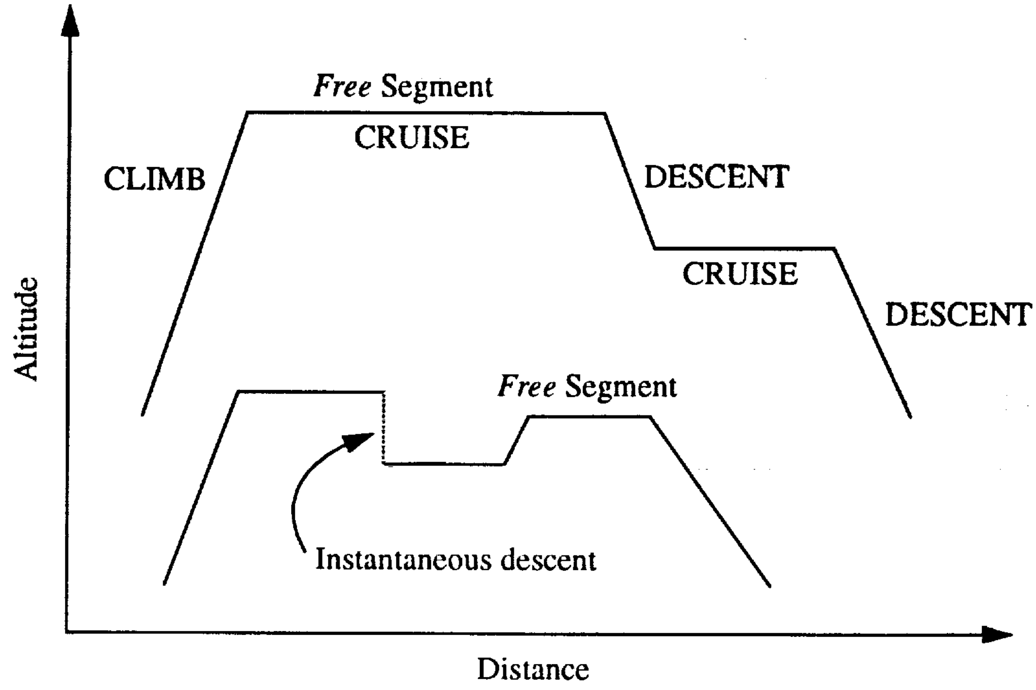

Figure 5.12: Example mission profiles as analyzed in FLOPS [68].

Several options are available to optimize the climb profile, depending on the desired mission performance. Allowable profiles include minimum fuel- and time-to-distance profiles, or a weighted combination of both. Instead of distance, minimum time- and fuel-to-climb can also be selected, again with the option of having a weighted combination of the two. Table 5.4 summarizes the different climb options. Applications of the different optimal climb profiles are suggested by the FLOPS manual, particularly to which type of vehicle configuration the climb profile should be applied. Climb profiles optimized on minimum fuel-to-distance are applicable to subsonic transports but should not be used for supersonic transports; minimum fuel-to-climb should only be used for interceptors; minimum time-to-climb is suggested only for fighters; both subsonic and supersonic transports can be optimized on minimum fuel-to-climb [67]. Any combination of climb profiles can be used in a mission profile, up to a maximum of ten climb segments with FAA climb restrictions below 10,000 feet applied.

Table 5.4: Climb schedule options for use in FLOPS climb segment analysis [67].

Flag	Description
1	Minimum fuel-to-distance
0	Minimum time-to-distance
0–1	Combination of minimum fuel- and distance-to-climb
-0.001	Minimum time-to-climb
-1	Minimum fuel-to-climb
-0.001– -1	Combination of minimum time- and fuel-to-climb

Cruise schedules can be optimized with more options than both the climb and descent schedules, with the options summarized in Table 5.5. Unlike the climb schedule, cruise schedule optimizations are discrete and a weighted combination of two options is not allowed. The cruise schedule options include different possible combinations of fixed Mach number, fixed altitude, optimal Mach number, optimal altitude, and maximum Mach number, which are optimized for either segment endurance or specific range, velocity divided by fuel flow. A fixed lift coefficient cruise schedule can also be selected. If a hold segment is specified, the cruise schedule options are applied to the hold segment. A maximum of fifteen cruise segments can be used in a mission profile, again any combination of cruise schedules can be chosen. Reserve cruise segments are included in the cruise schedule definitions [67, 68].

Descent segments in the mission profile have three schedule options, summarized in Table 5.6. In the case of military aircraft, no time, distance, or fuel credit is given for descent segments, so an option for no-credit descent is available with a zero flag. For all other aircraft types, a descent at maximum lift-to-drag ratio or constant lift coefficient can be selected, and FAA restrictions on calibrated airspeed below 10,000 feet applied, same as the climb schedule. Limits in the maximum dynamic pressure can also be chosen for

Table 5.5: Cruise schedule options for use in FLOPS cruise segment analysis [67].

Flag	Description
0	Optimum altitude and Mach number for specific range
1	Fixed Mach number and optimal altitude for specific range
2	Fixed Mach number at input maximum altitude or cruise ceiling
3	Fixed altitude and optimum Mach number for specific range
4	Fixed altitude and optimum Mach number for endurance
5	Fixed altitude at a constant lift coefficient
6	Fixed Mach number and optimum altitude for endurance
7	Optimum Mach number and altitude for endurance
8	Maximum Mach number at input fixed altitude
9	Maximum Mach number at optimum altitude
10	Fixed Mach number at constant lift coefficient

the descent schedule. A special property of the descent segment only, any descent segment followed by a climb segment will be considered, for all but one of those descent segments, an instantaneous (zero fuel, time, and distance) change in altitude [68].

Table 5.6: Descent schedule options for use in FLOPS descent segment analysis [67].

Flag	Description
0	No descent time, distance, or fuel credits
1	Descent at optimum lift-to-drag ratio
2	Descent at constant lift coefficient

With the primary mission completed, additional fuel must be added to account for operation variations due to weather, missed approach, etc. How the reserve fuel is calculated depends upon the type of reserve mission used, with various options available in FLOPS. Two variables, RESRFU and RESTRP, are used in the calculation of constant fuel reserves. If $RESRFU > 1$, a fixed reserve fuel weight is added to the mission fuel weight where the value is input in pounds, and if $RESRFU < 1$, a fraction of total usable fuel weight was added. RESTRP is used to add reserve fuel as a fraction of total trip fuel weight. An alternate airport can be used and the distance to the alternate input with the ALTRAN variable. Combinations of RESRFU, RESTRP, and ALTRAN can be used in the definition of the complete mission reserve [67].

Reserve fuel can be calculated one of three ways: 1) calculate reserve fuel required for trip to alternate airport plus RESRFU and/or RESTRP, 2) reserve fuel calculated using RESRFU and RESTRP only, and 3) the reserve fuel is the remainder after the primary mission has been flown [67]. Additional fuel is added for an input missed approach time.

This research used a typical transport aircraft mission profile with segments consisting of climb, cruise, and descent. The mission segments used in the FLOPS input file were START, CLIMB, CRUISE, DESCENT, and END, with a fuel reserve added using the RESTRP variable set to 5%. The single cruise segment was defined as a free segment. This profile matched the mission profile of the N+3 advanced concept study, defining the D8 configuration, from Ref. [10]. As minimization of total fuel burn was the objective of this research, minimum fuel-to-climb was the chosen schedule for the climb segment, restricted to the FAA operational constraint limiting calibrated airspeed to 250 knots for altitudes less than 10,000 feet. Cruise Mach number was specified in Ref. [10] and was used again here, set to Mach 0.72. With the cruise Mach number fixed, and an objective of minimizing fuel burn, the fixed Mach number with optimum altitude for specific range was the selected cruise schedule, allowing for a cruise climb. Cruise altitude was limited to a maximum of 41,000 feet. Maximum lift-to-drag ratio was selected for the descent schedule, with a two minute allowance for a missed approach.

5.2.7 Balanced Mission Analysis

Recalling Fig. 5.14, based upon an initial guess for gross weight the aircraft empty weight is calculated, and the difference between the operational weight fully loaded and gross weight is assumed to be fuel. The mission is then flown with the free segment flown with only the fuel remaining after all other mission segments, determining total range. In the case of a design range mission, if the calculated range is equal to the design range, the analysis moves on to the takeoff and landing analysis, a completely separate analysis process in FLOPS. Any difference between the design range and the calculated range from the performance process, the gross weight estimate will be updated and the analysis run again until convergence is achieved on the design mission range. All mission fuel, less defined reserves and taxi fuel, will be burned, while achieving the design range, leaving zero mission fuel at the end of the mission.

5.2.8 Takeoff and Landing Analysis

The detailed takeoff and landing analysis procedure was used in the multidisciplinary design optimization. Developed as a physics-based, first principles analysis, all FAR Part 25 (civilian transports) or MIL-STD-1793 (military aircraft) airworthiness requirements are applied. During takeoff, the time-integrated analysis captures the variation in thrust with velocity and the changes in lift and drag coefficients as the aircraft rotates, and lifts off. During the descent the aircraft will flare, which changes the lift and drag coefficients, touch down, deploy spoilers if included, and apply the brakes. In the takeoff analysis, numerous simulations are run in order to determine the balanced field length which is the greatest distance of the following:

- one engine inoperative (OEI) field length to clear 35 foot obstacle
- aborted takeoff at decision speed with one engine inoperative
- aborted takeoff at decision speed with all engines operating (AEO)
- 115% of distance to clear 35 foot obstacle with all engines operating

Excess thrust at the second segment climb gradient, dependent upon the number of engines in the event of an engine failure, must be greater than zero in order to have a successful takeoff.

The maximum takeoff distance allowed in the multidisciplinary design optimization was set to 8,000 feet. This was chosen to remain consistent with the previous research on the D8 geometry prior to the application of a 5,000 feet balanced field length requirement discussed in Ref. [10]. For the landing field length requirement, the Boeing Commercial Aircraft Company document for airport planning entitled, "737: Airplane Characteristics for Airport Planning" was used [72]. Standard day, sea level conditions were used at the maximum allowable landing weight, 146,300 pounds. Figure 5.13 shows at the maximum landing weight, the field length for a dry runway at sea level, standard day is 5,800 feet. This was chosen as the landing field requirement for the multidisciplinary design optimization.

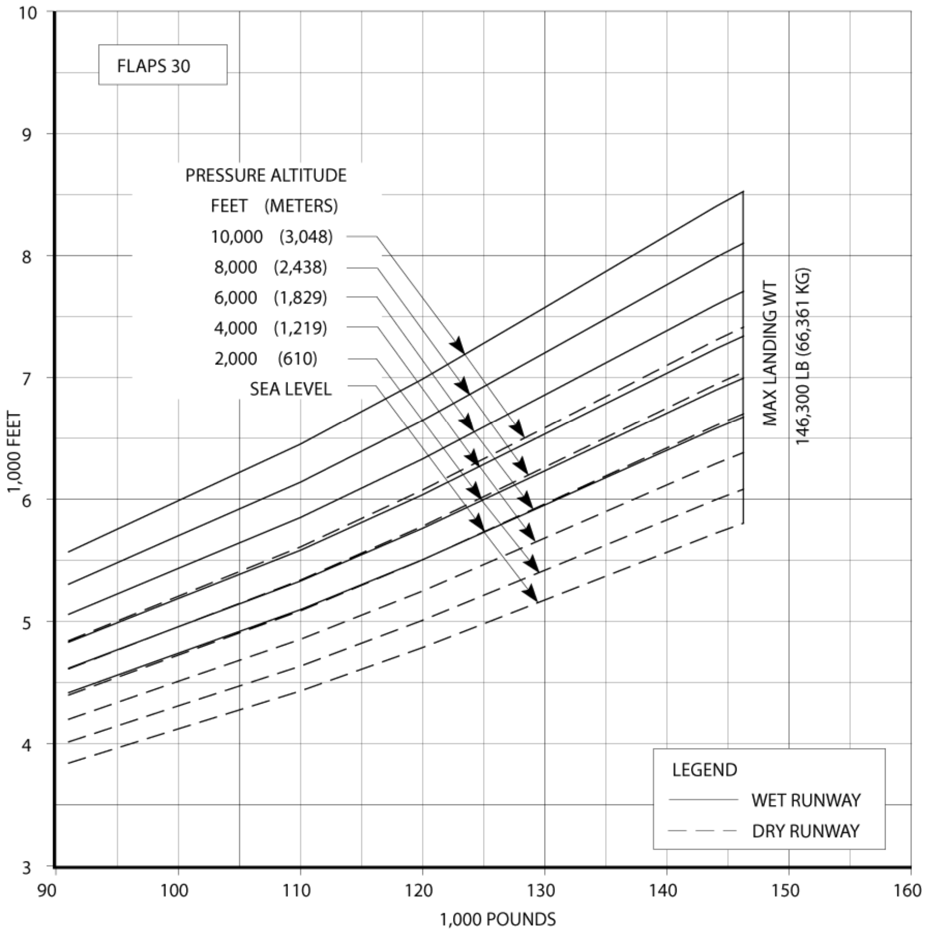

Figure 5.13: Boeing 737-800 landing field length plot for both wet and dry fields, various altitudes, at standard day temperature [72].

5.3 D8.2b System Analysis and Multidisciplinary Design Optimization

ModelCenter®, a tool used within the Aeronautics Systems Analysis Branch at NASA Langley Research Center, was used to integrate the numerous disciplines that have been discussed to this point. Developed by Phoenix Integration,[6] ModelCenter is a multidisciplinary integration, design, and optimization software that allows the user to integrate their various analysis tools methods while facilitating all data transfer. The design variables are specified and can be brought into any of the integrated optimization schemes, including gradient methods, response surface optimizers, genetic algorithms, and particle swarm optimizers. During an optimization, multiple instances are able to be run allowing for the parallelization of the analysis (if the optimization scheme allows), drastically decreasing optimization run time.

5.3.1 Integrated Analysis in ModelCenter®

FLOPS, the AVL input file generation, AVL, the flight condition calculations, and the MATLAB® dynamic analysis have all been seamlessly integrated into ModelCenter® to perform the multidisciplinary design analysis and optimization. Data was sent from each analysis component to the next through the linking capability in ModelCenter, where the output of a component was linked to the inputs of one or more components. This allowed components to be run in parallel, accelerating the analysis process. Additionally, using the Analysis Server software in collaboration with ModelCenter, multiple instances of the model were run allowing for multiple designs to be evaluated simultaneously, reducing the total time for the complex design optimization.

Figure 5.14 depicts the multidisciplinary design analysis, as implemented in ModelCenter, in a process diagram. The first step was the initialization of the design variables, controlled either by the user or by the optimization routine. The design variables allowed to vary were wing area, wing quarter-chord sweep, dihedral, wing longitudinal apex location,

---

[6] `http://www.phoenix-int.com/`

static thrust, horizontal tail area, vertical tail area, and vertical tail sweep. An additional design variable that was allowed to vary was the minimum static margin, depending on the design case. For the cases where minimum static margin was not a variable, it was fixed at 10% of the mean aerodynamic chord.

No weight buildup was used for the calculation of center of gravity. To allow the optimizer the flexibility to place the center of gravity anywhere on the configuration, the CG was placed based upon the aircraft neutral point and specified static margin. The aircraft neutral point was a function of the design variables allowing the optimizer to shift the neutral point, and by association, the center of gravity placement. This was chosen to open the design space, freeing the optimizer to place the center of gravity as desired, and eliminating the guesswork in placing each component center of gravity, including subsystems. This allows for potentially unique designs that would not be eliminated due to center of gravity constraints. As advanced air transport technologies evolve, high mass density subsystems, such as batteries, can be placed to allow for a larger range of center of gravity placements for a particular configuration. A summary of the design variables, and their allowable range, is summarized in Table 5.7. The ranges were selected as to not become active and corner the optimizer in the design space.

Table 5.7: Summary of design variables allowed to be varied by the optimizer with their allowable ranges. Static margin was only allowed to vary in select design cases.

Design Variable	Description	Nominal	Minimum	Maximum
T	Thrust (lb.)	25,000	10,000	30,000
S	Wing Area (sq. ft)	1100	800	2500
Λ	Wing Sweep (deg)	10	0	30
Γ	Wing Dihedral (deg)	5	0	10
S_{HT}	HT Area (sq. ft)	277	100	500
S_{VT}	VT Area (sq. ft)	74	50	300
Λ_{VT}	VT Sweep (deg)	40	0	65
$X_{W_{apex}}$	Wing Apex (ft)	55	20	75
SM	Static Margin	10%	-5%	30%

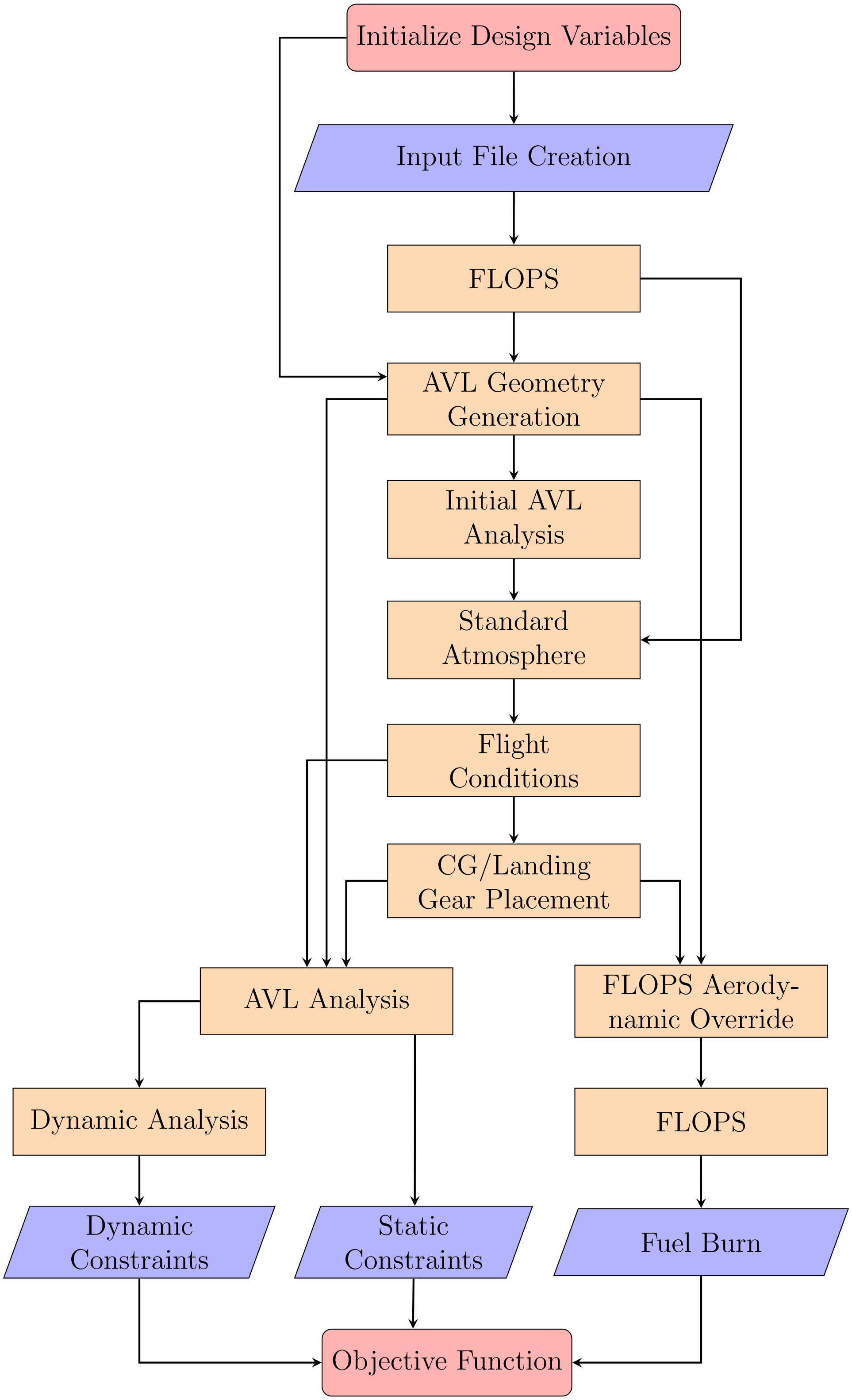

Figure 5.14: Multidisciplinary design analysis process chart with data flow direction indicated by the arrows.

For the horizontal stabilizer, only the planform area was allowed to be a design variable. Located at the tip of the twin vertical stabilizers, allowing the horizontal tail sweep to be a variable would disconnect the horizontal stabilizer from the tips of the verticals, resulting in a stabilizer floating in space. To ensure this did not happen, the design variables for the horizontal stabilizer were restricted, with any positional movement implemented by the vertical stabilizer geometry.

Wing aspect ratio was not allowed to be a design variable due to the fixed span requirement of the D8.2b configuration. The goal of the D8.2b configuration was to quantify some of the configuration and technology impacts while maintaining similar operational capabilities as the Boeing 737-800 aircraft. Increases in span would provide large induced drag benefits while moving the vehicle to a larger airport operations class. Also, increasing the airport operational class would cause the configuration to be non-comparable to the 737-800 in terms of operational destinations. Additionally, as aspect ratio, and therefore span, is increased, stress-based constraints become inactive in the design and are replaced by flutter constraints, an analysis well beyond the scope of this research. Therefore, the span was fixed at 118 feet, same as the 737-800, to eliminate these issues.

Similarly to the wing, the horizontal tail aspect ratio was also kept constant. This was done to reduce the number of design variables, limit the span due to flutter concerns, and maintain a constant lift curve slope as described in Section 4.5.3.

ModelCenter, through the use of an custom component called a ScriptWrapper, created the FLOPS input file and executed FLOPS. This first FLOPS execution was used to extract dependent geometry parameters that were required by AVL. To ensure consistency in the meta-geometries between all components, all the design parameters were linked to eliminate the possibility of failing to update an input in a later analysis. In addition to generating geometry information required for the AVL input file, FLOPS was used to estimate the system weights, takeoff rotation velocity, and start of cruise flight conditions. This information was used in the creation of the different flight conditions for the static and dynamic analysis, described in Section 4.4.2.

Any inputs not required by FLOPS, but necessary in the generation of an AVL input file, were directly sent to the AVL Geometry Generation component. Again, a custom ScriptWrapper created for this research, the AVL geometry generation component created the input file used in all AVL analyses. Required parameters for the generation of the AVL input file included the control surface sizes and locations, and the longitudinal wing root, leading edge apex location, $X_{W_{apex}}$.

The initial AVL analysis was used for two reasons: 1) to capture the lift coefficient and zero geometric angle of attack with deflected flaps in ground effect, and 2) to calculate the aircraft neutral point for placement of the center of gravity based upon the static margin design variable. Instead of using a fixed, approximated lift coefficient for the takeoff analysis, the initial run of AVL was able to predict the lift coefficient in ground effect, taking into account the change in lift due to the flap deflection. This made the lift coefficient used in the takeoff flight condition unique to each configuration in the design optimization. Also, unique to this research was the use of static margin as a design variable, where the center of gravity was placed based upon the neutral point and specified static margin instead of the typical calculation of center of gravity. To place the center of gravity, an initial run of the AVL model had to be used to determine the configuration neutral point.

The standard atmosphere component was used in the generation of the five flight conditions described in Section 4.4.2. Temperature, pressure, and density were calculated, as functions of altitude, using the standard atmosphere equations presented by Anderson [73]. Viscosity was calculated using Sutherland's formula.[7] With known altitude at each flight condition, determined from the initial FLOPS run, and calculated temperature, the speed of sound was calculated.

---

[7] `http://www.grc.nasa.gov/WWW/k-12/airplane/viscosity.html`

The five flight conditions, discussed in Section 4.4.2, were calculated in the flight conditions component. Data calculated in this component were passed to the full AVL analysis for evaluation of the static and dynamic vehicle performance, using steady state trim deflections and stability derivatives. Placed off the specified static margin, either fixed or as an optimization design variable, the rearmost center of gravity position was calculated in the CG placement component and fed into the AVL analysis and FLOPS aerodynamic override. The main landing gear position, placed a static distance of 1.874 feet aft of the rearmost center of gravity position and nine feet below the aircraft centerline (Section 5.1.2), was calculated in the takeoff flight condition and placed in the CG/Landing Gear Placement component. This set the reference point location for the takeoff trim analysis in AVL.

In the AVL analysis component, five flight conditions were analyzed with the moments trimmed to zero, resulting in a steady-state condition. The exception was the takeoff analysis pitching moment, which was trimmed to the required aerodynamic pitching moment for lifting the nose wheel off the ground, calculated in the takeoff flight condition. In the static flight conditions—takeoff, one engine inoperative, maneuver—the trimmed control surface deflections were output for evaluation against the static constraints, which were used in the evaluation of the objective function. In the dynamic flight conditions of stall and cruise, the steady-state angle of attack control surface deflections were output into the dynamic analysis. Additionally, the stability derivatives were calculated in AVL and passed to the dynamic analysis for use in the linearized perturbation equations of motion.

For both the stall and cruise flight conditions, the calculated stability derivatives, steady-state angle of attack, and trim deflections were input into the system dynamic equations of Section 4.1 in the Dynamic Analysis component. The optimal control gains were calculated and the system perturbation, atmospheric turbulence, and discrete gust responses were all evaluated in the dynamic analysis, with the detailed methodology described in Chapter 4. The stall and cruise flight conditions were analyzed independently allowing each flight condition to be evaluated in isolation against the dynamic constraint requirements. Violations of the constraints from the dynamic analysis were included in the objective function as penalties on the objective function, or otherwise fuel burn.

FLOPS contained a procedure for estimating the aerodynamic performance of the input parametric geometry, discussed in detail in Section 5.2. Given a fixed geometry, adjusting the static margin and center of gravity positions has no effect on the aerodynamic analysis in FLOPS as the analysis was insensitive to variations in drag due to trim or angle of attack. To capture the sensitivity of induced and trim drag due to changes in geometry, static margin, and center of gravity position, AVL was again used to create a series of drag polars, as a function of Mach number, to be included in the FLOPS input file as an aerodynamic override. A sweep of lift coefficients ranging from 0.0 to 0.6 in increments of 0.2 were used with three Mach numbers: a low-speed Mach number of 0.4, a mid-speed Mach number of 0.55, and the cruise Mach number of 0.72. Overriding the internal aerodynamic calculation with the aerodynamic calculation of AVL captured the configuration drag coefficient sensitivity to static margin and center of gravity location.

With the aerodynamics calculated in AVL, FLOPS was run a second time with the same input file as the first FLOPS run at the beginning of the analysis process, with the exception of the external aerodynamics substituted for the internal analysis. The second FLOPS analysis was used to capture the changes in fuel burn due to changes in trim drag, with the fuel burn output used as the minimized objective in the system optimization.

The overarching objective was to minimize system fuel burn, which was output from the second FLOPS analysis. Any violations of the static or dynamic constraints, or any performance constraints violations, resulted in a fuel burn penalty. Moderate violations of the constraints were possible in the case where the objective function, with the constraint violation penalty, would be less than the objective function with no penalties.

5.3.2 Optimization Methodology

Many different optimization routines and methodologies exist for determining an "optimal" design, such as gradient-based optimizers, surrogate model optimizers (such as Boeing's proprietary optimizer, Design Explorer,[8]) particle swarm optimizers, and genetic algorithm optimizers. The challenge lies in guaranteeing that the found optimum is the global optimum, not a local optimum in a design space encompassing multiple minima. Many times this guarantee is not possible. Thus, the goal of any optimization is to find a feasible design that minimizes the objective function while any improvements from the found design would be minimal.

Each optimization routine has benefits and detriments resulting in a trade-off between convergence speed and robustness of the routine in finding the optimal solution. Gradient-based optimizers have the benefit of converging to the optimal solution in a smaller number of iterations compared to other routines. The gradient-based optimizer is ideal in smooth and continuous design spaces, calculating a mathematically-provable global optimal design in a concave design space. However, a realistic design space is rarely concave and any design space encompassing functions greater than second order, with changes in concavity, will introduce local minima. Some optimization routines are driven to these local minima, dependent upon the sensitivity to initial conditions and the value of the local gradient. Additionally, gradient-based routines are not applicable to a discontinuous design space.

Generally, the next iteration in a gradient-based optimization routine depends upon the solution of the previous iteration, which does not lend itself well to parallel processing. If the solution execution time is small, this is not a problem, but if the solution time is large, then this can be quite limiting. The lack of parallel computing capability is made up by the speed of convergence, but only if the derivatives of the design space are available with respect to the design variables. If not, a method of computing the derivatives, such as finite difference, must be used which can result in an excess number of analysis executions,

---

[8] `http://www.boeing.com/news/frontiers/archive/2005/april/i_tt.html`

slowing the optimization process. Typically, the gradient-based optimizer is used when the execution time of the analysis is long and the design space is well-behaved, meaning it is smooth, continuous and local minima only differ slightly from the global minimum.

A problem with gradient-based optimizations in ModelCenter® is that the ModelCenter routines are incapable of handling analysis failures. Instances of the analysis may fail, due to the optimizer exploring extreme regions of the design space. The failure results in data output files that cannot be successfully parsed, extracting the required data to continue the optimization process. As an example, a case could be run in AVL that would be unable to trim, resulting from a trim convergence failure, and results of the analysis would not be parsed correctly.

A robust optimizer that can handle analysis failures, such as a surrogate or genetic algorithm optimizer, is required. It is desired to maintain fast convergence rates, while reducing the number of iterations to convergence. Boeing's Design Explorer, a surrogate model optimizer, is ideal for such an analysis. Design Explorer is designed to efficiently solve engineering problems where the analysis code run times are long, the design space is noisy and non-smooth, and failures can occur in the analysis. Additionally, the algorithm is designed to be less likely to stop at a local minima resulting in larger success rates in finding the global minimum [74]. Figure 5.15 shows the process flow of the Design Explorer optimizers. The process is started by carefully choosing values of the design variables, exploring the design space using an orthogonal array [74], then the analysis code is run to begin to develop a response model capturing the relevant responses.

From the results of the initial runs, surrogate models are developed to approximate the analysis with arbitrary values of the design variables, within the limits of the lower and upper bounds. These surrogate models are designed to be evaluated quickly, in comparison to the analysis code, and are continuous in order to predict the value of the objective as if the analysis code was run. The surrogate models are created using interpolating Kriging models, where they are able to be recalibrated as new data becomes available [74–76]. With

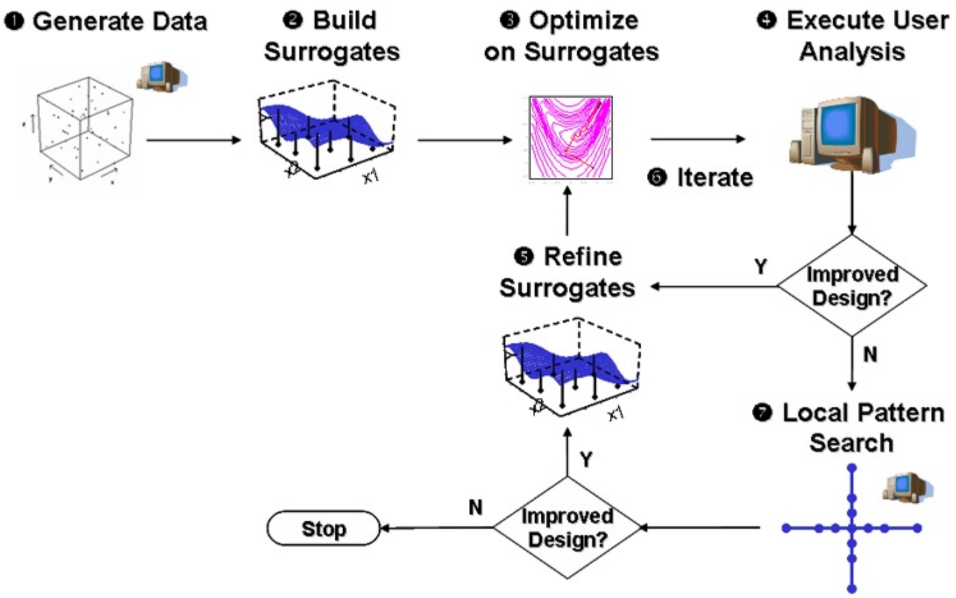

Figure 5.15: Process flow for Design Explorer optimizer as shown in the ModelCenter help menu [74].

the generated surrogate models, a gradient-based optimizer is run using the surrogate models numerous times from randomly generated starting points.

The results of the surrogate model optimization are one or more unique local minima. These solutions are compared to the solution of the analysis code run with the same design variable values. For simple problems, this comparison can be quite good after very few iterations. For complex design problems, the error between the analysis code and the surrogate model optimization can be large. The actual values obtained from running the analysis are used to tune, or calibrate, the surrogate model and the gradient-based optimizer is rerun. This process is repeated until either the maximums of the optimizer settings are reached, as input by the user (such as maximum function evaluations), or no improved designs have been found [74].

When no improved designs have been found from the iterative process of refining the surrogate model and running the gradient optimizer, a local pattern search is performed to explore the design space in the vicinity of the found optimum. If no improved designs are found, then the optimization process is terminated and the design is guaranteed to be at least a local minimum. If a better solution is found, the local pattern search is terminated and the surrogate model refinement process is restarted [74].

Design Explorer was the preferred optimizer for this research as the execution time of the full multidisciplinary analysis was long. Additionally, Design Explorer is capable of being run with parallel processors, thus taking advantage of ModelCenter's capability of running multiple instances of the model, drastically reducing overall computation time. Unfortunately, the design space was extremely noisy, discontinuous, and non-smooth, preventing the Design Explorer algorithm from generating surrogate models that accurately mapped the design space. As a result, the Design Explorer optimizer could not be used in the system optimization. It is possible that Design Explorer could be expertly set up to successfully perform the optimization with different algorithm settings, but the author was unsuccessful. As a result, computation time was sacrificed for algorithm robustness with the use of a genetic algorithm optimizer.

Optimization using the Darwin Algorithm

Darwin, a genetic algorithm search routine developed by Phoenix Integration, Inc.,[9] was the optimizer used in the multidisciplinary design optimization of this research. The algorithm is capable of using both discrete and continuous design variables with any specified number of constraints. Single objective optimization problems reach convergence when the fitness function has not improved over a specified number of generations, whereas a multi-objective optimization problem uses a Pareto front in determining convergence [74, 77]. The minimization of fuel burn was used as a single objective optimization problem. To determine convergence, a specified number of sequential generations without objective improvement was selected with a limit on the number of total generations to be analyzed.

The Darwin algorithm control options dialog box, as integrated in ModelCenter®, is shown in Fig. 5.16. Many of the options were left at the system defaults, such as population

---

[9] `http://phoenix-int.com`

size. The population size, a function of the number of design variables, was set to 63 and was constant throughout the optimization. Decreasing the population size reduces the optimization run time at the risk of being caught in local minima, a result of a lack of design diversity in the population [74]. Increasing the population size will increase the number of iterations, but will be more robust in avoiding local minima. The default value for population size, based on the number of design variables, was used in all optimization cases.

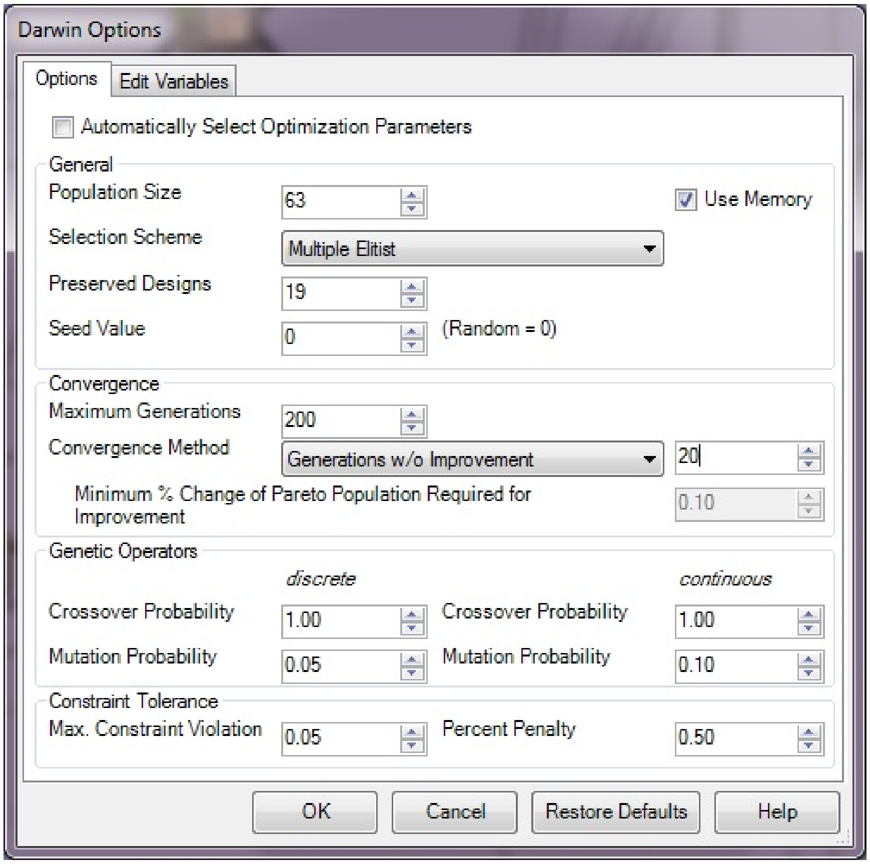

☐ Automatically Select Optimization Parameters

General
Population Size 63
☑ Use Memory
Selection Scheme Multiple Elitist
Preserved Designs 19
Seed Value 0 (Random = 0)

Convergence
Maximum Generations 200
Convergence Method Generations w/o Improvement 20
Minimum % Change of Pareto Population Required for Improvement 0.10

Genetic Operators

	discrete		*continuous*
Crossover Probability	1.00	Crossover Probability	1.00
Mutation Probability	0.05	Mutation Probability	0.10

Constraint Tolerance
Max. Constraint Violation 0.05
Percent Penalty 0.50

Figure 5.16: Darwin algorithm options as captured in a screen shot from ModelCenter. Options shown are the values used in the full static trim and dynamic optimization cases.

Darwin has the option of two different selection schemes: elitist and multiple elitist. Multiple elitist was chosen as it is more effective in problems where many local minima surround the global minima. Since the specific topography of the design space was unknown, this was deemed more robust. The multiple elitist selection scheme works by combining the parent and child populations into one list and ranking them based upon their fitness, the sum of the objective function and any penalties [74]. The next generation is created by taking the top N_p number of designs, where N_p is the specified number of preserved designs, to the new generation and filling the remaining designs with the top ranked child designs that have not already been selected. The number of preserved designs, N_p, should be kept small as that introduces the greatest number of new designs. Large values of N_p reduce the number of new designs and can result in the algorithm search becoming localized, trapping the search in a local minimum [74].

The initial population was generated randomly through the use of a seed value that was set to zero, which allows ModelCenter to randomly generate the seed. This results in successive runs not necessarily giving the same results, or if the result was the same, taking a different path to get there. However, if it is desired to recreate an optimization run, the randomly generated seed value is saved as part of the output during the optimization run. Inputting the same seed value, as long as all other settings remain unchanged, will reproduce the same optimization run. Darwin's memory function was also used with the goal of improving the efficiency of the design optimization [74]. A discrete design, along with its response, is stored in a binary tree, eliminating the need to reanalyze duplicate designs that are discovered in the optimization process [74].

The convergence criteria, as mentioned previously, differ between single objective and multi-objective optimizations. A single objective can be minimized, creating a best design, whereas a multi-objective optimization has no best design, but rather a trade-off between the different objectives, typically shown as a Pareto front. The Darwin algorithm can be stopped in two ways: stop after a fixed number of generations, or stop after the solution has converged without any improvement for a specified number of generations. The second option was used as the convergence criteria, where the number of sequential generations without improvement ranged from 10-20, depending on the run case; the larger the number of design variables and constraints, the larger the number of successive generations without improvement required for convergence. The maximum number of generations was reduced to 200 from the default of 1,000 to bound the runtime.

Along with the multiple elitist selection scheme, crossover and mutation are used in the creation of the next generation. A uniform crossover procedure was applied with a high probability, typically $0.8 \leq P_c \leq 1.0$, as suggested by the Darwin algorithm manual and ModelCenter default value, to traverse the design space [74, 77]. The child designs subjected to crossover are forced to be different than all other child and parent designs, and the process is repeated to fill the population of the next generation. Mutation of the design's genetic string introduces random alterations into the population while preventing premature loss of important genetic information [74, 77]. It also brings in design features that may have never been represented by the initial population, diversifying the overall design population. During mutation, a single value in the genetic string representing a particular design is changed, at random, to any other permissible value. This mutation process, applied with a low probability of $0.01 \leq P_m \leq 0.3$, occurs after the crossover operation and completes the creation of a new generation in the optimization process [74, 77], summarized by the process chart of Fig. 5.17.

Constraint tolerance is the last set of options for the Darwin algorithm displayed in the options toolbox window of Fig. 5.16. The designs in each generation, and each successive generation, are ranked according to their fitness. Calculated by Eq. 5.3 [74], the fitness, f, is a function of the objective function, o, and any penalties p due to violated constraints.

$$f = o + p \tag{5.3}$$

The "maximum constraint violation" and "percent penalty" options in the dialog box give the user control over how the penalty function is applied. Described in Eq. 5.4 [74], the penalty function only provides a slight penalty to violated constraints where the violation is

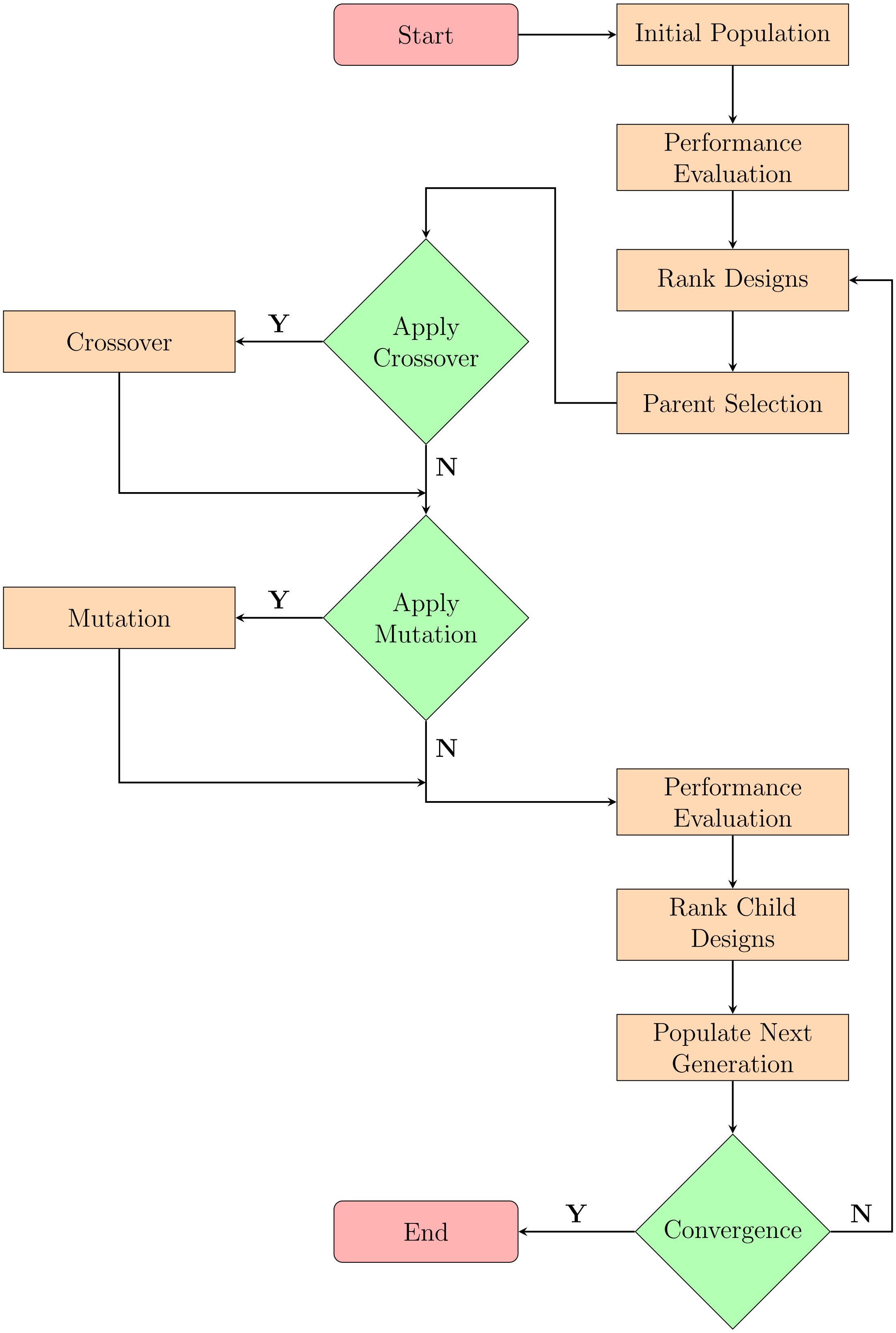

Figure 5.17: Darwin genetic algorithm process flow chart, recreated from Ref. [77].

less than the user specified maximum, in percent,

$$p = p^* \left(\frac{e_t}{e_m} \right)^{2.5} \tag{5.4}$$

where p^* is the percent penalty, e_t is the total constraint violation, and e_m is the maximum allowed constraint violation. In the case of Fig. 5.16, any constraint violation less than 5% will be only lightly penalized, but as the violation increases beyond the maximum allowed, the penalty increases drastically. If increased margin on the constraints is desired, the percent penalty weighting (50% in Fig. 5.16) should be reduced and/or the maximum constraint violation increased. To the contrary, the opposite changes would be made to tighten the tolerances on the optimization constraints. The default constraint tolerance values, 50% penalty, and 5% maximum constraint violation, were used in all optimization cases of this research.

Chapter 6

Verification and/or Validation of Methodology and Analysis Tools

6.1 Verification of Equations of Motion

The fully coupled nonlinear equations of motion were derived with the aide of the MATLAB® Symbolic Toolbox with both the aerodynamic and moment terms approximated using a Taylor series expansion, dropping all terms over first order. The derived perturbation equations were verified against Roskam, Napolitano, and Schmidt in Refs. [15, 34, 78].

An eigenanalysis was performed on the state matrix of the derived equations of motion to compare roots of the characteristic equation given in Napolitano [15] and eigenvalues calculated internally in AVL. The stability derivatives given in Refs. [15, 34] were input into the full-coupled perturbation equations and the eigenvalues of the state matrix were computed. The eigenvalues are compared in Fig. 6.1. The AVL calculated stability derivatives were input into the perturbation equations and the eigenvalues calculated for both methods. The results are plotted in Fig. 6.2. In both cases, the eigenvalues match with the input stability derivatives coming from separate sources indicating the derived equations of motion accurately represent the vehicle dynamics.

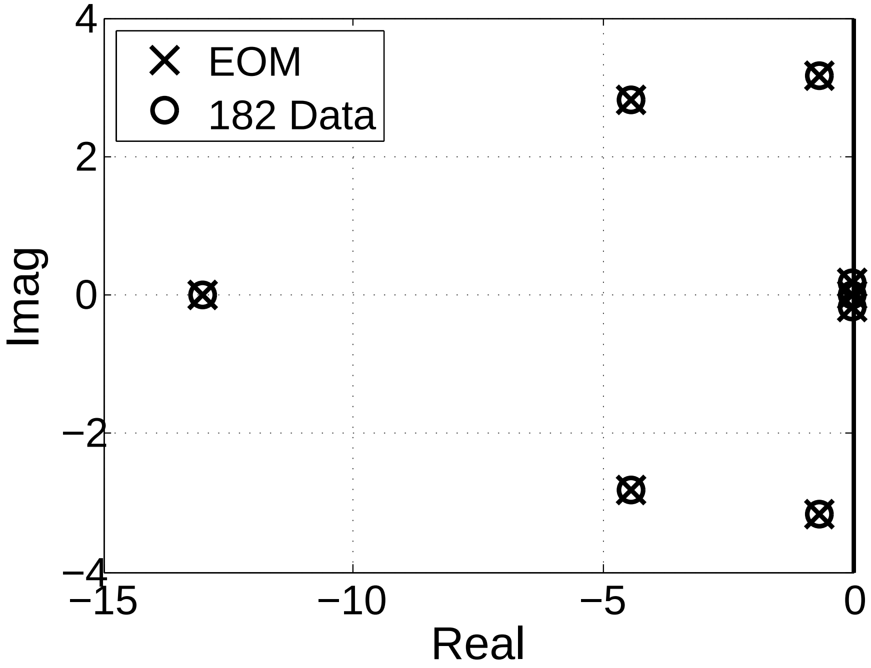

Figure 6.1: Derived equations of motion modes compared to modes presented by Napolitano [15].

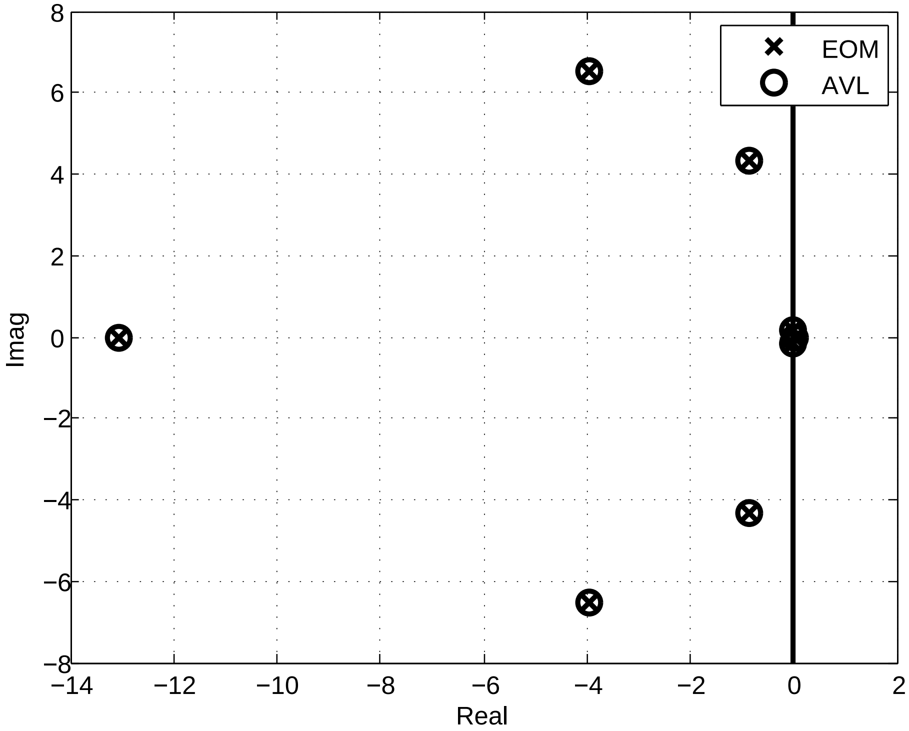

Figure 6.2: AVL computed modes compared modes of derived equations of motion.

6.2 Verification of the Atmospheric Disturbances

The von Kármán continuous turbulence spectrum was calculated for varying length scales to ensure the accurate calculation of the spectrums. Length scales of 500, 1,000, 2,000, and 5,000 feet were used in the vertical spectrum equation for varying spatial frequencies, Ω, between 10^{-4} to 10^{-1}. Figure 6.3 shows the vertical spectra calculated for the different length scales and these results agree with Fig. 9.56 in Ref. [30].

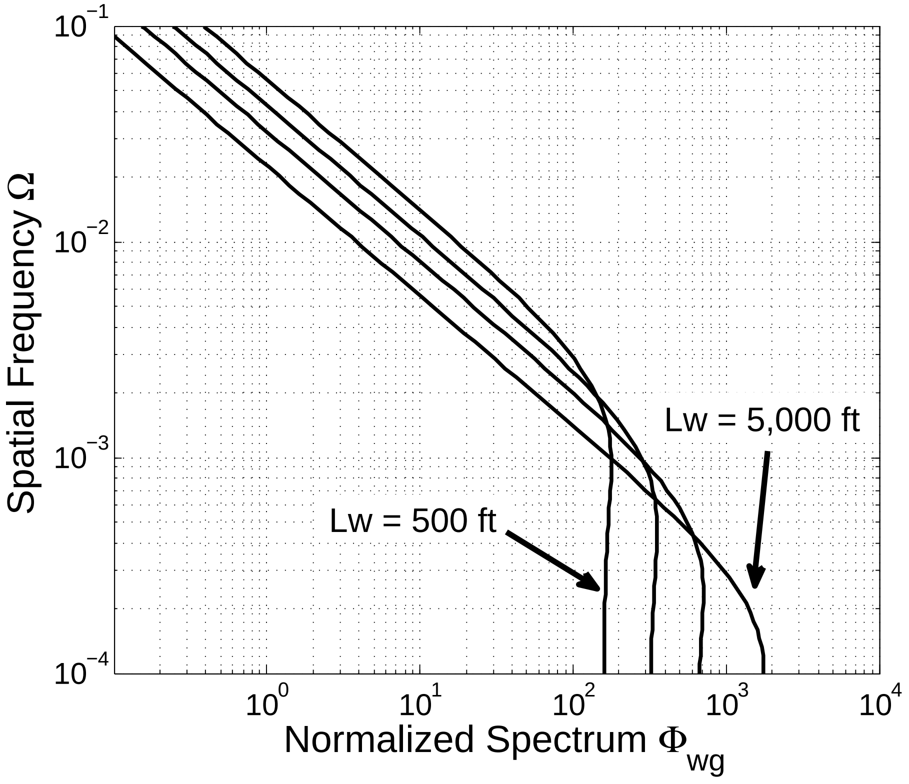

Figure 6.3: The von Kármán continuous turbulence spectrum.

Using the vertical spectra of Fig. 6.3, the results of the example in Section 13.4 of Ref. [29] were accurately recreated for the set of equations of motion, and appropriate stability derivatives, given in the example. In the example, the point approximation, applying the gust to the center of gravity of the aircraft, works very well in capturing the response of the motion states, α, θ, and u.

6.3 Validation of the Aerodynamic Analysis

Validation of the aerodynamic model was necessary to ensure the stability derivatives used in the dynamic analysis were a reasonable reflection of reality. In conceptual design where the design space is being rapidly explored, it is unrealistic to use high-order tools (CFD) and/or experimental testing to formulate the aerodynamic model. With each change in the geometry new aerodynamic models have to be created; the lack of fluidity in high-order tools and experimental testing eliminates this as a possibility with current capabilities. Lower-order methods must be used that can rapidly estimate the aerodynamic properties of a geometry while matching high-order tools or experimental results reasonably well. An accurate representation of the geometry is desired while keeping in mind the limitations of the low-order methods.

Experimental stability derivatives of the Cessna 182 in the cruise condition were available through Ref. [34] and were used to validate the Cessna 182T AVL model. The D8.2b geometry, due to the conceptual nature of the geometry, has no experimental data for comparison and so the AVL model was compared to results of Cart3D, a high-fidelity inviscid analysis CFD tool using Cartesian mesh methods developed jointly by NASA Ames and the Courant Institute at NYU.[1] The Cart3D analysis was run at multiple Mach numbers to capture the aerodynamic performance throughout the climb, cruise, decent mission segments.

6.3.1 Cessna 182T Aerodynamic Model

Stability derivative data at multiple flight conditions for the Cessna 182T were used for validation of the AVL model described in Section 5.1. As previously described, the AVL geometry had to be modified to model propulsion and fuselage effects on the aircraft stability. The stability derivatives used to validate the AVL model were from Ref. [34] in the cruise condition and are summarized in Table 6.1. The derivatives are listed in order of importance

---

[1] http://people.nas.nasa.gov/ aftosmis/cart3d/cart3Dhome.html

to the aircraft dynamics [79]. The strategy used for matching results placed the greatest emphasis on matching stability derivatives from top to bottom.

Table 6.1: Cessna 182T flight data stability derivatives at the cruise flight condition, angle units in radians [15].

Longitudinal	Value	Lateral/Directional	Value
C_{L_α}	4.41	C_{l_β}	-0.0923
C_{m_α}	-0.613	C_{n_β}	0.0587
C_{m_q}	-12.4	C_{l_p}	-0.484
C_{L_q}	3.9	C_{n_p}	-0.0278
		C_{l_r}	0.0798

For comparison, the stability derivatives of a simple Cessna 182T geometry are presented first to give an indication of why the fuselage and propulsion effects needed to be modeled. This simple AVL model, consisting of only the lifting surfaces, is shown in Fig. 6.4. For the comparison of the simple AVL model to the flight data, only the longitudinal stability derivatives are shown in Table 6.2.

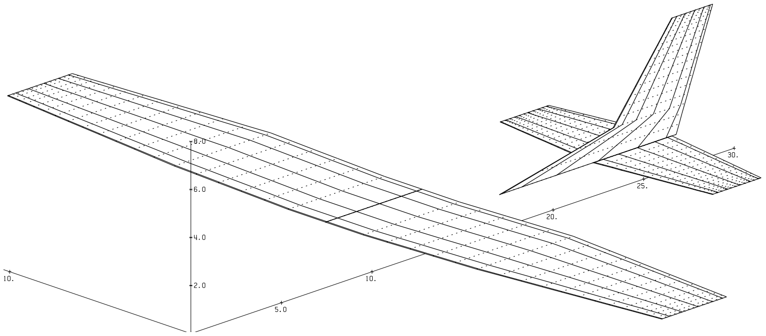

Figure 6.4: Simple AVL model of Cessna 182T geometry.

Table 6.2: Comparison of Cessna 182T longitudinal stability derivatives between the simple AVL model and the flight data, angle units in radians [34].

	C_{L_α}	C_{m_α}	C_{m_q}	C_{L_q}	$C_{L_{\delta_e}}$	$C_{m_{\delta_e}}$
Flight Data	4.41	-0.613	-12.4	3.9	0.43	-1.122
Simple AVL Model	5.25	-1.501	-15.7	9.5	0.62	-1.817
Error	19%	144%	27%	143%	44%	70%

The large error in the pitch stiffness, C_{m_α}, and pitching damping, C_{m_q}, results in a conservatively stable aircraft where the pitch dynamics will be overly damped. Evidence of this can be seen in Ref. [80], where the Cessna 182 dynamic model used in the perturbation and discrete gust responses was very stable. With very little control effort, the closed-loop system was able to alleviate the longitudinal disturbances that were described in Section 4.3. The static margin is calculated as the ratio of the pitch stiffness derivative over the lift curve slope. The large error in the pitch stiffness derivative indicates an overly large estimate of the static margin, and thus the location of the neutral point. The static margin of the Cessna 182T used to obtain the stability derivative data was 14%, or 9.53 feet measured from the front of the propeller spinner. The AVL results for the simple geometry predicts a static margin of 29%, more than double that of the flight data.

To obtain performance benefits by the reduction in static margin, a reasonable estimate of static margin from the aerodynamic tool was essential. Modeling the lifting surfaces alone clearly was insufficient in capturing the stability characteristics of the system. Discussed in Section 5.1, the fuselage and propulsion effects must be modeled in AVL to accurately represent the destabilizing effects they add. In Section 7.3 of Ref. [29], Etkin discusses the influence of the propulsion system on aircraft pitch stiffness. Running propeller alone has a destabilizing effect by reducing the pitch stiffness derivative through a radial force in the plane of the propeller. With the propeller in a tractor configuration, the slipstream creates a lift increment that is linear with alpha, effectively increasing the lift coefficient. This reduces the effect of the horizontal stabilizer on the neutral point location, decreasing the pitch stiffness and static margin. This effect will be even greater when using more than one propeller located directly in front of the wing. With the horizontal directly behind the propeller for the Cessna 182T, the downwash on the tail is altered and the effective angle of attack can be drastically reduced in the propeller wake. An example given by Etkin indicated a forward movement of the neutral point of 28% $\bar{c}$, where $\bar{c}$ is the reference length [81].

Since AVL was unable to directly model a propulsion system or its effects, the effects had to be simulated in the geometry definition. A canard-type lifting surface was added ahead of the horizontal fuselage surface to simulate the destabilizing effects of the propeller as seen in Fig. 5.6. Additionally, the section lift curve slopes on the main wing and the horizontal tail had to be adjusted. A default in AVL is to assume that each section lift curve slope is 2π. Obviously, for a three-dimensional wing this is unrealistic and so the section lift curve slopes were adjusted to the 2-D airfoil experimental results from [82]. However, this still produced an overly stable estimate of the neutral point. The size and location of the simulated propeller and the section lift curve slopes were used to adjust the AVL results to match the flight data stability derivatives. Since the horizontal stabilizer was directly behind the propeller, the section lift curve slopes were more heavily adjusted to simulate the reduced local angle of attack at that location. Finally, the gains on the elevator were adjusted to best match the control power derivatives for lift and pitching moment. Improving the accuracy of $C_{L_{\delta_e}}$ reduced the accuracy of $C_{m_{\delta_e}}$ and so the elevator gain was chosen to split the two. Table 6.3 summarizes the comparison of the longitudinal derivatives. The flight data neutral point was 9.53 feet as measured from the front of the propeller spinner. With the adjustments described here, the predicted neutral point in AVL was 9.54 feet, a drastic improvement from the simple Cessna 182T AVL geometry.

Table 6.3: Comparison of Cessna 182T longitudinal stability derivatives from AVL to flight data, angle units in radians.

	C_{L_α}	C_{m_α}	C_{m_q}	C_{L_q}	$C_{L_{\delta_e}}$	$C_{m_{\delta_e}}$
Flight Data	4.41	-0.613	-12.4	3.9	0.43	-1.122
Cessna 182T Model	4.40	-0.617	-12.4	5.9	0.39	-1.231
Error	-0.2%	0.7%	0%	51%	-9%	8%

The pitch-rate dependent lift stability derivative, C_{L_q}, was unable to be matched. However, according to Ref. [79] it is the least important longitudinal stability derivative, even including stability derivatives not included in this analysis, such as the tuck derivative. Because of the lack of influence on the longitudinal stability this error was considered to be irrelevant.

Validation of the lateral/directional stability derivatives was straightforward compared to the longitudinal stability derivatives. The vertical cross section of the fuselage was added, but the effects were over-destabilizing resulting in negative yaw stiffness ($C_{n_\beta} < 0$). The cross sectional area encompassing the windshield, side windows, and rear window was removed, improving the yaw stiffness. The influence of the vertical stabilizer on the dihedral derivative, $C_{l\beta}$, and the yaw stiffness, C_{n_β}, was under-predicted with the bottom of the vertical ending at the top of the rear fuselage. This under-estimates the theoretical reference area and therefore the vertical stabilizer was extended down to increase the area, improving the yaw stiffness and dihedral derivative. A summary of the AVL lateral/directional stability derivatives compared to the flight data values is given in Table 6.4. AVL under-predicts the dihedral derivative by over 20% and unfortunately this is the most important lateral/direction stability derivative. The dihedral derivative is a function mainly of the geometry, specifically the wing dihedral, wing location (low, mid, high), and wing leading edge sweep angle. The Cessna 182T geometry has very low wing dihedral as discussed in Section 3.2. In a high-wing configuration at a non-zero sideslip angle, vortices form in the flow under with wing increasing the circulation and overall lift of the one wing [15]. This effect is stabilizing but is due to the viscous effects of the flow which cannot be captured in a potential flow vortex lattice code. This indicates that, due to the high-wing Cessna 182T,

Table 6.4: Comparison of lateral/directional stability derivatives from AVL to flight data, angle units in radians [34].

	C_{l_β}	C_{n_β}	C_{l_p}	C_{n_r}	C_{n_p}	C_{l_r}	C_{Y_β}	C_{Y_r}	C_{Y_p}
Flight Data	-0.092	0.059	-0.484	-0.094	-0.028	0.080	-0.393	0.214	-0.075
AVL Model	-0.071	0.057	-0.449	-0.107	-0.020	0.113	-0.265	0.259	-0.046
Error	-23%	-3%	-7%	-14%	29%	41%	-33%	21%	-39%

Table 6.5: Control derivatives from Cessna 182T AVL model and flight data, units in radians [30].

	$C_{l_{\delta_a}}$	$C_{l_{\delta_r}}$	$C_{Y_{\delta_r}}$	$C_{n_{\delta_a}}$	$C_{n_{\delta_r}}$
Flight Data	-0.229	0.0147	0.187	0.0216	-0.0645
Cessna 182T	-0.231	0.0155	0.145	0.00372	-0.0688
Error	1%	5%	-22%	-82%	7%

AVL will under predict the dihedral derivative. This was not corrected as it was desired to keep the AVL geometry as close to the actual geometry as possible.

The lateral/directional control derivatives are summarized in Table 6.5. The gains for the aileron and rudder control surfaces were adjusted to best match the lateral/directional control derivatives. Three of the five control derivatives match well with one derivative having moderate error. The three most important control derivatives for a stability analysis match within 7% while $C_{n_{\delta_a}}$ completely misses the mark. Differences in drag between the asymmetrical deflection of the ailerons produces the yawing moment, but the drag due to the deflections was not accurately captured. The two derivatives that match poorly to the experimental data result as a secondary effect of the specific control surface deflection as opposed to the primary purpose of the control surface deflection. For example, a resulting side force is a secondary effect of a rudder deflection whereas a yawing moment is a primary effect.

6.3.2 D8.2b Aerodynamic Model

Experimental data for the D8.2b concept were unavailable for validation of the AVL model. Instead, Cart3D was used as a higher order method comparison [64, 65]. A high-fidelity inviscid analysis software, Cart3D imports a triangulated surface mesh, generates a Cartesian volume mesh, executes a flow solution, and finally post-processes the results into forces and moments. A unique feature of Cart3D is the adjoint-based mesh refinement capability, which allows the user to converge a flow solution while minimizing error within the mesh. This eliminates the time consuming necessity of creating a mesh, performing a mesh refinement study, and then modifying the mesh in areas of greatest error. A flow solution is generated for each mesh adaptation and was continued until the drag coefficient converged to within 5% of the previous adaptation cycle.

The geometry used in Cart3D was taken from an OpenVSP model of the D8.2b, shown in Fig. 3.5, where a surface mesh was generated using the OpenVSP surface meshing capabilities exported as a triangulated file. The "CompGeom" functionality in OpenVSP computes the structured surface mesh and, given no open meshes are removed, guarantees a watertight geometry. The cell size of the structured mesh is governed by the number of interpolated cross sections in the model, which is controlled by the user. The structured mesh, exported as a triangulated surface mesh to Cart3D, is shown in Fig. 6.5.

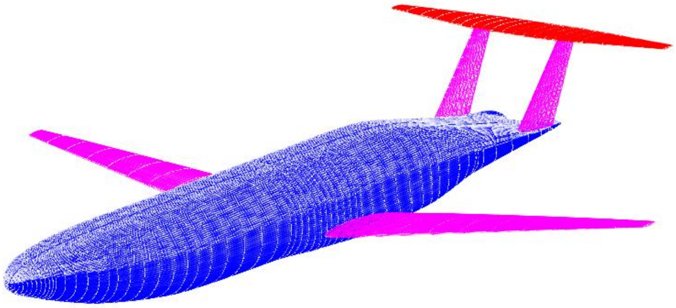

Figure 6.5: D8.2b mesh generated by *CompGeom* in OpenVSP.

A sweep of angles of attack and sideslip at two Mach numbers was used to generate a dataset of aerodynamic data to compare with AVL; Mach 0.72 was used as the cruise condition and Mach 0.4 was used for the low-speed condition. A clean configuration—no slat or flap deflections with landing gear retracted—was used at both Mach numbers. All control surfaces were fixed in the neutral position. Low Mach numbers, i.e. Mach numbers where compressibility becomes insignificant, suffer from convergence issues in Cart3D, and therefore Mach numbers less than Mach 0.4 were not used. The angle of attack was varied from plus and minus six degrees in two degree increments at both Mach numbers. Sideslip angles were varied from plus or minus four degrees at a constant two degree angle of attack.

As mentioned in Section 5.1.2, the baseline D8.2b AVL model did not accurately capture the aerodynamics predicted by Cart3D. Modeling strategies employed on the Cessna 182T did not provide accurate results as would have been expected. As a result, an iterative process of modifying the baseline D8.2b AVL model was used to find the best modeling strategy to match the Cart3D results. Table 6.6 describes the iterative steps taken along with the abbreviations used in Figs. 6.6 and 6.7. Each model in the iterative process was the same as the previous with the exception of the single modification described. For example, only the horizontal fuselage cut airfoils were changed from the baseline model and all remaining components remained the same.

Table 6.6: Description of D8.2b modeling steps with abbreviations defined.

Abbreviation	Description
AVL	Baseline AVL model closely matching OpenVSP model
AVL Sym	Horizontal fuselage cut airfoils made symmetric
AVL Swing	Horizontal fuselage removed, wing extended to centerline
AVL Swing 0	Wing incidence angle removed

Figure 6.6 shows the induced drag, lift, and pitching moment coefficient comparisons between Cart3D and the different AVL models of Table 6.6. For clarity, only Mach 0.72 results are shown as the Mach 0.4 results follow the same trends. The induced drag coefficient of Fig. 6.6(a) shows that the different modeling strategies had very little effect on matching the lift-induced drag. At lift coefficients below approximately 0.8, AVL follows the trend of Cart3D until compressibility effects begin to dominate. Similar to the lift coefficient curve, an offset was present between Cart3D and AVL; due to the coupling between induced drag coefficient and lift coefficient, the offset in lift coefficient prediction results in the offset of the drag coefficient. Also, a zero lift pressure drag offset captured by Cart3D was not captured by AVL. The lift and pitching moment coefficients were very sensitive to the modeling strategy as indicated in Figs. 6.6(b) and 6.6(c). From Ref. [79], the lift and pitching moment slopes are the most important derivatives in the prediction of longitudinal stability; the greatest emphasis was placed on matching those derivatives to best predict the longitudinal

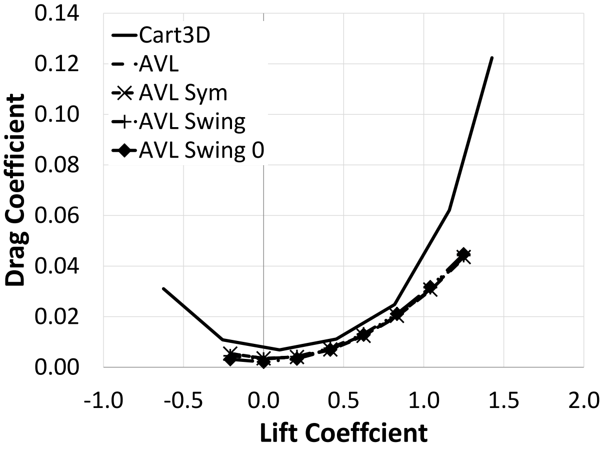

(a) Induced drag coefficient versus lift coefficient.

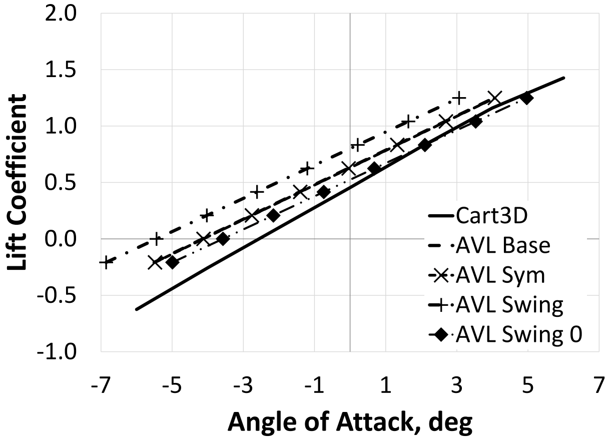

(b) Lift coefficient versus angle of attack.

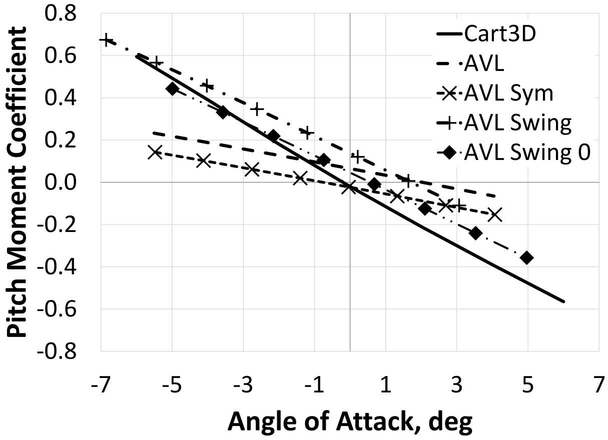

(c) Pitching moment coefficient versus angle of attack.

Figure 6.6: Drag, lift, and pitching moment coefficients for different AVL geometries. Data only from Mach 0.72 cases shown for clarity.

dynamics properties. The lift curve slope was impacted minimally by changes in the modeling geometry, but the lift coefficient at zero angle of attack changed greatly. AVL consistently over-predicted the zero angle of attack lift coefficient, with results improving as the horizontal fuselage was removed and the wing incidence removed. The lift curve slope was consistently under predicted when compared to Cart3D. Pitching moment coefficient was even more sensitive to the different models, especially when the horizontal fuselage was removed. With the horizontal fuselage, the pitching moment slope was drastically under predicted compared to Cart3D. The baseline model had a pitching moment offset at zero angle of attack and was the motivation for making the horizontal fuselage airfoils symmetric. With the symmetric airfoils for the fuselage, the zero angle of attack pitching moment offset was correct, but the under prediction in slope remained. Removing the horizontal fuselage reduced the pitching moment slope error, and removing the wing incidence decreased the offset at zero angle of attack.

Lateral/directional force and moment curves are shown in Fig. 6.7. Removal of the horizontal fuselage improved the dihedral derivative, C_{l_β}, while providing negligible impact on the yaw stiffness derivative, C_{n_β}. Addition of the vertical fuselage resulted in an excellent agreement between Cart3D and AVL for the yaw stiffness, Fig. 6.7(b), while increasing error in the side force coefficient due to sideslip, C_{S_β}, seen in Fig. 6.7(c). The dihedral derivative was unaffected by the addition of the vertical fuselage. A compromise between the side force coefficient curve and the yaw stiffness had to be made as the addition of the fuselage improves one while degrading the other. As discussed by Stevens and Lewis in Ref. [79], the yaw stiffness derivative has greater impact on the aircraft dynamics than the side force coefficient. In fact, in Section 8.5 of Ref. [29], Etkin states, "...the whole derivative $C_{[S]_\beta}$ often has negligible effect on the vehicle dynamics." Unfortunately, the dihedral derivative has some of the greatest impact on the flight dynamics and was unable to be matched with greater accuracy. As a function of dihedral angle, aspect ratio, and wing sweep [29], the dihedral derivative could not be improved as the geometry in terms of those parameters was fixed. As such, the error had to be accepted as a limitation in the aerodynamic modeling capabilities of the vortex lattice.

The baseline D8.2b AVL model did not accurately model the aerodynamics when compared to the Cart3D results. Figures 6.6 and 6.7 show that improvements can be made by modifying the AVL model. Using the comparison plots for the different D8.2b models, the final AVL model chosen for the multidisciplinary design optimization was when the horizontal fuselage lifting surface was removed, the simple wing extended to the centerline, wing incidence set to zero, and a vertical cut of the fuselage added.

Force and moment coefficient comparison plots of the final D8.2b aerodynamic model at both Mach 0.72 and Mach 0.4 are shown in Fig. 6.8. With the horizontal fuselage removed and the vertical fuselage added, the agreement between Cart3D and AVL was quite good, especially in the longitudinal forces and moments. It is worth noting that the trailing edge of the fuselage contained a sharp edge allowing Cart3D to enforce a Kutta condition, resulting in the production of forces and moments from the fuselage alone. Were no sharp trailing edge present, the fuselage would produce no forces or moments, regardless of the wind vector orientation with respect to the fuselage body axis, as no Kutta condition could be applied. This is similar to performing an aerodynamic analysis of an ellipsoid in an Euler aerodynamic solver, where any angle of attack will result in zero net forces. This is due to the rear stagnation point having the freedom to align with the forward stagnation point, maintaining the same streamline as if the object was not in the fluid flow.

The Mach number dependency is clearly visible for both Cart3D and AVL in all the plots of Fig. 6.8, with the exception of induced drag coefficient. At higher lift coefficients, compressibility drag begins to dominate as supercritical velocities begin to form on the surface, an effect captured by Cart3D. However, the compressibility correction in AVL, a Prandtl-Glauert correction [56], does not capture the increase in drag coefficient at Mach 0.72 and lift coefficients greater than 0.85. At both Mach numbers, the induce drag coefficient was the same for AVL. In all the other force and moment curves of Fig. 6.8, the Mach number

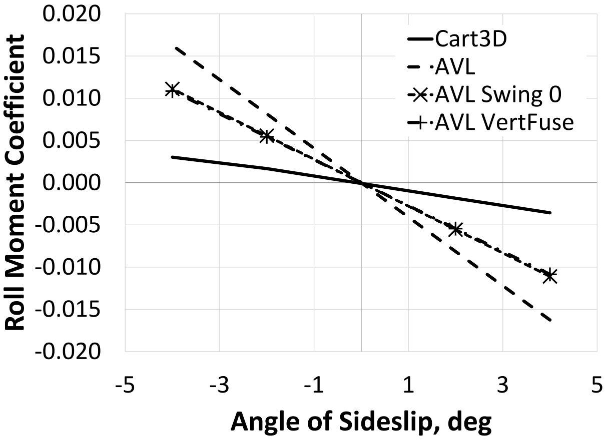

(a) Rolling moment coefficient versus angle of sideslip.

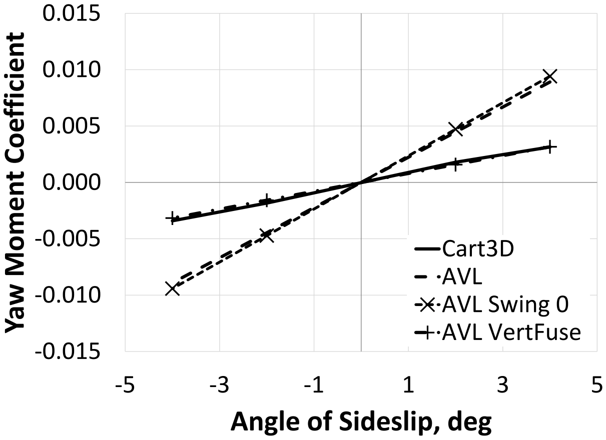

(b) Yawing moment coefficient versus angle of sideslip.

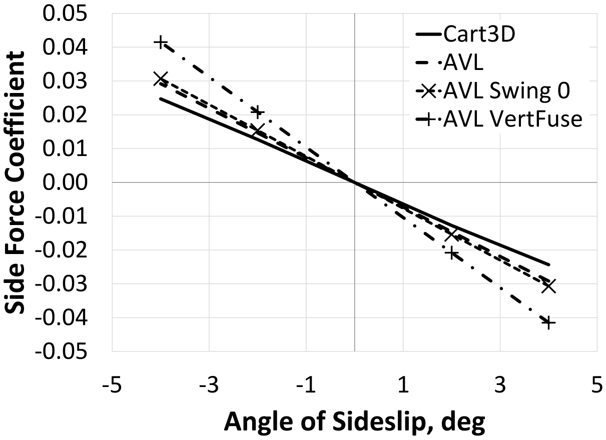

(c) Side force coefficient versus angle of sideslip.

Figure 6.7: Rolling moment, yawing moment, and side force coefficients for different AVL geometries. Data only from Mach 0.72 cases shown for clarity.

effects between Cart3D and AVL are similar, even though the slopes of the curves may differ.

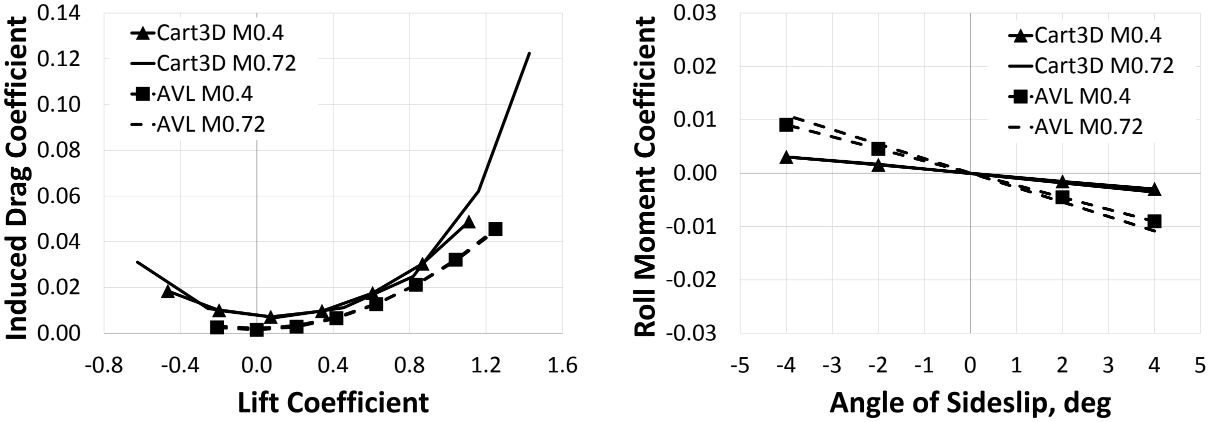

(a) Induced drag coefficient.

(b) Rolling moment coefficient.

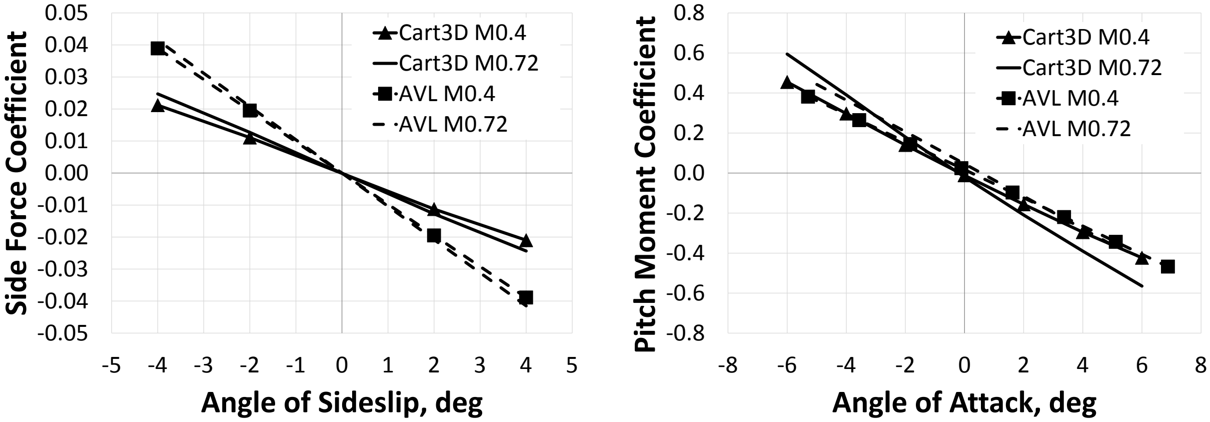

(c) Side force coefficient.

(d) Pitching moment coefficient.

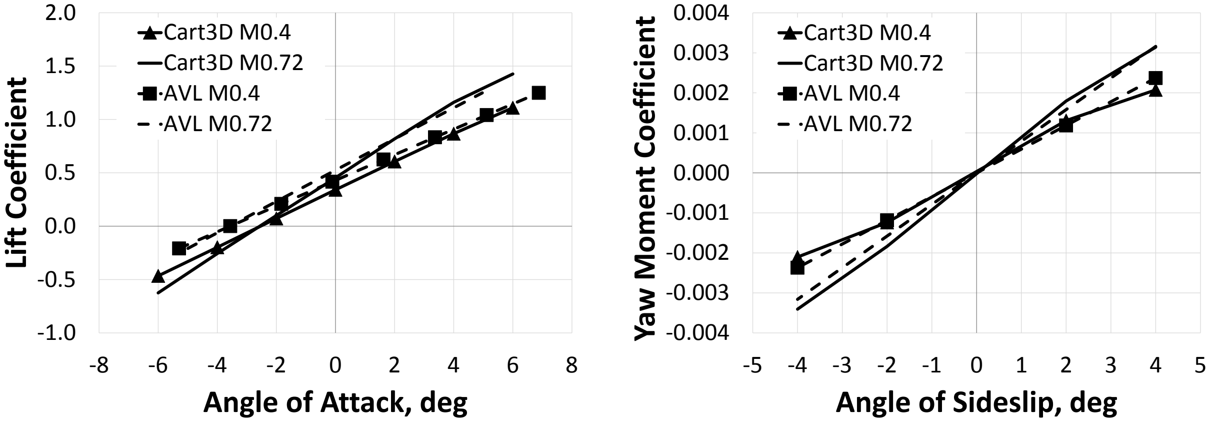

(e) Lift coefficient.

(f) Yawing moment coefficient.

Figure 6.8: Comparison of Cart3D and AVL force and moment coefficient predictions.

6.4 Cessna 182T Multidisciplinary Testing

The Cessna 182T model was used to test the flight dynamics and system disturbance components to ensure each were behaving as expected. A simple trade study was performed by reducing the horizontal and vertical tail volume coefficients, described in Section 6.3.1. Results of the trade study are presented with the variation in drag coefficient versus the volume coefficient shown. Additionally, dynamic response plots and continuous turbulence power spectral density plots are given.

Figure 6.9 shows the total drag coefficient as a function of the horizontal and vertical tail volume coefficients. As expected, the total drag decreased as the tail volume coefficients were reduced; the total drag was sensitive to both volume coefficients, but had a greater sensitivity to the vertical tail volume coefficient. Figure 6.10(a) shows the reduction in drag that resulted from decreasing the static margin. The drag benefit seen in Figs. 6.9 and 6.10(a) comes from the reduction in wetted area and the resulting decrease in parasitic drag. When trimmed, induced drag for this geometry actually increased with the reduction of static margin as shown in Fig. 6.10(b). This explains why the total drag was more sensitive to varying the vertical tail volume coefficient as mentioned previously. The resulting increase in induced drag comes not from the reduction of static margin but the reduction in the span, and increase in lift coefficient, of the horizontal stabilizer.

The elevator deflection angle, shown in Fig. 6.11, went from a slight negative deflection to a positive deflection. The Cessna 182T baseline geometry required less then a half degree of negative elevator deflection to trim at the cruise condition, which means the downwash from the main wing provided nearly sufficient induced angle on the horizontal stabilizer to trim. As the horizontal tail area and span were decreased, the required trim deflection on the stabilizer decreased, became neutral, and eventually positive. Even as the trim deflection increased the induced drag remained nearly constant, increasing by less than one percent. Because the location of the wing and center of gravity were fixed, the horizontal tail has to generate the same amount of moment to trim as the baseline case. As a result, a net increase

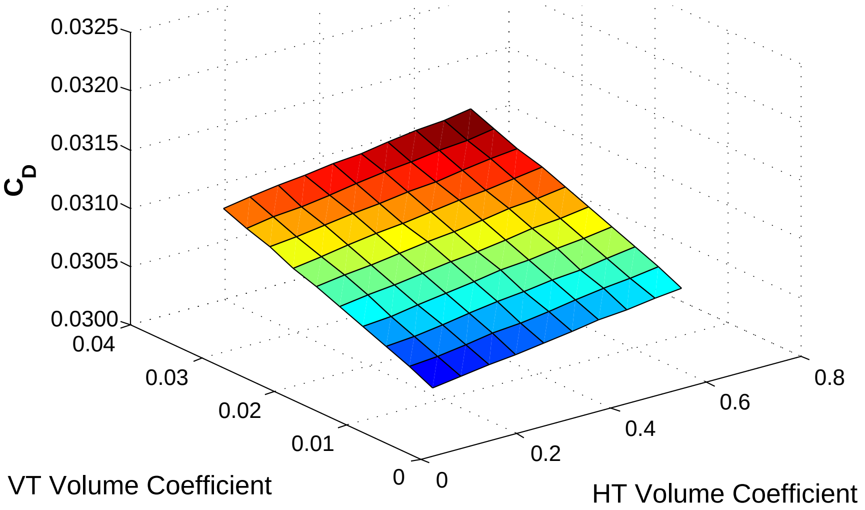

Figure 6.9: Cessna 182T drag coefficient for varying tail volume coefficients.

in configuration induced drag was realized from the decreased horizontal stabilizer decreased efficiency. This indicates that simply reducing the static margin does not decrease induced drag but that a system level design, with static margin being allowed to decrease, must be performed in order to achieve the induced drag benefits of relaxed static stability.

Initially, using moderate atmospheric disturbances with a probability of exeedance level of 10^{-3}, none of the configurations passed the heading hold turbulence check specified in SAE-AS94900. This resulted from the active control system not sufficiently driving the rudder in continuous turbulence. A great feature of the LQR is the flexibility in allowing for adjustments in the weighting matrices if a desired performance is not achieved. Due to the consistent failures in the heading hold check, the ψ weighting term in Eq. 4.29 was increased by a factor of 10, placing heavier penalties on non-zero values of yaw. This simple adjustment enabled all configurations to achieve adequate dynamic performance in the cruise flight condition. It should be noted, again, that the cruise flight condition alone does not adequately stress the control system for sizing the stabilizer surfaces. Additional flight conditions must be added to ensure proper sizing of the stabilizer surfaces.

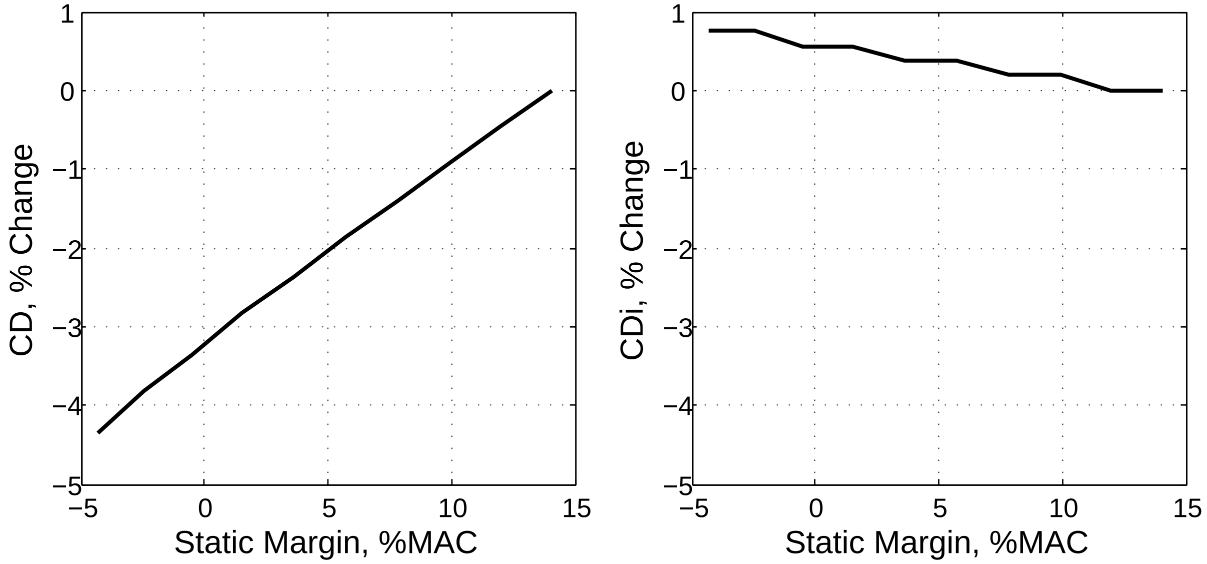

(a) Drag coefficient vs. static margin.

(b) Induced drag coefficient vs. static margin.

Figure 6.10: Sensitivity of total and induced drag coefficients to static margin.

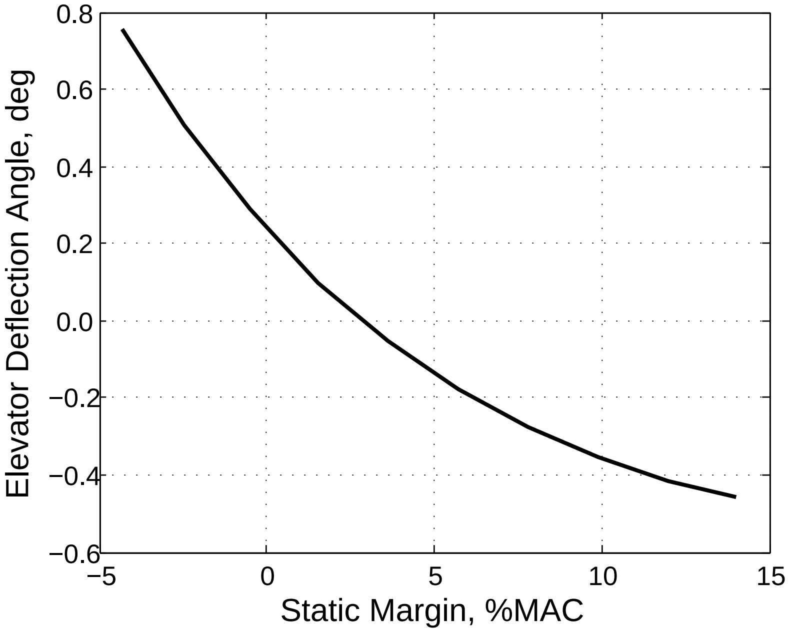

Figure 6.11: Elevator deflection angle versus static margin.

Figures 6.12–6.17 show the baseline configuration's dynamic response with the heavier yaw weighting to perturbations, continuous gust fields, and discrete gusts. These disturbances were used to check the dynamic performance of the active control system as summarized in Table 4.3. The airspeed hold and longitudinal gust responses were omitted for brevity due to their similarity to the pitch hold and vertical gust responses.

Time histories of the transient response to the perturbations specified by SAE-AS94900 are shown in Figs. 6.12 and 6.13. The figures were separated into longitudinal and lateral states, showing both the short time response—less than ten seconds—and the long time response—total response over 100 seconds. All control surface states shown in Figs. 6.12, 6.13, 6.16, and 6.17 are the total deflection angles, the sum of the perturbation and the steady-state deflection angle. Visible in the open-loop response of Fig. 6.12 is the phugoid mode which has been attenuated with little control power. Figure 6.13 shows the unstable spiral mode in the open-loop response that has been stabilized through a combination of aileron and rudder control surface deflections.

Power spectral densities of the mean-squared responses are plotted in Figs. 6.14 and 6.15. With a natural frequency of 0.19 rad/s, the phugoid sensitivity can be seen in the vertical continuous turbulence responses as a spike in the mean-squared response of the open-loop system. Less obvious is the short period mode, which had an open-loop natural frequency of 7.66 rad/s, that can be seen as a slight hump in the angle of attack, pitch rate, and pitch angle. The spikes in the lateral state responses of Fig. 6.15 correspond to the dutch roll natural frequency of 5.14 rad/s. The active control system successfully reduced the magnitude of the response of the phugoid and dutch roll modes while the short period response in turbulence was unchanged.

Figures 6.16 and 6.17 show the response to a lateral and vertical discrete gust. As with the pitch perturbations, the phugoid is quite visible in the open-loop response. Due to the model being extremely stable at cruise, even in a discrete gust, the required elevator deflection of the closed-loop system was extremely small while providing a heavily damped response.

The closed-loop lateral gust response, Fig. 6.16, provides increased damping when compared to the open-loop response, as would be expected. Heavier weighting in the performance index on the heading angle, ψ, improves the heading angle response but results in a sacrifice in the roll angle response. The heading perturbation state of Fig. 6.16 deviates from steady-state in response to the gust but immediately returns to the steady-state value, whereas the roll perturbation state has two full oscillation cycles before returning to the steady state.

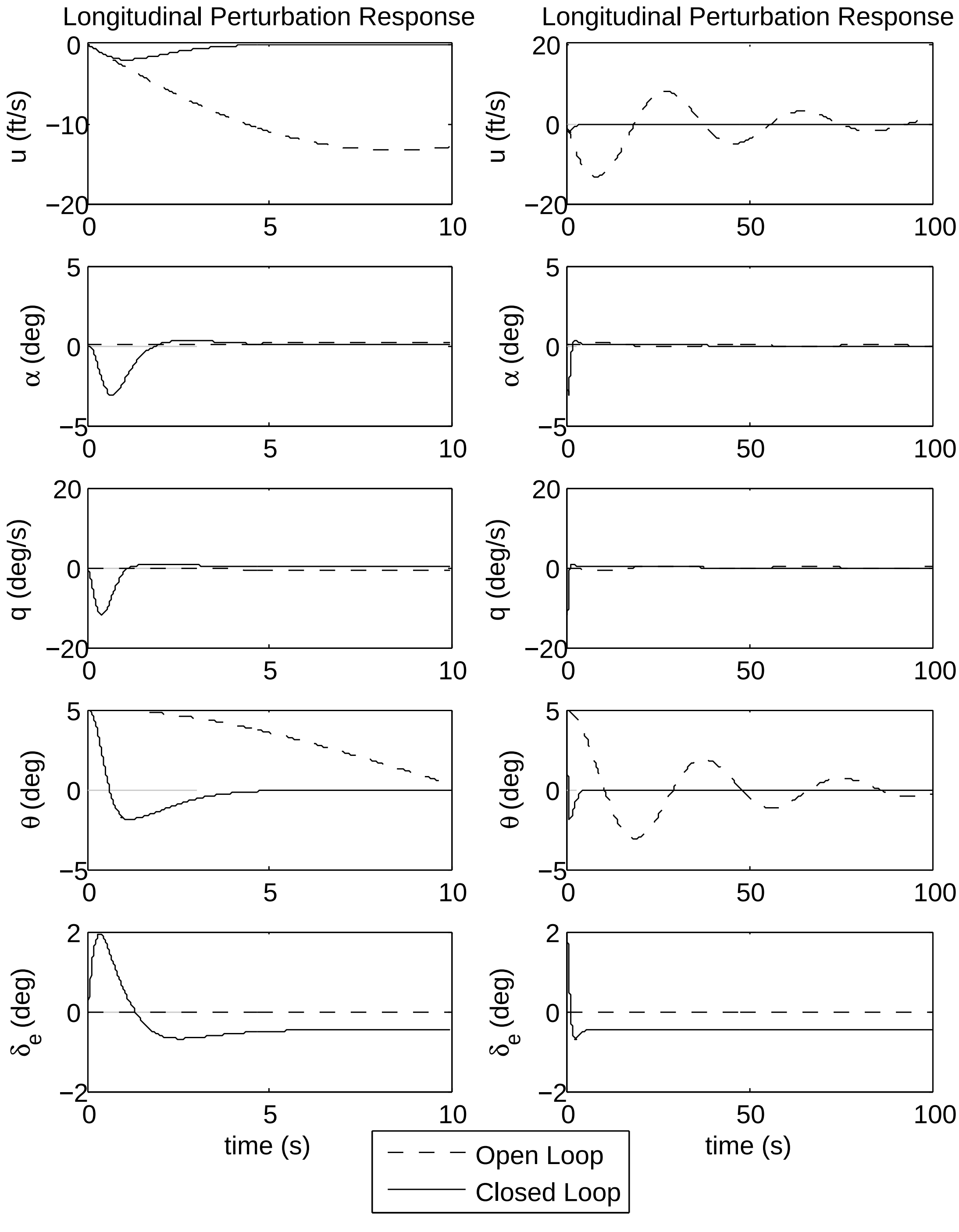

Figure 6.12: Pitch hold perturbation check.

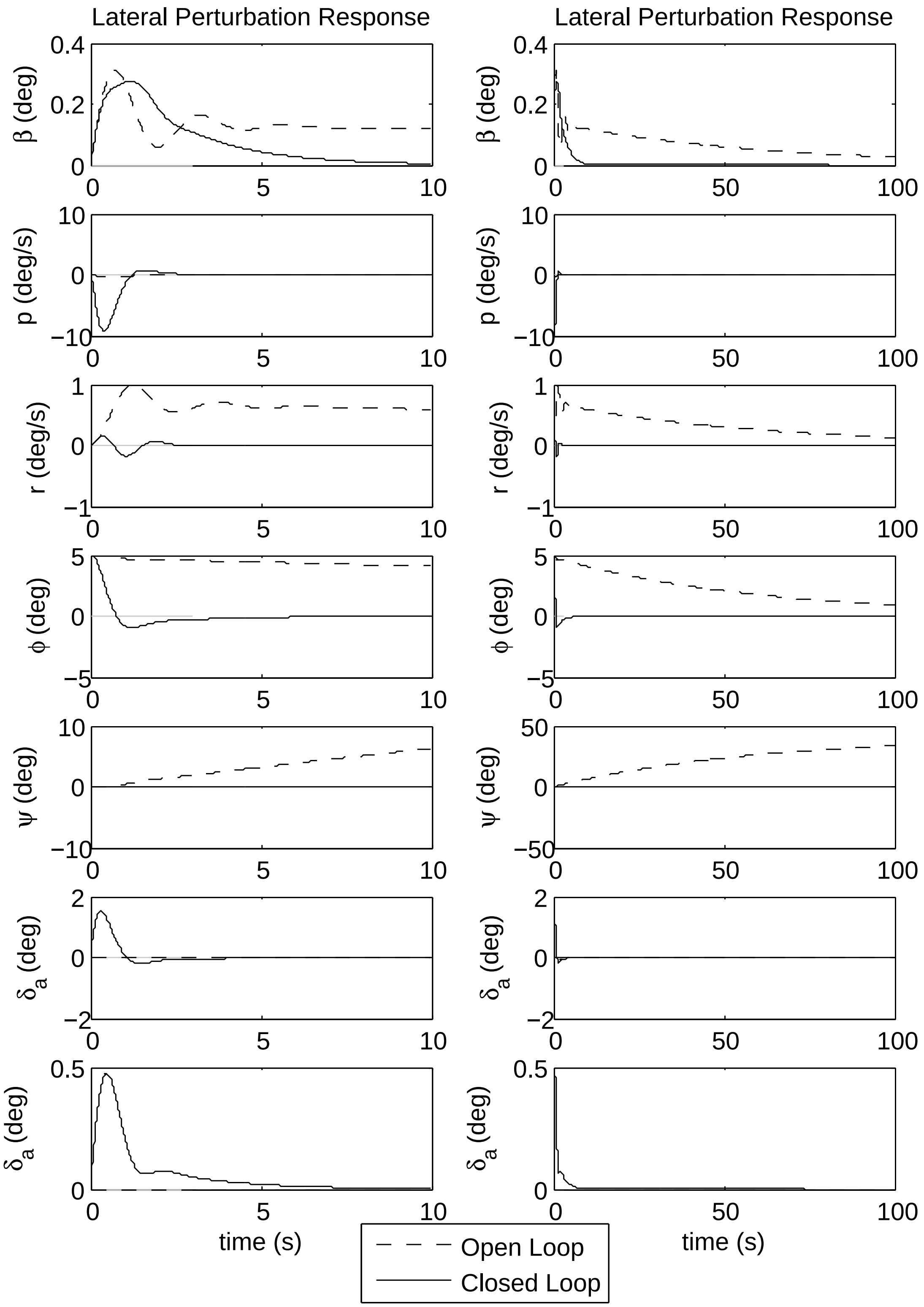

Figure 6.13: Roll hold perturbation check.

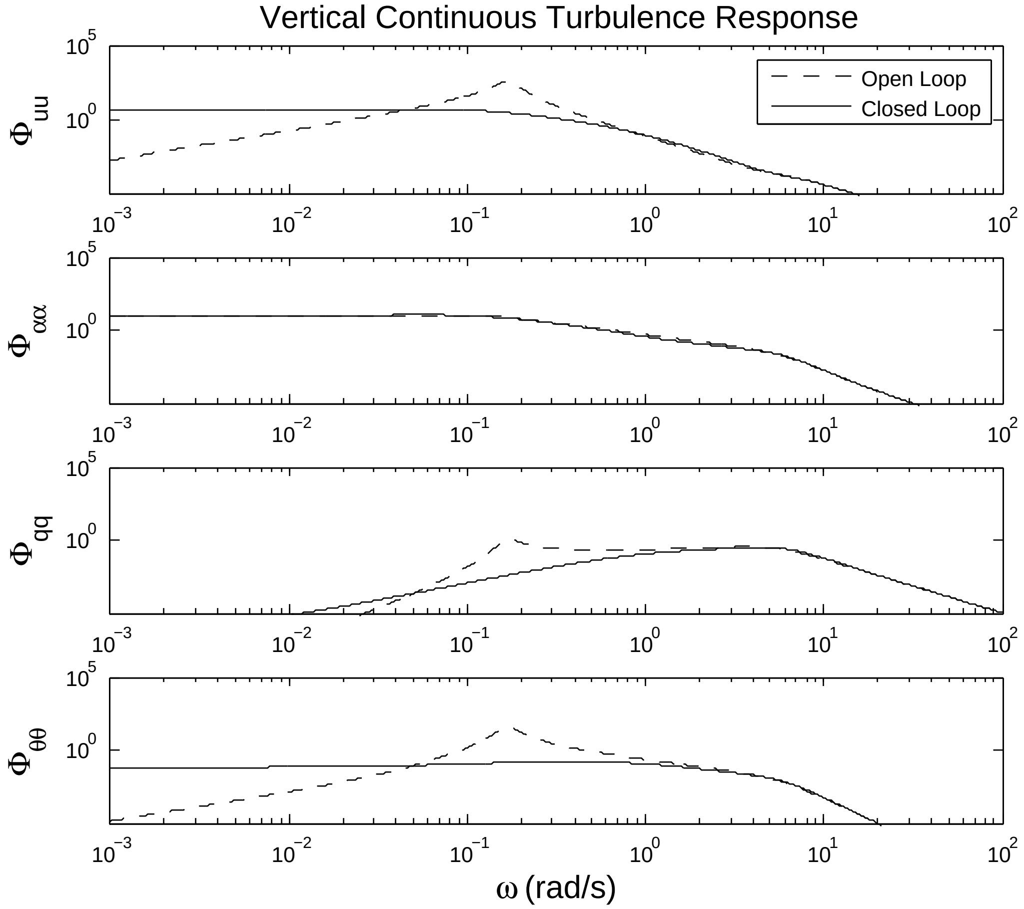

Figure 6.14: Continuous vertical turbulence response.

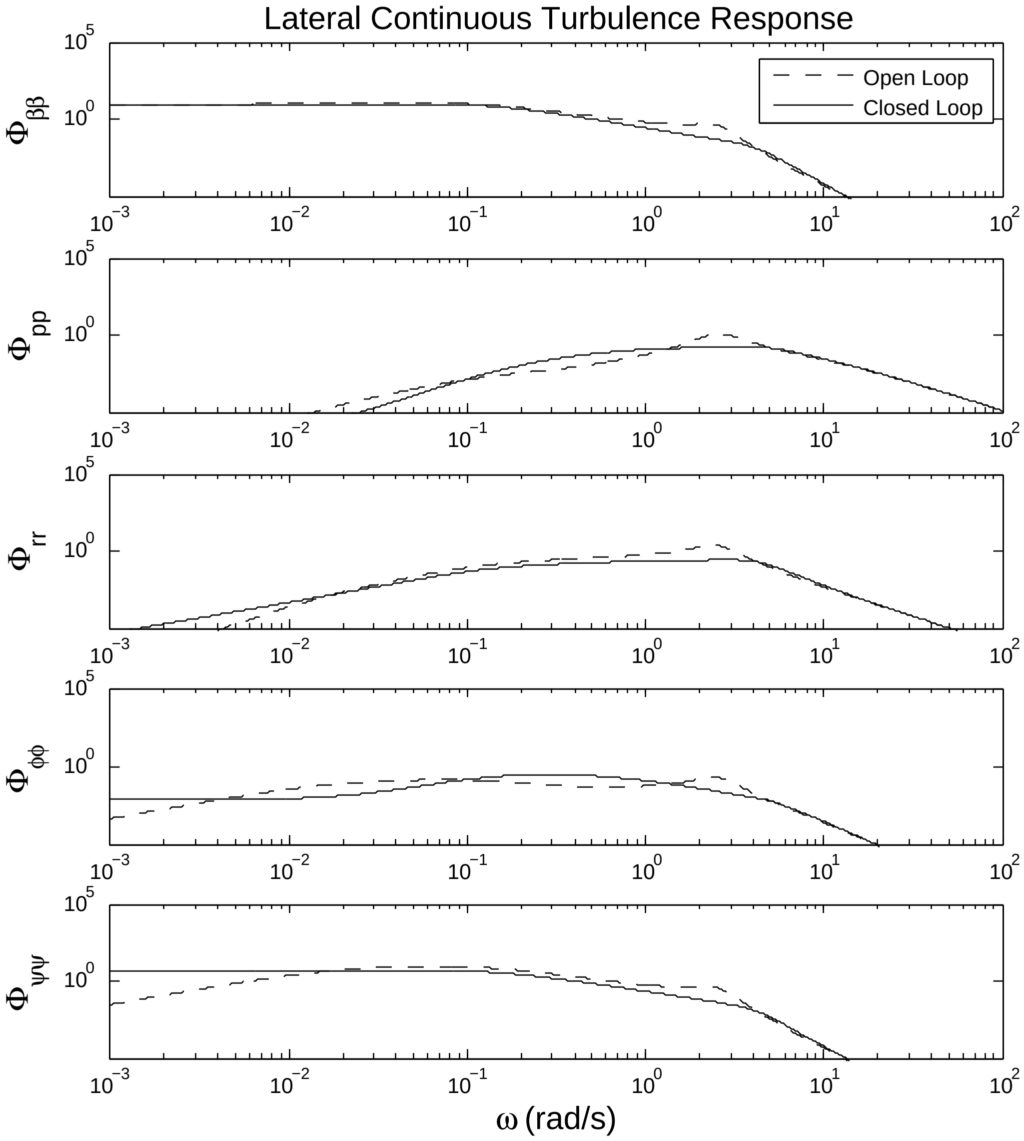

Figure 6.15: Continuous lateral turbulence response.

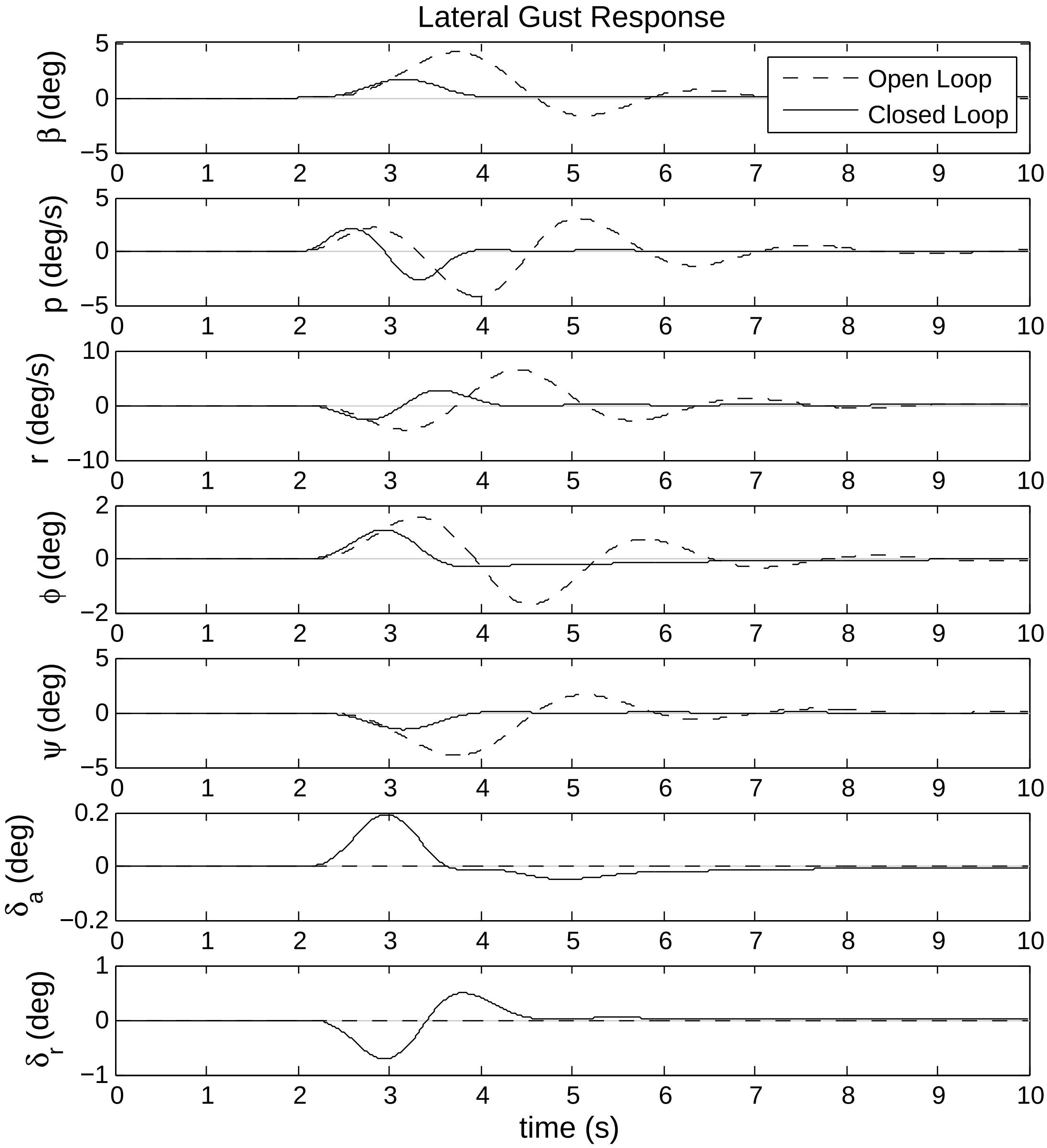

Figure 6.16: Lateral discrete gust response.

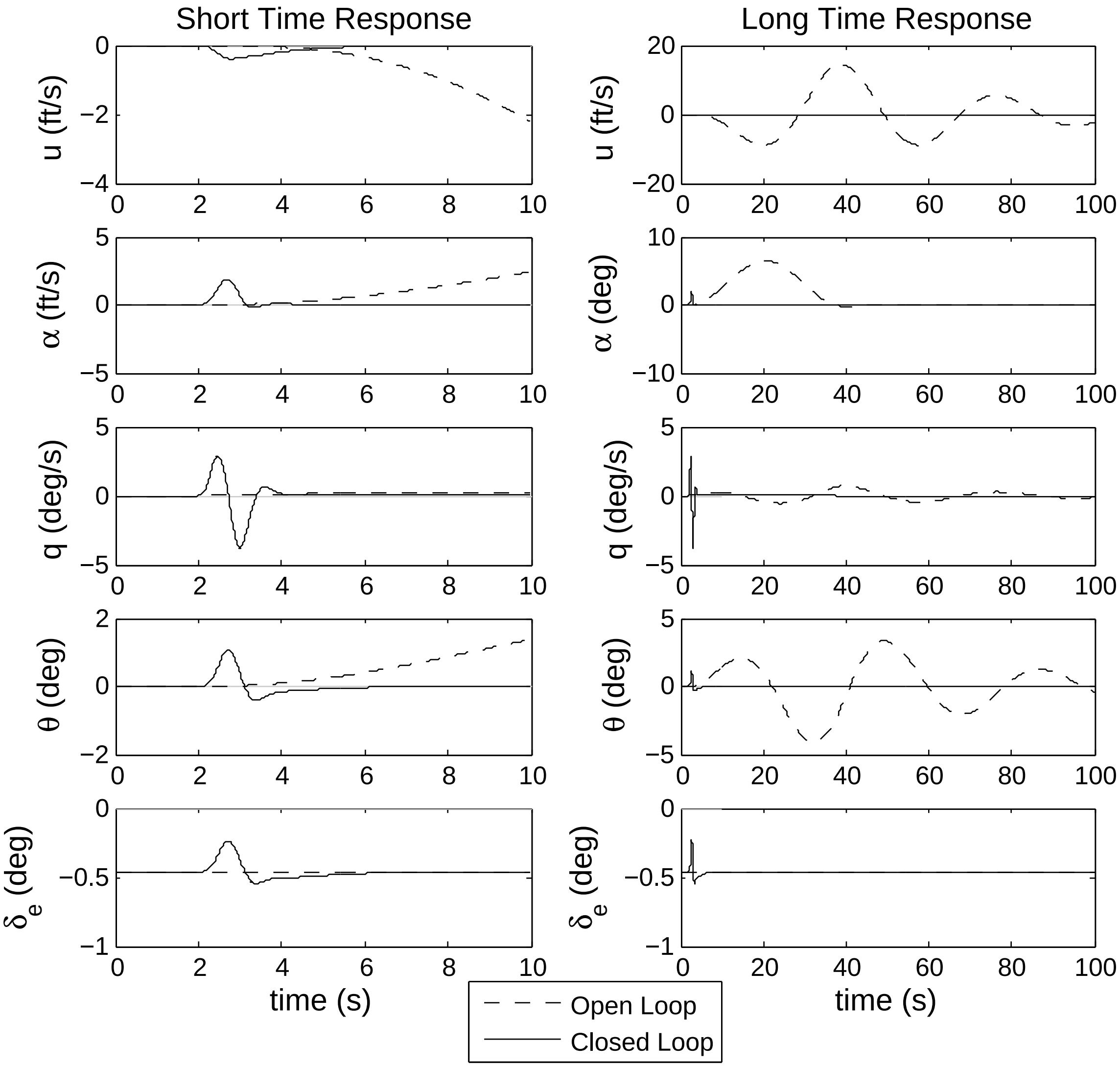

Figure 6.17: Vertical discrete gust response.

Chapter 7

Results and Discussion

Five optimization cases, each with different constraints and design variables, were run in an exploration of the design space, searching for the active design constraints and system design sensitivities. All the optimization cases began using the design variables from the baseline configuration, Fig. 7.1, giving identical starting points for all optimized designs. The shorthand labels for the optimization cases with the applied constraints indicated are shown in Table 7.1, ranging from a nearly unconstrained optimization with traditional volume coefficients to both static trim and dynamic response constraints applied to the optimization. The fixed tail volume coefficient optimization case used horizontal and vertical tail volume coefficients of 1.00 and 0.09 respectively, typical values for a jet transport [1]. Additionally, design cases with failed takeoff or minimum rate of climb capability at cruise were credited with zero range and fuel, resulting in a failed design as mission range was not met. The baseline configuration of Fig. 7.1 was unable to meet second segment climb gradient requirements as designed.

Table 7.1: Shorthand labels of each optimization case with the applied constraints indicated.

Case Label	Fixed Tail Volume	TOL Constraints	Static Constraints	Dynamic Constraints	Fixed Static Margin
FixedTailVol	✓	✓			✓
StaticConFixSM		✓	✓		✓
StaticConFreeSM		✓	✓		
SDynConFixSM		✓	✓	✓	✓
SDynConFreeSM		✓	✓	✓	

Figure 7.1 shows a top and side view of the baseline configuration AVL model resulting from the aerodynamic validation of Section 6.3.2. As designed, the baseline configuration

was unable to meet the specified takeoff and landing constraints, with field length distances of 11,076 and 7,081 feet respectively. Federal Aviation Administration requirements state that a positive climb gradient must be achieved in the event of an engine failure during second segment climb, also failed by the baseline configuration. Tables 7.2 and 7.3 show the complete analyses of the static trim and dynamic response results with exceeded limits indicated in red. The constraints were unused in the analysis (the baseline configuration was fixed geometry and not optimized) and are shown for comparison to the cases with static trim and/or dynamic response constraints. The elevator effective angle of attack exceeds the constraints in both longitudinal perturbations in the stall condition. A residual roll angle greater than the allowed plus or minus one degree after five seconds was experienced in the cruise condition.

Table 7.2: Baseline configuration static trim constraints.

Condition	Control Surface	Deflection Angle
OEI	Aileron	-0.33
	Rudder	-19.64
Takeoff	Elevator	1.65
Maneuver	Elevator	8.32

Figures 7.2 and 7.3 show the baseline configuration time response for the exceeded constraint limits highlighted in red in Table 7.3. The roll residual time responses in the cruise and stall flight conditions, Fig. 7.2, appear very similar. The roll angle starts at the perturbed value of five degrees and then decreases as the system returns to the steady-state condition. The horizontal dashed lines indicate the constraint limits and the vertical dashed line indicates the time that the roll angle must be within, and remain within, the constraint limits. The baseline configuration roll angle response in the cruise condition was too slow, failing to return to the allowed limits five seconds after the disturbance. In stall, the roll residual angle had an acceptable response.

Table 7.3: Baseline configuration dynamic response performance, in degrees unless otherwise noted.

Condition	Response Type	Cruise Condition	Stall Condition
Discrete Gust	Aileron	0.00	5.88
	Rudder	-1.38	-1.88
	Elevator (Long)	3.17	8.42
	Elevator (Vert)	3.23	9.52
Turbulence	RMS Pitch	0.05	1.08
	RMS Roll	1.29	1.16
	RMS Yaw	0.36	0.42
Perturbation	Aileron	0.00	6.37
	Rudder	4.46	1.75
	Elevator (Pitch)	7.41	20.49
	Elevator (Speed)	5.45	24.37
Residual	Pitch	-0.24	-0.29
	Roll	-1.77	-0.64
	Speed (fps)	0.00	0.00

The longitudinal perturbation responses of the baseline configuration are shown in Fig. 7.3. In the stall condition, the elevator was heavily loaded, almost to the upper constraint, prior to any perturbations being introduced into the system. When perturbed in pitch and airspeed, the elevator responded to the system disturbances and exceeded the allowable elevator effective angle of attack. This high loading during the perturbation response would cause the horizontal stabilizer to enter the nonlinear aerodynamics region, potentially entering a full stall and risking the loss of control.

Table 7.4 compares the design variables from each optimization to the baseline configuration. Side and top view comparisons of the AVL geometries are given in Figs. 7.4 and 7.5. Between all the optimal designs, thrust and wing area varied minimally as these were driven by the takeoff and landing field constraints. The only exception was the SDynConFixSM case with the wing area increasing to over 1,700 square feet. The wing apex location, for all designs, shifted forward, increasing the horizontal stabilizer moment arm. This was most evident in the optimization case where the traditional tail volume coefficient was used. Reducing horizontal tail area resulted in an empty weight and wetted surface area reduction,

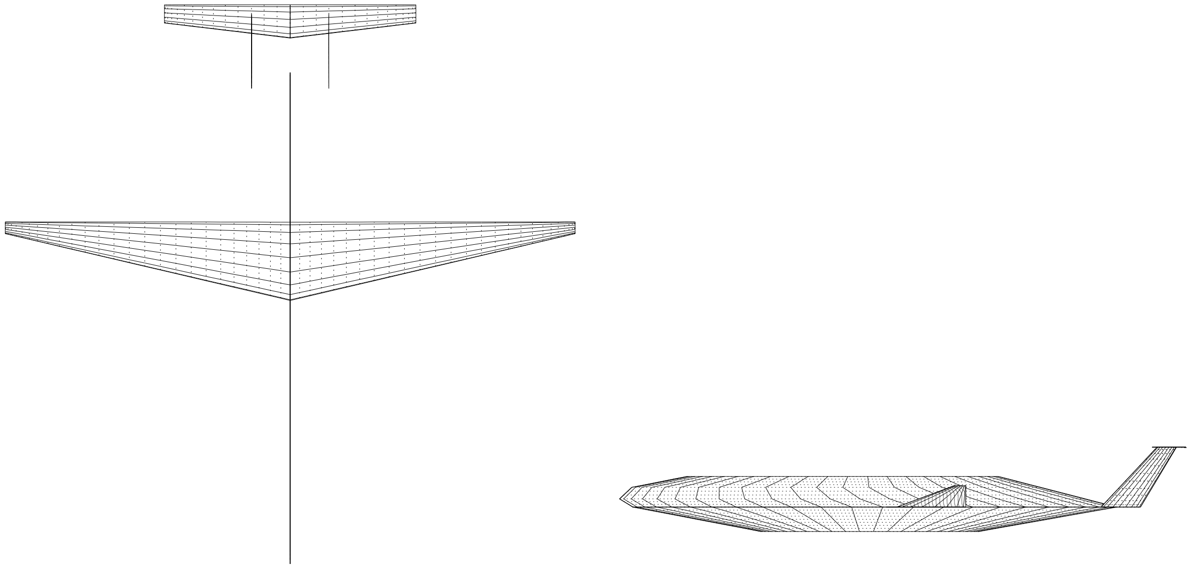
(a) Top view.

(b) Side view.

Figure 7.1: Top and side view of baseline D8.2b configuration, modeled in AVL.

a property exploited by the optimizer in fixed tail volume coefficient configuration. As the stabilizers' areas were calculated based upon fixed volume coefficients, the moment arms for both the vertical and horizontal stabilizers were maximized by shifting the wing apex to the forward-most limit and the stabilizers to the rear-most limit. This case highlights the limitation of multidisciplinary design optimization when only traditional performance requirements are used, and stability and control considerations are only captured through the inclusion of a volume coefficient.

Vertical stabilizer area varied in size throughout the five optimization cases. The vertical stabilizer area reached a minimum in the StaticConFreeSM case where the design was given the greatest flexibility without the burden of the dynamic response constraints. When the dynamic response constraints were added, the vertical stabilizer area increased to near the baseline configuration in the SDynConFixSM case. Having static margin as a design variable allowed the vertical stabilizer area to decrease, considering it a weight and viscous drag penalty. A similar behavior was seen with the horizontal stabilizer. Again, in the StaticConFixSM case, the horizontal stabilizer area increased to slightly more than the

Table 7.4: Summary of results for all optimization cases. Descriptions of the optimization case shorthand labels are described in Table 7.1.

Design Variable	Baseline	FixedTailVol	StaticConFixSM	StaticConFreeSM	SDynConFixSM	SDynConFreeSM
Thrust (lb)	25,000	22,590	22,120	22,220	23,670	22,200
Wing Area (ft^2)	1,100	1,451	1,422	1,411	1,730	1,426
Sweep (deg)	10.0	29.5	30.0	28.5	10.8	24.1
Dihedral (deg)	5.0	0.1	8.8	8.1	9.7	9.4
HT Area (ft^2)	276.9	222.1	118.8	102.1	288.7	169.5
VT Area (ft^2)	73.8	113.2	50.4	32.4	79.2	44.5
VT Sweep (deg)	40.3	65.0	26.9	10.6	16.7	12.3
Wing Apex (ft)	54.6	20.0	35.6	23.4	51.5	43.2
Static Margin (%)	10	10	10	15.1	10	22.4
Fuel Weight (lb)	27,769	27,739	25,603	25,888	30,304	26,349
Gross Weight (lb)	161,448	160,141	156,430	155,528	164,218	156,767

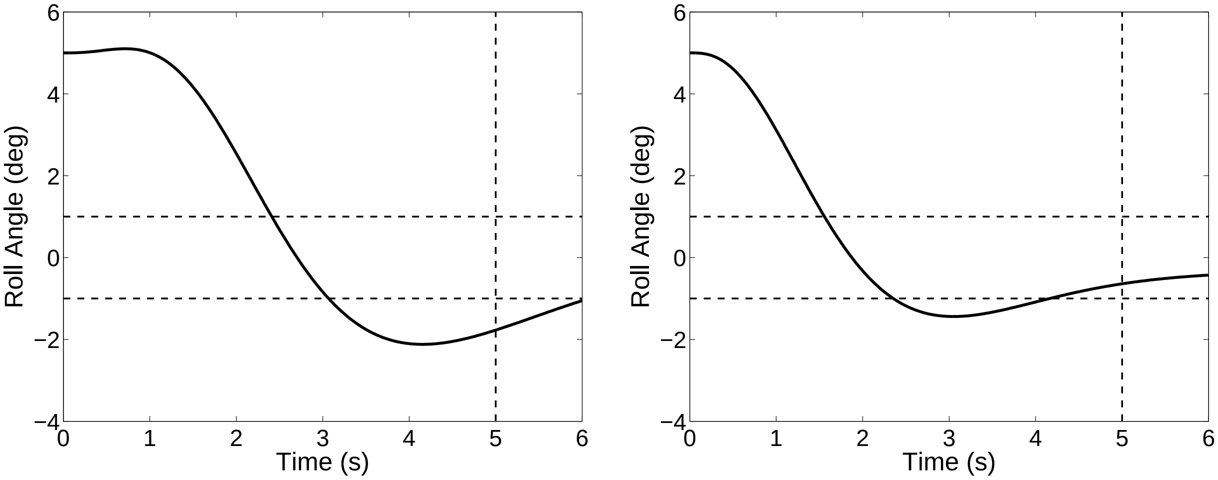

(a) Cruise roll residual.

(b) Stall roll residual.

Figure 7.2: Baseline configuration cruise and stall roll residual time responses. Horizontal dashed lines indicate the roll residual constraint limits and the vertical dashed line indicates the time where the residual constraint became active.

baseline configuration, but freeing static margin allowed the optimizer to freely shift the center of gravity and neutral point, reducing the required horizontal stabilizer area.

Static margin was allowed to vary for two designs, and in both cases the optimizer chose to increase the static margin, opposite as what would have been expected as discussed previously in Section 2.1. As a dependent variable, the center of gravity was placed based upon the static margin, a design variable. The optimizer discovered, as discussed in the detailed description of each configuration, a benefit of shifting the center of gravity forward, increasing the tail moment arm and providing greater control authority to the stabilizers. This allowed the stabilizers to be decreased in size giving a weight and viscous drag benefit. This was a unique solution in a design space not typically explored with a fixed center of gravity position; increasing the open loop stability provided a greater reduction in system fuel burn, through reduced stabilizer sizing, than the benefits of relaxed static stability for the given design space and controller design.

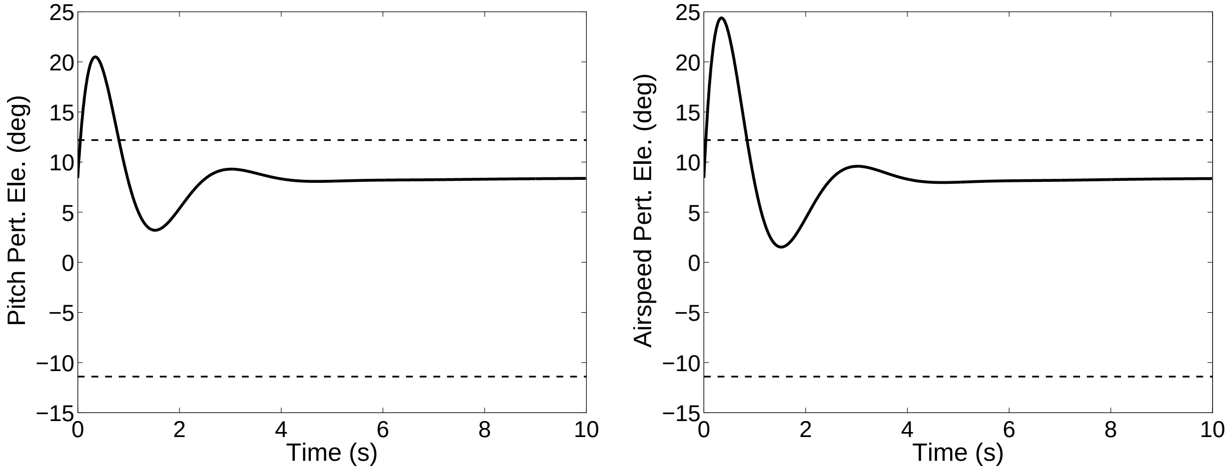

(a) Pitch perturbation elevator response. (b) Airspeed perturbation elevator response.

Figure 7.3: Baseline configuration elevator time responses to pitch and airspeed perturbations in the stall condition. The horizontal dashed lines indicate the elevator effective angle of attack limits.

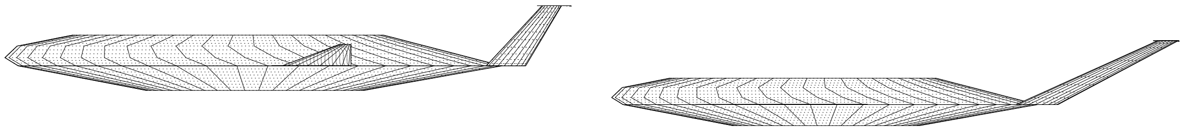

(a) Baseline configuration. (b) FixedTailVol configuration.

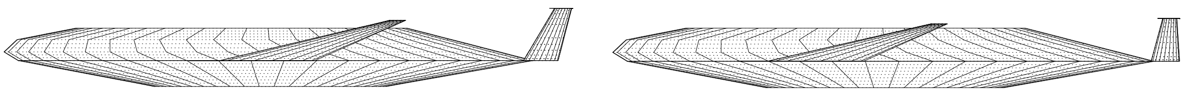

(c) StaticConFixSM configuration. (d) StaticConFreeSM configuration.

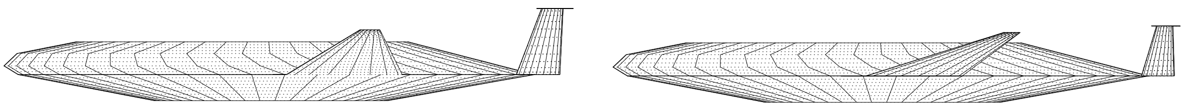

(e) SDynConFixSM configuration. (f) SDynConFreeSM configuration.

Figure 7.4: Side view of baseline configuration and all optimization cases.

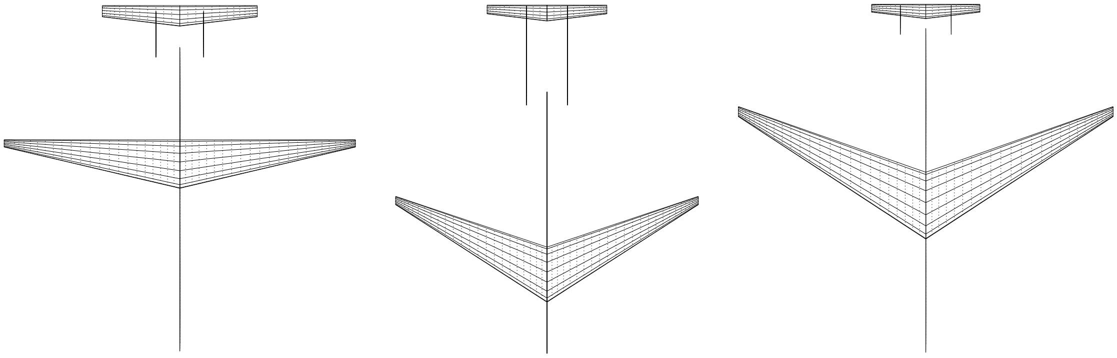

(a) Baseline configuration. (b) FixedTailVol configuration. (c) StaticConFixSM configuration.

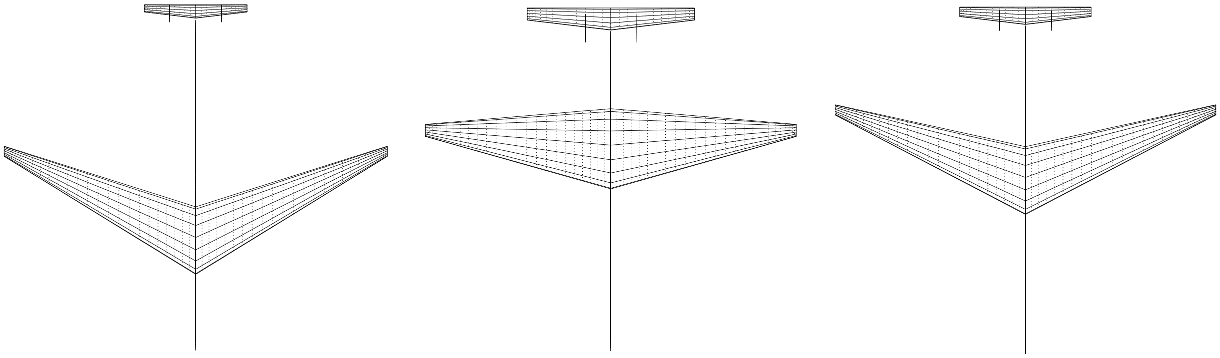

(d) StaticConFreeSM configuration. (e) SDynConFixSM configuration. (f) SDynConFreeSM configuration.

Figure 7.5: Top view of baseline configuration and all optimization cases.

7.1 Optimal Design using Fixed Tail Volume Coefficients

The optimal design using fixed tail volume coefficients with takeoff and landing (TOL) field constraints is shown in Fig. 7.6, and the associated design variables given in Table 7.5. As mentioned previously, the wing apex position was moved to the forward limit, 20 feet measured from the fuselage nose, while the vertical stabilizer sweep was increased to the upper limit, 65 degrees, shifting the horizontal tail to the aft limit. For a fixed horizontal tail volume coefficient, increasing the tail moment arm results in a reduction in horizontal stabilizer area, and thus wetted area, ergo viscous drag. With the vertical stabilizer root chord fixed to the fuselage rear and sweep limited to 65 degrees, the moment arm between the wing and vertical stabilizer aerodynamic centers was constrained, and for fixed tail volume coefficient caused the vertical stabilizer area to increase. Wing sweep was increased, giving a structural weight penalty, to take advantage of compressibility drag reductions at the cruise condition, resulting in fuel burn savings. Additionally, the wing sweep shifted the neutral

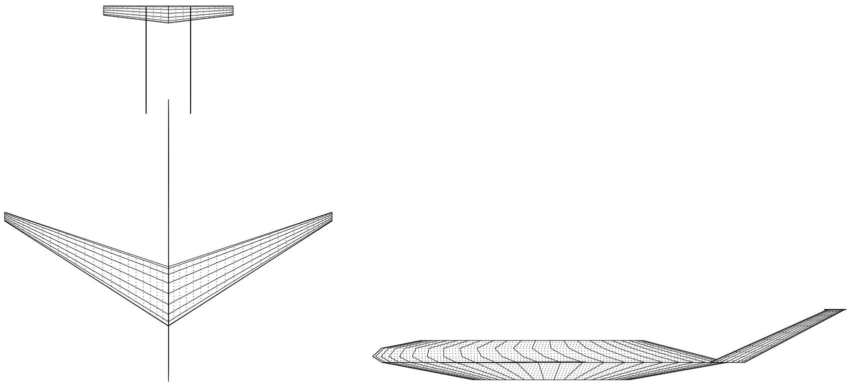

(a) Top view. (b) Side view.

Figure 7.6: FixedTailVol configuration top and side views.

Table 7.5: FixedTailVol design variable summary.

T (lb)	S (ft^2)	Λ (deg)	Γ (deg)	S_{HT} (ft^2)	S_{VT} (ft^2)	Λ_{VT} (deg)	$X_{W_{apex}}$ (ft)	SM (%)
22,590	1,451	29.5	0.1	222.1	113.3	65.0	20.0	10

point aft, and thus the center of gravity aft, increasing the nose up pitching moment due to the wing aerodynamic center being forward of the CG.

Figure 7.7 shows the takeoff and landing field performance of the design optimization using specified tail volume coefficients. Takeoff and landing were the only constraints on the optimization, other than mission range had to be met with a successful takeoff. Using only the best design from each generation, Fig. 7.7(a) shows the takeoff and landing field performance for each design, normalized by the constraint field lengths of 8,000 and 5,800 feet, respectively. To determine how active a constraint was throughout the design optimization, the takeoff and field length performance for every design evaluated in the optimization is shown in Fig. 7.7(b) as a histogram. Indicated in the histograms, takeoff and landing field length were active constraints in the design space with normal distributions centered near each field length constraint. Wing area and engine static thrust sizes are dependent on takeoff and landing field requirements, and any decrease in field length results in increased weight due to increased wing area and/or engine static thrust. No fuel burn benefit results from field length performances better than the constraints, so the optimizer minimized wing area and static thrust, pushing the design to the constraints.

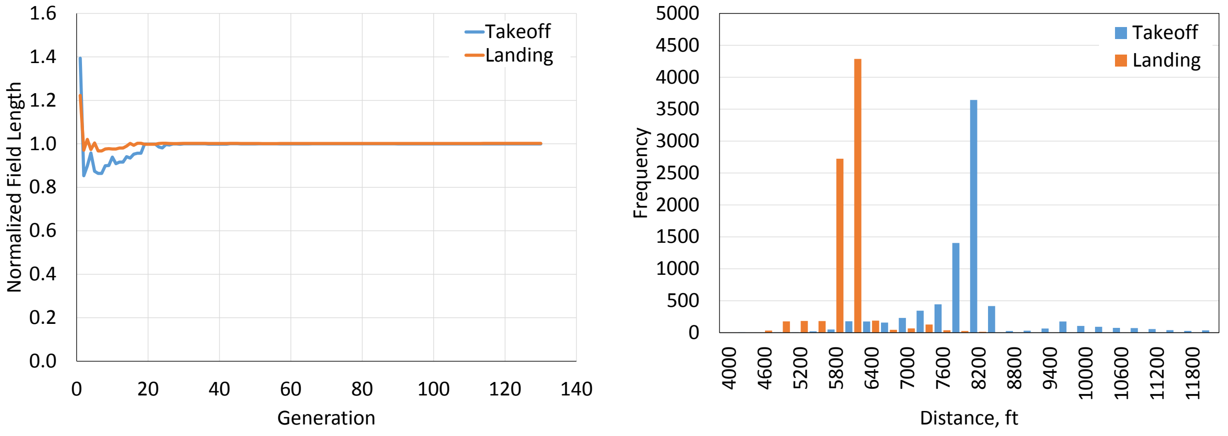

(a) Normalized takeoff and landing field lengths. (b) Histogram of takeoff and landing field distances.

Figure 7.7: FixedTailVol configuration takeoff and landing field length performance shown normalized by the constraints (a) and field length distances of all evaluated designs in a histogram (b).

The static trim and dynamic response analyses were run for the FixedTailVol case with results given in Tables 7.6 and 7.7. These constraints were not applied to the FixedTailVol optimization case, only takeoff and landing field constraints were applied, but the results give an indication of the shortcomings of only using performance constraints in an optimization. Red font in Tables 7.6 and 7.7 indicates a value that would have exceeded an allowable constraint limit had it been applied. In the one engine inoperative condition, the rudder deflection required to trim the yawing moment would result in stalling of the surface. The stall condition dynamic response analysis results of Table 7.7 show several limits that were exceeded. If the static trim and dynamic response constraints had been applied the FixedTailVol design would have been declared an infeasible design, rejecting it from the design space. Ignoring stability and control during the optimization, i.e., sizing the stabilizers using only tail volume coefficients, resulted in a design incapable of meeting all the handling and controllability requirements.

Table 7.6: FixedTailVol configuration static trim deflections, degrees.

Condition	Response Type	Deflection
OEI	Aileron	0.19
	Rudder	-33.26
Takeoff	Elevator	0.86
Maneuver	Elevator	10.89

The elevator effective angle of attack time responses to pitch and airspeed perturbations are shown in Fig. 7.8. After the perturbation was introduced into the system at time zero, the elevator effective angle of attack increased to approximately 20 degrees, far exceeding the allowable loading on the horizontal stabilizer. As the system returns to the steady-state condition after four seconds, the trim effective angle of attack was near the allowable limit, which indicated that nearly the maximum allowed loading was required to trim in the stall flight condition. With the stabilizer fully loaded for trim in the stall condition, no additional margin was available to respond to a system disturbance.

Table 7.7: FixedTailVol configuration dynamic response performance, in degrees unless otherwise noted.

Condition	Response Type	Cruise Condition	Stall Condition
Discrete Gust	Aileron	0.00	-11.79
	Rudder	1.92	7.40
	Elevator (Long)	1.00	11.06
	Elevator (Vert)	1.12	11.33
Turbulence	RMS Pitch	0.06	0.52
	RMS Roll	0.49	1.64
	RMS Yaw	0.40	2.63
Perturbation	Aileron	0.00	8.41
	Rudder	7.80	5.88
	Elevator (Pitch)	5.51	18.28
	Elevator (Speed)	3.42	22.33
Residual	Pitch	-0.18	-0.42
	Roll	-1.43	-0.61
	Speed (fps)	0.00	0.00

Figure 7.9 shows the FixedTailVol configuration roll response to a five-degree system perturbation in the cruise and stall flight conditions. After the disturbance, the system begins to return to the steady-state condition, but overshoots, and has to return. The overshoot in the cruise flight condition slowly returns to zero but fails to achieve the allowable residual five seconds after the disturbance. The stall condition roll residual behavior exhibited a slightly different behavior. The initial overshoot hits the lower bound of the residual limit, but returns to within the allowed residual prior to the five second cutoff. Unlike the cruise condition, a smaller, second oscillation occurred but never exceeded the limits.

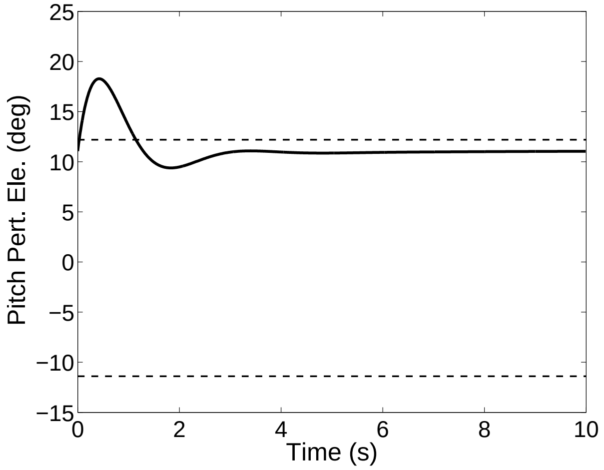

(a) Pitch perturbation elevator response.

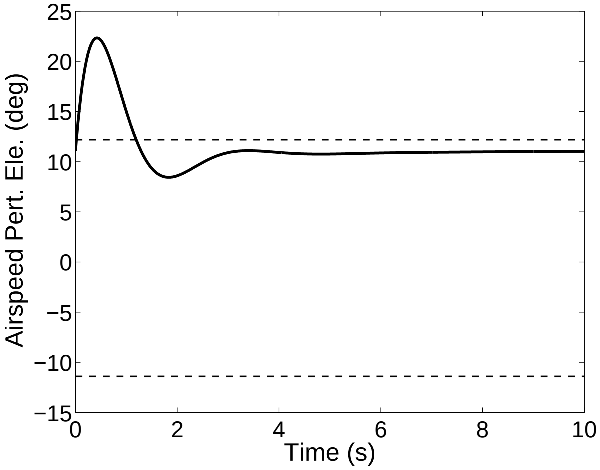

(b) Airspeed perturbation elevator response.

Figure 7.8: FixedTailVol configuration elevator time response to pitch and airspeed perturbations in the stall flight condition. The horizontal dashed lines indicate the maximum allowable elevator effective angles of attack.

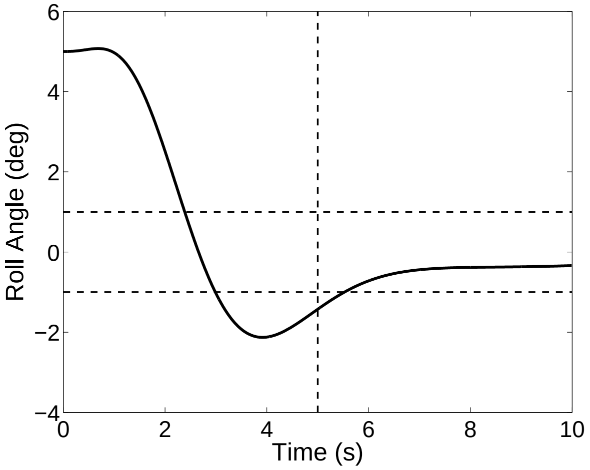

(a) Cruise roll residual.

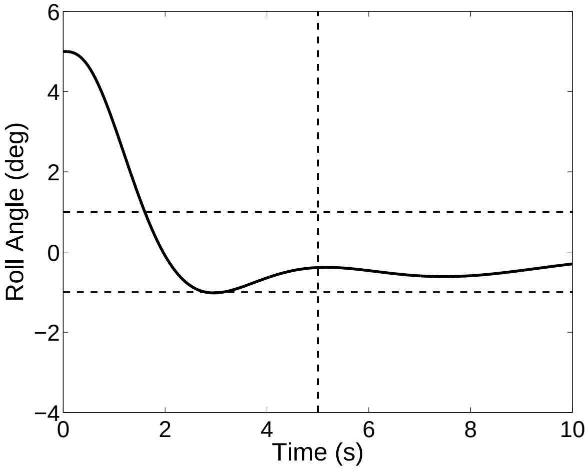

(b) Stall roll residual.

Figure 7.9: FixedTailVol configuration roll residual time responses in the cruise and stall flight conditions. The horizontal dashed lines indicate the maximum allowed deviations after five seconds, and the vertical dashed line indicates when the residual response was applied.

7.2 Optimal Designs with Static Trim Constraints

Applying static trim constraints to the multidisciplinary design optimization drastically altered the optimal designs compared to the case using traditional volume coefficients. Figures 7.4 and 7.5 compare the optimal designs with static trim constraints, both fixed and free static margin, with all the optimal design cases. Clearly, the vertical tail area and sweep were reduced from the FixedTailVol case, and the wing apex location, especially in the fixed static margin case, was moved aft toward the center of the fuselage. Optimizing with the static trim constraints instead of fixed tail volume coefficient resulted in very little change in wing area, engine static thrust, and wing sweep as indicated in Table 7.4, but a nonzero dihedral angle was introduced. As the tail areas were sized using static trim constraints, the horizontal and vertical stabilizer areas decreased. This indicated using fixed tail volume coefficients resulted in a poor optimal solution because the stabilizer areas were greater than the cases with static trim constraints, and the one engine inoperative trim deflection resulted in a stalled control surface. Removing the fixed tail volume coefficient requirement and adding static trim constraints allowed the wing apex to shift aft, allowing for a configuration with reduced load requirements on the stabilizers.

Allowing static margin to be a free design variable resulted in several design changes as seen in Fig. 7.10. The two configurations have a similar wing planform with the StaticConFreeSM wing apex farther forward than the StaticConFixSM case. Static margin increased to 15.1%, allowing for reduced horizontal and vertical stabilizer areas and wetted area reductions. Having only 10.6 degrees of vertical tail sweep results in structural weight and wetted area reductions. Table 7.8 summarizes the design variables of the two configurations.

Similar to Section 7.1, takeoff and landing field lengths were active constraints in the design space, heavily driving the wing sizing and static thrust. As gross weight decreased from the FixedTailVol configuration, both wing area and engine static thrust could be decreased to meet the same field length requirements. Figure 7.11 shows the normalized takeoff

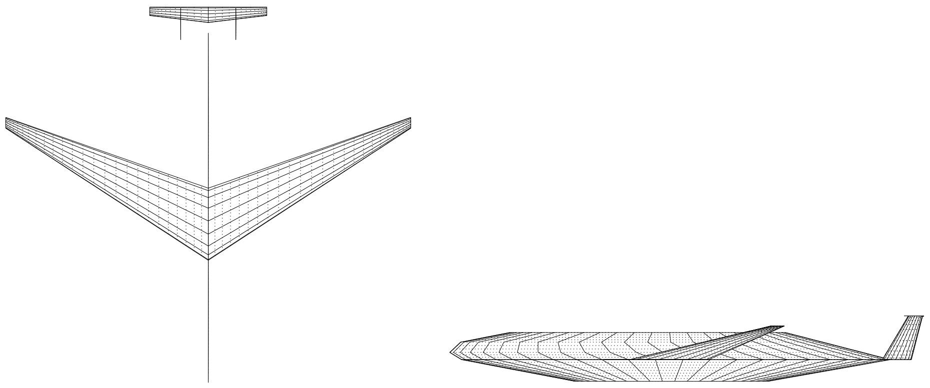

(a) StaticConFixSM top view. (b) StaticConFixSM side view.

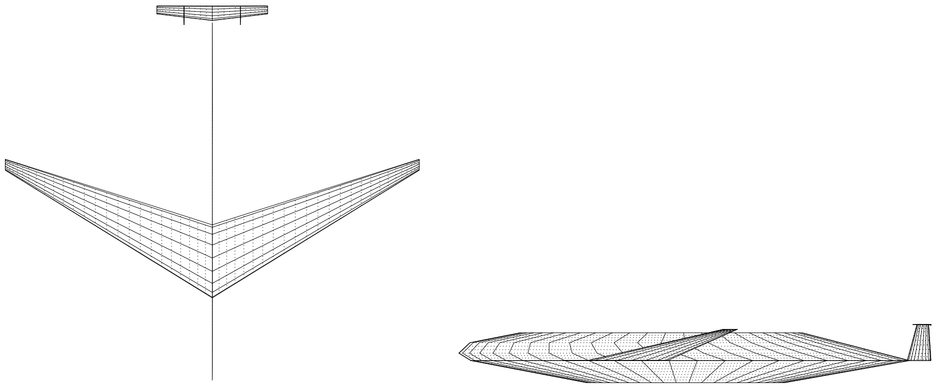

(c) StaticConFreeSM top view. (d) StaticConFreeSM side view.

Figure 7.10: StaticConFixSM and StaticConFreeSM optimization cases top and side views.

and landing constraints along with the associated histograms for all designs analyzed during the genetic algorithm search. The optimization pushed the upper bounds of the constraints as the histogram shows a large number of designs exceeding the 8,000 and 5,800 feet field lengths. In the case of takeoff, numerous designs had field lengths less than 8,000 feet, but at a greater system total fuel burn, increasing the system design objective function.

Table 7.8: Static trim cases design variable summary.

Design	T (lb)	S (ft^2)	Λ (deg)	Γ (deg)	S_{HT} (ft^2)	S_{VT} (ft^2)	Λ_{VT} (deg)	$X_{W_{apex}}$ (ft)	SM (%)
StaticConFixSM	22,200	1,422	30.0	8.8	118.8	50.4	26.9	35.6	10.0
StaticConFreeSM	22,120	1,411	28.5	8.1	102.1	32.4	10.6	23.4	15.1

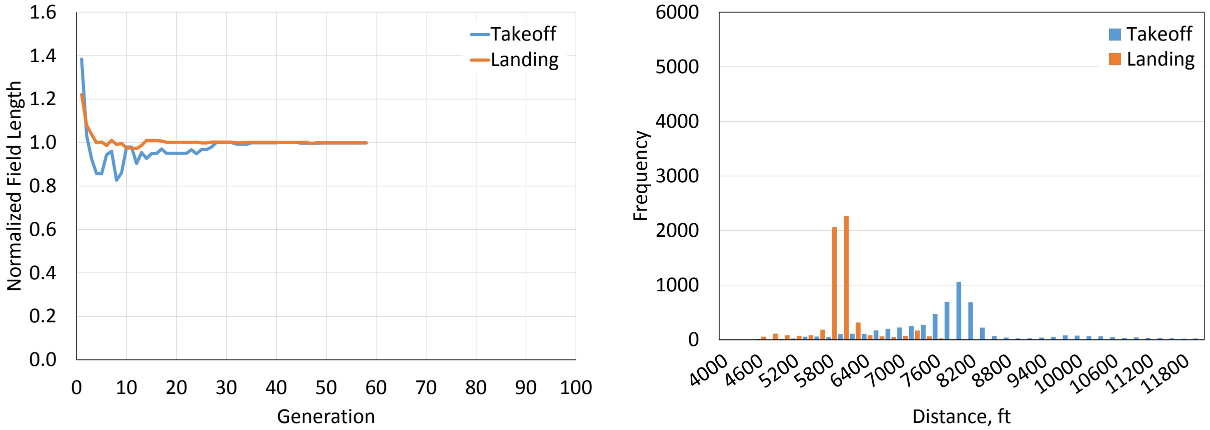

(a) StaticConFixSM normalized takeoff and landing field lengths.

(b) StaticConFixSM histogram of takeoff and landing field lengths.

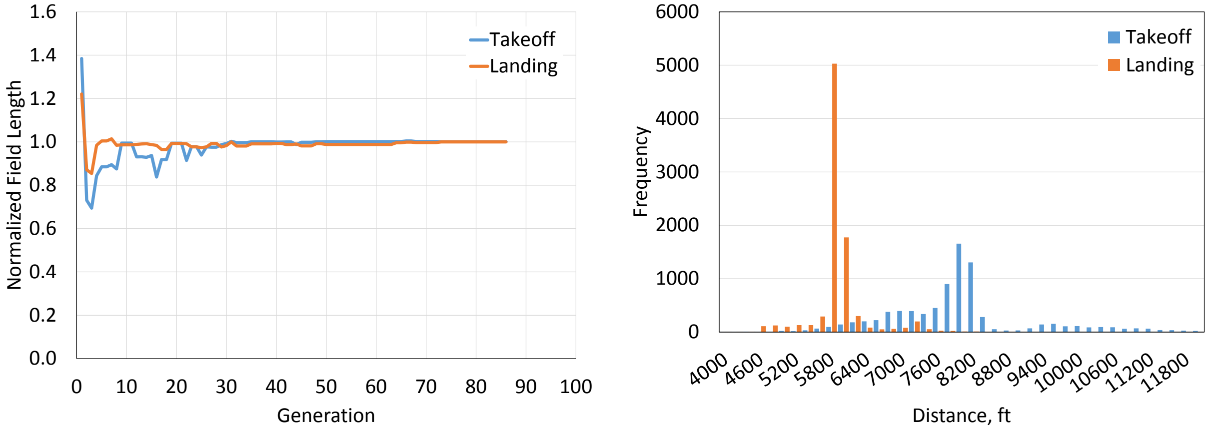

(c) StaticConFreeSM configuration normalized takeoff and landing field lengths.

(d) StaticConFreeSM configuration histogram of takeoff and landing field lengths

Figure 7.11: StaticConFixSM and StaticConFreeSM configurations takeoff and landing field length performance shown normalized by the constraints and field length distances of all evaluated designs in a histogram.

The static trim constraints included one engine inoperative (OEI) aileron and rudder deflection, takeoff elevator effective angle of attack, and maneuver condition elevator effective angle of attack limits. As expected, OEI rudder deflection and takeoff elevator effective angle of attack, the effective angle of attack required to lift the nose wheel at rotation speed, were increasingly active as the optimization progressed, indicating the desire to minimize the horizontal and vertical stabilizer areas. Figures 7.12(a) and 7.12(b) show the normalized trim constraints of the best designs. Only the rudder and elevator constraints were active, especially in later generations, and aileron deflection angle was minimal during the one engine inoperative flight condition.

Numerous designs had takeoff and maneuver trim constraints within the specified limits of -11.4 and 12.2 degrees. Figures 7.12(c) and 7.12(d) show the large distribution of elevator effective angles of attack. The maneuver elevator range of values were smaller in the fixed static margin case than the free static margin, but in both optimizations the majority of designs fell below the upper constraint of 12.2 degrees. Even though the maneuver elevator constraint was inactive in the best design of each generation, it can be seen that the constraint was active in the free static margin design space as several hundred designs violated the upper constraint bounds. Many designs evaluated in the fixed static margin case had maneuver elevator effective angles of attack approaching the upper limit, but few designs ever exceeded the upper limit.

An interesting feature of the configurations was the positive elevator lift required to trim during the maneuver condition. The wing, as designed in Ref. [10], had airfoils shaped to reduce the nose down pitching moment. As the airfoils were again used in this research, the combination of a heavily loaded wing, the wing lift vector forward of the center of gravity, and a small wing aerodynamic pitching moment resulted in a net nose up pitching moment required to be counteracted by the elevator. As the geometric deflection angle of the elevator was negative, the combination of geometric angle of attack, downwash, and deflection angle resulted in a positive lift coefficient to counteract the nose up pitching moment of the heavily

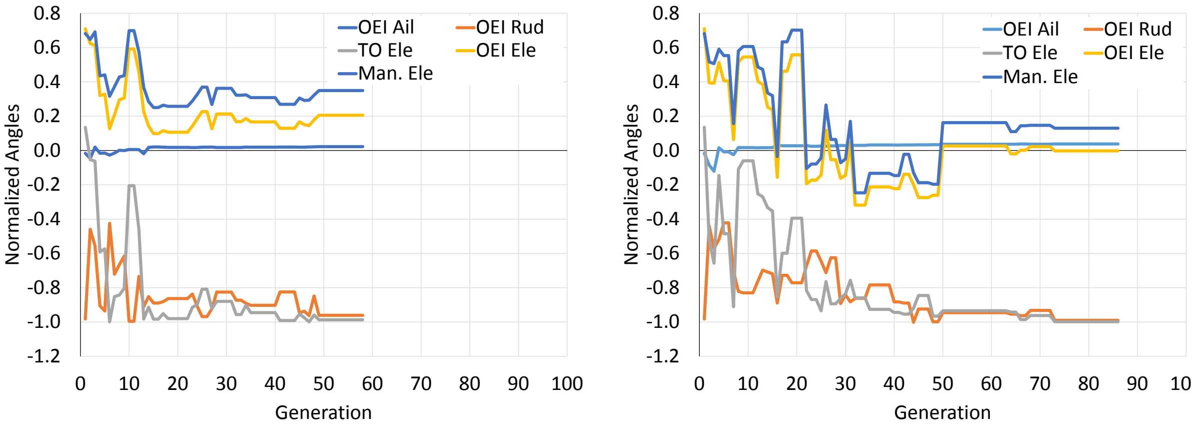

(a) StaticConFixSM normalized deflection angles, degrees.

(b) StaticConFreeSM configuration normalized deflection angles, degrees.

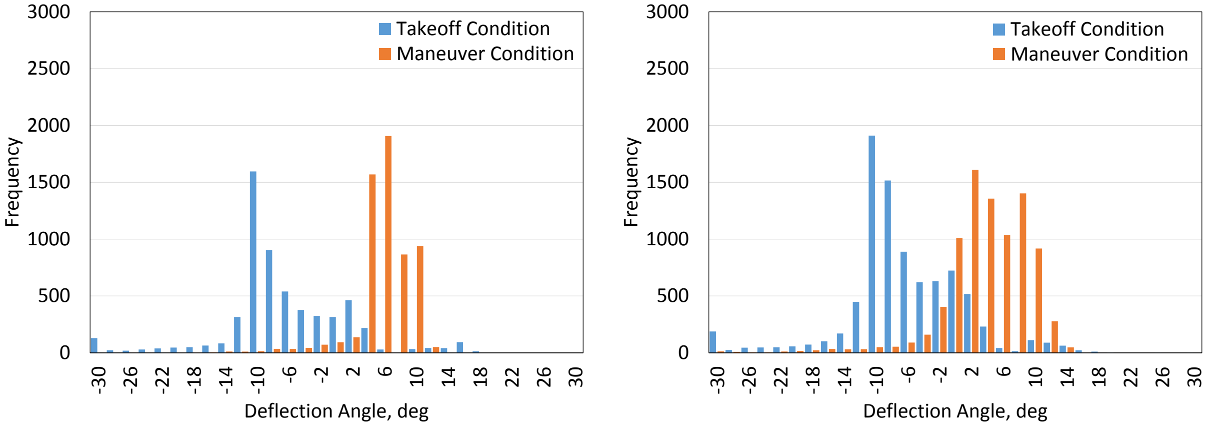

(c) StaticConFixSM takeoff and maneuver flight conditions elevator deflection histogram, degrees.

(d) StaticConFreeSM configuration takeoff and maneuver flight conditions elevator deflection histogram, degrees.

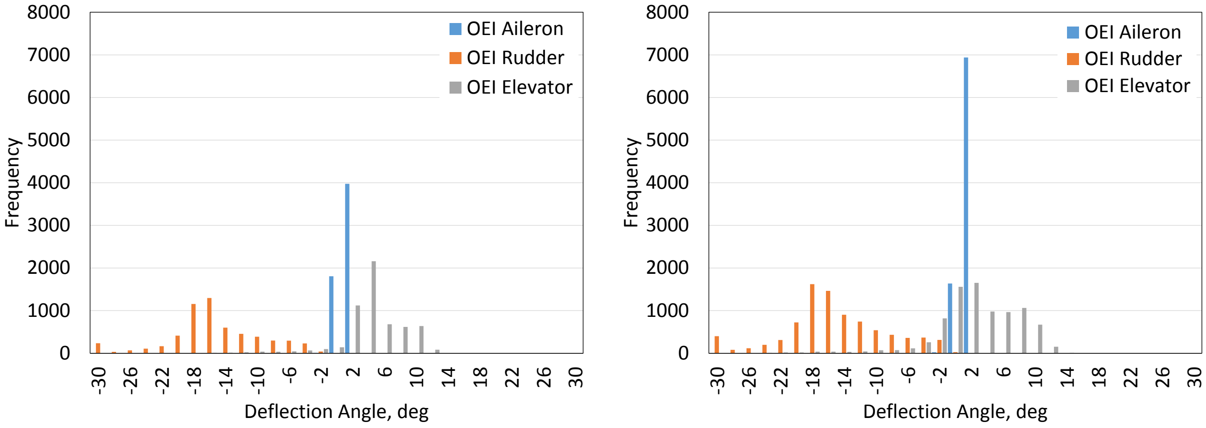

(e) StaticConFixSM OEI deflection angles histogram, degrees.

(f) StaticConFreeSM configuration OEI deflection angles histogram, degrees.

Figure 7.12: Static trim constraints with each generation best design deflection angles normalized by the constraints (a,b) and deflection angles histograms of evaluated designs (c–f).

loaded wing. Although the effective angle of attack may seem counterintuitive, geometrically the geometry was behaving as expected. This highlights the benefit of using the elevator effective angle of attack as the horizontal stabilizer sizing constraint instead of a geometry deflection angle.

Static trim constraints were applied to the optimization and were used to size the horizontal and vertical stabilizers in parallel with the planform geometry. Including the constraints in the optimization eliminated the necessity of tail volume coefficients while still considering trim controllability. Table 7.9 shows that, unlike the FixedTailVol case, all the static trim constraints were met, with rudder and elevator deflection angles being the most active constraints. The stabilizer and control surfaces were adequately sized to provide trim without exceeding the allowed deflections constraints or stall the surface.

Table 7.9: Trim deflection angles, in degrees, for static trim optimization cases.

Flight Condition	Control Surface	StaticConFixSM	StaticConFreeSM
OEI	Aileron	0.45	0.76
	Rudder	-19.22	-19.80
Takeoff	Elevator	-11.25	-11.38
Maneuver	Elevator	4.26	1.58

Reviewing Fig. 7.10, the horizontal and vertical stabilizer areas, even in a twin vertical tail configuration, were very small. Using only static trim constraints does not adequately size the stabilizer surfaces as the dynamic response performance was far from acceptable. Table 7.10 highlights the poor dynamic performance of the elevator in the stall condition. The pitch perturbation maximum elevator deflection and residual pitch angle both exceed the constraints. Additionally, both the fixed and free static margin cases had deficient roll residual performance in the cruise condition, not accounted for during the optimization with static trim constraints only.

Figures 7.13 to 7.15 show the time response plots for the constraints highlighted in red in Table 7.10. Figure 7.13 shows the elevator effective angle of attack time response to the airspeed perturbation for the StaticConFixSM and StaticConFreeSM configurations.

Table 7.10: Dynamic response performance for static trim optimization cases, in degrees unless noted otherwise.

Condition	Response Type	StaticConFixSM		StaticConFreeSM	
		Cruise	Stall	Cruise	Stall
Discrete Gust	Aileron	0.00	-11.55	0.00	-10.83
	Rudder	-1.76	8.44	-1.62	7.86
	Elevator (Long)	-0.74	4.89	-1.70	2.17
	Elevator (Vert)	-0.88	6.01	-1.85	3.54
Turbulence	RMS Pitch	0.11	0.74	0.14	0.81
	RMS Roll	1.97	2.33	1.81	2.05
	RMS Yaw	0.37	1.41	0.37	1.51
Perturbation	Aileron	0.00	6.72	0.00	6.89
	Rudder	3.15	3.77	3.47	3.80
	Elevator (Pitch)	5.35	13.60	4.68	11.16
	Elevator (Speed)	2.56	18.49	-1.79	16.21
Residual	Pitch	-0.37	-0.67	-0.35	-0.60
	Roll	-1.14	-0.77	-1.34	-0.75
	Speed (fps)	0.00	0.00	0.00	0.00

An elevator effective angle of attack of far greater than the allowed 12.2 degrees occurred in both configurations at the stall flight condition, settling out six seconds after the initial airspeed perturbation.

The residual pitch angle time responses for the StaticConFixSM and StaticConFreeSM configurations in the stall condition are shown in Fig. 7.14. Horizontal dashed lines indicate the maximum allowable pitch angle residual after five seconds, and the vertical dashed line indicates when the residual constraint began to be applied. The pitch angle response overshoots the steady-state condition before returning, exceeding the allowable deviation after five seconds. At five seconds the StaticConFixSM had a pitch residual of -0.67 degrees, and the StaticConFreeSM had a slightly better response with a residual of -0.60 degrees.

Table 7.10 shows that the static trim optimization cases failed to meet the roll residual constraint limits in the cruise flight condition. Figure 7.15 shows the roll angle residuals for both static trim constraint optimization cases in the cruise flight condition. Both cases failed to meet the allowed plus or minus one degree roll residual deviation from the steady-state

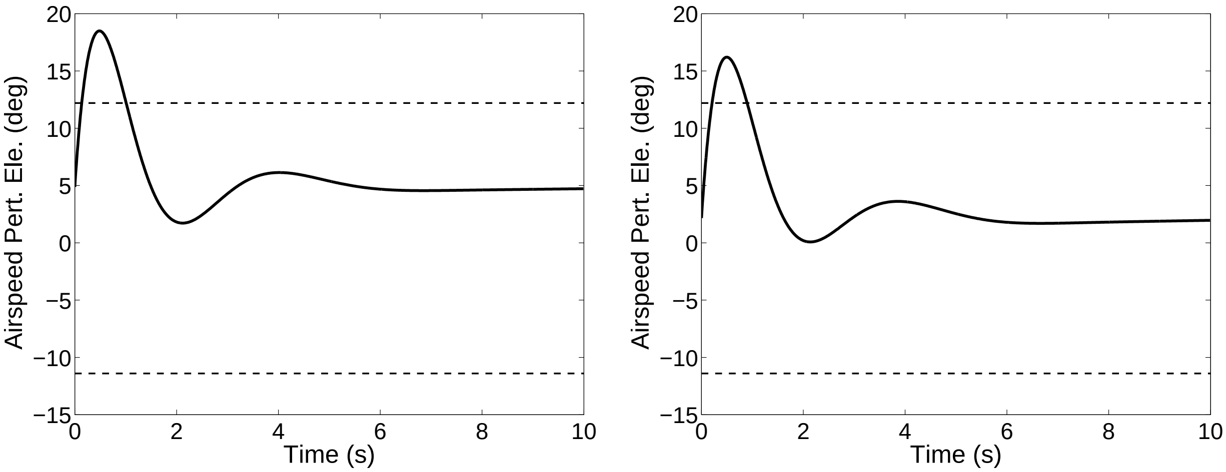

(a) StaticConFixSM configuration.

(b) StaticConFreeSM configuration.

Figure 7.13: StaticConFixSM and StaticConFreeSM configurations elevator response to an airspeed perturbation in the stall condition. The horizontal dashed lines indicate the maximum allowed elevator effective angle of attack.

condition five seconds after a perturbation. The responses between the two configurations were very similar, with the free static margin case having poorer performance.

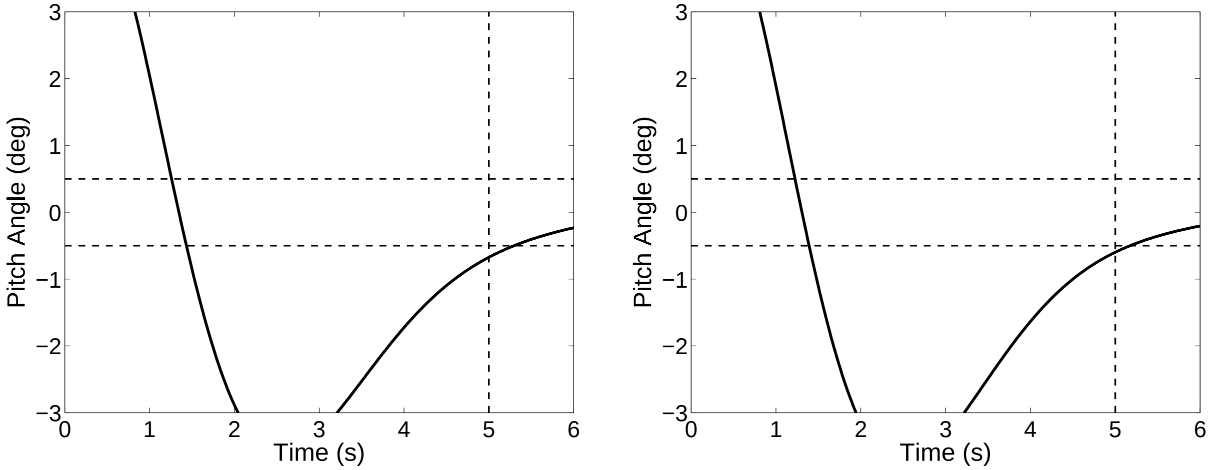

(a) StaticConFixSM configuration.

(b) StaticConFreeSM configuration.

Figure 7.14: StaticConFixSM and StaticConFreeSM configurations pitch residual time response in the stall condition. The horizontal dashed lines indicate the maximum allowable residual pitch angle five seconds after the initial perturbation, and the vertical dashed line indicates when the residual response was applied.

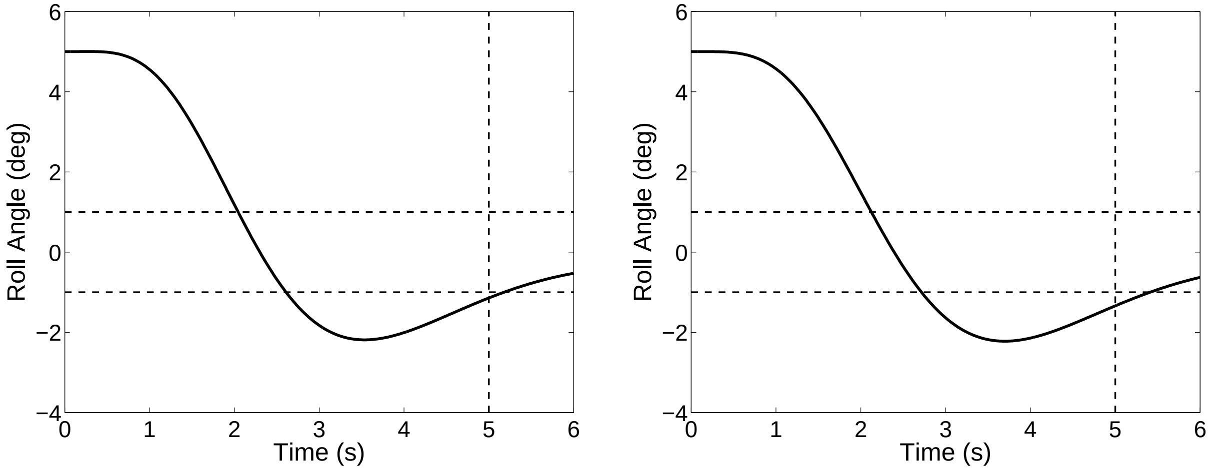

(a) StaticConFixSM configuration.

(b) StaticConFreeSM configuration.

Figure 7.15: StaticConFixSM and StaticConFreeSM configurations roll residual time responses in the cruise condition. The horizontal dashed lines indicate the maximum allowed deviations after five seconds, and the vertical dashed line indicates when the residual response was applied.

7.3 Optimal Designs Using Static Trim and Dynamic Response Constraints

Referring back to Figs. 7.4 and 7.5, comparisons can be drawn between the configurations optimized with and without dynamic constraints. The vertical stabilizer area increased for both the SDynConFixSM and SDynConFreeSM configurations, Figs. 7.4(e) and 7.4(f), compared to the StaticConFixSM and StaticConFreeSM configurations. Specifics of the dynamic constraint optimized designs can be seen in Table 7.4 where the vertical stabilizer area was increased from the baseline for the fix static margin configuration. With static margin fixed, the total fuel burn was greatest of all the optimized designs, totaling 30,304 pounds. Freeing static margin and optimizing with static trim and dynamic response constraints reduced the fuel burn by approximately 4,000 pounds. The SDynConFreeSM configuration gross weight, 156,767 pounds, was reduced to less than the baseline and FixedTailVol designs. Only the static constraint optimized designs, StaticConFixSM and StaticConFreeSM, had smaller gross and fuel weights.

To compare the fixed versus free static margin designs directly, Fig. 7.16 shows the top and side views of the two configurations, with design variable details provided in Table 7.11. Wing area of the SDynConFixSM case was 1,730 square feet, the only optimized design that was not in the region of 1,450 square feet. Static thrust was less for the free static margin case while also having a wing area of 1,426 square feet. Figure 7.17 shows that the field length for the SDynConFreeSM case was active throughout the optimization, unlike the SDynConFixSM case. The larger wing area of the SDynConFixSM design, with larger thrust than the other designs, alleviated the field length constraint. The histogram of Fig. 7.17(b) shows that for all the designs evaluated during the optimization, rarely was the takeoff or landing constraint violated for the SDynConFixSM configuration.

Takeoff and landing field lengths were active constraints for the SDynConFreeSM case, as indicated by the normalized field length plot and histogram of Figs. 7.17(c) and 7.17(d). Many of the evaluated designs had takeoff and landing field distances greater than the allowed

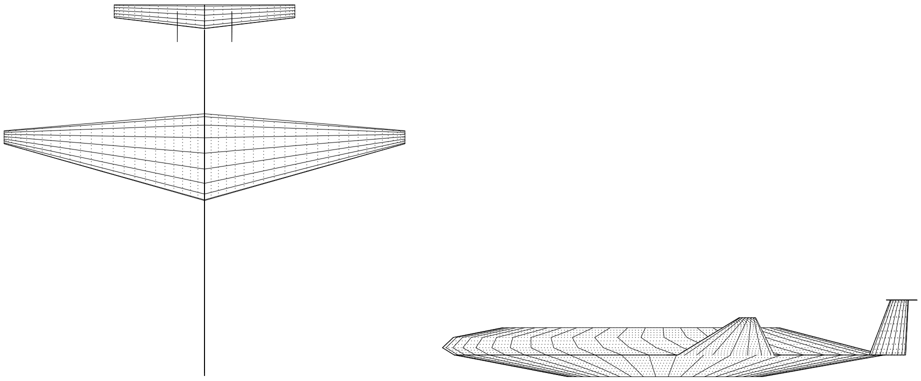

(a) SDynConFixSM top view. (b) SDynConFixSM side view.

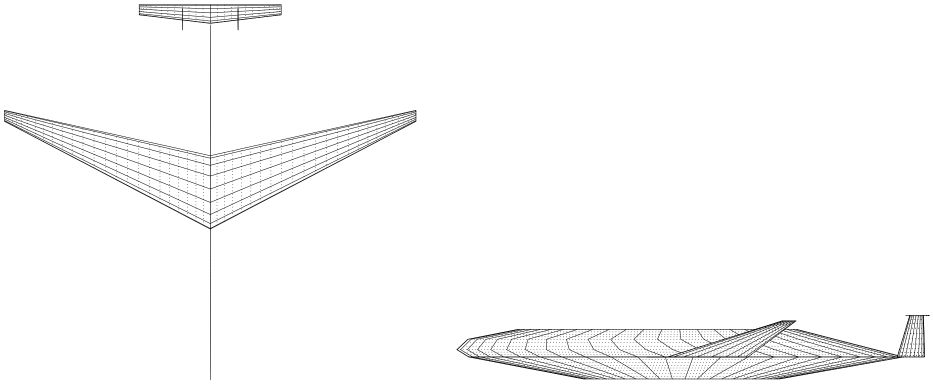

(c) SDynConFreeSM top view. (d) SDynConFreeSM side view.

Figure 7.16: SDynConFixSM and SDynConFreeSM optimization cases top and side view.

limits, resulting in infeasible designs. The normalized takeoff and landing distances for the best designs in each generation consistently pushed the upper constraint bounds.

Application of a moderate lateral discrete gust was used to stress the lateral/directional control system in the cruise and stall flight conditions. In the cruise flight condition for both the SDynConFixSM and SDynConFreeSM designs, deflection angles for both the aileron and rudder were small, less than two degrees for nearly all the designs, as indicated in the

Table 7.11: SDynConFixSM and SDynConFreeSM configurations design variable summary.

Design	T (lb)	S (ft^2)	Λ (deg)	Γ (deg)	S_{HT} (ft^2)	S_{VT} (ft^2)	Λ_{VT} (deg)	$X_{W_{apex}}$ (ft)	SM (%)
SDynConFixSM	23,670	1,730	10.8	9.7	288.7	79.2	16.7	51.5	10.0
SDynConFreeSM	22,200	1,426	24.1	9.4	169.5	44.5	12.3	43.2	22.4

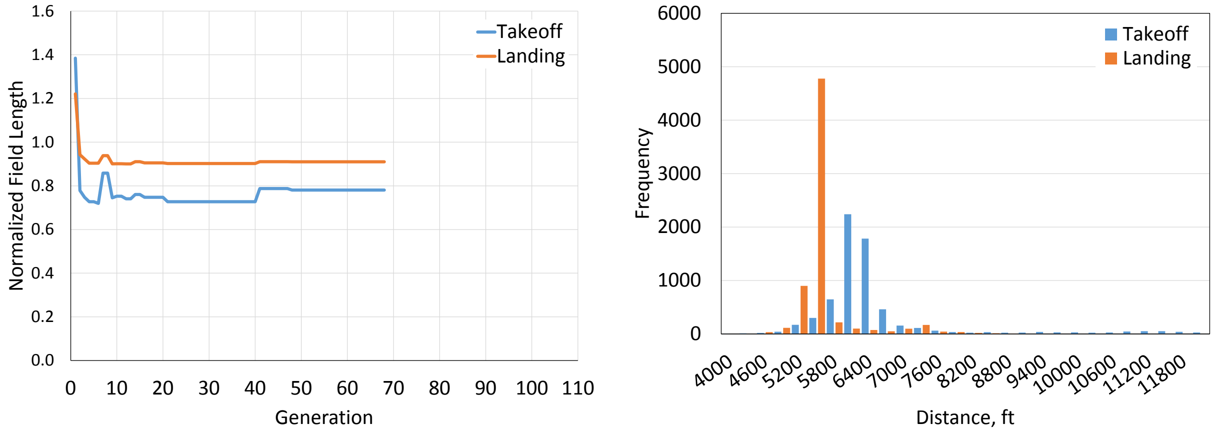

(a) SDynConFixSM normalized takeoff and landing field lengths.

(b) SDynConFixSM histogram of takeoff and landing field lengths.

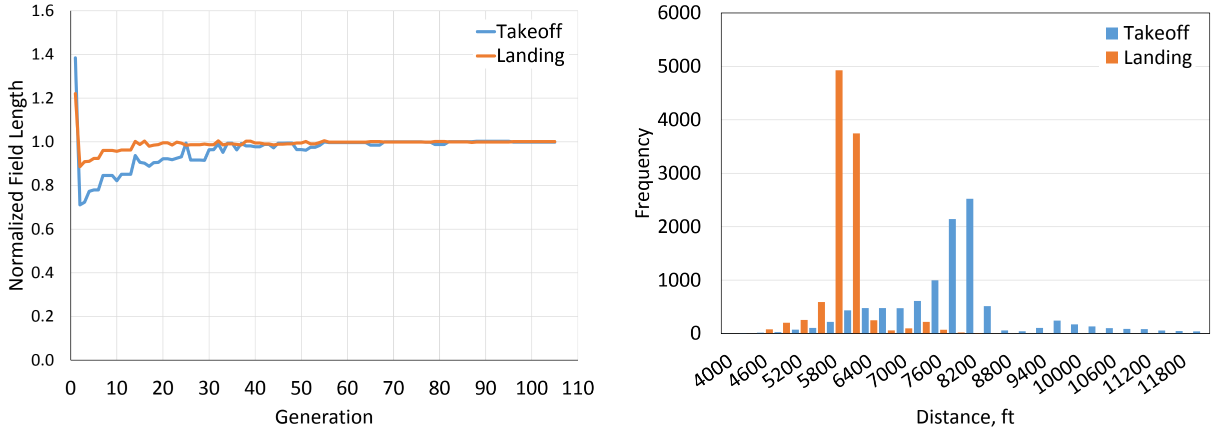

(c) SDynConFreeSM normalized takeoff and landing field lengths.

(d) SDynConFreeSM histogram of takeoff and landing field lengths.

Figure 7.17: SDynConFixSM and SDynConFreeSM configurations each generation best design normalized takeoff and landing field lengths and field length histograms of each evaluated design.

histograms of Fig. 7.18. The stall flight condition was more demanding on the flight control system, but never becoming an active constraint in the best designs. The maximum aileron and rudder deflections were nearly constant for the SDynConFixSM best designs, whereas the maximum aileron and rudder deflections in the SDynConFreeSM case increased throughout the optimization, settling only when the best solution was found. The histograms show that the aileron response to a lateral gust consistently had the largest deflection in both optimization cases, but no designs ever exceeded the upper constraint limit of 20 degrees.

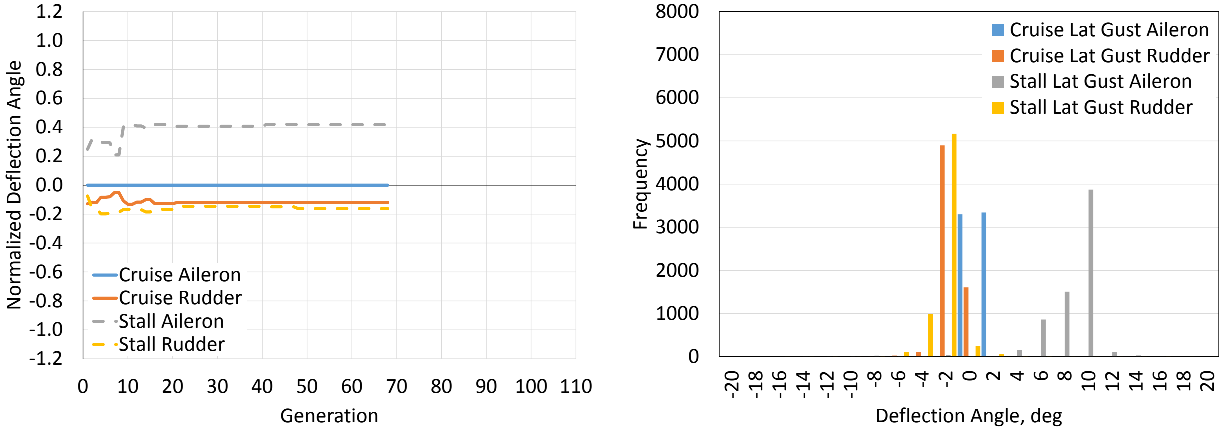

(a) SDynConFixSM normalized deflection angle responses to a lateral gust.

(b) SDynConFixSM histogram of deflection angle responses to a lateral gust, degrees.

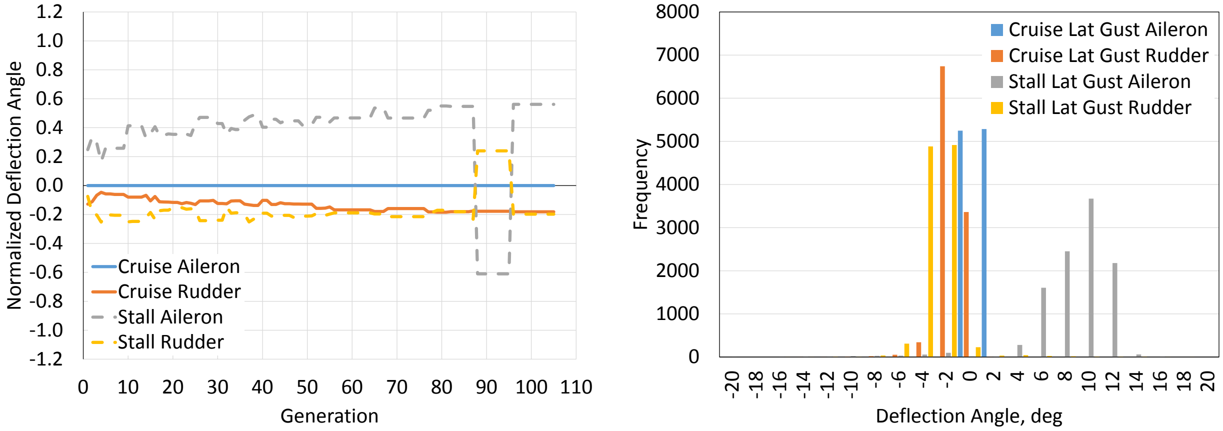

(c) SDynConFreeSM normalized deflection angle responses to a lateral gust.

(d) SDynConFreeSM histogram of deflection angle responses to a lateral gust, degrees

Figure 7.18: SDynConFixSM and SDynConFreeSM configurations aileron and rudder response to a lateral gust.

The maximum allowed root-mean-squared (RMS) deviation from moderate continuous turbulence was 5 degrees in both pitch and yaw, and 10 degrees in roll. Neither the SDynConFixSM nor SDynConFreeSM optimization cases struggled with this constraint, Fig. 7.19, as the best designs never neared the constraints. The closest approach to a continuous turbulence constraint was yaw in the stall flight condition. The RMS yaw was the only continuous turbulence response that exceeded three degrees, occurring in very few designs. Pitch and roll RMS angles, at both stall and cruise flight conditions, were well below the constraints.

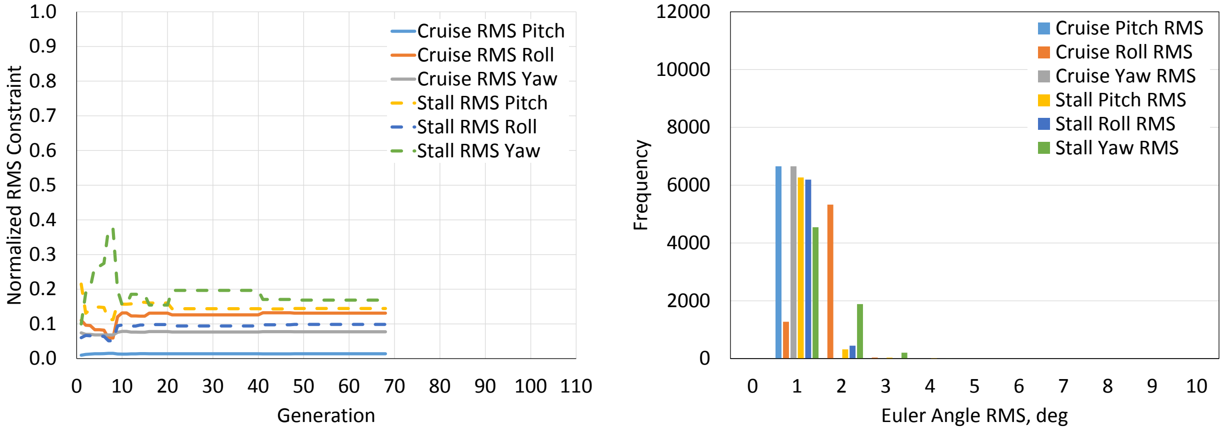

(a) SDynConFixSM normalized RMS turbulence response.

(b) SDynConFixSM histogram of RMS turbulence response, degrees.

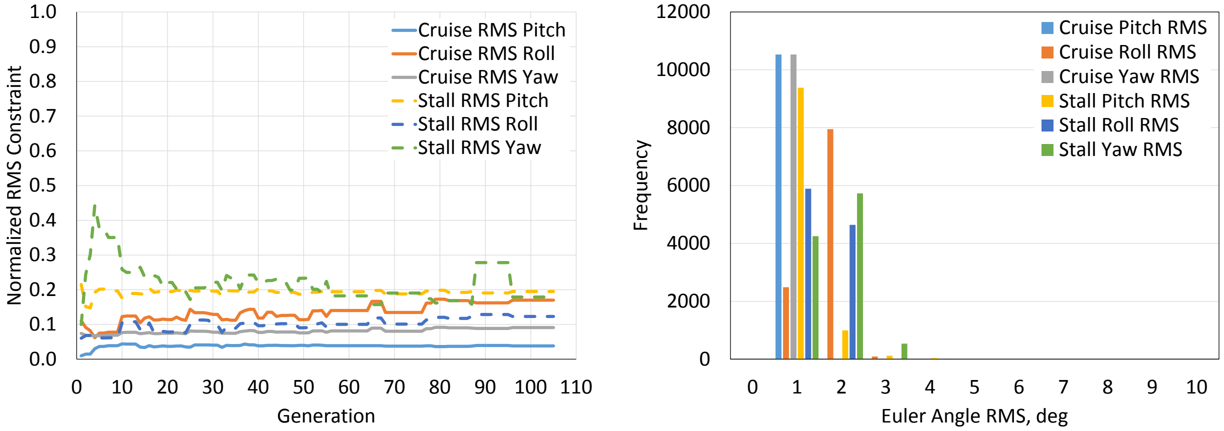

(c) SDynConFreeSM normalized RMS turbulence response.

(d) SDynConFreeSM histogram of RMS turbulence response, degrees.

Figure 7.19: SDynConFixSM and SDynConFreeSM configurations RMS turbulence response.

Maximum aileron and rudder deflections angles from the five degree roll perturbation were small in the cruise condition, with many of the aileron deflections being near zero, visible in Fig. 7.20. As the histograms of Figs. 7.20(b) and 7.20(d) show, the cruise roll perturbation maximum rudder deflection for nearly all the designs evaluated was less than eight degrees, indicating that the roll perturbation in the cruise condition had very little influence on the design. With the small maximum aileron deflections, the closed-loop system was relying on the natural roll stability provided by the wing dihedral.

In the stall flight condition, maximum aileron deflections were significantly higher than the cruise condition, with many designs having deflections between 12 and 14 degrees for

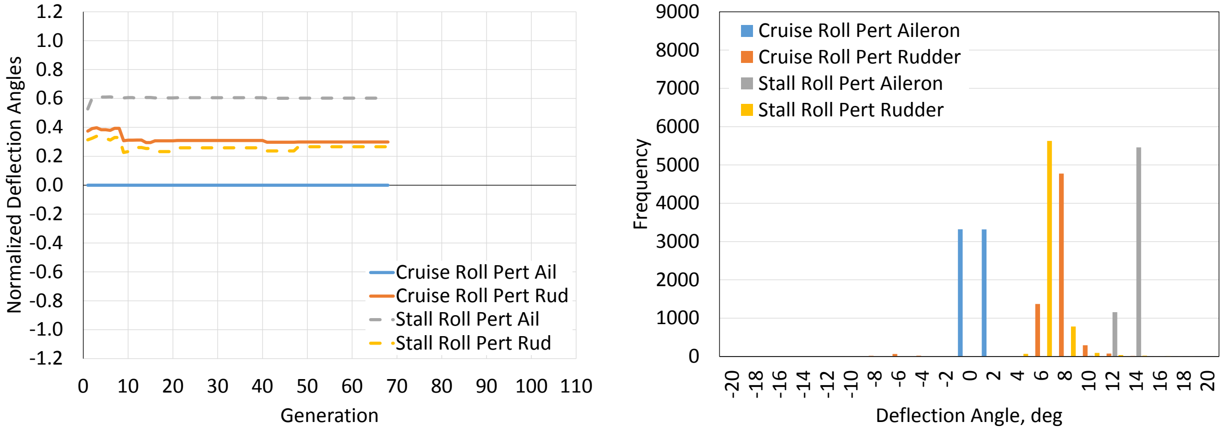

(a) SDynConFixSM normalized roll perturbation responses.

(b) SDynConFixSM histogram of roll perturbation responses.

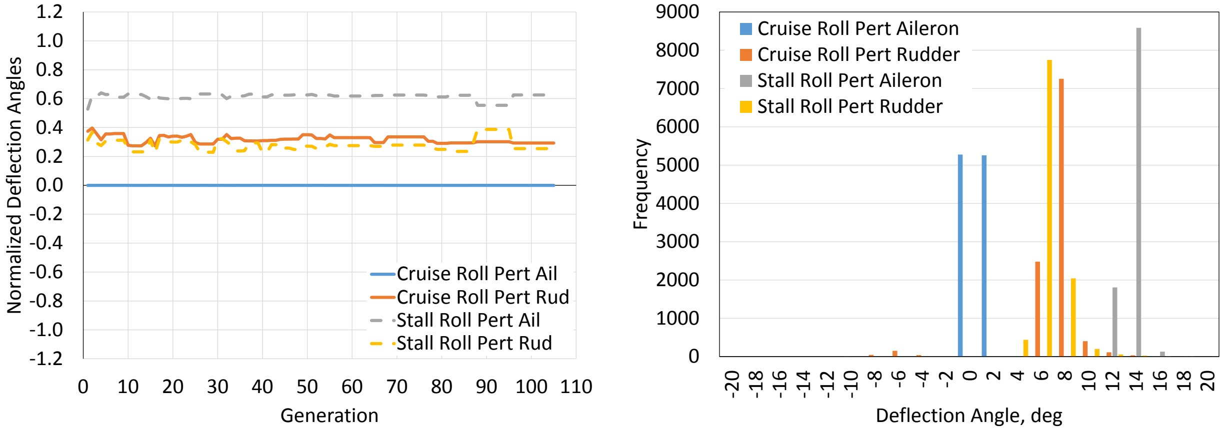

(c) SDynConFreeSM normalized roll perturbation responses.

(d) SDynConFreeSM histogram of roll perturbation responses.

Figure 7.20: SDynConFixSM and SDynConFreeSM configurations roll perturbation response performance.

both the SDynConFixSM and SDynConFreeSM cases. The rudder deflections in the stall condition closely resembled those in the cruise condition for both cases. Even though the aileron deflections were significantly higher in the stall condition, Figs. 7.20(a) and 7.20(c) show that the maximum deflections were far below the maximum of 20 degrees. Again, in terms of maximum deflections, the roll perturbation was inactive in the design space even for the stall flight condition.

A second requirement on the system perturbation response was the time to return to steady-state conditions within a residual tolerance. Five seconds after an initial system perturbation, the pitch and roll Euler angle residuals were required to return to within 0.5 and 1.0 degrees of the steady state, respectively. The Baseline, FixedTailVol, StaticConFixSM, and StaticConFreeSM configurations all failed to have an adequate roll response with a roll residual greater than the allowed limit. Also, during preliminary optimizations with the static trim and dynamic response constraints, the roll residual constraint was consistently active, resulting in the genetic algorithm struggling to find feasible designs. Given this experience, the roll angle weighting of Eq. 4.36 was increased by a factor of 10.

Figure 7.21 shows the normalized residual of the best designs and the residual histograms of all evaluated designs with the increased roll weighting. For both cases, neither the cruise nor the stall flight condition pitch residuals were constraining on the design space. Nearly all evaluated designs had pitch residuals within the allowed limits. In previous optimizations of the SDynConFixSM and SDynConFreeSM cases, a large number of designs exceeded the allowed roll residual in both the cruise and stall flight conditions. The normalized residuals of the best designs, shown in Figs. 7.21(a) and 7.21(c), show that the increased roll weighting reduced the roll residuals, removing it as an active constraint in the design space. Reviewing the histograms of Figs. 7.21(b) and 7.21(d), the heavier roll weighting made it to where there were no designs that exceeded the plus or minus one degree roll angle limit.

The airspeed deviation after 30 seconds in all cases was driven to zero as seen in the normalized residual plots. If an altitude state with a fixed altitude requirement was placed on the linear simulation, this constraint could become active, but would also require a throttle model, not currently included in the system dynamics used in this research. As this residual constraint was always zero, it will be discussed no further.

Elevator response to moderate longitudinal and vertical gusts is shown in Fig. 7.22. A large range of elevator effective angle of attacks resulted in the design space, none exceeding the constraint limits of -11.4 and 12.2 degrees. The best designs never approached the constraints while the center of the normal distributions in the histograms, the approximate

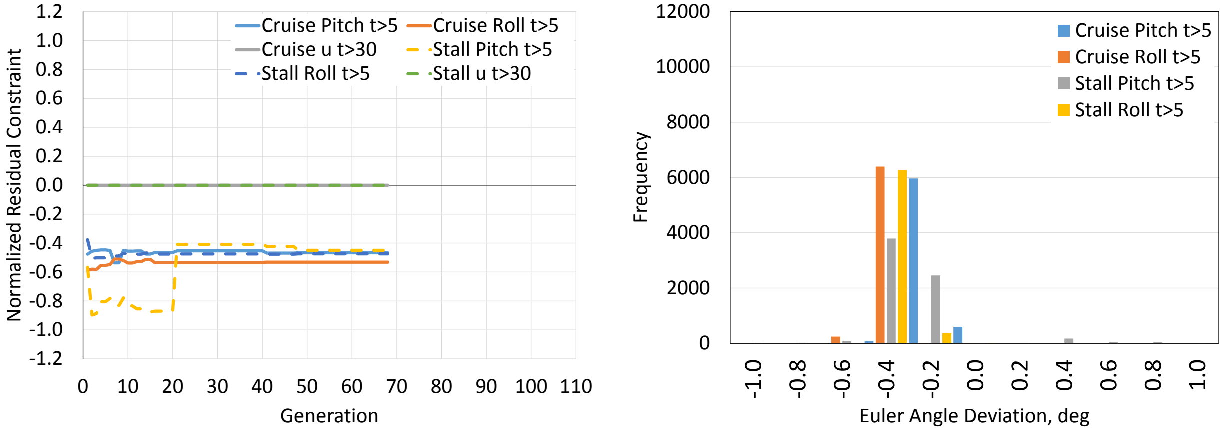

(a) SDynConFixSM normalized perturbation residual responses.

(b) SDynConFixSM histogram of perturbation residual responses.

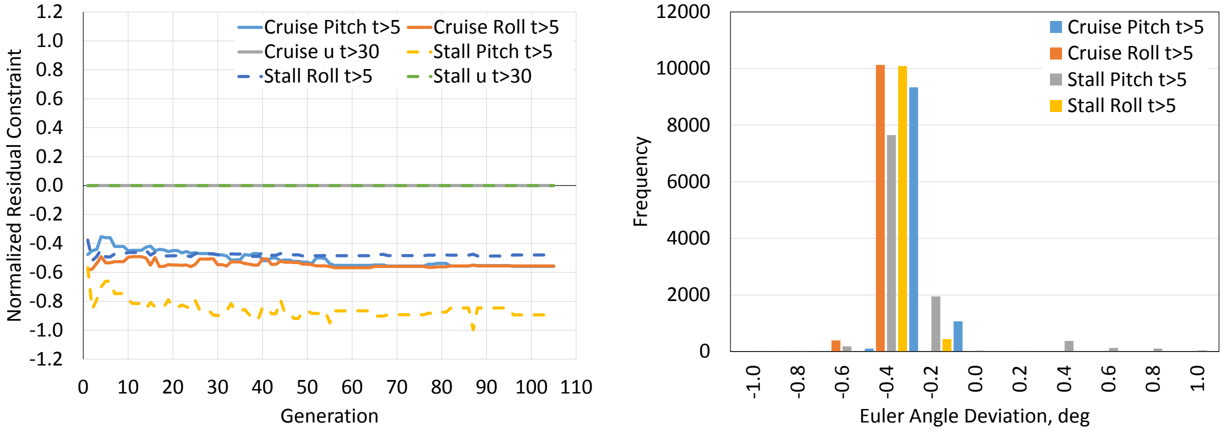

(c) SDynConFreeSM normalized perturbation residual responses.

(d) SDynConFreeSM histogram of perturbation residual responses.

Figure 7.21: SDynConFixSM and SDynConFreeSM configurations perturbation residual responses.

average deflections, were greater in magnitude for the fixed static margin case in the stall flight condition.

Contrary to the elevator discrete gust response, the maximum effective elevator deflections in response to perturbations were large, with many designs exceeding the allowed effective angle of attack as indicated in Fig. 7.23. The airspeed perturbation was the most constraining disturbance in the sizing of the horizontal stabilizer, with many designs significantly exceeding the upper limit of 12.2 degrees, shown in Figs. 7.23(b) and 7.23(d). The normalized effective angle plots indicate that the initial best designs violated this constraint,

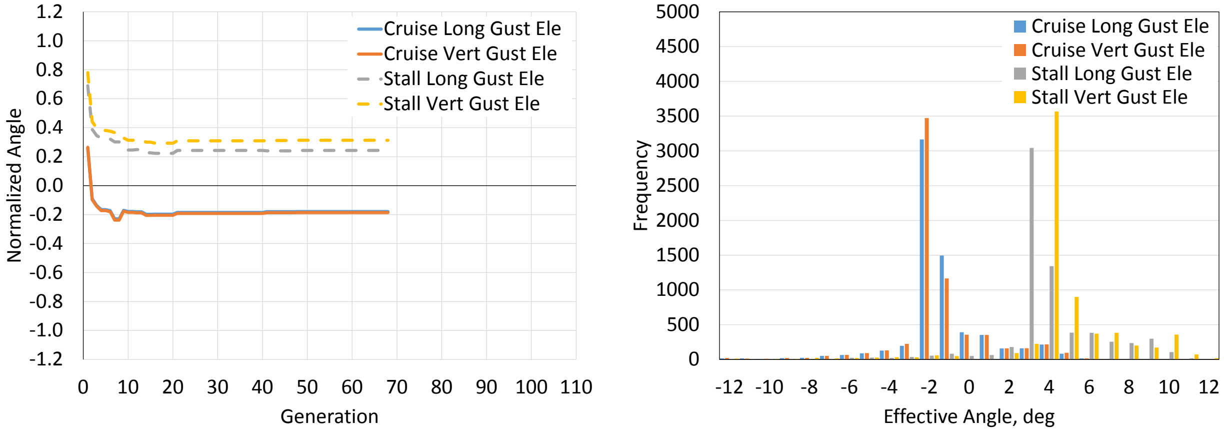

(a) SDynConFixSM normalized elevator gust responses.

(b) SDynConFixSM histogram of elevator gust responses.

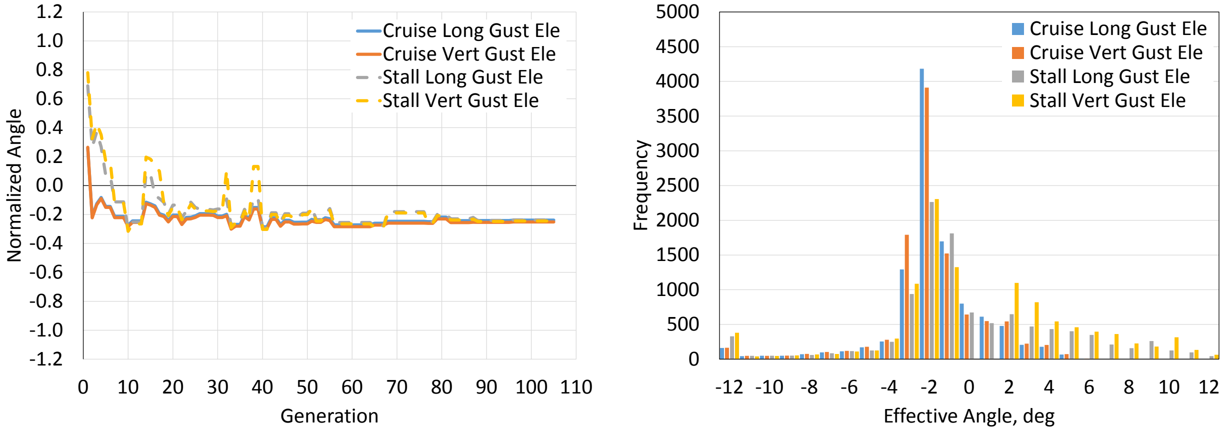

(c) SDynConFreeSM normalized elevator gust responses.

(d) SDynConFreeSM histogram of elevator gust responses.

Figure 7.22: SDynConFixSM and SDynConFreeSM configurations elevator responses to both longitudinal and vertical gusts.

and the optimization had to progress by finding designs that passed this constraint. The pitch perturbation was also approaching the upper constraint limit in both the fixed and free static margin case, with the histogram indicating numerous designs violating the upper constraint. An interesting behavior occurs in the cruise pitch perturbation response of Fig. 7.23(c). As the optimization progressed, the normalized constraint bounced back and forth between plus or minus 0.2. This behavior occurred due to some designs having the elevator response overshoot being more extreme than the initial deflection. As both extremes were similar in magnitude, some designs had a positive value of the constraint while

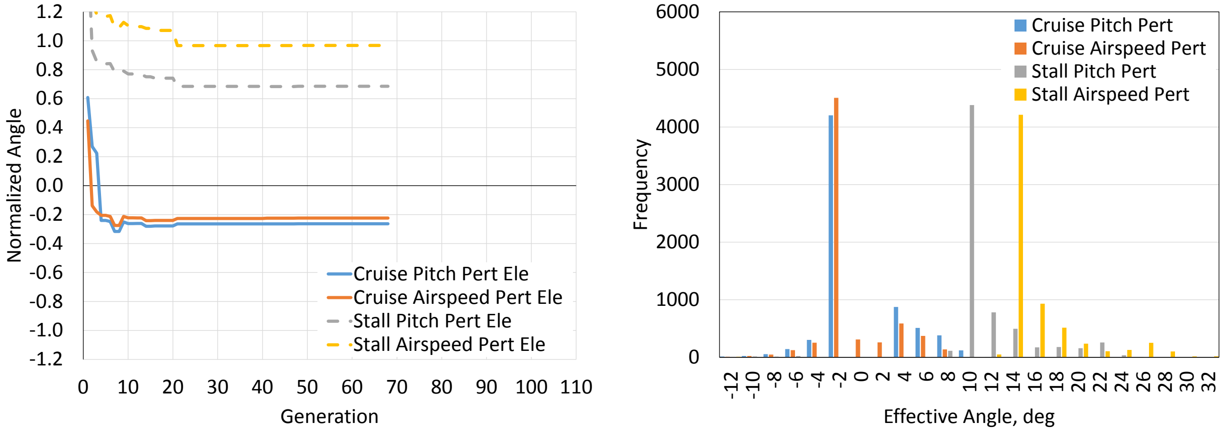

(a) SDynConFixSM normalized elevator responses to perturbations.

(b) SDynConFixSM histogram of elevator responses to perturbations.

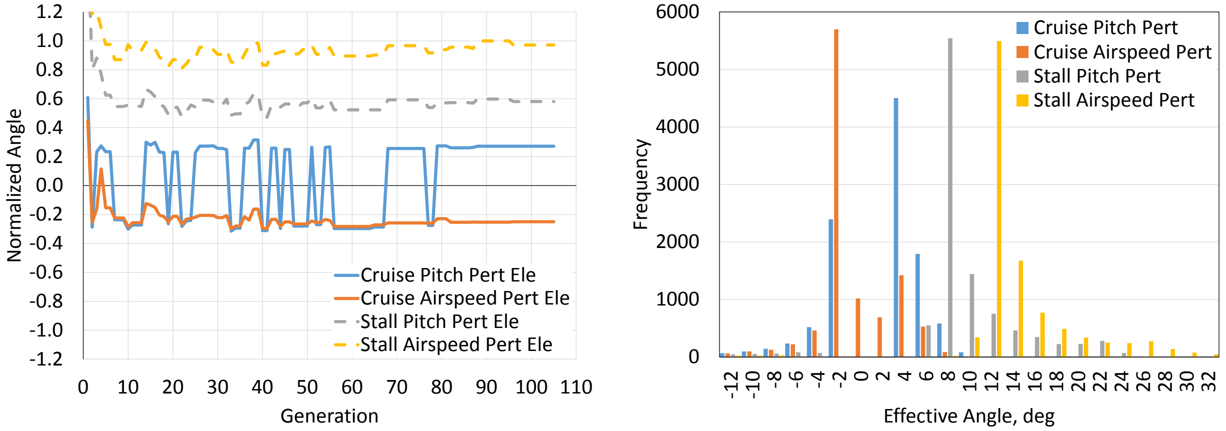

(c) SDynConFreeSM normalized elevator responses to perturbations.

(d) SDynConFreeSM histogram of elevator responses to perturbations.

Figure 7.23: SDynConFixSM and SDynConFreeSM configurations elevator response to pitch and airspeed perturbations.

others had a negative value of the constraint, resulting in the back and forth behavior of Fig. 7.23(c).

Examining the takeoff and maneuver condition static trim constraints, Fig. 7.24, the elevator effective angle of attack increased as the SDynConFreeSM optimization case progressed, whereas it remained nearly constant throughout the SDynConFixSM optimization. In both cases, the takeoff elevator constraint was active. The histograms of Figs. 7.24(b) and 7.24(d) show that nearly all the designs remained within the constraints with the SDynConFixSM case having more designs near the -11.4 degree constraint. As discussed previously, the

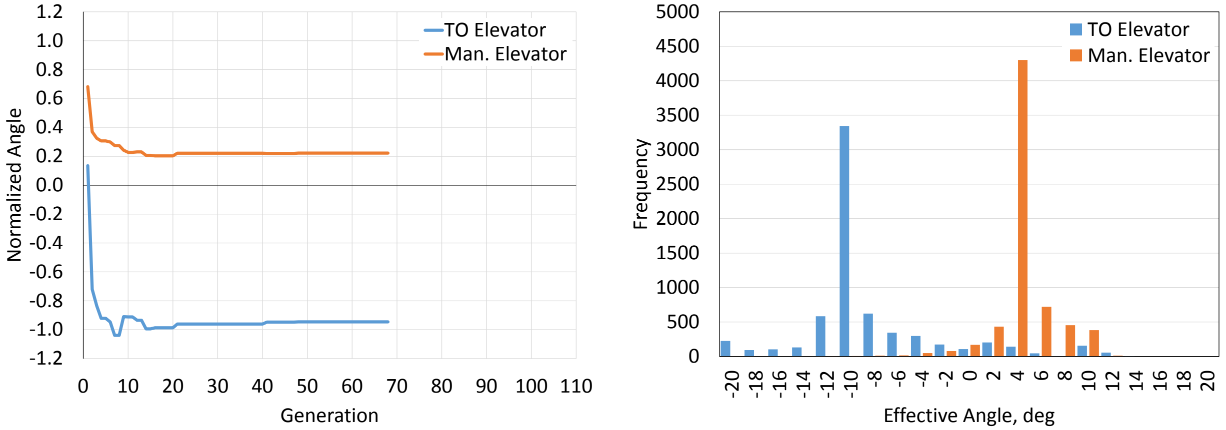

(a) SDynConFixSM normalized elevator deflections. (b) SDynConFixSM histogram of elevator deflections.

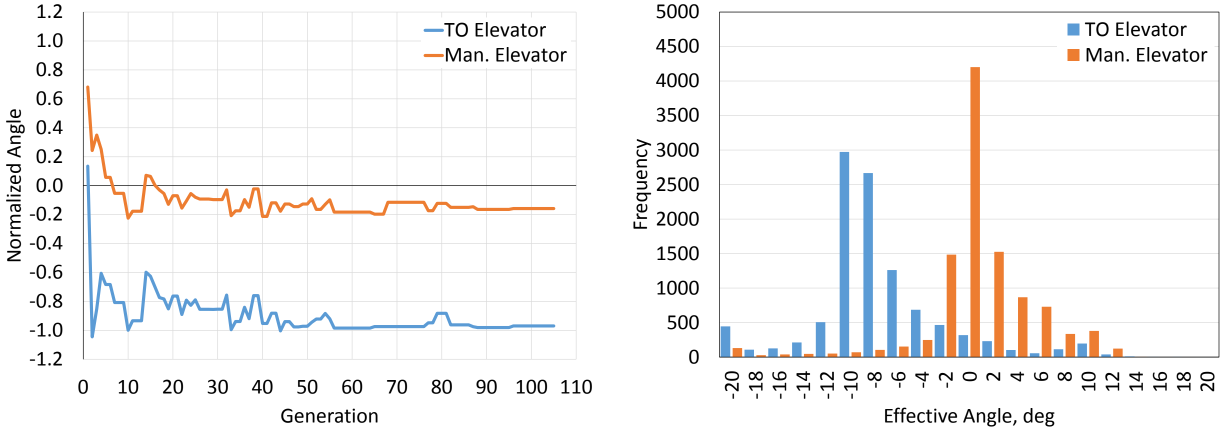

(c) SDynConFreeSM normalized elevator deflections. (d) SDynConFreeSM histogram of elevator deflections.

Figure 7.24: SDynConFixSM and SDynConFreeSM configurations trim deflection angles to the takeoff and maneuver flight conditions.

maneuver condition resulted in positive lift on the horizontal stabilizer giving a positive effective angle of attack. However, neither the SDynConFixSM nor the SDynConFreeSM cases were constrained by the maneuver elevator constraint, with very few designs in the SDynConFreeSM case that resulted in angles greater than 12.2 degrees.

Similar to the static trim constraint optimization cases described in Section 7.2, the one engine inoperative flight condition of Fig. 7.25 was a driving constraint on the vertical stabilizer sizing of the fixed and free static margin design optimizations. All aileron deflections, as before, were no greater than two degrees. Throughout the design optimization, shown in

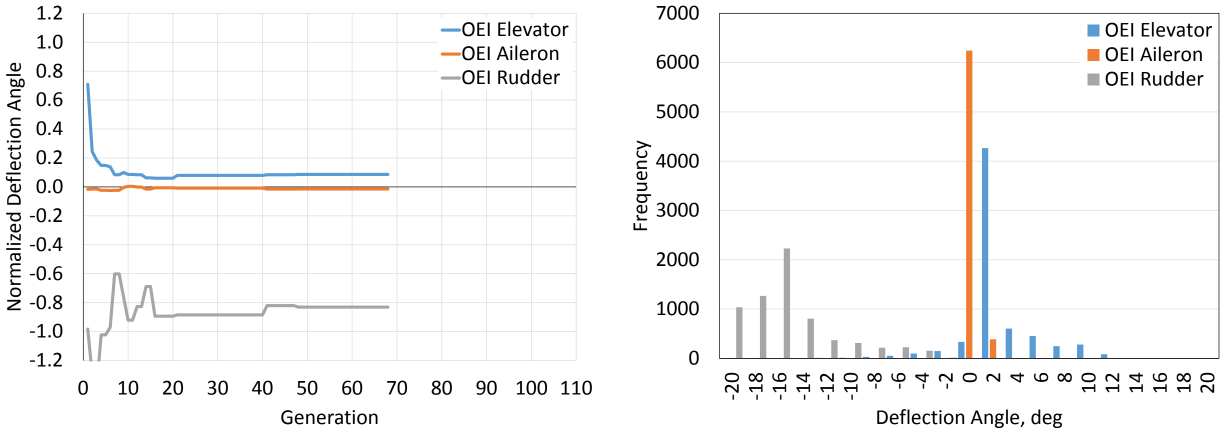

(a) SDynConFixSM normalized OEI deflections. (b) SDynConFixSM histogram of OEI deflections.

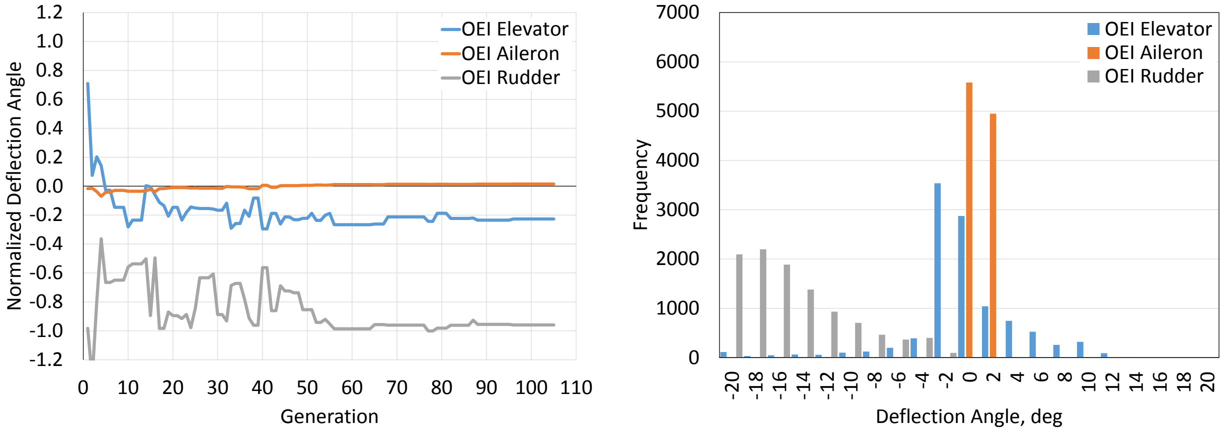

(c) SDynConFreeSM normalized OEI deflections. (d) SDynConFreeSM histogram of OEI deflections.

Figure 7.25: SDynConFixSM and SDynConFreeSM configurations trim deflection angles in a one engine inoperative flight condition.

the normalized deflection angles and histograms, the rudder deflection angles were within the constraint limits of plus or minus 20 degrees, but many designs were evaluated near the constraint. The best design rudder deflection angle increased throughout the optimization in the SDynConFreeSM optimization case reaching the constraint limit after 60 generations. Even though the total configuration geometry changed when the dynamic response constraints were added, the one engine inoperative trim constraint was the driving constraint behind the sizing of the vertical stabilizers.

Performing a multidisciplinary design optimization, including both static trim and dynamic response constraints, produced feasible designs that included stability and control considerations. Shown in Tables 7.12 and 7.13, none of the constraints were violated for either the SDynConFixSM or SDynConFreeSM optimal designs. The elevator effective angle of attack was nearing the negative constraint at takeoff while the rudder was having large deflection angles in the one engine inoperative condition. The lateral discrete gust placed a large demand on the aileron and rudder in the optimal SDynConFreeSM stall flight condition, but remained within the 20 degree deflection limit. Both the optimal designs easily met the roll residual constraint in both the cruise and stall flight conditions with the heavier roll weighting. The pitch residual performance was much improved from the static trim constraint optimization cases.

Table 7.12: SDynConFixSM and SDynConFreeSM configurations static trim constraints.

Condition	Response Type	SDynConFixSM	SDynConFreeSM
OEI	Aileron	-0.28	0.28
	Rudder	-16.62	-19.62
Takeoff	Elevator	-10.78	-11.23
Maneuver	Elevator	2.71	-1.66

Table 7.13: SDynConFixSM and SDynConFreeSM configurations dynamic response performance.

Condition	Response Type	SDynConFixSM		SDynConFreeSM	
		Cruise	Stall	Cruise	Stall
Discrete Gust	Aileron	0.00	8.36	0.00	-17.36
	Rudder	-2.39	-3.23	-3.73	17.59
	Elevator (Long)	-2.04	2.97	-2.72	1.19
	Elevator (Vert)	-2.12	3.82	-2.87	-1.31
Turbulence	RMS Pitch	0.07	0.72	0.19	0.96
	RMS Roll	1.31	0.99	1.72	1.24
	RMS Yaw	0.39	0.84	0.45	0.86
Perturbation	Aileron	0.00	12.06	0.00	12.45
	Rudder	5.98	5.32	5.84	5.46
	Elevator (Pitch)	-3.00	8.36	3.31	7.31
	Elevator (Speed)	-2.55	11.81	-2.84	12.11
Residual	Pitch	-0.23	-0.23	-0.28	-0.44
	Roll	-0.53	-0.47	-0.56	-0.48
	Speed	0.00	0.00	0.00	0.00

It was expected that the vertical gust would be sufficient to capture the largest deflections placed on the elevator, and this appears to be the case. Table 7.13 shows that the longitudinal gust, for both the SDynConFixSM and SDynConFreeSM cases, placed a lower demand on the elevator in both the cruise and stall flight conditions. Although small in difference, this indicates the longitudinal gust could be excluded in the analysis, reducing both the computation time and number of design constraints.

As the residual roll angle was consistently violated by the optimization cases not including the dynamic response constraints, and an additional roll angle weighting was added. Roll angle time response plots have been included in Fig. 7.26. The roll response was very similar for both configurations in the cruise and stall flight conditions. As indicated in Table 7.13, all cases had a roll residual angle within one degree of steady state five seconds after the initial perturbation. This can be seen in Fig. 7.26, as all the response lines were well above the intersection of the lower allowable constraint and the five second vertical dashed line. With the heavier weighting on the roll angle, the roll response has little to no overshoot in response to the perturbation, giving an excellent roll response.

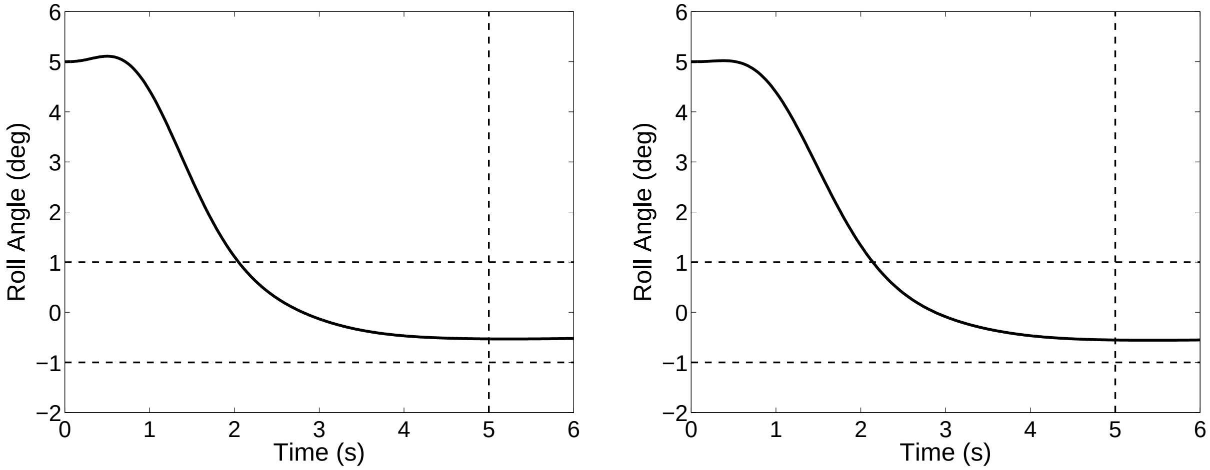

(a) SDynConFixSM configuration cruise condition. (b) SDynConFreeSM configuration cruise condition.

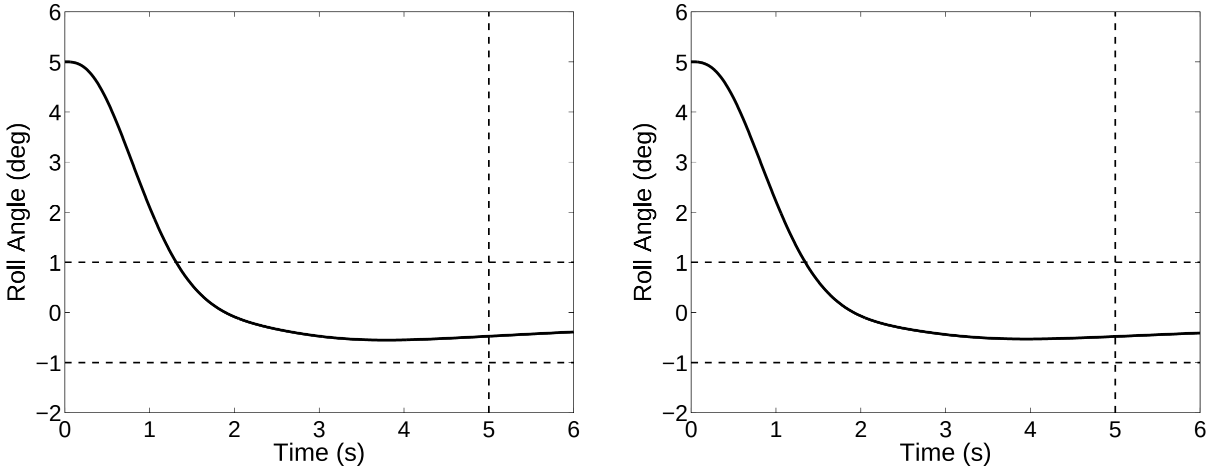

(c) SDynConFixSM configuration stall condition. (d) SDynConFreeSM configuration stall condition.

Figure 7.26: SDynConFixSM and SDynConFreeSM configurations roll residual time responses in the cruise and stall conditions. The horizontal dashed lines indicate the maximum allowed deviations after five seconds, highlighted with the vertical dashed line.

Chapter 8

Summary and Conclusions

A methodology for integrating stability and control into the conceptual design process, specifically focusing on multidisciplinary design optimization, was presented. Focus was placed on creating a controller that guaranteed closed-loop stability, providing system robustness during an optimization, while eliminating the necessity of the user being intimately involved with the controller design. This research broke away from the traditional military specifications on handling qualities, MIL-F-8785C and MIL-STD-1797A, where linear dynamic modes must be identified, and requirements on mode natural frequencies and damping specified. Instead, this research used SAE-AS94900, which specified requirements on the system state response to perturbations, continuous turbulence, and discrete gusts. This eliminated the need to identify each linear mode during an optimization, which is especially important for configurations, both with and without closed-loop control, where the traditional linear modes may not be present. Relying on the state response allowed for quantitative analysis of the system handling qualities, perfect for integration into a system optimization. The atmospheric disturbances and perturbations, along with static control system constraints, allowed for the geometric sizing of the system using actual system response requirements instead of the empirical tail volume coefficients often used during conceptual design. Key contributions of this research are summarized as:

- Integrated stability and control into the conceptual design process in ModelCenter® using AVL, MATLAB®, and NASA's Flight Optimization System (FLOPS)
- Implemented a linear quadratic regulator (LQR) controller into the conceptual design process with gains selected using optimal control techniques

- Applied both static trim and dynamic response constraints to a multidisciplinary design optimization that negated the need to identify specific linear modes, focusing on state variable responses

- Performed a multidisciplinary design optimization integrating mission performance using FLOPS, aerodynamic analysis using AVL, and stability and control with a linear quadratic regulator stressed by atmospheric disturbances and perturbations

Optimal control theory implementing a time-weighted linear quadratic regulator (LQR) was used for the closed-loop control design. The LQR methodology employed combined multiple techniques described in Ref. [4], but the complete derivation of the LQR technique used was described in Section 4.2, with additional information and derivations provided in Appendices B and C. The set of fully-coupled, linearized perturbation equations used were developed in conjunction with this research. Thrust terms and negligibly small terms were assumed to be zero, but greater knowledge of the system aerodynamic and thrust models will only improve the accuracy of the system dynamics. Increased accuracy in the information provided to the methodology will improve results as the technique is subject to the quality of information given to it. Sections 6.1 and 6.2 described the verification of the system dynamics and atmospheric disturbances using multiple publicly available resources including Refs. [15, 29, 30, 78].

A Cessna 182T model was used as a test case throughout the methodology and analysis development. The geometry was taken from Ref. [15] and used to develop an AVL model. Techniques for modeling the fuselage and propeller effects were discussed, and the AVL model was validated using known stability data, presented in Refs. [15, 34]. A simple trade study was performed by varying the horizontal and vertical tail areas, which verified that the controller, the atmospheric disturbances, and the perturbations were working as expected.

Described in Section 3.1, the D8.2b geometry was defined and used in the creation of OpenVSP and AVL models. Changes from the D8.1 geometry, reported in Ref. [10], were discussed. Experimental data for the D8.2b geometry was unavailable, so Cart3D, an inviscid

Euler solver, was used as validation of the D8 AVL model. From the aerodynamic validation study, modifications to the AVL model were made to better match the aerodynamic results of the Euler analysis. The modified AVL model was then used in a multidisciplinary design optimization. NASA's Flight Optimization System (FLOPS) was used to size the D8 and estimate the weights, mission profile, and performance, and was integrated using ModelCenter with the flight dynamics and controls analysis and AVL. Phoenix Integration's genetic algorithm, Darwin, was used in the system optimization, running five optimization cases, each with an increasing number of design variables and constraints.

Overall, using fixed tail volume coefficients produced the expected design; the tail moment arm was maximized to minimize the stabilizer area, resulting in reduced viscous drag and structural weight. This was accomplished by moving the wing apex to the forward most limit and sweeping the vertical stabilizer to the upper most limit, shifting the horizontal stabilizer to the most aft location. Adding the static trim constraints at takeoff, maneuver, and one engine inoperative flight conditions allowed the stabilizers to be sized using the static trim constraints instead of a fixed tail volume coefficient. This resulted in the wing apex shifting aft and the horizontal and vertical stabilizer areas decreasing dramatically, achieving a minimum total fuel burn and gross weight in the free static margin with static trim constraints optimization case, StaticConFreeSM. Takeoff trim and OEI constrained the elevator and rudder sizes, respectively.

Using only the static constraints produced unreasonably small stabilizer areas that were increased with the addition of the dynamic constraints, placing a greater demand on the control system and stabilizer sizing. Nose-up trim at takeoff remained a constraining flight condition for the elevator, but the airspeed perturbation also became an active constraint. The elevator size was increased for the cases optimized with the dynamic constraints compared to the static trim constraints only. One engine inoperative remained the active sizing constraint on the rudder even with the dynamic constraints added. Takeoff and landing field lengths were active constraints for all design optimizations except SDynConFreeSM, specifically sizing the wing area and static thrust.

It was surprising that in the cases where static margin was allowed to be a free variable, the optimizer consistently chose to increase the static margin to take advantage of the natural stability benefits while decreasing the horizontal and vertical stabilizer areas. This indicated that the benefits from relaxed static stability, within the design space specified, were less than the weight and viscous drag benefits of downsizing the tails and shifting the neutral point/center of gravity, resulting in increased static margin. If center of gravity can be shifted as desired, the stabilizer areas should be decreased and static margin used to provide additional stability to take full advantage of the weight and viscous drag reductions.

The residual pitch and roll angles after a system perturbation were active constraints in the design space, indicating that the design was seeking more authority from the controller. The weighting on the controller was selected to have an unbiased weighting on the state variable error; one degree of error was weighted the same as one foot per second of error. An additional weighting on the roll angle had to be added to improve the optimized solutions. It is hypothesized that additional performance gains could be achieved through adjustments to the LQR weighting matrices and time weighting. Adjusting the weighting matrices could allow a controller to have increased authority where needed, alleviating some of the active constraints.

It was expected that the static trim constraints would have a greater impact on the horizontal and vertical stabilizer areas. In the one engine inoperative case, the engines were embedded in the fuselage, placing them near the center line. This resulted in a small moment arm in an engine-out case, requiring very little rudder authority. This allowed the twin-vertical stabilizers to be decreased far more than expected. It would be interesting to see how the OEI static trim constraint would affect the design with a podded or wing-mounted engine configuration.

Nose-up trim during the takeoff roll was far less constraining than anticipated on the optimization cases with only static trim constraints. The optimizer manipulated the geometries to place the neutral point and center of gravity in such a way as to have the wing lift counteract the nose-down pitching moment, reducing the required load to lift the nose wheel at the end of the takeoff roll. This was enabled by the center of gravity being dependent upon the neutral point placement and specified static margin. This flexibility in the placement is not usually feasible in conventional configurations but may be enabled in future concepts with large weight and density subsystems, such as batteries.

Reviewing the disturbances used to stress the control system, it was seen that the RMS turbulence was never an active constraint in the design space. It was thought that the turbulence analysis would provide a unique constraint on the design space, eliminating designs that otherwise would have been acceptable. This did not occur. No cases evaluated ever had an RMS value over the constraint. It is possible the turbulence constraint could become active if a higher turbulence intensity was used, but this may become more of a structural problem than a stability and control problem.

As anticipated, the cruise flight condition had little impact on the design space. When the dynamic constraints were not applied, the cruise condition roll residual was greater in the cruise condition than the stall condition. When the dynamic constraints were applied, both the stall and cruise residuals met the constraint and were close in value. It is believed that the stall residual constraint would capture the influence of the cruise roll residual constraint, eliminating the need to perform a dynamic analysis at the cruise condition. This would allow the addition of a new flight condition, perhaps a descent condition, that could add a new set of constraints on the design space without increasing the computation time.

Reviewing the results, it is clear that going from fixed tail volume coefficients to static trim constraints, and then to static trim and dynamic constraints, drastically changed the optimal designs. Wing area and static thrust were nearly unchanged between the different optimization cases as they were driven by the takeoff and landing constraints, applied equally to each optimization case. All other design variables changed dramatically as stability and control constraints were added to the design space. This shows the importance of including stability and control early in conceptual design, allowing it to influence the design space, thus taking advantage of the benefits it can provide instead of introducing penalties late in the design phase. The SDynConFreeSM case had reduced fuel burn compared to the baseline D8.2b, and the SDynConFreeSM configuration boasts an unblemished record of passing all constraints. It could be argued that the baseline design could pass the dynamic constraints with a controller redesign, as no static trim constraints were violated. However, the analysis performed here indicated that a horizontal stabilizer upload was required at the nose-up takeoff condition, even at the forward center of gravity position. This indicated that as the airplane accelerates down the runway and lift production increases, the natural tendency would be for an uncommanded pitch rotation counteracted only by a nose-down control input. As currently designed, this is perceived as a safety concern.

Overall, including the dynamic constraints beyond the static trim constraints placed a great influence on the design space while showing that fixed tail volume coefficients and static trim constraints do not appropriately size the stabilizers. The dynamic constraints resulted in increased fuel burn compared to the StaticConFixSM and StaticConFreeSM cases, but the static trim only constraint cases produced infeasible designs when looking at stability and control considerations. The fuel burn for the SDynConFreeSM case was reduced compared to the baseline and fixed tail volume cases with additional reductions anticipated through adjustments in the LQR weighting matrices. Including stability and control in conceptual design only benefits the design, allowing for design space exploration in ways not possible when using the typical conceptual design disciplines.

Chapter 9

Future Work

Two studies that could be performed using the methodology as presented include an exploration of the system sensitivity to the system disturbances and an optimization study. The methodology presented used moderate disturbances in the discrete gust and continuous turbulence analysis, as specified in SAE-AS94900 [39]. The disturbance level increases as the probability of exceedance decreases, going all the way to an extreme disturbance. It would be interesting to see if the optimal designs shift with the introduction of higher disturbance intensities. As the disturbance probability decreases, the disturbance shifts to a more structural concern than a stability and control concern, assuming the disturbance does not cause an upset condition. If the configurations remain largely unchanged, the large disturbances should be considered mainly as a structural problem. However, if the configurations change drastically, considerations may have to be made to include these large disturbances in the configuration design or to resolve any upset potential in future detailed controller design.

An optimization study would give greater confidence that the optimal solutions found were indeed the solutions that minimize fuel burn while meeting the applied constraints. Modifications to the population size, crossover, and mutation percentage would all have to be explored and any differences in results compared. This optimization study would require long computation times but would give greater confidence in the optimal solutions obtained. A current shortcoming is the system memory required for this type of optimization study, which results in halted optimizations from a combination of a large population size and a large number of generations.

Improvements to any analysis methodology can always be made by incorporating higher-order analysis methods, given the increased computation time is acceptable and the higher-order tools correlate to a higher fidelity solution. This research focused on maintaining a conceptual design level of configuration knowledge, catering each component to maintain that level of detail. Future capabilities that would increase the capability of the discussed methodology include:

- Weight and balance calculations with higher-order mass moment of inertia calculations
- Increase the number of flight conditions used to stress the configuration and flight control system placing additional constraints on the design space
- Include elements of the performance output weighting matrix, W, and the control inputs weighting matrix, R, as design variables in the optimization

The center of gravity was intentionally used as a dependent variable of neutral point location and static margin as part of the design space exploration in order to understand the system sensitivities. However, center of gravity is not a component that can be simply placed. The aircraft components and subsystems must be placed and configured to shift the center of gravity to the desirable position, making static margin dependent upon the configuration and subsystem layout. Static margin would become an optimization constraint instead of a design variable, restricting the allowable distance between the neutral point and center of gravity. This would require a weight and balance buildup needing either detailed placement of each component and subsystem or empirical data on each subsystem's center of gravity.

It has been emphasized that including stability and control in the conceptual design process is beneficial to the configuration design. A challenge of including flight dynamics early in the design is the detailed information required for accurate analysis, detail not typically available in conceptual design. Calculating highly accurate mass moments of inertia requires detailed component layouts and weight statements, much of which is unknown, undecided, or fluidly changing. Implementing a method of calculating reasonably accurate mass moments of inertia using conceptual design level details would be extremely beneficial to the methodology presented. Detailed design information would be unknown, so it is envisioned the calculations would use a semi-empirical methodology. Conventional and unconventional configurations, ranging from hybrid wing bodies to distributed propulsion concepts, would have to be included to give the greatest flexibility in exploring the design space.

Discussed previously was the possibility of removing or replacing the dynamic analysis of the cruise flight condition, as it was not uniquely constraining on the design space. Any constraint violations in the cruise condition were also captured by the stall condition, making the cruise condition a potential unnecessary analysis. Adding a new flight condition to the analysis, such as a descent condition with flaps in the landing configuration, may impose new constraints on the design space. If computation time is not a concern, the new flight condition can simply be added to the current analysis with an additional set of constraints. This may provide a challenge to the optimization because currently a large number of constraints exist relative to a small number of design variables. In this case, there were 37 constraints to 9 design variables (8 if static margin was fixed). The other option would be to replace the cruise condition with a new flight condition such as the descent flight condition.

The cruise condition was only constraining on the design space in the pitch and roll residual constraints. It is hypothesized that the pitch and roll residual constraints could be alleviated through a modification of the LQR weighting matrices, placing greater weight on the pitch and roll states. The LQR weights were originally chosen as an unbiased weighting on each of the states as it was unknown what influence particular weights would have on each design. It is desired to add elements of the LQR weighting matrices as design variables in the design optimization, giving greater controller design authority to the optimizer. It is envisioned that this expansion could provide additional benefits to the methodology presented, potentially improving the optimal designs and fuel burn reductions.

Even though minimization of analysis run time was a point of emphasis, further improvements could be made to reduce the total system optimization time. The controller methodology and atmospheric disturbances were all coded using MATLAB®, which requires licensing and additional overhead in ModelCenter®. Using a compiled language, such as Fortran or C++, would allow for ModelCenter to simply call the executable without having to obtain a license, and performance improvements from a compiled versus interpreted language could be obtained.

Replacing the vortex lattice aerodynamic analysis with a panel code would increase the order of the aerodynamic analysis, better capturing the actual geometry being modeled. A risk of using a panel code is the potential for increased computation time with the model being overly sensitive to panel size, especially as the configuration deviates from the baseline design during an optimization. Care would have to be taken to ensure the surface mesh generation was adequately automated to provide reasonable results (being better than the vortex lattice). This would be especially important for configurations that deviate from the traditional tube-and-wing concepts with conventional propulsion systems.

Even though many configuration concepts are being explored for the future generation advanced air transport, concepts for the future 737 class air transport remain in the tube-and-wing configuration [10,83,84]. These advanced concepts work well with the current methodology as traditional control effectors were used, including ailerons, rudders, and an elevator. In these configurations the longitudinal and lateral/directional controls are mostly decoupled, meaning the elevator is used primarily for longitudinal control and the ailerons and rudder for lateral/directional control. As currently implemented, the gain matrix contains all the cross-coupled terms in a 36-element matrix, resulting in a large number of variables minimized by the simplex algorithm. In the tube-and-wing concepts, the lateral/directional controls have negligible impact on the longitudinal controls. The gain matrix could possibly be reduced in size, removing the insignificant terms and, thus, reducing the number of variables in the simplex algorithm for minimizing the LQR performance index. This should accelerate the LQR gain calculation convergence, saving computation time throughout the entire optimization.

Decoupling the gain matrix would only be applicable for concepts with decoupled controls. For current military aircraft such as the F-22 and F-35, this would not work as their flight control systems actuate numerous effectors in response to a given input command, requiring cross-coupled control gains. Future air transport concepts, such as a blended wing body, will employ this control structure as well, requiring an expansion of the equations of motion used here. Non-unique control deflection solutions for redundant controls will also have to be addressed as researched by Garmendia in Ref. [85].

Distributed propulsion and boundary layer ingestion may require the equations of motion to be modified to capture the unique aerodynamic-propulsion coupling provided by those technologies. Their effect on the concept stability control is not known, making historical data useless for conceptual design of stabilizing surfaces. The methodology presented here, with the appropriate system sensitivities captured in the equations of motion and stability derivatives, would be perfect for assessing the stability and control characteristics of advanced concepts employing these technologies. The challenge would be in verifying and validating that the enhanced equations of motion accurately capture the complex coupling propulsion-airframe effects.

Bibliography

[1] Raymer, D. P., *Aircraft Design: A Conceptual Approach*, 4th ed., AIAA Education Series, American Institute of Aeronautics and Astronautics, Reston, VA, 2006.

[2] Roskam, J., *Airplane Design, Pt. II*, DARcorporation, Ottawa, KS, 1997.

[3] Nicolai, L. M. and Carichner, G. E., *Fundamentals of Aircraft and Airship Design: Volume I*, AIAA Education Series, American Institute of Aeronautics and Astronautics, Reston, VA, 2010.

[4] Stevens, B. L. and Lewis, F. L., *Aircraft Control and Simulation*, 2nd ed., John Wiley & Sons, Inc., Hoboken, NJ, 2003.

[5] Pamadi, B. N., *Performance, Stability, Dynamics, and Control of Airplanes*, 2nd ed., AIAA Education Series, American Institute of Aeronautics and Astronautics, Reston, VA, 2004.

[6] Coleman, G. and Chudoba, B., "A Generic Stability and Control Tool for Conceptual Design: Prototype System Overview," *AIAA Aerospace Sciences Meeting and Exhibit*, Reno, NV, 2007, AIAA-2007-659.

[7] Perez, R. E., Liu, H. H. T., and Behdinan, K., "Multidisciplinary Optimization Framework for Control-Configuration Integration in Aircraft Conceptual Design," *Journal of Aircraft*, Vol. 43, No. 6, 2006, pp. 1937–1947.

[8] MIL-F-8785C, "U.S. Dept. of Defense Military Specification: Flying Qualities of Piloted Airplanes," Tech. rep., Nov. 1980.

[9] Department of Defense, *Flying Qualities of Piloted Aircraft*, January 1990, MIL-STD-1797A.

[10] Greitzer, E. M. et al., "N+3 Aircraft Concept Designs and Trade Studies, Final Report: Volume 1," Tech. Rep. CR-2010-216794/VOL1, National Aeronautics and Space Administration, 2010.

[11] Ng, L. W. T. and Willcox, K. E., "A Multifidelity Approach to Aircraft Conceptual Design Under Uncertainty," *10th AIAA Multidisciplinary Design Optimization Conference*, American Institute of Aeronautics and Astronautics, National Harbor, MD, Jan. 2014, AIAA-2014-0802.

[12] Uranga, A., Drela, M., Greitzer, E. M., Tetchener, N. A., Lieu, M. K., Siu, N. M., and Huang, A. C., "Preliminary Experimental Assessment of the Boundary Layer Ingestion Benefit for the D8 Aircraft," *52nd Aerospace Sciences Meeting*, American Institute of Aeronautics and Astronautics, National Harbor, MD, Jan. 2014, AIAA-2014-0906.

[13] Pandya, S. A., Huang, A., Espitia, A., and Uranga, A., "Computational Assessment of the Boundary Layer Ingesting Nacelle Design of the D8 Aircraft," *52nd Aerospace Sciences Meeting*, American Institute of Aeronautics and Astronautics, Jan. 2014, AIAA-2014-0907.

[14] McCullers, L. A., "Aircraft Configuration Optimization Including Optimized Flight Profiles," *Proceedings of the Symposium on Recent Experience in Multidisciplinary Analysis and Optimization*, Apr. 1984, NASA CP 2327.

[15] Napolitano, M. R., *Aircraft Dynamics: From Modeling to Simulation*, John Wiley & Sons, Inc., Hoboken, NJ, 2012.

[16] Cessna Aircraft Company, Wichita, KS, *Pilot's Operating Handbook and FAA Approved Airplane Flight Manual: Skylane*, December 2007.

[17] Perez, R. E., Liu, H. H. T., and Behdinan, K., "Flight Dynamics and Control Multidisciplinary Integration in Aircraft Conceptual Design Optimization," *AIAA/ISSMO Multidisciplinary Analysis and Optimization Conference*, American Institute of Aeronautics and Astronautics, Albany, NY, 2004, AIAA-2004-4435.

[18] Perez, R. E., Liu, H. H. T., and Behdinan, K., "Relaxed Static Stability Aircraft Design via Longitudinal Control-Configured Multidisciplinary Design Optimization Methodology," *Canadian Aeronautics and Space Journal*, Vol. 52, No. 1, 2006, pp. 1–14.

[19] Chudoba, B. and Smith, H., "A Generic Stability and Control Methodology for Novel Aircraft Conceptual Design," *AIAA Atmospheric Flight Mechanics Conference and Exhibit*, Austin, TX, 2003, AIAA-2003-5388.

[20] Cabral, L. V. and Paglione, P., "Conceptual Design of Families of Aircraft Using Multi Objective Design Optimization Theory and Genetic Algorithm Techniques," *6th World Congresses of Structural and Multidisciplinary Optimization*, Rio de Janeiro, 2005.

[21] Morris, C. C., Sultan, C., Allison, D. L., Schetz, J. A., and Kapania, R. K., "Towards Flying Qualities Constraints in the Multidisciplinary Design Optimization of a Supersonic Tailless Aircraft," *AIAA Aviation Technology, Integration, and Operations Conference*, Indianapolis, IN, 2012, AIAA-2012-5517.

[22] Boyd, S., Ghaoui, L. E., Feron, E., and Balakrishnan, V., *Linear Matrix Inequalities in System and Control Theory*, Vol. 15 of *Studies in Applied and Numerical Mathematics*, Society for Industrial and Applied Mathematics (SIAM), 1994.

[23] Kaminer, I. I., Howard, R. M., and Buttrill, C. S., "Development of Closed-Loop Tail-Sizing Criteria for a High Speed Civil Transport," *Journal of Aircraft*, Vol. 34, No. 5, 1997.

[24] Morris, C. C., Sultan, C., Schetz, J. A., and Kapania, R. K., “Variance Constrained Flying Qualities Metrics for Conceptual Design Feasibility Studies,” *AIAA Guidance, Navigation, and Control Conference*, Boston, MA, 2013, AIAA-2013-4927.

[25] Richardson, T. S., Beaverstock, C., Isikveren, A., Meheri, A., Badcock, K., and Ronch, A. D., “Analysis of the Boeing 747-100 using CEASIOM,” *Progress in Aerospace Sciences*, Vol. 47, 2011, pp. 660–673.

[26] Rizzi, A., Eliasson, P., McFarlane, C., Goetzendorf-Grabowski, T., and Vos, J., “Virtual-Aircraft Design & Control of TransCruiser - a Canard Configuration,” *AIAA Atmospheric Flight Mechanics Conference*, Toronto, Ontario, Canada, 2010, AIAA-2010-8245.

[27] von Kaenel, R., Oppelstrup, J., Goetzendorf-Grabowski, T., Ghoreyshi, M., Cavagna, L., and Bérard, A., “CEASIOM: Simulating Stability & Control with CFD/CSM in Aircraft Conceptual Design,” *International Congress of the Aeronautical Sciences*, Anchorage, AK, 2008.

[28] Rizzi, A., “Modeling and Simulating Aircraft Stability & Control - the SimSAC Project,” *AIAA Atmospheric Flight Mechanics Conference*, Toronto, Ontario, Canada, 2010, AIAA-2010-8238.

[29] Etkin, B., *Dynamics of Atmospheric Flight*, Dover Publications, Inc., Mineola, NY, 2000.

[30] Roskam, J., *Flight Dynamics of Rigid and Elastic Airplanes*, Jan Roskam, 1973.

[31] Nelson, R. C., *Flight Stability and Automatic Control*, 2nd ed., McGraw-Hill Companies, Inc., 1998.

[32] Etkin, B. and Reid, L. D., *Dynamics of Flight*, 3rd ed., John Wiley & Sons, Inc., Hoboken, NJ, 1996.

[33] Raymer, D. P., *Aircraft Design: A Conceptual Approach*, 4th ed., AIAA Education Series, American Institute of Aeronautics and Astronautics, Reston, VA, 2006, p. 502.

[34] Roskam, J., *Flight dynamics and Automatic Flight Controls Pt. 1*, DARcorporation, 2011.

[35] Cessna Aircraft Company, Wichita, KS, *Specification and Description: Exhibit “A”*, January 2012.

[36] Kalman, R. E., “On the General Theory of Control Systems,” *Automatic and Remote Control (Proc. IFAC Moscow 1960)*, Vol. I, Butterworth, London, 1961, pp. 481–492.

[37] Levine, W. and Athans, M., “On the Determination of the Optimal Constant Output Feedback Gains for Linear Multivariable Systems,” *IEEE Transactions on Automatic Control*, Vol. AC-15, No. 1, February 1970, pp. 44–48.

[38] Cook, M. V., *Flight Dynamics Principles: A Linear Systems Approach to Aircraft Stability and Control*, 3rd ed., Elsevier Aerospace Engineering Series, Elsevier Ltd., 2013.

[39] SAE International, *Aerospace - Flight Control Systems - Design, Installation, and Test of Piloted Military Aircraft, General Specification For*, July 2007, SAE-AS94900.

[40] Etkin, B., "A Theory of the Response of Airplanes to Random Atmospheric Turbulence," *Journal of the Aerospace Sciences*, Vol. 26, No. 7, 1959, pp. 409–420.

[41] Etkin, B., "Theory of the Flight of Airplanes in Isotropic Turbulence - Review and Extension," Tech. rep., Advisory Group for Aeronautical Research and Development, Paris, 1961.

[42] Etkin, B., "Turbulent Wind and Its Effect on Flight," *Journal of Aircraft*, Vol. 18, No. 5, 1981, pp. 327–345.

[43] MathWorks, *Von Karman Wind Turbulence Model (Continuous)*, 2014, `http://www.mathworks.com/help/aeroblks/wind.html` [cited 6 February 2014].

[44] Etkin, B., *Dynamics of Flight*, John Wiley & Sons, Inc., 1959.

[45] Chudoba, B. and Cook, M. V., "Identification of Design-Constraining Flight Conditions for Conceptual Sizing of Aircraft Control Effectors," *AIAA Atmospheric Flight Mechanics Conference and Exhibit*, Austin, Tx, 2003, AIAA-2003-5386.

[46] Boeing Commercial Airplane Group, Seattle, WA, *737-800 Airplane Flight Manual*, Jul. 2013.

[47] Drela, M., "XFOIL: An Analysis and Design System for Low Reynolds Number Airfoils," *Conference on Low Reynolds Number Airfoil Aerodynamics*, University of Notre Dame, South Bend, IN, June 1989.

[48] Drela, M. and Giles, M. B., "Viscous-Inviscid Analysis of Transonic and Low Reynolds Number Airfoils," *AIAA Journal*, Vol. 25, No. 10, October 1987, pp. 1347–1355.

[49] Drela, M., "Integral Boundary Layer Formulation for Blunt Trailing Edges," *7th Applied Aerodynamic Conference*, Seattle, WA, August 1989.

[50] Margason, R. J. and Lamar, J. E., "Vortex-Lattice FORTRAN Program for Estimating Subsonic Aerodynamic Characteristics of Complex Platforms," NASA TN D-6142, Feb. 1971.

[51] Lamar, J. E. and Gloss, B. B., "Subsonic Aerodynamic Characteristics of Interacting Lifting Surfaces with Separated Flow around Sharp Edges Predicted by a Vortex-Lattice Method," NASA TN D-7921, Sep. 1975.

[52] Lamar, J. E. and Frink, N. T., "Experimental and Analytical Study of the Longitudinal Aerodynamic Characteristics of Analytically and Empirically Designed Strake-Wing Configurations and Subcritical Speeds," NASA TP-1803, Jun. 1981.

[53] Lamar, J. E. and Herbert, H. E., "Production Version of the Extended NASA-Langley Vortex Lattice FORTRAN Computer Code," NASA TM 83303, Apr. 1982.

[54] Lan, C. E., "A Quasi-Vortex-Lattice Method in Thin Wing Theory," *Journal of Aircraft*, Vol. 11, No. 9, 1974, pp. 518–527.

[55] Miranda, L. R., Elliot, R. D., and Baker, W. M., "A Generalized Vortex Lattice Method for Subsonic and Supersonic Flow Applications," NASA CR-2865, Dec. 1977.

[56] Drela, M. and Youngren, H., "AVL 3.30 User Primer," Aug. 2010, `http://web.mit.edu/drela/Public/web/avl/avl_doc.txt` [cited 13 Feb 2014].

[57] Welstead, J., Reitz, B. C., and Crouse, Jr., G. L., "Modeling Fuselage Aerodynamic Effects in Aircraft Design Optimization," *AIAA Aerospace Sciences Meeting*, Nashville, TN, 2012, AIAA-2012-0394.

[58] Jacobs, E. N. and Ward, K. E., "Interference of Wing and Fuselage from Tests of 209 Combinations in the NACA Variable-Density Tunnel," NACA TR 540, March 1935.

[59] "737-800 Technical Characteristics," 2014, `http://www.boeing.com/boeing/commercial/737family/pf/pf_800tech.page` [cited 5 August 2014].

[60] Torenbeek, E., *Synthesis of Subsonic Airplane Design*, Delft University Press, Delft, Holland, 1982, p. 531.

[61] "USAF Stability and Control Datcom," Tech. rep., Wright Patterson Air Force Base, 1968.

[62] Lawry, J. G. and Polhamus, E. C., "A Method for Predicting Lift Increment due to Flap Deflection at Low Angles of Attack," Tech. Rep. NACA TN-3911, National Advisory Committee on Aeronautics, 1957.

[63] Olson, E. D., "Semi-emperical Prediction of Aircraft Low-speed Aerodynamic Characteristics," *AIAA Science and Technology Forum and Exposition (SciTech 2015)*, American Institute of Aeronautics and Astronautics, Kissimmee, FL, 2015, (to be published).

[64] Aftosmis, M., Berger, M., Melton, J., and Nemec, M., "Cart3D," Jun. 2004, `http://people.nas.nasa.gov/aftosmis/cart3d_v1.3/cart3Dhome.html` [cited 30 June 2014].

[65] Desktop Aeronautics, Inc., *Cart3D Flow Solver User Manual*, Feb. 2014, `http://docs.desktop.aero/docs/cart3d/index.php/Cart3D_Flow_Solver_User_Manual` [cited 30 June 2014].

[66] Feagin, R. C. and Morrison, W. D., "Delta Method, An Empirical Drag Buildup Technique," Tech. Rep. NASA CR-151971, National Aeronautics and Space Administration, Dec. 1978.

[67] McCullers, L. A., "Flight Optimization System: User's Guide," Release 8.23, Jul. 2011.

[68] Geiselhart, K. A., "A Technique for Integrating Engine Cycle and Aircraft Configuration Optimization," Tech. Rep. NASA CR-191602, National Aeronautics and Space Administration, Feb. 1994.

[69] Geiselhart, K. A., Caddy, M. J., and Morris, Jr., S. J., "Computer Program for Estimating Performance of Air-breathing Aircraft Engines," Tech. Rep. NASA TM 4254, National Aeronautics and Space Administration, May 1991.

[70] Caddy, M. J. and Shapiro, S. R., "NEPCOMP - The Navy Engine Performance Computer Program, Version I," Tech. Rep. NADC-74045-30, Naval Air Development Center, Apr. 1975.

[71] Berton, J., "FLOPS Overview," PowerPoint Presentation.

[72] Boeing Commerical Airplanes, *737: Airplane Characteristics for Airport Planning*, Sept. 2013, D6-58325-6.

[73] Anderson, Jr., J. D., *Introduction to Flight*, 6th ed., McGraw-Hill, New York, NY, 2008, pp. 451-462.

[74] Phoenix Integration, Inc., Blacksburg, VA, *ModelCenter 11.1 Manual: Darwin Algorithm*, 2014.

[75] Booker, A. J., "Design and Analysis of Computer Experiments," *7th AIAA/USAF/NASA/ISSMO Symposium on Multidisciplinary Analysis & Optimization*, St. Louis, MO, Sept. 1998, pp. 118–128, AIAA-98-4757.

[76] Audet, C., Dennis, J. E., Moore, D. W., Booker, A. J., and Frank, P. D., "A Surrogate-Model-Based Method for Constrained Optimization," *41st AIAA/ASCE/AHS/ASC Structures, Structural Dynamics & Materials Conference*, Long Beach, CA, Sept. 2000, AIAA-2000-2891.

[77] Busquets-Monge, S., *Application of Optimization Techniques to the Design of a Boost Power Factor Correction Converter*, Master's thesis, Virginia Polytechnic Institute and State University, Blacksburg, VA, 2001.

[78] Schmidt, D. K., *Modern Flight Dynamics*, McGraw-Hill, 2011.

[79] Stevens, B. L. and Lewis, F. L., *Aircraft Control and Simulation*, 2nd ed., John Wiley & Sons, Inc., Hoboken, NJ, 2003, pp. 129–137.

[80] Welstead, J. and Crouse, Jr., G. L., "Conceptual Design Optimization of an Augmented Stability Aircraft Incorporating Dynamic Response and Actuator Constraints," *AIAA Aerospace Sciences Meeting*, National Harbor, MD, 2014, AIAA-2014-0187.

[81] Etkin, B., *Dynamics of Atmospheric Flight*, Dover Publications, Inc., Mineola, NY, 2000, pp. 253–255.

[82] Anderson, J. D., *Fundamentals of Aerodynamics*, 4th ed., McGraw-Hill, New York, NY, 2007.

[83] Bradley, M. K. and Droney, C. K., "Subsonic Ultra Green Aircraft Research: Phase I Final Report," Tech. Rep. NASA/CR-2011-216847, Boeing Research and Development, Huntington Beach, CA, Apr. 2011.

[84] Bradley, M. K. and Droney, C. K., "Subsonic Ultra Green Aircraft Research Phase II: N+4 Advanced Concept Development," Tech. Rep. NASA/CR-2012-217556, Boeing Research and Development, Huntington Beach, CA, May 2012.

[85] Garmendia, D., Chakraborty, I., Trawick, D., and Mavris, D. N., "Assessment of Electrically Actuated Redundant Control Surface Layouts for a Hybrid Wing Body Concept," *14th AIAA Aviation Technology, Integration, and Operations Conference*, American Institute of Aeronautics and Astronautics, Atlanta, GA, 2014, AIAA-2014-2428.

[86] MacFarlane, A. G. J., "The Calculation of Functionals of the Time and Frequency Response of a Linear Constant Coefficient Dynamical System," *Quarterly Journal of Mechanics and Applied Mathematics*, Vol. 16, No. 2, 1963.

Appendices

Appendix A

Dynamic System Full Matrix Definitions

The matrices of the fully coupled, perturbation equations are provided below. These matrices are used in Eqs. 4.1, 4.3, and 4.6.

$$E = \begin{bmatrix} m & 0 & \frac{C_{D_{\dot{\alpha}}}\,S\,c\,q_{\infty}}{2\,\bar{U}^2} & 0 & 0 & 0 & 0 & 0 & 0 \\ 0 & m - \frac{C_{Y_{\dot{\beta}}}\,S\,b\,q_{\infty}}{2\,\bar{U}^2} & 0 & 0 & 0 & 0 & 0 & 0 & 0 \\ 0 & 0 & m + \frac{C_{L_{\dot{\alpha}}}\,S\,c\,q_{\infty}}{2\,\bar{U}^2} & 0 & 0 & 0 & 0 & 0 & 0 \\ 0 & -\frac{C_{l_{\dot{\beta}}}\,S\,b^2\,q_{\infty}}{2\,\bar{U}^2} & 0 & I'_X & 0 & -I'_{XZ} & 0 & 0 & 0 \\ 0 & 0 & -\frac{C_{m_{\dot{\alpha}}}\,S\,c^2\,q_{\infty}}{2\,\bar{U}^2} & 0 & I'_Y & 0 & 0 & 0 & 0 \\ 0 & -\frac{C_{n_{\dot{\beta}}}\,S\,b^2\,q_{\infty}}{2\,\bar{U}^2} & 0 & -I'_{XZ} & 0 & I'_Z & 0 & 0 & 0 \\ 0 & 0 & 0 & 0 & 0 & 0 & 1 & 0 & -\sin\left(\bar{\theta}\right) \\ 0 & 0 & 0 & 0 & 0 & 0 & 0 & \cos\left(\bar{\phi}\right) & \cos\left(\bar{\theta}\right)\,\sin\left(\bar{\phi}\right) \\ 0 & 0 & 0 & 0 & 0 & 0 & 0 & -\sin\left(\bar{\phi}\right) & \cos\left(\bar{\phi}\right)\,\cos\left(\bar{\theta}\right) \end{bmatrix} \tag{A.1}$$

$$\hat{A}(:,1:3) = \frac{S\,q_{\infty}}{\bar{U}} \times$$

$$\begin{bmatrix} C_{T_{X_u}} - C_{D_u} + C_{T_{Z_u}}\,\bar{\alpha} + \frac{2\,g\,m\,\sin\left(\bar{\theta}\right)}{S\,q_{\infty}} & \frac{\bar{R}\,\bar{U}\,m}{S\,q_{\infty}} - C_{D_{\beta}} & \bar{C}_L - C_{D_{\alpha}} + C_{T_{X_{\alpha}}} + C_{T_{Z_{\alpha}}}\,\bar{\alpha} \\ \frac{C_{T_{Y_u}}\,q_{\infty} + C_{Y_u}\,q_{\infty}}{q_{\infty}} + \frac{\bar{R}\,\bar{U}\,m - 2\,g\,m\,\cos\left(\bar{\theta}\right)\,\sin\left(\bar{\phi}\right)}{S\,q_{\infty}} & C_{T_{Y_{\beta}}} + C_{Y_{\beta}} & 0 \\ C_{T_{Z_u}} - C_{L_u} - C_{T_{X_u}}\,\bar{\alpha} - \frac{2\,g\,m\,\cos\left(\bar{\phi}\right)\,\cos\left(\bar{\theta}\right)}{S\,q_{\infty}} & 0 & C_{T_{Z_{\alpha}}} - C_{L_{\alpha}} - \bar{C}_D - C_{T_{X_{\alpha}}}\,\bar{\alpha} \\ b\,\left(C_{T_{l_u}} + C_{l_u} + C_{T_{n_u}}\,\bar{\alpha}\right) & b\,\left(C_{T_{l_{\beta}}} + C_{l_{\beta}} + C_{T_{n_{\beta}}}\,\bar{\alpha}\right) & -\bar{C}_n\,b \\ c\,\left(C_{T_{m_u}} + C_{m_u}\right) - \frac{2\,I'_{XZ}\,\bar{R}^2}{S\,q_{\infty}} & 0 & c\,\left(C_{T_{m_{\alpha}}} + C_{m_{\alpha}}\right) \\ b\,\left(C_{T_{n_u}} + C_{n_u} - C_{T_{l_u}}\,\bar{\alpha}\right) & b\,\left(C_{T_{n_{\beta}}} + C_{n_{\beta}} - C_{T_{l_{\beta}}}\,\bar{\alpha}\right) & \bar{C}_l\,b \\ 0 & 0 & 0 \\ 0 & 0 & 0 \\ 0 & 0 & 0 \end{bmatrix} \tag{A.2}$$

$$\hat{A}(:,4:9) = \frac{S\,q_\infty}{\bar{U}}\times$$

$$\begin{bmatrix} 0 & -\frac{C_{D_q}\,c}{2} & 0 & 0 & -\frac{\bar{U}\,g\,m\,\cos\left(\bar{\theta}\right)}{S\,q_\infty} & 0 \\ \frac{C_{Y_p}\,b}{2} & 0 & \frac{C_{Y_r}\,b}{2}-\frac{\bar{U}^2\,m}{S\,q_\infty} & \frac{\bar{U}\,g\,m\,\cos\left(\bar{\phi}\right)\,\cos\left(\bar{\theta}\right)}{S\,q_\infty} & -\frac{\bar{U}\,g\,m\,\sin\left(\bar{\phi}\right)\,\sin\left(\bar{\theta}\right)}{S\,q_\infty} & 0 \\ 0 & \frac{\bar{U}^2\,m}{S\,q_\infty}-\frac{C_{L_q}\,c}{2} & 0 & -\frac{\bar{U}\,g\,m\,\cos\left(\bar{\theta}\right)\,\sin\left(\bar{\phi}\right)}{S\,q_\infty} & -\frac{\bar{U}\,g\,m\,\cos\left(\bar{\phi}\right)\,\sin\left(\bar{\theta}\right)}{S\,q_\infty} & 0 \\ \frac{C_{l_p}\,b^2}{2} & \frac{\bar{R}\,\bar{U}\,\left(I'_Y-I'_Z\right)}{S\,q_\infty} & \frac{C_{l_r}\,b^2}{2} & 0 & 0 & 0 \\ -\frac{\bar{R}\,\bar{U}\,\left(I'_X-I'_Z\right)}{S\,q_\infty} & \frac{C_{m_q}\,c^2}{2} & \frac{2\,I'_{XZ}\,\bar{R}\,\bar{U}}{S\,q_\infty} & 0 & 0 & 0 \\ \frac{C_{n_p}\,b^2}{2} & -\frac{I'_{XZ}\,\bar{R}\,\bar{U}}{S\,q_\infty} & \frac{C_{n_r}\,b^2}{2} & 0 & 0 & 0 \\ \frac{\bar{U}}{S\,q_\infty} & 0 & 0 & 0 & 0 & 0 \\ 0 & \frac{\bar{U}}{S\,q_\infty} & 0 & 0 & 0 & 0 \\ 0 & 0 & \frac{\bar{U}}{S\,q_\infty} & 0 & 0 & 0 \end{bmatrix} \tag{A.3}$$

$$\hat{B} = S\,q_\infty \begin{bmatrix} -C_{D_{\delta_e}} & 0 & -C_{L_{\delta_e}} & 0 & C_{m_{\delta_e}}\,c & 0 & 0 & 0 & 0 \\ 0 & C_{Y_{\delta_a}} & 0 & C_{l_{\delta_a}}\,b & 0 & C_{n_{\delta_a}}\,b & 0 & 0 & 0 \\ 0 & C_{Y_{\delta_r}} & 0 & C_{l_{\delta_r}}\,b & 0 & C_{n_{\delta_r}}\,b & 0 & 0 & 0 \end{bmatrix}^{\mathrm{T}} \tag{A.4}$$

$$\hat{B}_g = S\,q_\infty \begin{bmatrix} \frac{2\,g\,m\,\sin\left(\bar{\theta}\right)}{S\,\bar{U}\,q_\infty} & -\frac{C_{D_\beta}}{\bar{U}} & \frac{\bar{C}_L-C_{D_\alpha}+C_{T_{X_\alpha}}+C_{T_{Z_\alpha}}\,\bar{\alpha}}{\bar{U}} \\ \frac{2\,m\,\left(\bar{R}\,\bar{U}-g\,\cos\left(\bar{\theta}\right)\,\sin\left(\bar{\phi}\right)\right)}{S\,\bar{U}\,q_\infty} & \frac{C_{T_{Y_\beta}}+C_{Y_\beta}}{\bar{U}} & 0 \\ -\frac{2\,g\,m\,\cos\left(\bar{\phi}\right)\,\cos\left(\bar{\theta}\right)}{S\,\bar{U}\,q_\infty} & 0 & -\frac{\bar{C}_D+C_{L_\alpha}-C_{T_{Z_\alpha}}+C_{T_{X_\alpha}}\,\bar{\alpha}}{\bar{U}} \\ 0 & \frac{b\,\left(C_{T_{l_\beta}}+C_{l_\beta}+C_{T_{n_\beta}}\,\bar{\alpha}\right)}{\bar{U}} & -\frac{\bar{C}_n\,b}{\bar{U}} \\ -\frac{2\,I'_{XZ}\,\bar{R}^2}{S\,\bar{U}\,q_\infty} & 0 & \frac{c\,\left(C_{T_{m_\alpha}}+C_{m_\alpha}\right)}{\bar{U}} \\ 0 & \frac{b\,\left(C_{T_{n_\beta}}+C_{n_\beta}-C_{T_{l_\beta}}\,\bar{\alpha}\right)}{\bar{U}} & \frac{\bar{C}_l\,b}{\bar{U}} \\ 0 & 0 & 0 \\ 0 & 0 & 0 \\ 0 & 0 & 0 \end{bmatrix} \tag{A.5}$$

$$E_{aug} = \left[\begin{array}{c:ccc} E & & 0 & \\ \hdashline & 1 & 0 & 0 \\ 0 & 0 & 1 & 0 \\ & 0 & 0 & 1 \end{array}\right] \tag{A.6}$$

$$\hat{A}_{aug} = \left[\begin{array}{c:ccc} \hat{A} & & \hat{B} & \\ \hdashline & -{}^{1}/_{\tau} & 0 & 0 \\ 0 & 0 & -{}^{1}/_{\tau} & 0 \\ & 0 & 0 & -{}^{1}/_{\tau} \end{array}\right] \tag{A.7}$$

$$\hat{B}_u = \begin{bmatrix} 0 & 0 & 0 & 0 & 0 & 0 & 0 & 0 & 0 & {}^{1}/_{\tau} & 0 & 0 \\ 0 & 0 & 0 & 0 & 0 & 0 & 0 & 0 & 0 & 0 & {}^{1}/_{\tau} & 0 \\ 0 & 0 & 0 & 0 & 0 & 0 & 0 & 0 & 0 & 0 & 0 & {}^{1}/_{\tau} \end{bmatrix}^{\mathrm{T}} \tag{A.8}$$

$$\hat{B}_{g_{aug}} = S\, q_{\infty} \left[\begin{array}{c:ccc} & 0 & 0 & 0 \\ \hat{B}_g^{\mathrm{T}} & 0 & 0 & 0 \\ & 0 & 0 & 0 \end{array}\right]^{\mathrm{T}} \tag{A.9}$$

The symbols used in Eqs. A.1–A.9 are defined as

b = wingspan

q_{∞} = dynamic pressure

$\bar{\alpha}$ = steady-state angle of attack

$\bar{R}$ = steady-state roll rate

$I'_X,\ I'_Y,\ I'_Z$ = stability axis mass moments of inertia

S = wing reference area

m = aircraft mass

g = gravity constant

c = mean aerodynamic chord

I'_{XZ} = stability axis cross-product of inertia

Appendix B

Derivation of the Standard PI State-feedback Constraint Equations

The derivation of Eqs. 4.22–4.24 is given in this Appendix. Equations 4.20 and 4.21 from Section 4.2.1 are repeated here for clarity.

$$g \equiv A_c^{\mathrm{T}} P + P A_c + Q + K^{\mathrm{T}} R K = 0 \tag{B.1}$$

$$\mathscr{H} = tr(PX) + tr(gS) \tag{B.2}$$

For the derivation of the state-feedback constraint equations some matrix calculus properties are required and are given as [4]

$$tr(AB) = tr(BA) \tag{B.3}$$

$$\frac{\partial}{\partial B} tr(ABC) = A^{\mathrm{T}} C^{\mathrm{T}} \tag{B.4}$$

$$\frac{\partial y}{\partial B^{\mathrm{T}}} = \left[\frac{\partial y}{\partial B}\right]^{\mathrm{T}} \tag{B.5}$$

Taking the partial derivative of Eq. B.2 with respect to P gives

$$0 = \frac{\partial \mathscr{H}}{\partial P} = X^{\mathrm{T}} + \frac{\partial}{\partial P}\left(tr\left(gS\right)\right) \tag{B.6}$$

Expanding the last term on the right side of Eq. B.6 to get

$$\frac{\partial}{\partial P}\left[tr\left(gS\right)\right] = \frac{\partial}{\partial P}\left[tr\left(A_c^{\mathrm{T}} P S\right)\right] + \frac{\partial}{\partial P}\left[tr\left(P A_c^{\mathrm{T}} S\right)\right] \tag{B.7}$$

which simplifies to

$$0 = A_c S + S A_c^{\mathrm{T}} + X \tag{B.8}$$

as given in Eq. 4.23. Taking the derivative of the Hamiltonian with respect to the matrix of Lagrange multipliers is straightforward resulting in the original constraint equation, g, given in Eq. B.9.

$$\frac{\partial \mathscr{H}}{\partial S} = \frac{\partial}{\partial S}\left[tr\left(PX\right) + tr\left(gS\right)\right] = g \tag{B.9}$$

The final derivative of the Hamiltonian is taken with respect to the gain matrix, K

$$\frac{\partial \mathscr{H}}{\partial K} = \frac{\partial}{\partial K}\left[tr\left(\overset{①}{A_c^{\mathrm{T}}}PS\right) + tr\left(\overset{②}{P}A_cS\right) + tr\left(QS\right) + tr\left(\overset{③}{K^{\mathrm{T}}}RKS\right)\right] \tag{B.10}$$

where each term will be examined separately and are numbered accordingly. The term containing Q is independent of K and therefore has been neglected. Looking at the first term of Eq. B.10 and expanding for A_c^{T}

$$tr\left(A_c^{\mathrm{T}}PS\right) = tr\left[\left(A - BK\right)^{\mathrm{T}}PS\right] = tr\left(A^{\mathrm{T}}PS\right) - tr\left(K^{\mathrm{T}}B^{\mathrm{T}}PS\right) \tag{B.11}$$

The first term on the right hand side of Eq. B.11 is independent of the gain matrix goes to zero as the partial derivative is taken with respect to K. The second term on the right hand side of Eq. B.11 is a function of both K and K^{T} requiring the use of the matrix property shown in Eq. B.5.

$$\frac{\partial}{\partial K}\left[-tr\left(K^{\mathrm{T}}B^{\mathrm{T}}PS\right)\right] = \left\{\frac{\partial}{\partial K^{\mathrm{T}}}\left[-tr\left(K^{\mathrm{T}}B^{\mathrm{T}}PS\right)\right]\right\}^{\mathrm{T}} = -B^{\mathrm{T}}PS \tag{B.12}$$

Repeating the same methodology of Eqs. B.5 and B.12 on the second term of Eq. B.10 yields

$$tr\left(PA_cS\right) = tr\left[P\left(A - BK\right)S\right] = tr\left(PAS\right) - tr\left(PBKS\right) \tag{B.13}$$

$$\frac{\partial}{\partial K}\left[-tr\left(PBKS\right)\right] = -B^{\mathrm{T}}PS \tag{B.14}$$

Finally, the third term in Eq. B.10 is a function of both K and K^{T} and so the product rule must be employed using the matrix calculus properties above to obtain

$$\frac{\partial}{\partial K}\left[tr\left(K^{\mathrm{T}}RKS\right)\right] = \left(K^{\mathrm{T}}R\right)^{\mathrm{T}}(S)^{\mathrm{T}} = RKS \tag{B.15}$$

$$\left[\frac{\partial}{\partial K^{\mathrm{T}}}\left(tr\left(K^{\mathrm{T}}RKS\right)\right)\right]^{\mathrm{T}} = \left[\frac{\partial}{\partial K^{\mathrm{T}}}\left(tr\left(RKSK^{\mathrm{T}}\right)\right)\right]^{\mathrm{T}} = RKS \tag{B.16}$$

Summing the right hands side of Eqs. B.12, B.14, B.15, and B.16 and dividing by two gives

$$0 = \frac{1}{2}\frac{\partial \mathscr{H}}{\partial K} = RKS - B^{\mathrm{T}}PS \tag{B.17}$$

which is the final constraint equation for the standard performance index linear quadratic regulator of Section 4.2.1, Eq. 4.24.

Appendix C

Derivation of the Modified PI State-feedback Constraint Equations

A cost function with time-dependent weighting is defined as

$$J = \frac{1}{2}\int_0^\infty \left(t^k e^{\mathrm{T}} e + u^{\mathrm{T}} R u + \dot{z}^{\mathrm{T}} W \dot{z}\right) dt \tag{C.1}$$

with the following:

$$\begin{aligned} u &= -Kx \\ e &= z = Hx \\ P &= H^{\mathrm{T}} H \end{aligned} \tag{C.2}$$

Substituting Eq. C.2 into Eq. C.1 gives

$$J = \frac{1}{2}\int_0^\infty \left[t^k x^{\mathrm{T}} P x + x^{\mathrm{T}}\left(K^{\mathrm{T}} R K + A_c^{\mathrm{T}} H^{\mathrm{T}} W H A_c\right) x\right] dt \tag{C.3}$$

Splitting the cost function into two integrals

$$J = \frac{1}{2}\int_0^\infty t^k x^{\mathrm{T}} P x dt + \frac{1}{2}\int_0^\infty x^{\mathrm{T}}(K^{\mathrm{T}} R K + A_c^{\mathrm{T}} H^{\mathrm{T}} W H A_c) x dt \tag{C.4}$$

Using the method of integration by parts where $u = t^k$, $du = kt^{(k-1)}dt$, $dv = x^{\mathrm{T}} P x$, and $dv = x^{\mathrm{T}} P x$ and define $-\frac{d}{dt}(x^{\mathrm{T}} P_0 x) = x^{\mathrm{T}} P x$, Eq. C.4 can be rewritten as [86]

$$J = \frac{1}{2}\left[-t^k x^{\mathrm{T}} P_0 x\Big|_0^\infty + \int_0^\infty k t^{k-1} x^{\mathrm{T}} P_0 x dt\right] + \frac{1}{2}\int_0^\infty x^{\mathrm{T}}(K^{\mathrm{T}} R K + A_c^{\mathrm{T}} H^{\mathrm{T}} W H A_c) x dt \tag{C.5}$$

For an asymptotically stable system this simplifies down to

$$J = \frac{1}{2}\int_0^\infty kt^{k-1}x^{\mathrm{T}}P_0xdt + \frac{1}{2}\int_0^\infty x^{\mathrm{T}}(K^{\mathrm{T}}RK + A_c^{\mathrm{T}}H^{\mathrm{T}}WHA_c)xdt \tag{C.6}$$

The first iteration of the cost function in Eq. C.6 is subject to the constraint [4]

$$-\frac{d}{dt}(x^{\mathrm{T}}P_0x) = x^{\mathrm{T}}Px \tag{C.7}$$

and using the definition $\dot{x} = A_cx$ in Eq. C.7 gives the first of the nested Lyapunov equations

$$A_c^{\mathrm{T}}P_0 + P_0A_c + P = 0 \tag{C.8}$$

This is the first constraint equation in a series of nested Lyapunov equations that were shown in Eq. 4.31. Continuing the process for another iteration, the method of integration by parts is again employed, using Eq. C.6, with $u = kt^{(k-1)}$, $du = k\,(k-1)\,t^{(k-2)}dt$, $dv = x^{\mathrm{T}}P_0x$, and $v = -x^{\mathrm{T}}P_1x$, which defines $-\frac{d}{dt}\left(x^{\mathrm{T}}P_1x\right) = x^{\mathrm{T}}P_0x$. This gives the second iteration of the cost function as

$$\begin{aligned} J = \frac{1}{2}\Big[-kt^{(k-1)}x^{\mathrm{T}}P_1x\Big|_0^\infty + \int_0^\infty k\,(k-1)\,t^{(k-2)}x^{\mathrm{T}}P_1xdt\Big] \\ + \frac{1}{2}\int_0^\infty x^{\mathrm{T}}\left(K^{\mathrm{T}}RK + A_c^{\mathrm{T}}H^{\mathrm{T}}WHA_c\right)xdt \end{aligned} \tag{C.9}$$

which, for an asymptotically stable system, simplifies to

$$J = \frac{1}{2}\int_0^\infty k\,(k-1)\,t^{(k-2)}x^{\mathrm{T}}P_1xdt + \frac{1}{2}\int_0^\infty x^{\mathrm{T}}\left(K^{\mathrm{T}}RK + A_c^{\mathrm{T}}H^{\mathrm{T}}WHA_c\right)xdt \tag{C.10}$$

As in the previous iteration, Eq. C.10 is subject to the constraint

$$-\frac{d}{dt}\left(x^{\mathrm{T}}P_1x\right) = x^{\mathrm{T}}P_0x \tag{C.11}$$

Substituting $\dot{x} = A_c x$ into Eq. C.11 results in the second nested Lyapunov equation

$$A_c^{\mathrm{T}} P_1 + P_1 A_c + P_0 = 0 \tag{C.12}$$

The process of integrating the performance index by parts can be repeated until the following is obtained

$$J = \frac{1}{2} \int_0^{\infty} \prod_{n=0}^{k-1} (k-n)\, x^{\mathrm{T}} P_{k-1} x dt + \frac{1}{2} \int_0^{\infty} x^{\mathrm{T}} (K^{\mathrm{T}} R K + A_c^{\mathrm{T}} H^{\mathrm{T}} W H A_c) x dt \tag{C.13}$$

which can be simplified down to

$$J = \frac{1}{2} \int_0^{\infty} x^{\mathrm{T}} (k! P_{k-1} + K^{\mathrm{T}} R K + A_c^{\mathrm{T}} H^{\mathrm{T}} W H A_c) x dt \tag{C.14}$$

Define

$$-\frac{d}{dt} x^{\mathrm{T}} P_k x = x^{\mathrm{T}} (k! P_{k-1} + K^{\mathrm{T}} R K + A_c^{\mathrm{T}} H^{\mathrm{T}} W H A_c) x \tag{C.15}$$

When the left hand side of Eq. C.15 is substituted into Eq. C.14 and evaluated at the limits for an asymptotically stable system, the result is

$$J = \frac{1}{2} x^{\mathrm{T}}(0) P_k x(0) \tag{C.16}$$

Using $\dot{x} = A_c x$ in Eq. C.15, the last Lyapunov equation is found to be

$$A_c^{\mathrm{T}} P_k + P_k A_c^{\mathrm{T}} + k! P_{k-1} + K^{\mathrm{T}} R K + A_c^{\mathrm{T}} H^{\mathrm{T}} W H A_c = 0 \tag{C.17}$$

This is the last of the nested Lyapunov equations which are constraints to the solution to the modified performance index, Eq. C.16. The nested Lyapunov equations are summarized below which matches Eq. 4.31 of Section 4.2.2.

$$\begin{aligned}
0 &= g_0 \equiv A_c^{\mathrm{T}} P_0 + P_0 A_c + P \\
0 &= g_1 \equiv A_c^{\mathrm{T}} P_1 + P_1 A_c + P_0 \\
&\vdots \\
0 &= g_{k-1} \equiv A_c^{\mathrm{T}} P_{k-1} + P_{k-1} A_c + P_{k-2} \\
0 &= g_k \equiv A_c^{\mathrm{T}} P_k + P_k A_c + k! P_{k-1} + K^{\mathrm{T}} R K + A_c^{\mathrm{T}} H^{\mathrm{T}} W H A_c
\end{aligned} \tag{C.18}$$

The Hamiltonian for the modified performance index is defined as [4]

$$\mathscr{H} = \frac{1}{2} tr\left(P_k X\right) + \frac{1}{2} tr\left(g_0 S_0\right) + \frac{1}{2} tr\left(g_1 S_1\right) + \cdots + \frac{1}{2} tr\left(g_{k-1} S_{k-1}\right) + \frac{1}{2} tr\left(g_k S_k\right) \tag{C.19}$$

where the derivative with respect to each independent variable P_i, S_i, and K is taken, where $i = 0, 1, 2, \ldots, k-1, k$. Taking the derivative of the Hamiltonian with respect to the matrix of Lagrange multipliers, S_0, S_1, …, S_{k-1}, and S_k results in

$$\frac{\partial \mathscr{H}}{\partial S_i} = g_i, \qquad i = 0, 1, 2, \ldots, k \tag{C.20}$$

which are the nested Lyapunov equations given in Eq. C.18.

First, taking the partial derivative of the Hamiltonian with respect to P_0 gives

$$0 = \frac{\partial \mathscr{H}}{\partial P_0} = \frac{1}{2} \frac{\partial}{\partial P_0} = \left[tr\left(g_0 S_0\right) + tr\left(g_1 S_1\right) \right] \tag{C.21}$$

where the terms independent of P_0 have been removed for clarity. Expanding and simplifying Eq. C.21 results in

$$A_c S_0 + S_0 A_c^{\mathrm{T}} + S_1 = 0 \tag{C.22}$$

The process repeats following the same pattern as Eq. C.22 until the $k-1$ term is reached giving

$$0 = \frac{\partial \mathscr{H}}{\partial P_{k-1}} = A_c S_{k-1} + S_{k-1} A_c^{\mathrm{T}} + k! S_k \tag{C.23}$$

Finally, taking the derivative of the Hamiltonian with respect to P_k gives

$$0 = \frac{\partial \mathscr{H}}{\partial P_k} = A_c S_k + S_k A_c^{\mathrm{T}} + X \tag{C.24}$$

The nested Lyapunov equations of Lagrange multipliers is summarized as

$$\begin{aligned}
0 &= A_c S_k + S_k A_c^{\mathrm{T}} + X \\
0 &= A_c S_{k-1} + S_{k-1} A_c^{\mathrm{T}} + k! S_k \\
&\vdots \\
0 &= A_c S_1 + S_1 A_c^{\mathrm{T}} + S_2 \\
0 &= A_c S_0 + S_0 A_c^{\mathrm{T}} + S_1
\end{aligned} \tag{C.25}$$

Taking the derivative of the Hamiltonian with respect to the gain matrix, K, is best shown by breaking down Eq. C.19 into the individual terms. The second term on the right hand side of Eq. C.19 is the first term dependent on K. The first partial derivative gives

$$\frac{1}{2}\frac{\partial}{\partial K} tr\left(g_0 S_0\right) = \frac{1}{2}\frac{\partial}{\partial K}\left[tr\left(A_c^{\mathrm{T}} P_0 S_0\right) + tr\left(P_0 A_c S_0\right) + tr\left(P S_0\right)\right] \tag{C.26}$$

The last term on the right hand side of Eq. C.26 is independent of K and is therefore zero. The closed-loop state matrix is dependent on K and must be expanded. The expanded right hand side, neglecting the last term in Eq. C.26 produces

$$\frac{1}{2}\frac{\partial}{\partial K}\left\{tr\Big[\left(A - BK\right)^{\mathrm{T}} P_0 S_0\Big] + tr\Big[P_0\left(A - BK\right) S_0\Big]\right\} \tag{C.27}$$

Using the matrix properties given in Eqs. B.3–B.5, the solution to Eq. C.27 is

$$\frac{1}{2}\frac{\partial}{\partial K} tr\left(g_0 S_0\right) = -B^{\mathrm{T}} P_0 S_0 \tag{C.28}$$

This process can be repeated for all terms of the form $\frac{1}{2} tr\left(g_i S_i\right)$ in the Hamiltonian, for $i = 0, 1, \ldots, k-1$, with the solution being

$$\frac{1}{2}\frac{\partial}{\partial K} tr\left(g_i S_i\right) = -B^{\mathrm{T}} P_i S_i, \qquad i = 0, 1, \ldots, k-1 \tag{C.29}$$

Looking at the last term of the Hamiltonian, the k^{th} term, and neglecting terms independent of K gives

$$\begin{aligned}&\frac{1}{2}\frac{\partial}{\partial K} tr\left(g_k S_k\right) = \\ &\qquad \frac{1}{2}\frac{\partial}{\partial K} tr\left[tr\left(A_c^{\mathrm{T}} P_k S_k\right) + tr\left(P_k A_c S_k\right) + tr\left(K^{\mathrm{T}} R K S_k\right) + tr\left(A_c^{\mathrm{T}} H^{\mathrm{T}} W H A_c S_k\right)\right]\end{aligned} \tag{C.30}$$

The first two terms of Eq. C.30 will give $-B^{\mathrm{T}} P_k S_k$, which is of the same form as Eq. C.29. Taking the derivative of the third term is quite simple and results in

$$\frac{1}{2}\frac{\partial}{\partial K}\left[tr\left(K^{\mathrm{T}} R K S_k\right)\right] = \frac{1}{2}\left(R K S_k + R K S_k\right) = R K S_k \tag{C.31}$$

The last term of the Hamiltonian needs to be expanded and factored in order to take the partial derivative with respect to K. First, substituting for the closed-loop state matrix gives

$$\frac{1}{2}\frac{\partial}{\partial K}\left[tr\left(A_c^{\mathrm{T}} H^{\mathrm{T}} W H A_c S_k\right)\right] = \frac{1}{2}\frac{\partial}{\partial K}\left\{tr\left[\left(A^{\mathrm{T}} - K^{\mathrm{T}} B^{\mathrm{T}}\right) H^{\mathrm{T}} W H \left(A - BK\right) S_k\right]\right\} \tag{C.32}$$

Expanding the right hand side of Eq. C.32 results in four terms to look at individually as

$$\begin{split}\frac{1}{2}\frac{\partial}{\partial K}tr\Bigg(A^{\mathrm{T}}H^{\mathrm{T}}\overset{\text{①}}{W}HAS_k-A^{\mathrm{T}}H^{\mathrm{T}}\overset{\text{②}}{W}HBKS_k-\\ K^{\mathrm{T}}B^{\mathrm{T}}H^{\mathrm{T}}\overset{\text{③}}{W}HAS_k+K^{\mathrm{T}}B^{\mathrm{T}}H^{\mathrm{T}}\overset{\text{④}}{W}HBKS_k\Bigg)\end{split} \tag{C.33}$$

The first term in Eq. C.33 is independent of K and therefore goes to zero. Taking the derivative of the second and third term results in

$$\frac{1}{2}\frac{\partial}{\partial K}tr\left(-A^{\mathrm{T}}H^{\mathrm{T}}WHBKS_k\right)=-\frac{1}{2}B^{\mathrm{T}}H^{\mathrm{T}}WHAS_k \tag{C.34}$$

$$\frac{1}{2}\frac{\partial}{\partial K}tr\left(-K^{\mathrm{T}}B^{\mathrm{T}}H^{\mathrm{T}}WHAS_k\right)=-\frac{1}{2}B^{\mathrm{T}}H^{\mathrm{T}}WHAS_k \tag{C.35}$$

Using the chain rule in the fourth term, the derivative is found be

$$\frac{1}{2}\frac{\partial}{\partial K}tr\left(K^{\mathrm{T}}B^{\mathrm{T}}H^{\mathrm{T}}WHBKS_k\right)=B^{\mathrm{T}}H^{\mathrm{T}}WHBKS_k \tag{C.36}$$

Summing all the components gives the full solution

$$\begin{split}\frac{\partial\mathscr{H}}{\partial K}=RKS_k-B^{\mathrm{T}}\left(P_0S_0+P_1S_1+\cdots+P_{k-1}S_{k-1}+P_kS_k\right)\\ +B^{\mathrm{T}}H^{\mathrm{T}}WHBKS_k-B^{\mathrm{T}}H^{\mathrm{T}}WHAS_k\end{split} \tag{C.37}$$

When using a simplex algorithm for the minimization of the performance index, only Eqs. C.16 and C.18 need to be used. However, when a gradient-based minimization routine is used, Eqs. C.16, C.18, C.25, and C.37 need to be used, where Eq. C.37 is used as the gradient.